Enhanced vibration suppression using linear and nonlinear locally resonant acoustic metamaterials, inerters and friction dampers

Thesis submitted to the University of Nottingham for the degree of
Doctor of Philosophy, October 2024.

Yuhao Liu

20322239

Supervised by

Jian Yang
Xiaosu Yi

Signature Yuhao Liu.

Date 30 / 6 / 2024

Abstract

Vibration suppression and noise control of mechanical equipment are critical aspects of engineering and design, aiming to mitigate the adverse effects of unwanted but inevitable vibrations and noise on human comfort, structural integrity, and overall system performance. This study focused on passive control methods that utilised isolators and absorbers to isolate or dissipate vibrations. Vibration control faces several challenges, including the need to address space constraints, low-frequency control, nonlinear dynamic characteristics, and complex coupled system dynamics. Advances in control techniques, manufacturing, and computational tools have facilitated significant progress in these fields. However, further research and development about novel structural design and analysis methods are needed to overcome challenges and achieve optimal control strategies for diverse applications. This thesis has dedicated considerable efforts and endeavors to address the aforementioned challenges.

The study began by proposing the application of linear and geometrically nonlinear inerter-based resonator in locally resonant acoustic metamaterials (LRAM) and their performance on the low-frequency wave attenuation was evaluated. The LRAM was modeled as 1-D chain system composed of mass-in-mass unit cells connected by springs, and the geometrical nonlinearity was achieved by two lateral inerters linking the resonator and lumped mass symmetrically with respect to the horizontal springs. Compared with linear inerter-based LRAM, the proposed nonlinear inerter-based structure had the property of a low-frequency bandgap with sufficient width. The nonlinearity could extend the original material parameter restrictions, leading to lower-frequency bandgap.

Furthermore, a diatomic-chain LRAM structure with a negative-stiffness mechanism was presented for enhanced suppression of vibration transmission. The bandgap properties were studied and shown to enhance perfor-

mance benefits by introducing two extra bandgaps that exploit Bragg scattering. With the application of negative-stiffness mechanism, the bandgap shifted toward the lower frequency range, effective from zero frequency, thus achieving ultralow frequency vibration control. The proposed implementation was shown to yield desirable bandgap properties, providing potential benefits for vibration suppression.

A novel Flexnertia metastructure concept was subsequently proposed to perform vibration suppression through coupling rotational inerter to structural flexural motion. Theoretical analysis and experimental test of the proposed structure with emphasis on dissipating structural flexural motion was exhibited. The results were in good agreement, confirming that the average overall response of the metastructure was significantly reduced. The attenuation became most pronounced in the low-frequency range where structures tend to suffer most due to high response around the regime of the first flexural modes.

The study further explored a coupled structure based on a nonlinear hysteresis friction damper subjected to harmonic forces for vibration suppression. The forced response was well controlled by the normal force applied to the friction damper, and the amplitude and frequency of the resonance peaks could be varied within a certain range by changing force magnitude. The results indicated that the friction damper participates in the energy dissipation in the frequency band around the resonance frequency, thereby enabling high-amplitude vibration filtering. It confirmed that such friction dampers have the potential to be designed to be adjustable and meet different vibration control objectives.

Overall, the research results presented herein make a significant contribution to the development of linear and nonlinear advanced mechanisms for vibration control. Several novel configurations were demonstrated with obvious dynamic advantages from the perspective of power flow and vibration transfer. Further research endeavors were warranted to concentrate on the nonlinear systems based on the excellent properties of acoustic metamaterials, inerters and friction dampers.

Keywords: Vibration control; Locally resonant acoustic metamaterial; Inerter; Hysteresis friction damper; Nonlinear; Vibration power flow.

Acknowledgements

It has been almost eight years since I started my undergraduate studies at UNNC. This place has held so many experiences and memories that I will forever cherish.

First and foremost, I would like to express my sincere gratitude to my lead supervisor, Prof. Jian Yang, who advised and encouraged me to embark on the path of pursuing a PhD degree. The scientific work and findings of this thesis would not be possible without all the support and guidance he provided. The promotion to full professor is a recognition and reward for his passion and dedication to work, congratulations!

I would like to express my gratitude to my co-supervisor Prof. Xiaosu Yi for his support and invaluable comments. My gratitude is also extended to my internal examiner Dr. Yung-Tsang Chen for his suggestions on my research work. I would like to thank my colleagues for their support, keep up the good work! Thanks to the companionship of my friends, Jiayi Wang, Yuan Chen, and Dr. Weixuan Chen.

A deep gratitude is extended to Dr. Dimitrios Chronopoulos, who invited me to exchange at KU Leuven. I really enjoyed living and studying there, thanks to my tutors Dr. Claus Claeys and Dr. Elke Deckers, as well as my colleagues Dr. Régis Boukadia and especially Dr. Luiz Henrique Marra da Silva Ribeiro, who helped me a lot with my research and led me to enjoy fitness and bodybuilding. More importantly, I met my girlfriend and best friend, Qianwen Liang, there. Thank you for all the good things you have brought to me, thank you for accompanying me to bring my dreams into reality, and thank you for letting me feel pure love and being loved.

I would like to acknowledge the full scholarship from the New Materials Institute and the financial support for exchange abroad from the China

Scholarship Council.

Special thanks go to my parents and sister, who always believe in me and provide unconditional and endless love. They have made my life complete and sustained me through these difficult times.

List of Publications

1. **Liu, Y.**, Yang, J., Yi, X., and Chronopoulos, D. (2022). Enhanced suppression of low-frequency vibration transmission in metamaterials with linear and nonlinear inerters. *Journal of Applied Physics*, 131(10). [Chapter 4]

2. **Liu, Y.**, Yang, J., Yi, X., Guo, W., Feng, Q., and Chronopoulos, D. (2022). Enhanced vibration suppression using diatomic acoustic metamaterial with negative stiffness mechanism. *Engineering Structures*, 271:114939. [Chapter 5]

3. **Liu, Y.**, Yang, J., Zhou, C., Elmadih, W., Zhu, J., and Chronopoulos, D. (2023). Flexnertia: A novel dissipation mechanism for structural vibration reduction through coupling of flexural motion with an inerter. *Mechanics of Advanced Materials and Structures*, pages 1–10. [Chapter 6]

4. **Liu, Y.**, Dai, W., Shi, B., Chronopoulos, D., and Yang, J. (2024). Enhanced suppression of vibration response and energy transfer by using nonlinear hysteresis friction damper. *Nonlinear Dynamics*, 112(14):11765–11783. [Chapter 7]

5. **Liu, Y.**, Chronopoulos, D., and Yang, J. (2022). Vibration power flow and wave transmittance analysis of inerter-based dual-resonator acoustic metamaterial. In Dimitrovová, Z., Biswas, P., Gonçalves, R., and Silva, T., editors, *Recent Trends in Wave Mechanics and Vibrations*, pages 966–975. Springer International Publishing.

6. Yang, J., Chao, C., **Liu, Y.** (2024). A harmonic-balance power flow analysis method for nonlinear vibration systems. In *IUTAM Symposium on Nonlinear dynamics for design of mechanical systems across different length/time scales* (Accepted).

Contents

List of Tables

List of Figures

Acronyms

1D	One Dimensional
2-DoF	Two Degrees of Freedom
AFT	Alternating Frequency–Time
AM	Acoustic Metamaterials
FE	Finite Element
FEM	Finite Element Method
GNIM	Geometrically Nonlinear Inertance Mechanism
HB	Harmonic Balance
LR	Local Resonance
LRAM	Local Resonant Acoustic Metamaterials
NSM	Negative-Stiffness Mechanism
PFA	Power Flow Analysis
QZS	Quasi-Zero Stiffness
RK	Runge–Kutta
SDoF	Single Degree of Freedom

List of Symbols

A	Cross-section area
D, U, X, Y, Z	Nondimensional displacement
E	Young's modulus
F	Force
I	Second moment of area
L	Lattice constant
P	Power
Δ	Nondimensional relative displacement
$\Im$	Imaginary part
Ω	Nondimensional frequency
$\Re$	Real part
β	Stiffness ratio
δ	Relative displacement
λ	Inertance-to-mass ratio
μ_f	Friction coefficient
μ	Mass ratio
ω	Frequency
ϕ	Phase angle
π	Ratio of circumference to diameter
e	Natural constant

i	Imaginary unit
τ	Nondimensional time
θ	Angle
ζ	Damping ratio
b	Inertance
c	Damping coefficient
d, u, x, y, z	Displacement amplitude
k	Stiffness coefficient
l	Length
m	Mass
q	Wave number
t	Time
v	Velocity

Chapter 1

Introduction

1.1 Engineering background

High-end equipment manufacturing is a strategic emerging industry that China has vigorously cultivated and developed. The 'fourteenth five-year plan', the plan 'Made in China 2025' and other Chinese national policies have emphasised the importance of tackling key technologies in the field of high-end equipment manufacturing. China's transformation plan of raising the country's manufacturing power also puts forward higher requirements for the level of mechanical design in the new era. According to the 'Classification of Strategic Emerging Industries' issued by the National Bureau of Statistics of China (NBSPRC, 2018), high-end equipment manufacturing industries encompass various sectors such as rail transit, aviation, intelligent manufacturing, satellite and marine engineering equipment industries, etc. The vibration and acoustic performance of these equipment play a crucial role in their overall performance.

Mechanical vibration is inevitable in equipment operation, which may not only cause structural fatigue or even damage the mechanical structure, but also affect the measurement accuracy of precision instruments (Wu et al., 2016). Mechanical vibration is a significant source of noise, contributing to the adverse impact it has on human daily work and life. The presence of noise pollution in everyday life has severe consequences on the well-being of individuals as a form of environmental contamination. The physical, mental, and overall well-being of individuals are greatly affected by this noise pollution, directly impacting their quality of life. For example, the vibration and noise of vehicles such as trains and vehicles will reduce the comfort of passengers, and even break the components, becoming a security hazard.

The noise caused by the speeding train will also affect the residents around the railway, ranging from irritability and reduced sleep quality, to severe heart disease and hearing loss (Wu et al., 2007). Noise is also a worldwide problem, and the European Environment Agency (EEA) (Peris et al., 2020) provides an assessment of people exposed to high levels of environmental noise and its associated health effects in Europe in 2020, in line with new recommendations from the World Health Organisation (WHO). The report identifies noise pollution as a growing environmental problem, affecting one in five people in Europe (Fig. 1.1). Noise can disrupt sleep and make it more difficult to study at school. It can also cause or exacerbate many health problems. The report also documents actions taken to manage and reduce noise exposure and reviews progress towards policy goals. The assessment of the current state of environmental noise exposure in Europe is based on the latest data collected under the Environmental Noise Directive (END). The report also describes other relevant issues, such as inequalities in environmental noise exposure and impacts on wildlife. Hence, it is of utmost importance to prioritize the study of mechanical structure design for effective vibration control and thorough evaluation of dynamic performance. By focusing on these aspects, the negative impacts of mechanical vibration and noise pollution can be mitigated, thereby enhancing the overall performance of equipment and the well-being of individuals in various environments.

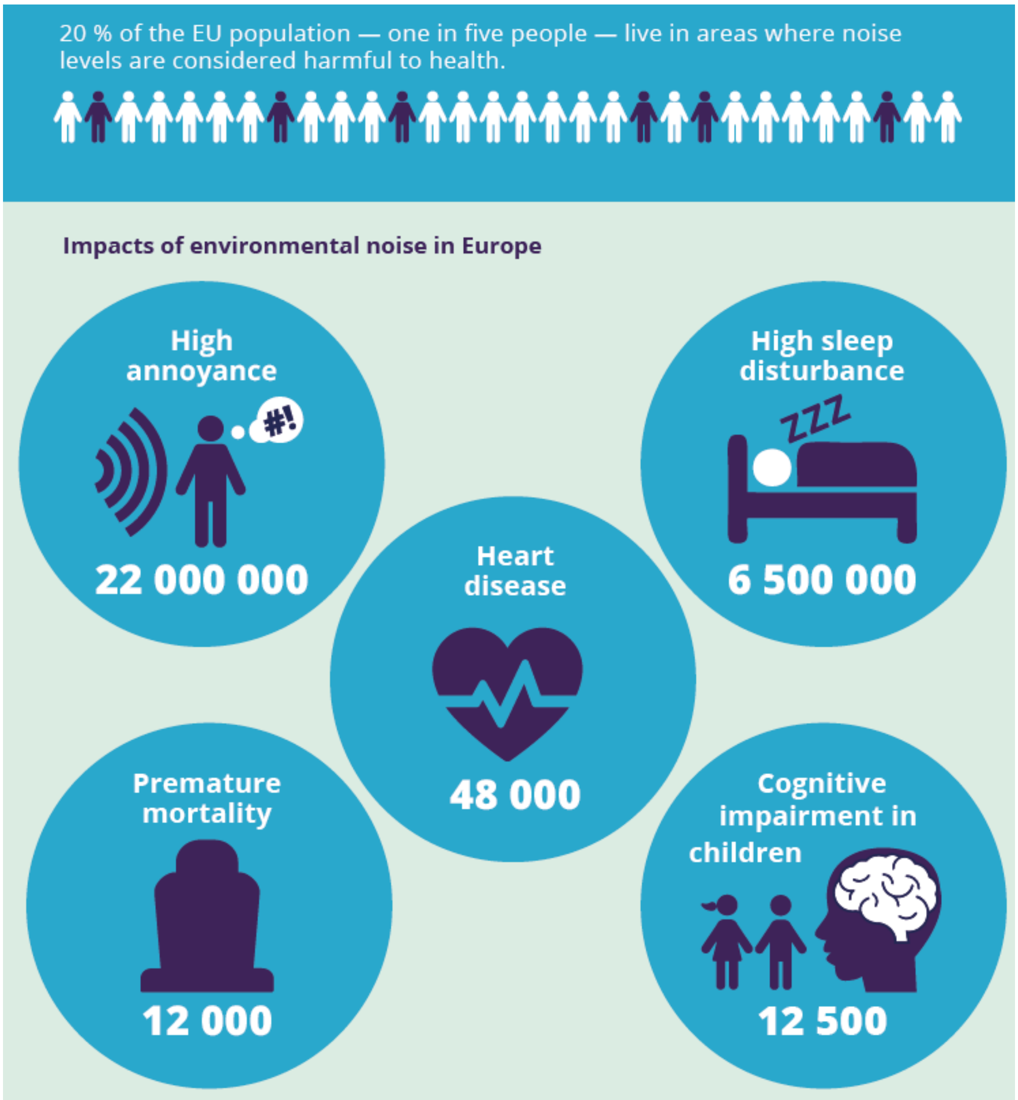

Figure 1.1: Impacts of environmental noise in Europe, data collected by EEA in 2020. (Peris et al., 2020).

New material technology is one of the main directions of scientific and technological development in the 21st century. It marks a deeper expansion of human being's understanding and application of material properties. It plays a major role in promoting the progress of science and technology and the development of the national economy. Together with the energy technology and information technology, it is one of the three pillars of modern science and technology, while the development of the energy and information industry also depends to a large extent on the development of materials. Therefore, countries with advanced industrial technology attach great importance to the research and development of new materials. Mechanical equipment is composed of materials, which themselves are composed of atoms and molecules arranged in a certain pattern. Generally, the macroscopic properties of materials such as mechanical, thermal, electromagnetic and optical properties are all determined by the microscopic atom and molecule types and their arrangement. If the microscopic composition and arrangement are determined, its mechanical, electromagnetic, thermal and other parameters will be fixed.

Since the continuous development of science and technology forces researchers to have higher and higher requirements for material performance, new material design technologies and concepts are needed (NSFC and CAS, 2012). Due to the limitations of traditional materials in practical engineering applications, artificial composite materials with special physical properties have drawn increasing attention. In September 1999, a general invitation was stated that the Defense Advanced Research Projects Agency was seeking information regarding artificially constructed materials, named 'metamaterial', that exhibit qualitatively new responses not found in nature (Ziolkowski, 2014). This invitation expressed Defense Advanced Research Projects Agency's interest in exploring the possibilities and potential of metamaterials with unique properties and characteristics. Later in 2001, Walser explained at the workshop that the choice of name came from the desire to achieve material performances 'beyond' the limitations of conventional composites (Walser, 2001). The excellent properties of metamaterials are considered resulting from the integration of artificial and external inhomogeneity. This concept inspires engineers to get rid of the performance restrictions of traditional materials to have more innovative ideas. In the past 20 years, artificial composite materials have been used in the field of dynamics to control the mechanical waves, some three-dimensional acoustic metamaterials examples are shown in Fig. 1.2.

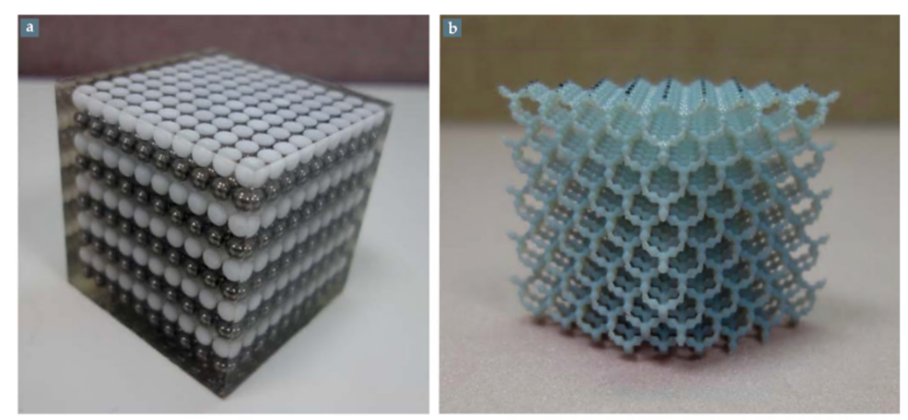

Figure 1.2: Real-world three-dimensional acoustic metamaterials (a) Sonic crystals and (b) Pentamode materials (Haberman and Guild, 2016).

The growing demand for high-performance vibration suppression mechanisms has contributed to the proposal of a new type of passive mechanical element called 'inerter', which has gained significant attention for its unique functionality and potential applications in various dynamic systems. Unlike traditional passive mechanical elements such as springs and dampers, the inerter introduces a novel concept of providing a dynamic inertance force, related to the the relative acceleration of the two terminals (Smith, 2002), that can significantly impact the behavior of mechanical systems. Since its introduction in 2001, the inerter was initially employed in the suspension systems of Formula 1 racing cars (Fig. 1.3), and has subsequently become established commercially in suspension systems for high-performance motor vehicles as the third passive element, alongside the spring and damper (Smith, 2020). One of the key advantages of the inerter is its ability to provide a purely inertial force, which is independent of displacement or velocity. This property allows for the decoupling of stiffness and damping characteristics, enabling more precise control over system dynamics. By incorporating inerter devices into mechanical systems (Papageorgiou et al., 2009), engineers can tailor the dynamic response to specific requirements, such as improving ride comfort, reducing vibrations, or enhancing energy efficiency. Despite its promising potential, the practical implementation and optimisation of inerter devices present ongoing challenges. Extensive research and development efforts are underway to refine the design, characterization, and application of inerter technology for various engineering disciplines.

Figure 1.3: One version of Penske's Formula One ball-screw inerter (Smith, 2020).

Meanwhile, most mechanical structures comprise multiple substructures interconnected through joints and they take a crucial role in the dynamic behaviour of the system (Bograd et al., 2011). Friction is generated between the contact surfaces of the two jointed components, which affects the dynamic performance of the overall coupled structure. Considering that it can convert mechanical energy into thermal energy, effectively damping vibrations and reducing their amplitudes, friction-based dampers (Fig. 1.4) are proposed (Pall et al., 1980) to utilise its energy dissipation mechanism to mitigate unnecessary vibrations, suppress resonant frequencies, and enhance the stability and performance of dynamic systems. With their simplicity, versatility, and cost-effectiveness, friction dampers continue to be valuable tools in the field of vibration control, addressing vibration-related challenges and improving the dynamics of diverse engineering applications.

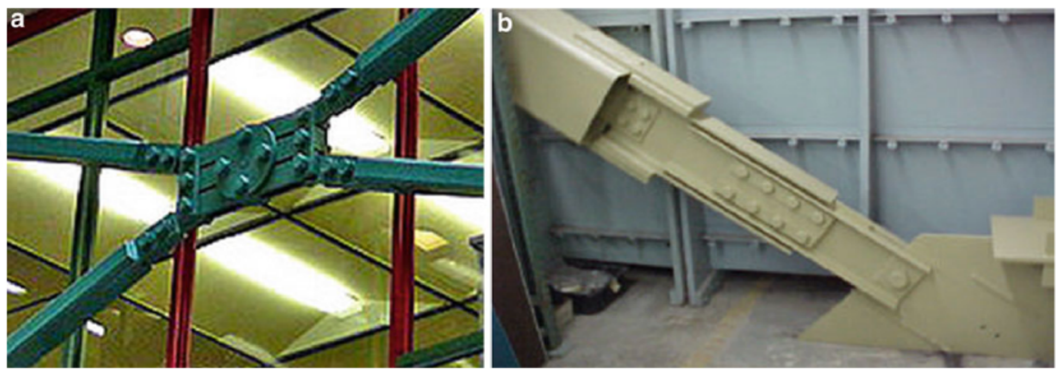

Figure 1.4: Pall friction dampers (a) installed in X-bracing at Concordia Library, Montreal, and (b) installed in single-diagonal brace at Boeing Commercial Airplane Factory Everrett, USA (Tirca, 2015).

1.2 Research motivation

Vibration control is a critical area of research that has significant implications for various engineering fields. In recent years, a lot of researchers are focusing on the exploration of various linear and nonlinear advanced mechanism for high-performance vibration control. The motivation for studying and advancing vibration control arises from several key factors:

- **Metamaterials**: Overcoming Limitations of Traditional Materials and Good Customizability

  Traditional acoustic materials and structures often have limitations in achieving desired acoustic properties. Locally resonant acoustic metamaterials offer an alternative approach to overcome these limitations by leveraging the unique properties of engineered structures and their resonant behavior, allowing for the manipulation of wave propagation, absorption, and scattering characteristics. This opens up new possibilities for designing materials and structures with tailored acoustic properties, leading to improved vibration control and energy management. By customising the unit cell design, e.g. incorporating nonlinearity, adjusting geometric parameters, and even applying other high-performance mechanical element, it is potential to develop acoustic metamaterials with advanced acoustic control capabilities.

- **Inerter**: Dynamic System Performance Enhancement and Decoupling of Stiffness and Damping

  The inerter provides an additional degree of freedom in controlling dynamic systems by introducing a dynamic inertance force. This force can be strategically utilised to improve the performance of mechanical systems in terms of stability, response time, energy efficiency, and overall dynamic behavior. The key advantages of the inerter is its ability to decouple stiffness and damping characteristics. Unlike traditional mechanical elements such as springs and dampers, the inerter provides a purely inertial force that is independent of displacement or velocity. This decoupling property enables engineers to precisely control and tailor the dynamic response of systems, leading to improved vibration isolation and system stability. By further understanding and harnessing this decoupling effect, researchers aim to develop advanced control strategies and design methodologies for a wide range of applications.

- **Friction damper**: Enhanced Energy Dissipation, Efficiency and Nonlinear Behavior

  Friction dampers offer the advantage of converting mechanical energy into heat through the dissipation of frictional forces. This energy dissipation mechanism provides an effective way of reducing the amplitude and duration of vibrations, thereby improving the dynamic response of structures. Friction dampers exhibit nonlinear behavior, which can be advantageous in certain dynamic scenarios. The nonlinear characteristics of friction dampers enable them to adapt to varying vibration amplitudes and frequencies, providing effective damping across a wide range of operating conditions. Researchers are motivated to investigate the nonlinear behavior of friction dampers, develop accurate modeling techniques, and explore the potential benefits of nonlinear damping in improving system performance and stability.

1.3 Aims and objectives

The objective of this thesis is to study linear and nonlinear advanced mechanism for high-performance vibration suppression performance. To achieve this aim and according to the current main research content mentioned above, the below points should be paid more attention:

- **Develop Innovative Metamaterial-Based Vibration Control Devices**

  The aim is to design and develop novel vibration control devices based on metamaterials. The objective is to utilise the unique properties of metamaterials to create devices that can passively suppress vibrations in mechanical systems, providing low-frequency bandgaps.

- **optimise the Design and Performance of Inerter-Based Vibration Control Systems**

  The aim is to investigate the application of inerters in mechanical vibration control and optimise the design and performance of inerter-based systems, which provide a high level of relative motion between two end, enabling effective vibration isolation and damping. The focus is on developing efficient inerter configurations and control strategies to improve overall vibration control performance.

- **Enhance the Efficiency and Effectiveness of Friction Dampers**

  The aim is to enhance the efficiency and effectiveness of friction dampers in mechanical vibration control and investigate friction damper design parameters, such as the normal force applied and friction coefficient, to improve their energy dissipation capabilities and broaden their operating range. The focus is on developing advanced friction damper designs that can effectively mitigate vibrations across a wide frequency spectrum.

- **Integration of Metamaterials, Inerters, and Friction Dampers**

  The aim is to explore the synergistic effects of combining metamaterials, inerters, and friction dampers in vibration control systems and investigate how these technologies can complement each other to provide enhanced vibration attenuation and control. The focus is on developing integrated systems that leverage the unique properties of each technology to achieve superior vibration control performance.

1.4 Thesis outline

Chapter 1 introduces the research background, motivation, aims and objectives.

Chapter 2 includes the literature review about the metamaterials, inerter and friction damper. It starts with the characteristics and current research summary of acoustic metamaterials. The inerter is then basically introduced with its properties and applications. At last the contact friction damper in jointed structure is discussed with emphasis on the hysteresis behavior.

Chapter 3 presents the fundamental theories for metamaterials and fundamental calculation for arc beam. The vibration power flow analysis method is also introduced.

Chapter 4 proposes linear and geometrical nonlinear inerter based metamaterials configurations for enhanced suppression of low-frequency vibration transmission.

Chapter 5 investigates a diatomic acoustic metamaterial configuration with negative stiffness mechanism for zero frequency vibration control.

Chapter 6 presents a novel dissipation mechanism for structural vibration reduction through coupling of flexural motion with an inerter.

Chapter 7 evaluates the dynamic performance of a friction damper with hysteresis behavior and demonstrates its application on SDoF and 2DoF coupled structure for enhanced suppression of vibration response and power transfer by tailoring contact friction.

Chapter 8 summarises the main contributions of this study, emphasizes the potential of metamaterials, inerter and friction damper in mechanical vibration control and provides recommendations for future research.

Chapter 2

Literature Review

2.1 Metamaterials

2.1.1 Locally resonant acoustic metamaterial

Noise pollution is a major global problem and, unfortunately, conventional acoustic materials fail to offer substantial progress in vibration and noise control. Metastructures are rapidly becoming a key engineering research focus as artificial composite structures can exhibit unique properties not found in natural materials. The past decade has seen the fast development of metastructures in the field of bionics (Luo et al., 2022), optics (Singh et al., 2021; Mohammadi Estakhri et al., 2019), electromagnetics (Fan et al., 2020b) and especially acoustics (Kumar et al., 2018; Kumar and Lee, 2020). Noise is one of the types of pollution that severely affects the daily life of citizens worldwide, which is mainly induced by machine vibration. The vibration of the equipment will also lead to inevitable mechanical structural fatigue or even damage, affecting service life and operational safety. While the demand for high-performance vibration control systems in society and industry continues to increase, the development and popularization of advanced technologies (Banhart, 2001) such as additive manufacturing (Fabro et al., 2020) has provided solid assistance for the realization of metastructures and their applications in vibration control. Novel 3D phononic metastructures (Muhammad and Lim, 2021a,b) were proposed and analysed analytically, numerically and experimentally, shown to be able to have wide three-dimensional complete bandgaps, beneficial for low-frequency vibration suppression.

Metamaterials were originally designed for the aim of controlling electromagnetic waves (Pendry, 2000; Sachan and Majetich, 2005). And because mechanical waves are similar to electromagnetic waves, researchers have begun investigating the analogy of using electromagnetic metamaterials to deal with sound waves (Cheng et al., 2008; Li and Chan, 2004; Milton and Willis, 2007). Acoustic metamaterials does not yet have a strict definition, but based on its development history and commonality, it can be defined as: orderly design microstructures on sub-wavelength physical scales (generally a few tenths of the controlled wavelength) to obtain artificial periodic or non-periodic structures with extraordinary acoustic or mechanical properties that conventional materials do not have (Huang et al., 2009; Wu et al., 2007). It is notable that the most intuitive impression of acoustic metamaterials is that they have special properties such as negative mass, negative elastic modulus, low frequency bandgap at resonance, and extraordinary absorption. For example, negative mass implies that the effective mass of a unit cell of a metamaterial structure may be negative over a certain range of excitation frequencies. However, its far-reaching significance lies in greatly improving researchers' ability to manipulate elastic waves.

Material parameters such as positive, negative and zero elastic modulus and mass can be realised with relative freedom through the design of unit structures, thus allowing waves to reflect, refract, or even propagate with arbitrary bending in a specific frequency range. This concept represents a brand-new composite material or structural design concept, whereby new materials are designed and manufactured as they are intended to be, based on understanding and utilising them to their fullest potential.

As one of the important branches of metamaterials, acoustic metamaterials (AMs) are investigated for vibration wave propagation suppression and sound reduction (Li et al., 2017b; Sainidou et al., 2006). Over the last few decades, extensive research has been conducted to explore the distinctive acoustic properties of acoustic metamaterials compared with conventional materials, as well as their potential applications, as shown in Fig. 2.1. Researchers have utilised the specific acoustic parameters of AMs to develop various innovative physical effects and functional acoustic devices. These include metamaterial insulators, metamaterial absorbers, topological acoustics, hydroacoustic metamaterials, programmable metamaterials and acoustic metasurfaces, among others. Despite being inspired by electromagnetic metamaterials, AMs have played a significant role in diverse applications such as architectural acoustics, urban noise control, acoustic landscape design, acoustic functional devices, acoustic stealth, acoustic imaging, and acoustic levitation (Gao et al., 2022).

Compared with phononic crystals designed to control waves through Bragg scattering (BS), which is associated with periodic crystal structures (Deymier, 2013; Jensen, 2003; Sigalas, 1992), AMs can also generate local resonance (LR) characteristics to control and guide wave propagation (Huang et al., 2009; Liu et al., 2000; Moscatelli et al., 2019; Pai, 2010; Pai

Figure 2.1: Diagram illustrating the broad categorization and application of acoustic metamaterials (Gao et al., 2022).

et al., 2014; Zhao et al., 2005). This function works based on the properties of bandgap, which is generated by periodic structures. The bandgaps can inhibit the propagation of elastic waves in specific frequency ranges and it can also be called stopband (Li et al., 2019b). They can provide a vibration-free working or processing environment for special precision instruments or equipment to improve work accuracy and reliability, extending equipment life.

However, the wave suppression properties and bandgap structure of BS and LR are evidently different from each other. As for BS, it can be used to obtain a very broad bandgap with good wave suppression performance (Jia et al., 2018). But the gaps are normally located at high-frequency areas because the center of bandgap frequency range for BS is determined by periodic configuration lattice constant and wave velocity, which means a very large structure is required with a low-frequency target BS bandgap (Jiang et al., 2017). Hence, it is confined to applying the BS mechanism for controlling low-frequency vibration because the engineering size is strictly restricted on most occasions. Since Liu et al. (2000) proposed a local resonance unit (as shown in Fig. 2.2(a)) that uses a rubber material to coat a high-density magnetic core and developed a theory for a local resonance phononic crystal in 2000, the study of acoustic metamaterials based on sub-wavelength structures to explore acoustic supernormal physical properties has attracted the attention of many researchers. Li and Chan (2004) take a soft rubber spheres composite suspending in water to show the negative equivalent elastic modulus and negative equivalent mass density within a defined frequency range, and they clearly put forward the concept of acoustic metamaterials for the first time. Liu et al. (2005) analysed the effective parameter densities of the three-component local resonance structure in 2005, and the results showed that effective mass densities are negative in the low frequency bandgap. They found that the size of the resonant unit cell is much smaller than the elastic wave wavelength in the bandgap, so the mechanism of the local resonance bandgap is proposed, which makes the acoustic metamaterials potential to be used in practical engineering. Following this discovery, several research groups utilised conventional phononic-crystal theory to identify a wide frequency range of acoustic metamaterials characterised by a negative equivalent mass density and bulk modulus (Li and Chan, 2004). In 2006, the arrangement of Helmholtz resonators in a periodic manner (as depicted in Fig. 2.2(b)) was experimentally demonstrated to exhibit a negative equivalent elastic modulus within the resonant frequency range (Fang et al., 2006). Subsequently, multiple research teams employed conventional phononic crystal theory and made groundbreaking discoveries of acoustic metamaterials encompassing a wide frequency range (Ding et al., 2007; Garcia-Chocano et al., 2012; Chen et al., 2013).

On the other hand, the bandgap location and width of LR are only related to the resonant frequency, which is a material parameter. Each unit has its own mechanical vibration, and the unit size can be small so that there is basically no interaction, resulting in the natural frequency of the resonator being insensitive to structural size parameters and direction (Chang et al., 2018). It is able to achieve sub-wavelength bandgaps, which can overcome the objective material limitations of the BS-based phononic crystals. Therefore, with the consideration of suitable dimensions of a periodic configuration, the bandgap in LR can have a much lower frequency location compared with that of the BS bandgap. While phononic crystals are designed to mitigate waves by the use of Bragg scattering (Jensen, 2003; Deymier, 2013; Sainidou et al., 2006; Sigalas, 1992), locally resonant acoustic metamaterials (LRAMs) can generate local resonance characteristics to guide and suppress wave propagation (Moscatelli et al., 2019; Pai, 2010; Pai et al., 2014; Sheng et al., 2003). They are designed by attaching substructures to the master structure, and waves in certain frequency ranges cannot propagate in these periodic structures (Liu et al., 2000). To realise a bandgap to control long wavelengths, a relatively large cell size is required. LRAMs have the potential to overcome such limitations by the introduction of local resonance mechanisms (Brillouin, 1953; Raghavan and Phani, 2013). The most typical feature of LRAM is the subwavelength size and abnormal dynamic effective parameters. When sound waves propagate in such structures, they will be affected, which causes the suppression

(Cummer et al., 2016). Therefore, through the design of this special structure, many new physical characteristics and phenomena such as reflection, absorption, filtering, focusing and stealth of sound waves can be realised, which has important potential application value in national defense and daily life.

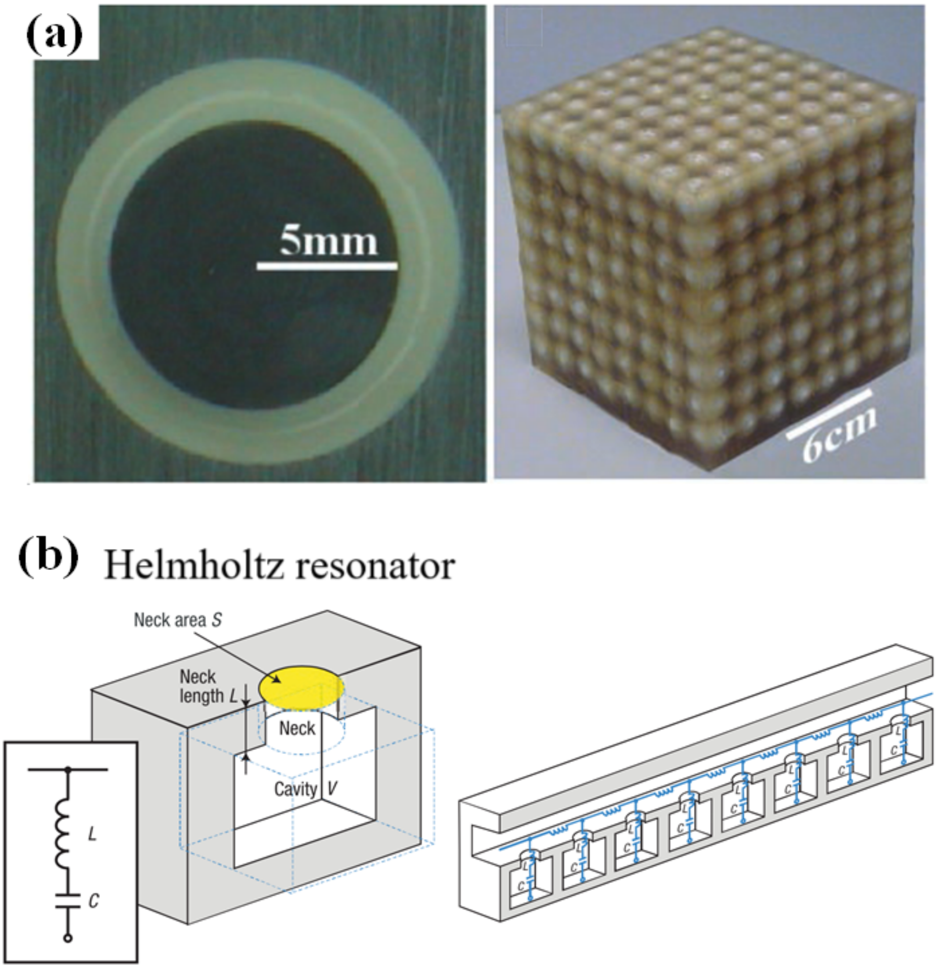

Figure 2.2: The initial developments of LRAMs. (a) Images of the sample that achieved the first realization of an anomalous mass effect induced by local resonance (Liu et al., 2000). Left: a cut-away view showcases a sample unit cell composed of a small metallic sphere coated with a thin, uniform layer of silicone rubber. Right: the units shown on the left are connected using epoxy to create the final sample. (b) An illustration of another sample which successfully demonstrated frequency dispersion for the bulk modulus (Fang et al., 2006). Left: one of the Helmholtz resonator sample. Right: a sample consisting of a series of Helmholtz resonators connected to one side of a conduit.

Early AMs mainly consisted of periodic microstructures embedded in a matrix material with specific resonance properties. These structures exhibited a negative acoustic response, but were limited to a small frequency range near the resonance frequency, resulting in a narrow working bandwidth. In 2008, Fok et al. (2008) introduced the concept of localised resonance units in acoustic metamaterials, which were able to produce unique acoustic effects at sub-wavelength scales. Subsequently, Torrent and Sánchez-Dehesa (2008) defined 'acoustic metamaterials' as any artificial acoustic structure that utilises repetitive or random structural units to significantly alter the material's equivalent acoustic parameters, which has broadened the scope of AMs. In 2012, Liang and Li (2012) theoretically realised a wide bandwidth of negative refractive indices using spatially folded structures. The problem of narrow bandwidth was also compensated by realising double negative parameters without relying on local resonance mechanisms.

The research on acoustic metamaterials has only been a few years since the concept was put forward, and it is still in the exploratory development stage. Many attempts focusing on LRAMs configuration design have been reported to optimise vibration control performance and expand the scope of application, for example, tunable acoustic metamaterials (Fig. 2.3) (Wang et al., 2014), sandwich structures (Arunkumar et al., 2017), and filled honeycomb composite structures (Fig. 2.4), multiresonator structures (Bao et al., 2021; Stein et al., 2022), membrane-type acoustic metamaterials (Zhou et al., 2018), piezoelectric acoustic metamaterial plates (Wang et al., 2021), inerter-based configurations (Kulkarni and Manimala, 2016), inertial amplification mechanisms based LRAMs (Settimi et al., 2021), metamaterial-based barriers and foundations (Wang et al., 2022b), graded flexible metamaterials (Li et al., 2021a), double-resonator-based metaconcrete composite slabs (Liu et al., 2022a), the dual-resonator metamaterial beam (Bao et al., 2021), (Lu et al., 2016; Li et al., 2020b; Xie et al., 2020), and geometrical nonlinear mechanism-based structures (Wang et al., 2019a; Li et al., 2021b). Performance benefits using LRAM in the noise reduction of an automobile panel structure (Jung et al., 2019) have also been reported. An interesting idea of considering periodically arranged urban trees as natural metamaterials is proposed (Fig. 2.5), which can help design artificially engineered arrays of trees with low-frequency Rayleigh wave bandgaps Their study provides a new concept for the quantitative design of urban forests to reduce ground vibration in a specific frequency range (Liu et al., 2019).

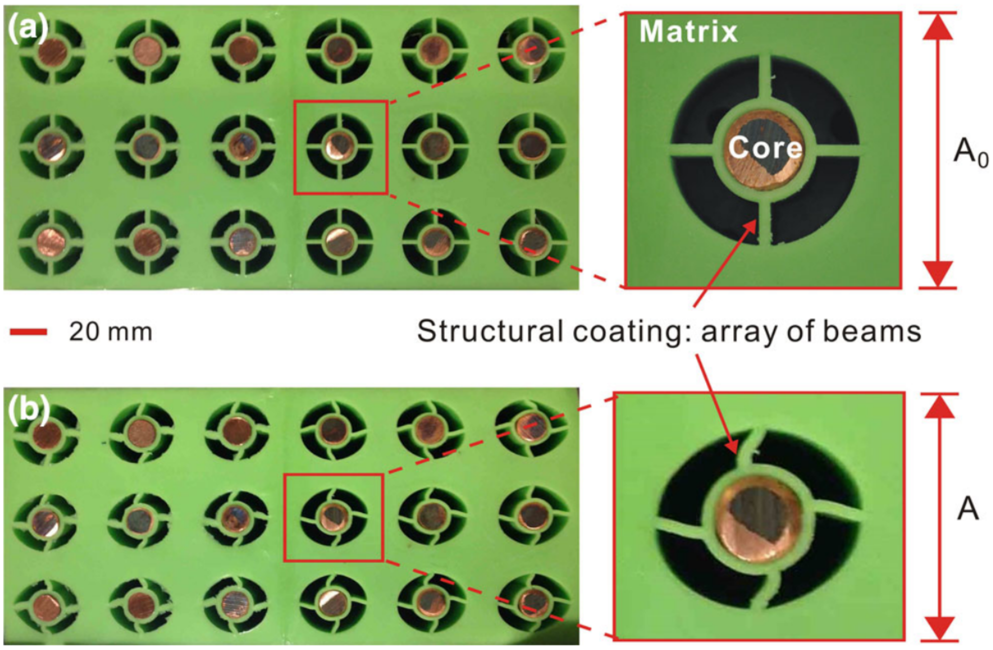

Figure 2.3: Tunable acoustic metamaterial: (a) The initial configuration consists of resonating units distributed within an elastomeric matrix. Each resonator consists of a metallic mass connected to the matrix through elastic beams, forming a structural coating. (b) By applying a compressive strain vertically, the beams experience buckling, leading to a notable change in the effective stiffness of the structure (Wang et al., 2020).

The bandgap properties of LRAM arise from the generation of neg-

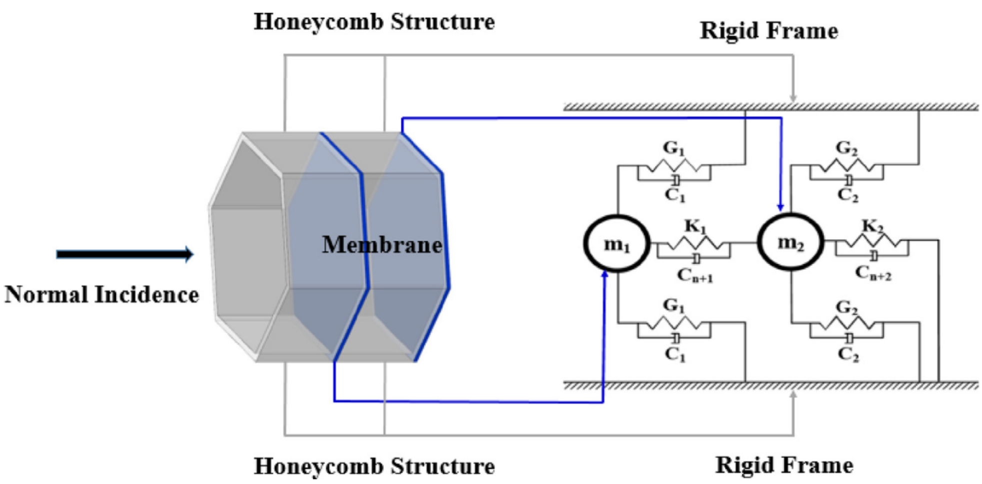

Figure 2.4: The corresponding relationship between the multilayer honeycomb single unit cell, which is made from high-strength and light-weight aramid fiber sheets, and the finite simplified mass-spring model, where the mass of membrane is simplified as a lumped mass, the spring is used to simulate the elastic stiffness and damping of the membrane (Li et al., 2020b).

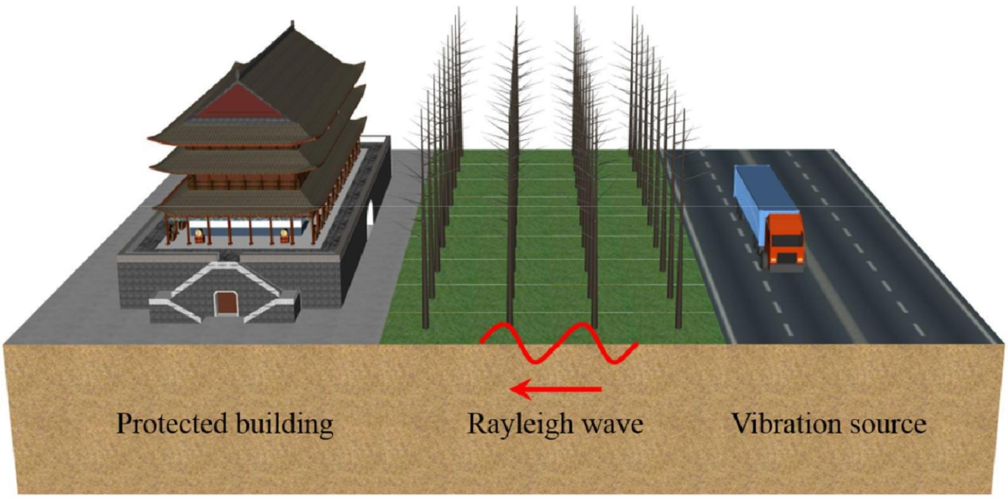

Figure 2.5: The periodic arrangement of urban forests surrounding a building can be regarded as a natural metamaterial (Liu et al., 2019). The resonance produced by the trees interacts with elastic waves in the soil, particularly Rayleigh waves. The propagation of Rayleigh waves can be effectively suppressed at specific frequencies.

ative effective mass of unit cells (Huang et al., 2009; Li and Chan, 2004; Milton and Willis, 2007; Pendry, 2000). Considering a 2DoF mass-in-mass unit cell comprising an inner mass connected to an outer mass via a spring, it has been shown that when the spring suspended outer mass is subjected to a force, the effective mass of the whole unit cell could be negative in a range of excitation frequencies (Cummer et al., 2016). According to the Newton's second law, the direction of the acceleration of a forced negative mass is opposite to that of the applied force. Using this property, vibration reduction designs can be realised (Chang et al., 2018; Dong et al., 2021; Li et al., 2021c). Many previous investigations (Liu et al., 2000; Pai et al., 2014; Hussein and Frazier, 2013) of LRAM have shown that in the dispersion curve diagram, there will be one bandgap near the resonant frequency. The bandgap is caused by the local resonance of the inner mass, and its location and width only depend on the material parameters of the system but not the excitation force.

2.1.2 Novel configurations

Previous studies have focused on the monatomic chain structure with a low-frequency bandgap generated by local resonance characteristics. Because the frequency range of the locally resonant bandgap can be changed by tuning the material parameters, LRAMs can provide highly customised design services to satisfy demanding conditions. Their application can provide a vibration-free processing or working environment, improving the performance and reliability of the equipment. Studies on LRAMs have been extended to diatomic-based configurations, which are achieved by alternating the distribution of lumped masses of the main structure. The unit cell investigated in a monatomic configuration usually consists of a single mass resonator mechanism, whereas that in a diatomic configuration comprises dual mass resonator mechanisms. The use of diatomic structure can lead to multiple bandgaps due to the existence of different resonant frequencies (Porubov and Andrianov, 2013; Zhou et al., 2017b; Li et al., 2017a). Novel phenomena and band characteristics have been observed in LRAMs of diatomic configuration. Alamri et al. (2019) developed a diatomic LRAM to realise asymmetric elastic-wave transmission in multiple broadband ranges, which was experimentally observed and verified. Zhou et al. (2021) designed and fabricated a 3D-printed diatomic LRAM for impact mitigation and vibration suppression. The similarities between electrons in crystals, photons in phononic crystals, and phonons have prompted the extension of topological concepts from electrons to electromagnetism and acoustics, and further to mechanical vibrations (Xin et al., 2020; Fan et al., 2020a; Chen et al., 2019; Chaunsali et al., 2018). Zhao et al. (2018) proposed a locally resonant topological MTM structure (Fig. 2.6). The diatomic configuration induces two additional Bragg scattering bandgaps located on both sides of the local resonant bandgap, and topological interface states appear in these two bandgaps. Compared with other complex monatomic configuration LRAMs optimised for better vibration control performance, the cost of converting the monatomic configuration to the diatomic configuration is considerably lower. The design of LRAMs in diatomic configurations is highly cost-effective. Different spring constants can be obtained by adjusting the separation of the resonators in one diatomic unit. Hu et al. (2022) presented the use of springs linking resonators in one diatomic unit cell, making it straightforward to obtain topological interface states by only adjusting the resonators.

At present, many nonlinear mechanisms are initially investigated and applied in single-degree-of-freedom (SDoF) systems, and the use of some of them has led to good performance. For the SDoF geometrical nonlinear damping vibration isolator, Wu and Tang (2020) presented a modified harmonic balance (HB) method to derive the force and displacement trans-

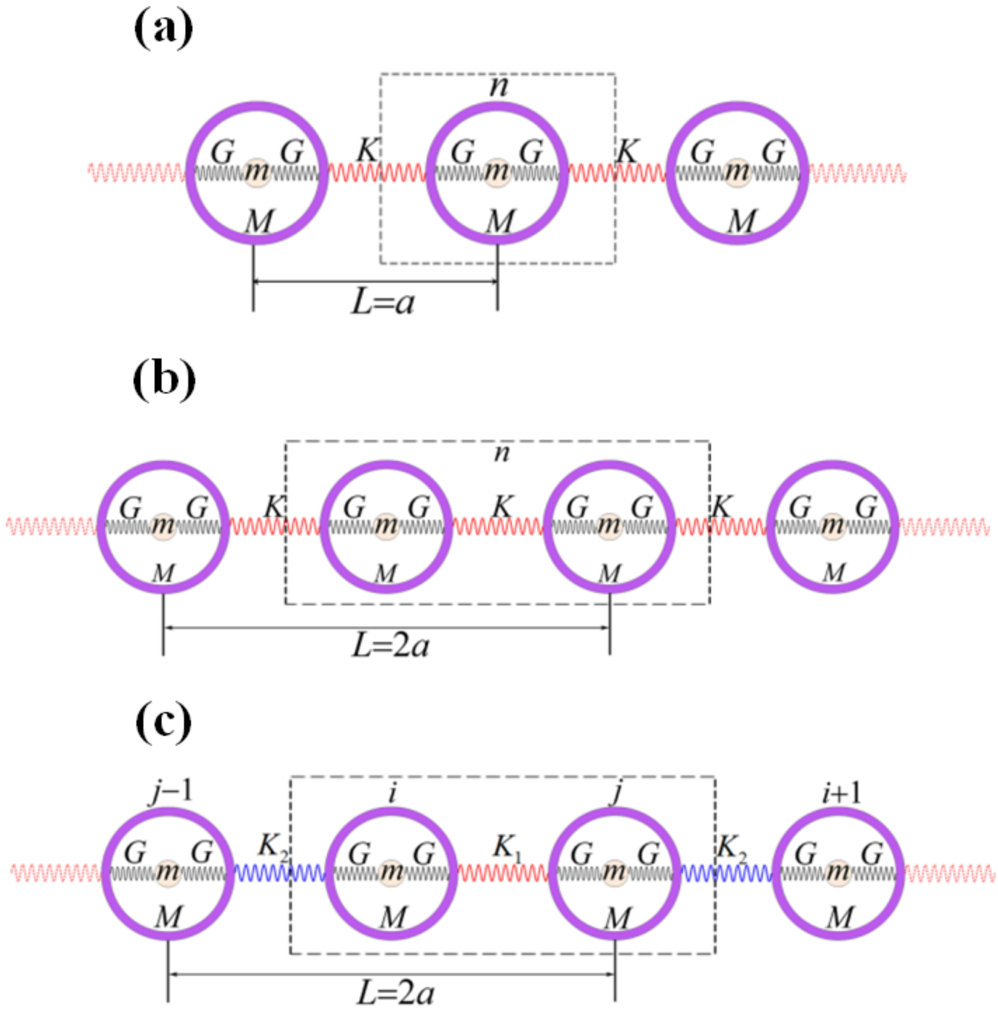

Figure 2.6: Spring-mass models of a one-dimensional array of local resonant unit cells. (a) Monatomic configuration. (b) Modified chain configuration similar to the monatomic chain in (a), but with a new unit cell consisting of two unit cells in (a). (c) Diatomic chain with different springs. The dashed frames indicate the unit cells of three different configurations.

missibility. Nonlinear elements have been exploited in the design of LRAMs designs for further performance improvement. Sepehri et al. (2022) combined exclusive properties of nonlinear chains with electromagnetic actuation to actively manipulate the propagating waves in a monatomic chain structure. The study related to the active control effects on nonlinear piezoelectric PCs can create a new bandgap, whose width between the acoustic and optic branches is influenced by nonlinearity (Wang and Wang, 2018).

The introduction of nonlinear mechanisms provides the potential to realise low-frequency vibration control of LRAMs, by achieving relatively low resonant frequencies and bandgap shifting. The effects of temperature-induced stiffness nonlinearity on the wave propagation of shape memory alloys based nonlinear diatomic lattices were investigated (Sepehri et al., 2021). Bae and Oh (2022) presented a geometric nonlinearity-based LRAM to achieve the bandgap tunability at the quasi-static frequency range. Lin et al. (2021) proposed a quasi-zero stiffness (QZS)-based LRAM (Fig. 2.7) that can achieve an ultralow frequency bandgap. It is noted that many QZS mechanisms lead to nonlinear restoring force, which can yield undesirable nonlinear behaviour. Negative-stiffness mechanism (NSM) has the potential to be applied to LRAM designs for better performance, and its use in SDoF vibration isolation systems has been extensively studied (Shi et al., 2021; Antoniadis et al., 2015; Wang et al., 2018; Sun et al., 2021; Wang et al., 2019b; Nagarajaiah and Sen, 2020).

Yang et al. (2020) also proposed a nonlinear vibration isolator with a geometrical nonlinear inertance mechanism (GNIM), which improves vibration isolation performance through achieving a broader frequency band of vibration transmission. Chen et al. (2020b) focused on the effects of nonlinearity on the band properties of diatomic mass-in-mass chain with active control. It showed that it is possible to close the band-folding-induced gaps in the nonlinear LRAM if negative nonlinearity is applied. Bae and Oh (2020) reported a new type of bandgap phenomenon called amplitude induced bandgap, which is induced by amplitude in nonlinear metamaterials. Yu et al. (2021b) proposed a combinational design of linear and nonlinear LRAM, which has both chaotic bands and bandgaps. It has better robustness, higher efficiency, and broader bandwidth for the wave

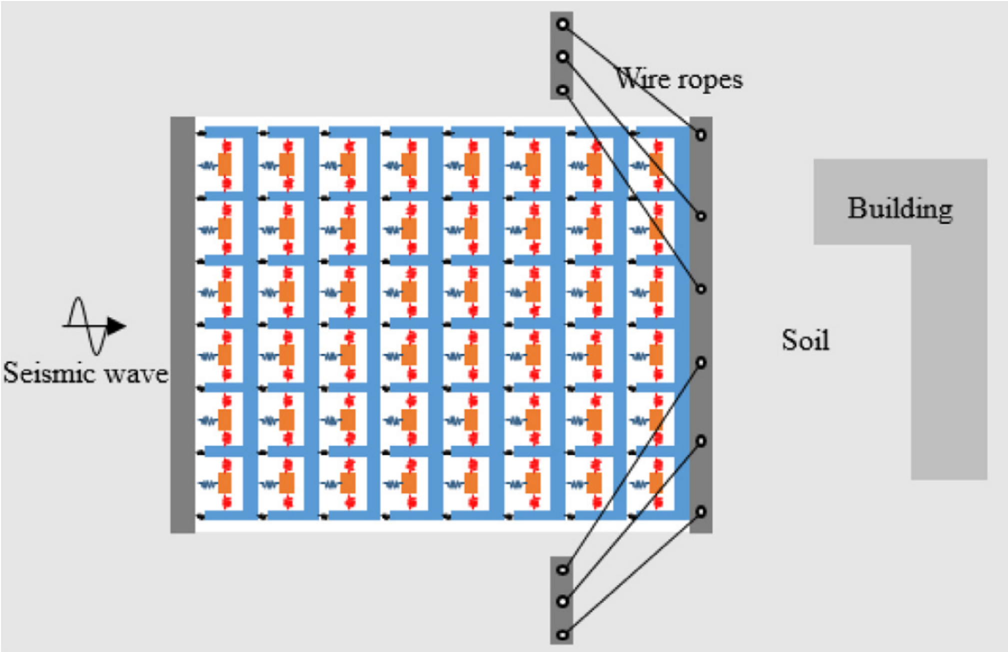

Figure 2.7: The proposed conceptual physical model to suppress the horizontal component of Rayleigh waves. The proposed structure mainly consists of four components: built-up steel barriers, resonators, RC retaining walls and wire ropes (Lin et al., 2021).

suppression effect relative to the noncombined linear or nonlinear LRAM. Yang et al. (2022) studied the effect of prestress on bandgaps. They used super-elastic alloy and horseshoes lattices to propose a novel approach to design metamaterial rods with amplitude-dependent bandgaps. Ji et al. (2021) presented a review of metamaterials and origami-based structures and the applications to wave control. Some researchers focused on the study of the geometrical nonlinear LRAM. Zhou et al. (2017a) realised multi-low-frequency bandgaps by using multiple resonators with negative-stiffness mechanisms. The numerical experiments showed that as the resonator number in one unit cell with the target frequency increases, the bandgaps are notably broadened. Wang et al. (2019a) investigated a high-static-low-dynamic-stiffness mechanism-based LRAM, and the theoretical results showed that the nonlinearity will affect the central frequency and width of the bandgaps. The multi-body dynamic analyses and numerical simulations all validated the existence of the low-frequency bandgap. Inspired by all the related research studies, it might be possible to combine the inerter and geometrical nonlinearity to obtain both advantages. Settimi et al. (2021) proposed a 1D cellular mechanical lattice configuration consisting of pantograph mechanisms in the tetra-atomic cell as minimal physical realization of an inertially amplified metamaterial. The results showed that the center-frequency of the bandgap significantly decreased with the relative mass of the inertia amplifiers. Xu et al. (2019) presented a nonlinear dissipative elastic metamaterial in a triatomic mass-spring chain to explore the interplay between nonlinearity and dissipation and provided a design approach for materials capable of suppressing blast-induced shock waves or impact generated pulses. Many other research studies based on nonlinear metamaterials have shown the value of nonlinearity on vibration control (Fang et al., 2016; Lazarov and Jensen, 2007; Xia et al., 2020; Mosquera-Sánchez and De Marqui Jr, 2021).

For a majority of the studies on LRAMs, the results primarily showed dispersion relations and force transmissibility; however, limited studies have used the vibration power flow analysis (PFA), which is a widely accepted method for displaying the dynamic characteristics of complex structures. PFA expresses the combined effect of the velocity amplitudes, forces, and their relative phase angles as a single quantity that can be used as a unified measure to directly evaluate the vibrational energy transfer between different components within a structure (Yang et al., 2013). The theory has been well developed and the time-averaged power flow variables have been used in many studies (Xing and Price, 1999; Xiong et al., 2003) as indices to evaluate the vibration dissipation for dynamic analysis. PFA has been performed on many nonlinear dynamic systems, such as oscillating systems incorporating bilinear stiffness and damping elements (Shi et al., 2019), impact oscillators with linear and nonlinear constraints (Dai et al., 2020), impact oscillators with nonlinear motion constraints created by a diamondshaped linkage mechanism (Dai and Yang, 2021), the geometric nonlinear system of a linkage mechanism with embedded linear springs (Dai et al., 2022a), the geometrical nonlinear system with a diamond-shaped inerter-based linkage mechanism (Shi et al., 2022a), a harmonically excited L-shaped laminated composite structure with flat sub-plates connected (Zhu et al., 2021a), laminated composite box structures (Zhou et al., 2024b) and laminated composite plates with a cutout and a variable angle tow design (Zhou et al., 2024a). With the development of metamaterials, PFA has been used to quantify the dynamic properties associated with bandgaps. Al Ba'ba'a and Nouh (2017) presented an approach to investigate the behaviour of bandgap by analysing structural power flowing in different constituents of LRAM, which can be further extended to complex LRAM structures. Attarzadeh et al. (2018) used power flow in LRAMs to quantify the energy transfer modes related to the nonreciprocal response. The results can help in designing a class of low-frequency configurations at subwavelength scales. In our previous work (Liu et al., 2022b), PFA was applied to validate the dispersion relations and investigate the bandgap characteristics of the proposed geometrical nonlinear inerter-based LRAM configuration from a new perspective for structural optimisation. The above applications have demonstrated the advantages and potential of PFA in the study of complex structures.

2.2 Inerters

2.2.1 Introduction

By attaching energy dissipation vibration damping devices or tuned mass damper to the structure, passive control is currently the most widely used method to control the structure vibration. It mainly applies three basic mechanical elements of mass, damper and spring to the structure (one or more types) to achieve the purpose of changing the dynamic properties of the structure and reducing the dynamic response of the structure. Among these three types of basic mechanical elements, dampers and springs are two-terminal elements at both ends, and the force at their ends is related to the relative speed and relative displacement between the two ends. But the mass is always a single-terminal mechanical element. Because the spring and damper are easier to install in the structure, the vibration damping devices based on these two types of mechanical elements are widely used in the field of structural vibration control. As a single-terminal device, the mass element requires a large volume to achieve the desired control effect, so it is inconvenient to install, and at the same time, adding mass to the structure will also cause additional dynamic effects.

The idea of a liquid pump using the inertial resistance of flowing liquid firstly came up by Kawamata et al. (1973). But at that time the two-terminal 'inerter' was used incidentally. The concept of the inerter was first introduced by Malcolm Smith in 2002 using a force-current analogy between mechanical and electrical networks (Smith, 2002), as shown in Fig. 2.8. The definition of inerter is somewhat abstract that a two-terminal device with the characteristic that the equal and opposite forces at two ends are proportional to the relative acceleration between them is recognised as an inerter (Smith, 2020). Different from the normal mass element, as the inerter model shown in Fig. 2.9, the inertial force, F, generated by inerter is related to the relative acceleration, $\ddot{u}$, between the two ends. The corresponding proportional coefficient is named 'inertance', b:

$$b = \frac{F(t)}{\ddot{u}_1(t) - \ddot{u}_2(t)} \tag{2.1}$$

They also summarised the principle of inertial elements from a theoretical perspective. Then at the beginning of the 21st century, the teams of Ikago and Inoue from Tohoku University proposed a structural damping device using the principle of inertia at both ends and conducted a systematic study on the principles of inertial efficiency and damping efficiency (Saito and Inoue, 2007; Saito, 2007). This is the first reported literature that the inerter system was applied in the field of Civil Engineering.

The inerter itself only has the functions of inertial adjustment and energy transfer. In order to more effectively achieve the purpose of vibration damping and control, it is necessary to connect the inerter with springs, dampers and other mechanical components to work in cooperation. Compared with the traditional vibration absorption system, the inerter system can achieve flexible adjustment of frequency and change the effective structure mass without substantially changing the physical mass of the structure. The inertance can be much larger than the actual physical mass of the inerter. What's more, it can improve energy consumption efficiency of energy dissipater (Zhang et al., 2019a).

Many engineering structures, such as racing cars (Smith, 2002) and airplanes (Arunkumar et al., 2017), experience harmful low frequency vibra-

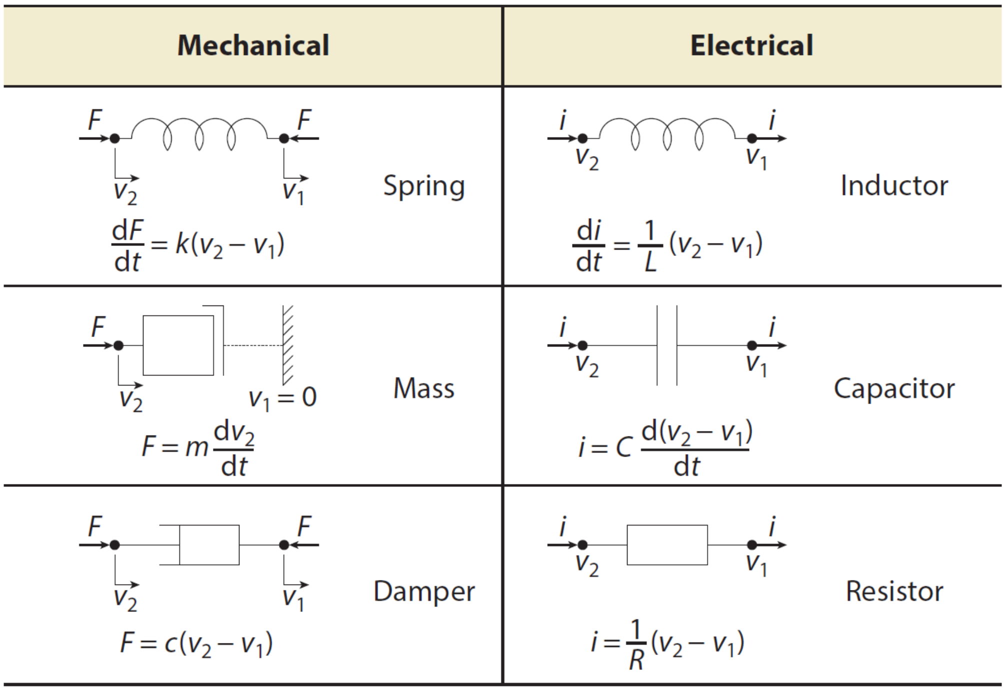

Figure 2.8: Force–current analogy, where stiffness k, inductance L, mass m, capacitance C, damping c, and resistance R are positive constants (Smith, 2020).

tions of which effective suppression is a challenge. For LRAM, its bandgap can be shifted to lower frequencies by having a heavier mass of the resonator or a softer spring. However, having a heavy resonator mass is impractical in most real-world applications due to weight constraints. Also, a soft resonator spring will lead to undesirable large static deflections. Therefore, it is still challenging to realise low-frequency wave suppression (Hussein et al., 2014). The inerter, which is a two-terminal passive mechanical element, provides a possible solution to low-frequency wave attenuation using LRAM.

2.2.2 Application

The inerter provides flexible frequency shifts and effective mass adjustment without substantially changing the physical mass of the configuration. Re-

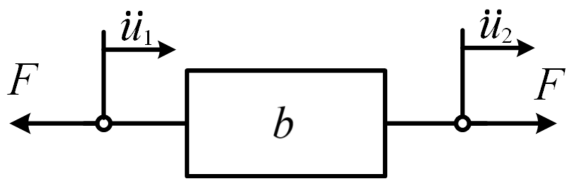

Figure 2.9: The two-terminal inertial element, inerter. The inertial force generated by inerter is related to the relative acceleration between the two ends.

cent evidence suggests that the inerter has a good application prospect in engineering fields (Dai et al., 2019; Zhao et al., 2020; Javidialesaadi and Wierschem, 2019; Liu et al., 2022b). The theoretical results on the performance benefits of vibration suppression devices may become less convincing without the required experimental verification. Therefore in the past two decades, a number of inerter prototypes have been designed in practice, including the rack-and-pinion inerter (Papageorgiou et al., 2009; Sun et al., 2017), ball-screw inerter (Papageorgiou et al., 2009; Li et al., 2012), helical fluid inerter (De Domenico et al., 2019; Zhang et al., 2018, 2020), hydraulic inerter (Wang et al., 2011), electromagnetic inerter (Gonzalez-Buelga et al., 2015) and living-hinge inerter (John and Wagg, 2019). Different from the normal mass element, the inerter can generate large effective mass with small physical mass. Based on this characteristic, inerters have been used to upgrade the traditional dynamic vibration absorber because it can reduce the natural frequency of the vibration system (Chen et al., 2014).

Fig. 2.10(a) illustrates a schematic representation of a typical ball-screw inerter. The device comprises several components, including a ball screw, a flywheel, a radial bearing, and a housing connected to the ball nut. The ball screw plays a crucial role in this inerter by converting linear motion between its two ends into the rotation of the ball nut, which subsequently results in the rotation of the flywheel. This design allows for the amplification of the physical mass of the flywheel, thereby achieving a substantial inertance. Since 2008, Penske Racing Shocks has been at the forefront of the commercial development and provision of inerters (Smith, 2020). Fig. 2.10(b) displays a specific version of Penske's ball-screw inerter used in Formula One. The construction of this inerter closely resembles the schematic depicted in Fig. 2.10(a). Notably, there is no internal mechanism within the device to prevent rotation. Instead, the rod and housing have terminal attachments with a clevis mount that individually locks them against rotation. In this particular example, the ball screw is lubricated with grease and operates without seals.

A schematic illustration of a rack-and-pinion inerter is presented in Fig. 2.11(a), comprising components such as a rack, pinions, gears, a housing and a flywheel. In this configuration, the rack is capable of sliding within the housing and driving the rotation of the flywheel through the pinions and gears. The relative translation of the terminals is thereby converted into the rotational movement. By utilizing the rotational motion of the flywheel, the desired inertance is achieved in this system. Fig. 2.11(b) shows an inerter device prototyped in the Cambridge University Engineering Department (CUED) workshops.

Many inerter-based vibration control systems have been proposed and developed (Shi et al., 2022b). Hwang et al. (2007) proposed the research of rotational inertia dampers with toggle bracing in building structure vibration reduction. The numerical results indicate the rotational inertia damper is effective in structural vibration control and the efficiency of the damper depended heavily on the ball screw lead length. Hessabi and Mercan (2016) carried out both experimental and theoretical analysis on a gyro-mass damper inerter device for controlling building structures vibra-

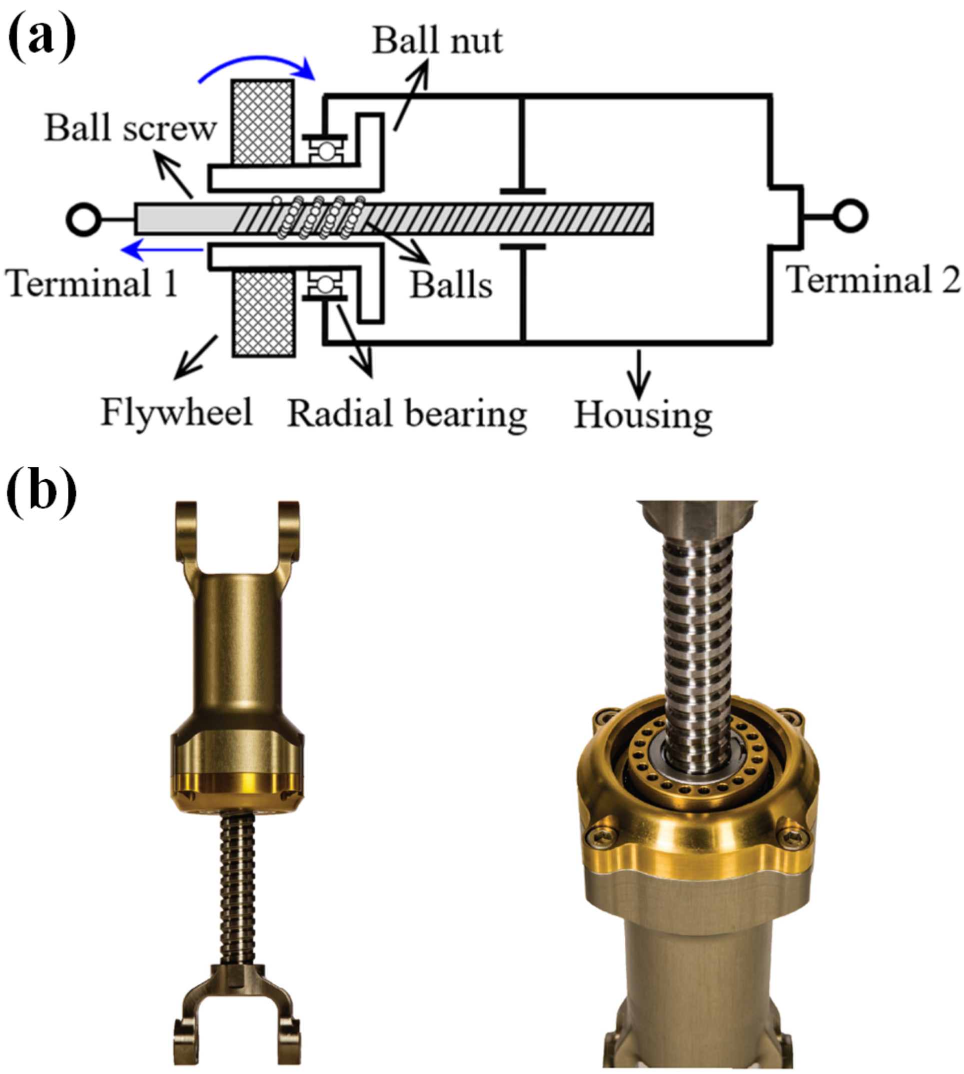

Figure 2.10: Ball-screw inerter. (a) Schematic drawing (Ma et al., 2021) and (b) One version of the Penske ball-screw inerter (Smith, 2020).

tion. Enhancing the acceleration difference of two inerter terminals can improve the performance of the inerter device on vibration control. Dai et al. (2022b) investigated an innovative nonlinear tuned mass-damper-inerter (TMDI) in the application of the ship propulsion shafting system. The numerical results indicate that the analysed TMDI can increase energy dissipation and reduce energy transmission, which has better performance than the conventional mass-spring-damper device. Giaralis and Petrini (2017) investigated the application of TMDI to suppress excessive wind-

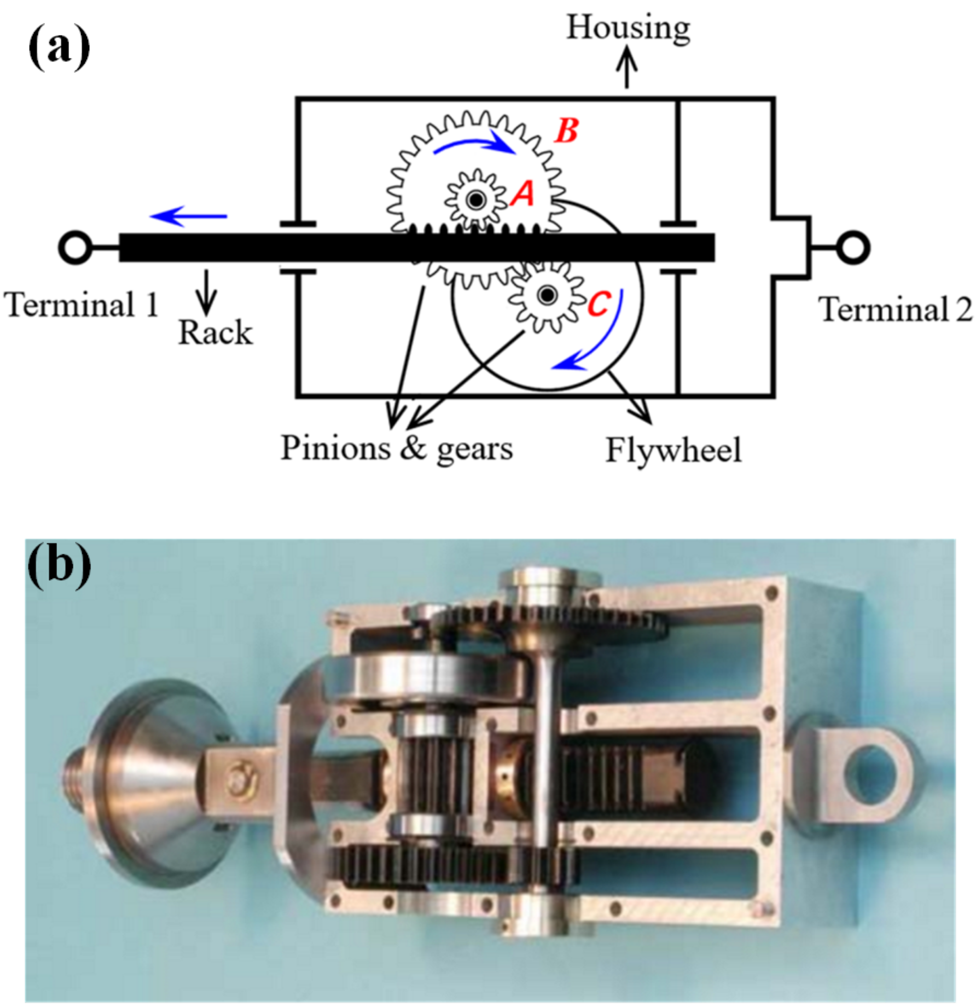

Figure 2.11: Rack-and-pinion inerter. (a) Schematic drawing (Ma et al., 2021) and (b) One rack-and-pinion inerter mechanism designed by Papageorgiou et al. (2009).

induced oscillations in tall buildings. In this research, one terminal of the TMDI was attached to the top floor while the other terminal was connected to the lower floor. It was found that as the number of floors spanned by the TMDI increased, the peak acceleration on the top floor decreased. Subsequent study (Petrini et al., 2020) also demonstrated the robustness of the TMDI to host structure is increased by spanning more floors to connect the secondary mass to the host structure by inerter device. The deflected shape and external force distribution on the host structure are also analysed for TMDI performance evaluation, combining optimal TMDI tuning with host structure design to enhance performance for dynamic loads. Su et al. (2022) went a step further, proposing empirical formulas as guidance for determining optimal TMDI design parameters related to inerter location.

In recent years, the nonlinear energy sink with an inerter has been investigated and has shown good vibration reduction effects (Chen et al., 2020a; Zhang et al., 2019b). Based on all these benefits, it is a practicable choice to apply the inerter to the structure design of LRAM with low-frequency bandgap. A few studies based on the application of linear inerters in LRAM have already shown its potential and advantages. Kulkarni and Manimala (2016) studied the different inerter-based configurations. The results showed that the bandgap frequency range can be shifted both up and down by adjusting the parameters, and it is possible to retain a minimum resonator mass ratio. Another study has shown the wave dispersion and bandgap of the so-called inertially amplified acoustic metamaterials and proposed an alternative resonator-free acoustic metamaterial structure, which exhibits local resonance effects under appropriately tuned conditions (DePauw et al., 2018). However, the existing configurations still have a lot of room for improvement.

Most of the inerter research in the literature focused on theoretical analysis and there are a limited number of experimental studies reported investigating the dynamic behaviour of the inerter-based metastructure (Yu et al., 2021a; Pietrosanti et al., 2020; Gonzalez-Buelga et al., 2017). Li et al. (2019a) designed a novel inerter-based damper termed electromagnetic inertial mass damper for the vibration suppression of a 135 m long full-scale cable, which can provide excellent vibration mitigation performance with optimal inertance and damping coefficient. Zhang et al. (2022) performed an experimental investigation of a novel crank inerter with a variable negative stiffness effect. The experimental data match well with the theoretical results, proving it can be effective for providing an apparent mass effect and variable negative stiffness. Brzeski et al. (2017) presented the experimental verification of a novel TMD which enables changes of inertance. The results showed that it can offer superior damping efficiency in a broad range of excitation frequencies. Our research group also have studied several inerter based systems and demonstrated the potential for inerter to enhance performance (Shi et al., 2022b; Dai et al., 2022b; Zhu et al., 2021b; Shi et al., 2024; Chao et al., 2023; Dai et al., 2024; Dong et al., 2021).

2.3 Friction dampers

2.3.1 Contact friction of jointed structures

Many mechanical structures comprise multiple substructures interconnected through joints and high-performance vibration suppression connections are critically needed to reduce vibration propagation within them. There are various types of connections used in engineering structures, such as welded joints (Ceglarek et al., 2015; Lee et al., 2011), bolted joints (Gaul and Lenz, 1997; Dano et al., 2007), assembled joints (Tian et al., 2023; Yang et al., 2023). As common components of complex mechanical systems, joint connections play a crucial role in the dynamic behaviour of the system (Bograd et al., 2011). Contrary to ideal pinned or rigid connections, dry friction has a strong influence on the dynamic behaviour of joints in bolted and riveted assembled structures.

Friction is a very complex topic, which is the property of a dynamic system (tribosystem) instead of the property of materials or surfaces sliding against each other. The fundamental question about friction is how energy is actually dissipated. When two distinct surfaces slide against each other, part of the kinetic energy is dissipated through elastic and inelastic deformation of the asperity tips. Part of the energy is dissipated through viscous mechanisms. The rest is dissipated through a number of factors such as fracture, adhesion and other chemical processes. Therefore, as shown in Fig. 2.12, friction dissipation can be ultimately regarded as a conversion of kinetic energy into thermal and potential energy, which is released into the surroundings (Akay, 2002).

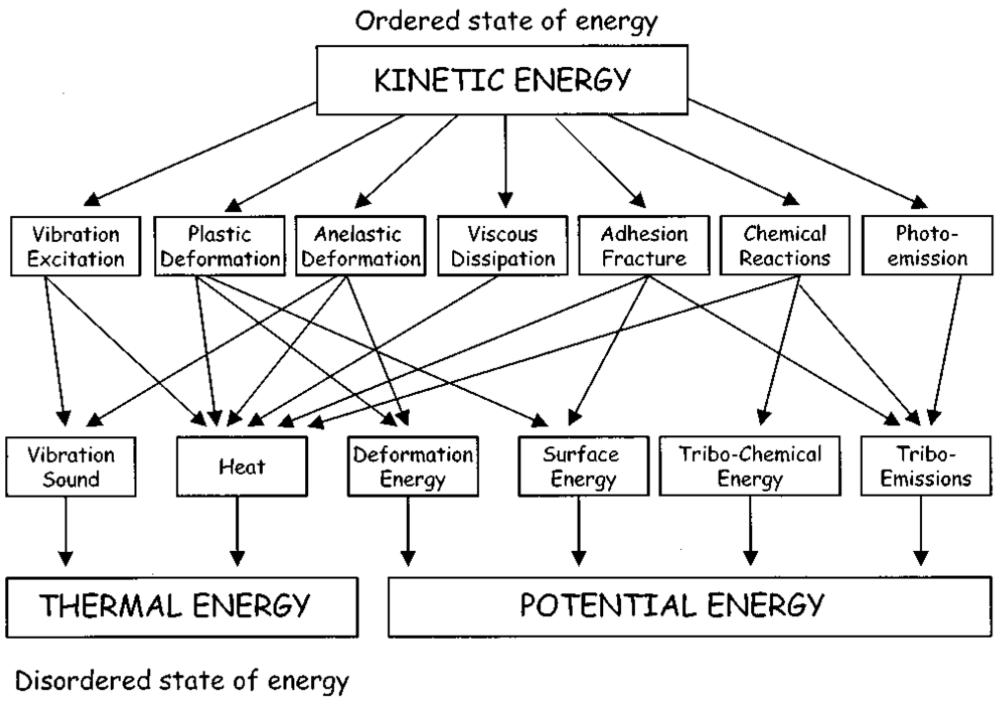

Figure 2.12: Friction energy flow path diagram (Akay, 2002).

Based on tribology, which is the study of friction, wear and lubrication, and design of bearings, science of interacting surfaces in relative motion, plowing and adhesion are the two main sources of dry friction between two metallic sliding bodies. Adhesive friction arises due to plastic deformation of the asperities, i.e., microscopical contact points or micro-junctions, of two sliding surfaces, normally under mutual loading. This plastic deformation results in a 'cold welded' joint that requires a certain amount of lateral sliding force to shear its sliding. Plowing, on the other hand, occurs when the roughness of hard metal penetrates into softer metal. Therefore, in order for these objects to slide against each other, the natural roughness needs to be skipped. The following are three classic dry friction theories that lay the foundation of tribology (Halling and Burton, 1977; Persson, 2013):

1. The first law of Amonton's states that for any object which is under motion the friction is proportionate and perpendicular to normal load.
2. Amonton's second law states that friction of an object is determined by the characteristics of the surface it comes into contact with.
3. The Coulomb's Law of Friction states that the amount of the relative surface velocity has no effect on the kinetic friction exerted between the contact surfaces of two dry objects.

The summary of these three theories is usually stated as follows:

$$F = \mu N \tag{2.2}$$

where μ denoted the coefficient of friction, representing the ratio of the frictional force, F, that acts against the motion of two contacting surfaces, and the normal force, N, which is the force exerted perpendicular to the surfaces, pressing them together.

The static friction coefficient and the kinetic friction coefficient possess distinct numerical values. Static friction acts in opposition to the applied force on an object, preventing its movement until the force surpasses the threshold of static friction. On the other hand, kinetic friction opposes the motion of an object that is already in motion. Hence, it gives rise to the concept of the stick-slip phenomenon, which occurs when objects in contact slide over each other. Instead of smooth and continuous motion, these objects exhibit irregular movement characterised by intermittent accelerations (slips) followed by halts (sticks). Stick-slip motion is typically attributed to friction and can result in vibration, noise and mechanical wear of the moving objects, making it undesirable in mechanical devices (Berman et al., 1996). However, in certain situations, stick-slip motion can have advantageous applications, such as producing musical tones when a bow moves across a string in a bowed string instrument (Gao et al., 1993).

2.3.2 Hysteresis nonlinearity

The motion of the joints exhibits global stiffness and damping properties due to nonlinear contact friction and sliding that occurs at the microscopic scale of the joint region (Gaul and Nitsche, 2001). These elements, which have both stiffness and dissipation properties within a certain area, exhibit typical hysteretic properties. Moreover, nonlinear softening effects occur near the resonant frequency because of the sliding effects that occur when joints have large vibration amplitudes. The hysteresis phenomenon of a multitude of connections may cause a large portion of the energy dissipation in the structural system, leading to discontinuities and nonlinearities in the system stiffness and damping, and making the whole structure exhibit complex nonlinear dynamic behaviour (Liu et al., 2021). If the connections between substructures are assumed to be rigid during modelling without considering the effect of joints, it may result in properties that are very different from those of the actual physical structure. Many studies have been carried out to suppress or even completely eliminate the effect of friction in vibration (Dehkordi et al., 2022). But on the other hand, there is the potential to utilise the effects of friction to reduce vibration transfer between subsystems (Ferri, 1995), e.g. friction component based vibration transfer suppression device.

Many passive linear isolators in the transmission path have been inserted in the transmission path for preventing excessive vibration transmission (Rivin, 2004). Passive nonlinear vibration isolators have been further proposed because of their advanced performance in vibration control, which overcome the limitations of linear vibration isolators (Shi et al., 2019; Dai et al., 2020). Hysteresis nonlinearities typically exhibit greater complexity than geometric and polynomial nonlinearities due to their damping and stiffness dependence on response amplitude. The hysteresis can occur in different shape cycles, but the typical discontinuity point on the restoring force curve has a certain affinity with piecewise nonlinearity (Casini and Vestroni, 2022). The hysteresis nonlinearity is considered to be a strong nonlinearity, which reveals a great number of nonlinear phenomena as compared to the weak nonlinearity, and thus brings a lot of research interest on its dynamic response. For example, seismic isolation bearings play a vital role in mitigating the seismic risk of a structure. Numerous studies have shown that lead-rubber bearing (LRB), consisting of lead plug inserts, can provide a characteristic hysteretic energy dissipation effect (Zheng et al., 2022; Yasar et al., 2024; Dezfuli et al., 2017; Providakis, 2008).

Several methods are available in the literature to tackle the hysteresis dynamic aspects of jointed systems (Gaul and Nitsche, 2001; Ferri, 1995; Mathis et al., 2020; Berger, 2002). Nonlinear finite element analysis (FEA) describes contact interfaces considering hundreds of degrees of freedom and can provide models with high fidelity (He, 2011). However the simulation of these models in a nonlinear dynamic state is computationally expensive, especially for obtaining the time-domain response. For most applications where the modelling of contact surfaces is not of great concern, a lumped model in the form of a single-degree-of-freedom (SDoF) oscillator driven by a hysteresis term is the ideal solution for reconstructing the global dynamics of a jointed structure (Miguel et al., 2022). One of the most fundamental and uncomplicated ways of conveying the dry friction behaviour is the Coulomb model, which determines the system's sliding state solely through the use of a sign function of relative velocity (Gaul and Lenz, 1997). The Coulomb model defines friction force in sliding and sticking situations, which should be dealt with separately. An elastic spring in series with a Coulomb slider creates a Jenkins element, which exhibits a bilinear hysteresis force-displacement curve capable of tracing both sliding and sticking states (Kashani, 2017; Li et al., 2022). The hysteresis curves for the Jenkins elements show nonlinear force-displacement relationships, with closed regions corresponding to dissipated frictional energy (Bograd et al., 2011). To achieve smooth switching rather than the hard switching between sticking and sliding states that bilinearity would cause, the Iwan model (Iwan, 1966) can be implemented, which is a combination of several Jenkins elements in parallel. This model has a specific distribution of friction thresholds and spring coefficients that smooth the resulting hysteresis loop. The Maxwell-slip model (Al-Bender et al., 2005) improves on Ivan's model by considering the inertial properties of the slider. An alternative method of smoothing the hysteresis curve is to replace the bilinear function with a smooth function. Other smooth hysteresis models such as the Dahl model (Dahl, 1976), the Duhem model (Padthe et al., 2008), the Lugre model (Johanastrom and Canudas-De-Wit, 2008) and the Bouc-Wen model (Wen, 1976; Zhu et al., 2019; Nguyen et al., 2022) have been introduced, improved or adopted.

2.3.3 Dry friction damper

On the other hand, hysteresis dampers can also be used to suppress structural vibrations, and dry friction dampers, as one of the most common types, are widely used in many structural systems to achieve vibration damping. A comprehensive literature review was conducted (Jaisee et al., 2021), systematically examining cited and reviewed studies from 1985 to 2020. Fig. 2.13 displays a graphical representation depicting the quantity of research throughout the entire period. The trends observed in Fig. 2.13 distinctly demonstrate the increasing popularity of friction dampers since their inception in civil engineering approximately four decades ago. The bar graph highlights a significant surge in the number of studies conducted during the present decade, indicating the rapid progress and widespread implementation of friction dampers.

Pall et al. (1980) first developed dampers to dissipate seismic energy by generating mechanical damping through sliding friction by analogy with vehicle braking in 1980. The authors developed a solution called Limited Slip Bolted joints to effectively dissipate energy at the joints of large panel structures. Through a series of static and dynamic tests, they identified a system that exhibits consistent and foreseeable frictional behavior, prioritizing it overachieving maximum energy dissipation. However, a significant issue was identified in braced steel frames equipped with the proposed device (Pall and Marsh, 1981). The braces were primarily designed to func-

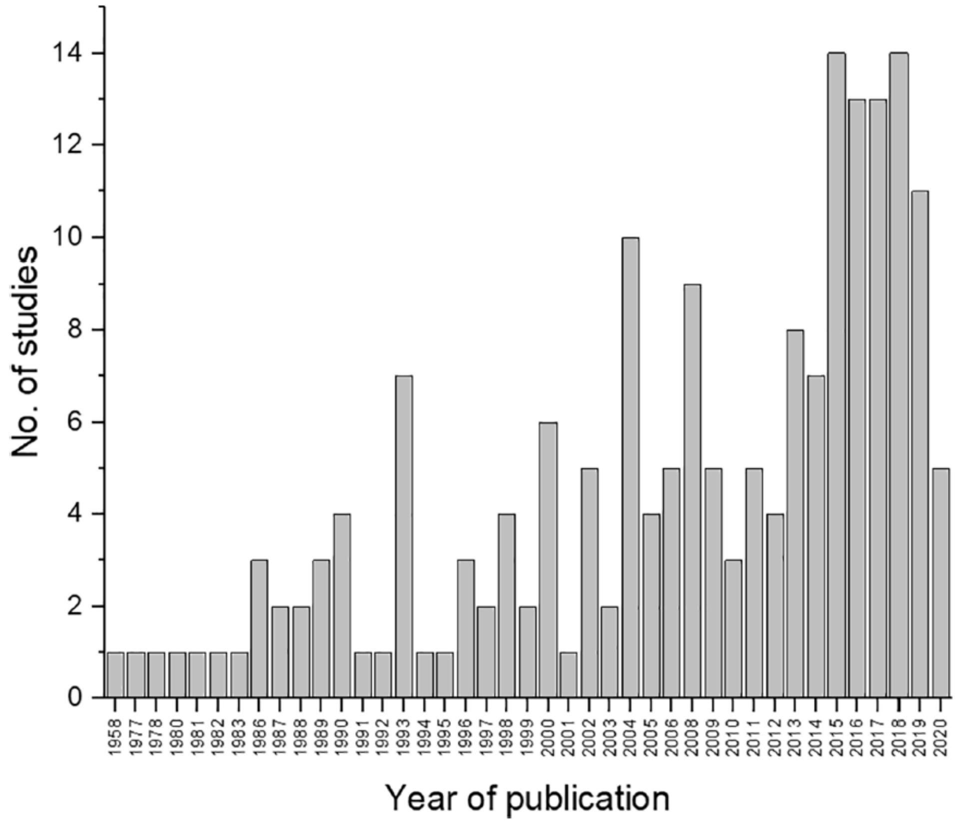

Figure 2.13: Bar chart of the number of literature related to friction damper and the year published (Jaisee et al., 2021).

tion efficiently under tension loading for economic reasons. Nevertheless, when subjected to repeated tension loading, the braces did not perform effectively, requiring them to be stretched beyond their original elongated length to regain their usual functionality, which was deemed undesirable. In order to address this concern, Pall and Marsh (1982) introduced a modification to the sliding friction joint in 1982. They proposed securing the friction pad at the intersection of cross braces using four links. This revised design resulted in the creation of the Pall frictional damper as shown in Fig. 2.14(a), which served as both a friction damper and a safety valve (Pall and Pall, 1996; Pall et al., 2004). In a subsequent development in 2005, Wu et al. (2005) introduced further enhancements to the Pall Frictional Damper and named it the improved Pall friction damper (Fig. 2.14(b)). The authors conducted numerical calculations to assess the hysteretic response of the improved Pall friction damper, considering geometric nonlinearity. The research demonstrated that the improved Pall friction damper replicated the mechanical behavior of the Pall frictional damper while offering additional advantages such as simplified analysis, reduced manufacturing costs, and easier assembly.

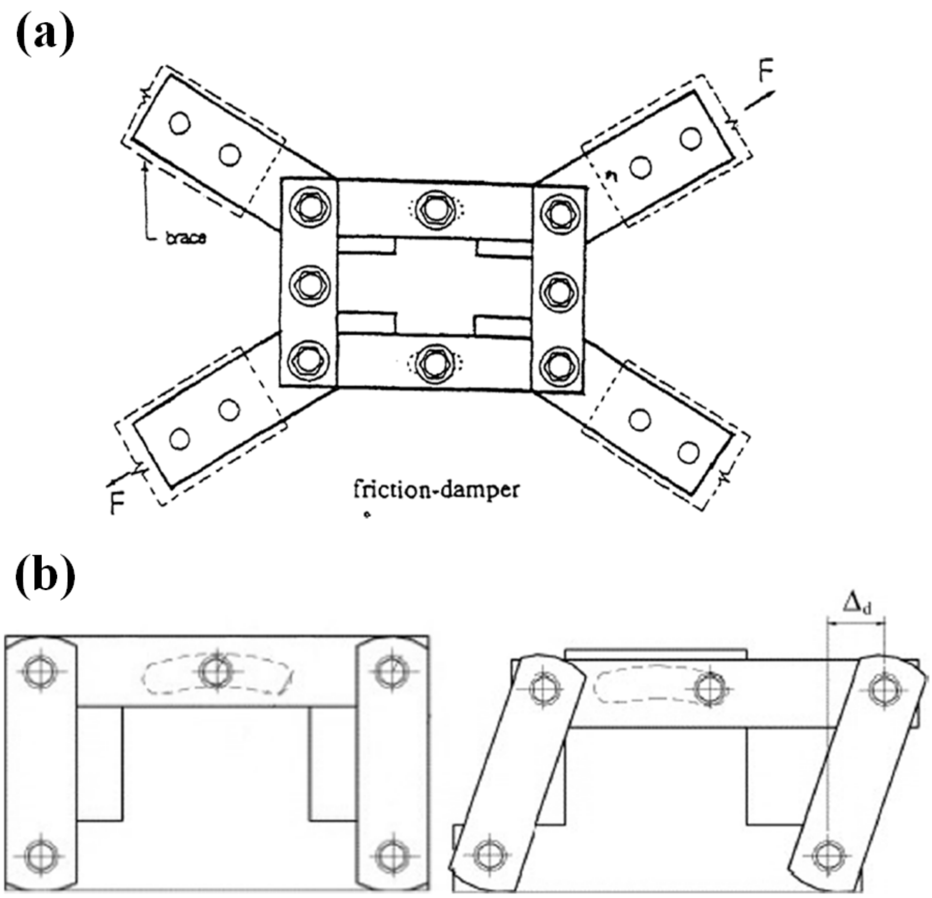

Figure 2.14: Differnt dampers: (a) Pall Friction Damper (Vezina et al., 1992). (b) Construction and operation of Improved Pall Friction Damper (Wu et al., 2005).

While the Pall frictional damper served as a viable option for energy dissipation in moment resisting frames and braced frames, its capacity to resist loads was found to be relatively low (Filiatrault and Cherry, 1987). Moreover, its manufacture required precise workmanship and its installation demanded specialised training, resulting in additional expenses (Grigorian et al., 1993). To address these limitations, Fitzgerald et al. (1989) introduced a simplified design for friction damper in 1989, known as the Slotted Bolted Connection, as shown in Fig. 2.15(a). The proposed slotted bolted connection functioned by sliding a channel bracing plate over a gusset plate, interconnected by high-strength bolts with washers used for adjusting bolt tension.

The Symmetric Friction Connection is a variation of the slotted bolted connection that consists of a main plate with slotted holes, two brass shims, two outer plates, and high-strength bolts, as presented in Fig. 2.15(b). Grigorian (1994) conducted multiple tests on the symmetric friction connection to investigate the frictional behavior between sliding mild steel surfaces and between mild steel and brass surfaces. They discovered that the symmetric friction connection exhibited stable and repeatable characteristics under cyclic loading. Other researchers (Kim and Christopoulos, 2008; MacRae et al., 2010) have also explored the frictional behavior of various materials such as aluminum, stainless steel, and brake-line pads. Numerous scholars (Loo et al., 2014; Iyama et al., 2009; Tsai et al., 2008) have integrated the symmetric friction connection into various other seismic mitigation systems.

Comparing passive friction dampers with other passive energy dissipation devices, several observations can be made. Dry friction dampers exhibit a larger hysteretic loop compared to other devices, enabling them to dissipate more energy per cycle. Additionally, their performance remains unaffected by ambient temperature variations. The highly non-linear behavior of friction dampers adds complexity to their analysis, and without an external restoring mechanism, permanent deformation may occur.

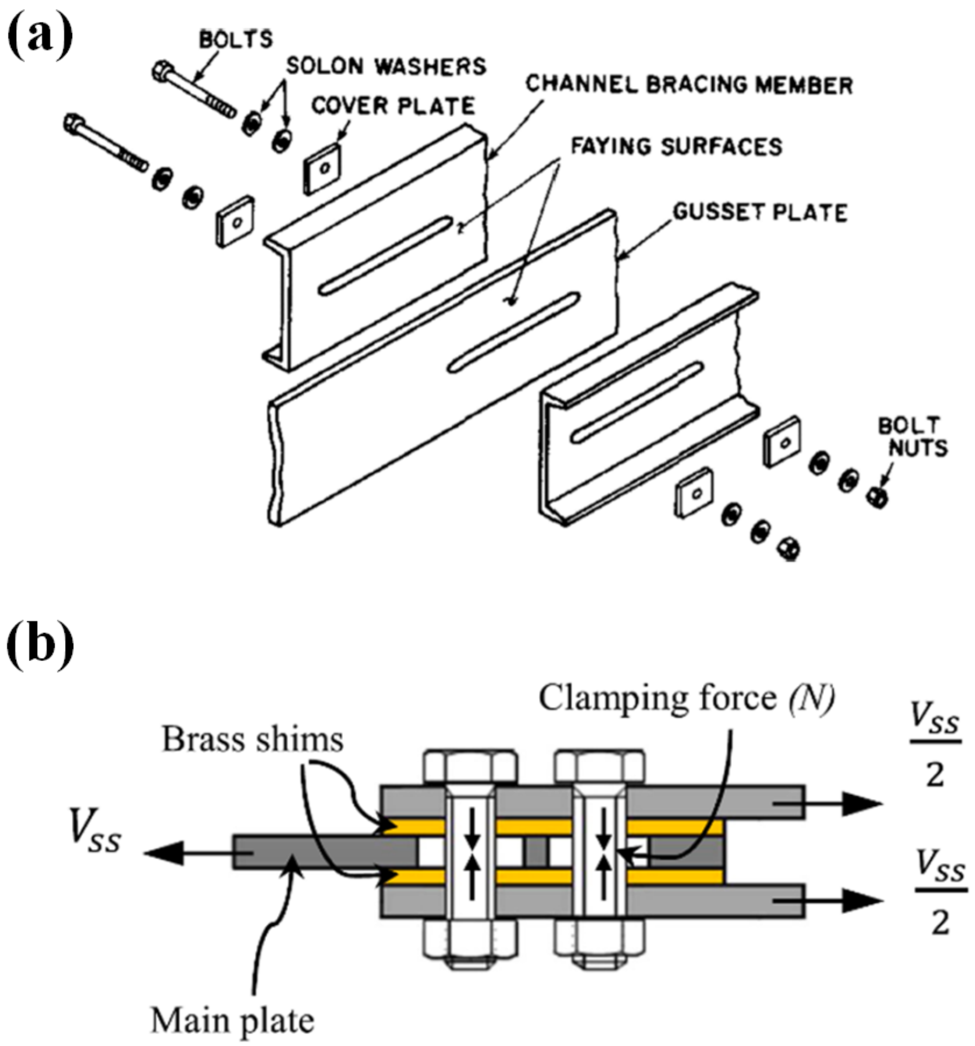

Figure 2.15: (a) Exploded view of Slotted Bolted Connection (Fitzgerald et al., 1989). (b) Symmetric Friction Connection (Khoo et al., 2015).

Metallic dampers, similar to friction dampers, exhibit non-linear behavior and are insensitive to ambient temperature. In contrast, viscoelastic dampers possess restoring ability and are activated at low displacements. Unlike metallic, viscous, and friction dampers, they can restore their original shape. A comparison of passive dry friction dampers with other passive energy dissipation devices is presented in Fig. 2.16.

In addition, the performance of the friction damper is less affected by load frequency, amplitude and number of cycles, and its characteristic of

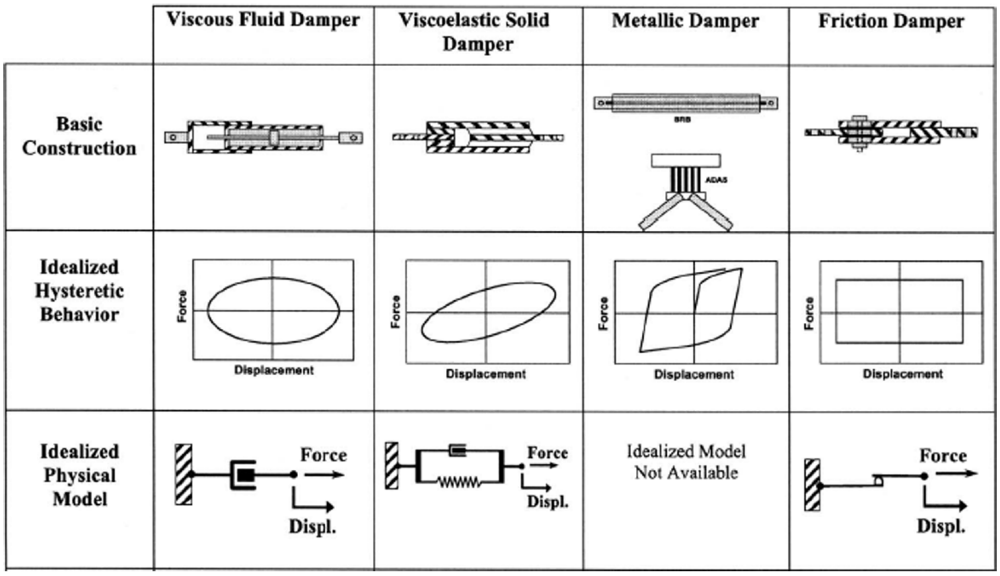

Figure 2.16: Comparison of friction damper with other passive energy dissipation devices (Symans et al., 2008).

dissipating maximum energy by generating a rectangular hysteresis loop makes it superior to other hysteretic devices. They have been applied extensively in various fields such as civil engineering (Jaisee et al., 2021), aviation engineering (Ciğeroğlu and Özgüven, 2006), automotive engineering (Wang et al., 2022a) and railway engineering (Lopez et al., 2004). There have also been a number of related studies in recent years. An equivalent modelling method for spatial lattice structures based on hysteretic nonlinear joints was presented by Liu et al. (2021). Donmez et al. (2020) proposed a nonlinear quasi-zero stiffness vibration isolator coupled with a dry friction damper. Wu et al. (2019) focused on the design of semi-active dry friction dampers and conducted sensitivity analysis and experimental studies. Salvatore et al. (2022) proposed an isolation system with negative stiffness and superelastic hysteresis.

If further insight into the effects of hysteresis friction on the dynamic performance of vibrating systems is desired, then vibration transfer and energy dissipation can provide additional perspectives to understand. However, there are very few studies on vibration transmission in structures involving friction (Dai et al., 2022c; Marino and Cicirello, 2020), much less vibration transmission studies in coupled structures based on hysteresis friction dampers. Hua et al. (2021) proposed a hysteretic friction tuned inerter damper for seismic control of engineering structures, and parameter optimisation was achieved by minimising the maximum force as well as the displacement transmission. Meanwhile, previous studies of the dynamic response of nonlinear systems have paid little attention to their vibration power and energy transfer. As a well-accepted method (Shi et al., 2023), power flow analysis (PFA) can also be used to evaluate the vibration and energy transfer levels of complicated dynamic systems. The idea was initially introduced by Goyder and White (Goyder and White, 1980) with further development in the study of different linear and nonlinear systems (Royston and Singh, 1996; Xiong et al., 2001, 2003, 2005). This method has been applied to the analysis of vibration characteristics of various complex structures, such as smooth or non-smooth joint based coupled structures (Shi et al., 2019; Dai et al., 2020), composite plates (Zhu and Yang, 2022; Zhou et al., 2023), acoustic metamaterials (Liu et al., 2022c,b), and inerter based vibration isolators (Dong et al., 2022; Liu et al., 2023). PFA can bring another point of view to study the dynamic behaviour of the friction damper based system.

Chapter 3

Basic theories and dynamic analysis methods

3.1 Acoustic metamaterials for wave attenuation

When electromagnetic waves enter the material, their magnetic and electric fields will interact with the electrons of the material and other charges of molecules and atoms. This interaction changes the wavelength and speed of the wave, especially when local optical resonance occurs. Therefore, this electromagnetic interaction can be used to design materials with negative electric and magnetic permeability, and thus with negative refractive index (Pendry, 2000). Elastic waves in a continuum may interact with their subsystems, which is similar to electromagnetic waves. This interaction will influence the speed and wavelength of the waves, especially when local mechanical resonance occurs in the subsystems. Therefore, this mechanical interaction can also be utilised to design acoustic metamaterials with negative effective mass or stiffness. However, there are natural materials with negative dielectric constants, but no natural materials with negative stiffness or mass. Therefore, acoustic metamaterials could be achieved by applying microstructures, and the experimental results have proved the existence of negative effective mass. (Li and Chan, 2004; Milton and Willis, 2007; Wu et al., 2007; Cheng et al., 2008; Huang et al., 2009; Pai, 2010). This theory will also be presented later.

The bandgaps of LRAMs are mainly based on the theory of negative mass. If one of the unit cells in the metamaterials system is selected to be investigated, it is clear to get its equations of motion. If the internal structure of the unit cell is assumed to be unknown, which means the 2-DOF unit cell could be recognised as a SDoF lumped mass, the equation of the effective mass of the lumped mass could be derived based on the equations of motion. And it shows in some specific range of excitation frequency, the effective mass could be negative. It is clear that according to Newton's second law of motion, if the mass is negative, the corresponding acceleration will be opposite to the applied force, and the response amplitude will be decreased (Chang et al., 2018; Wu et al., 2016). Making use of this theory and Bloch's theorem (Brillouin, 1953), the dispersion curve equations of the LRAMs system could be derived, which could be used to get the dispersion curve diagram. Many existing researches about the locally resonant metamaterials have already shown that there will be one bandgap near to resonant frequency observed because of the local resonance (Huang and Sun, 2011; Liu et al., 2000; Zhao et al., 2005). The location and width of the bandgap are only controlled by the system material parameters but not the excitation force. Normally the low frequency vibration is the main target to control because it is more harmful and difficult to suppress. And in the LRAMs, the resonator with heavier mass and softer spring will lead to a desired stop band which is located at a lower frequency area.

3.1.1 Unit cell negative effective mass

Figure 3.1 shows a two-degree-of-freedom (2-DoF) mass-in-mass system by which the theory of negative effective mass could be clearly verified. In this system, m_1, m_2 and u_1, u_2 are respectively the masses and displacements of the outer shell and the inner lump. k_1 represents the stiffness of the spring connecting the shell and lump mass. F is the external harmonic excitation force with excitation frequency ω_0 and time t.

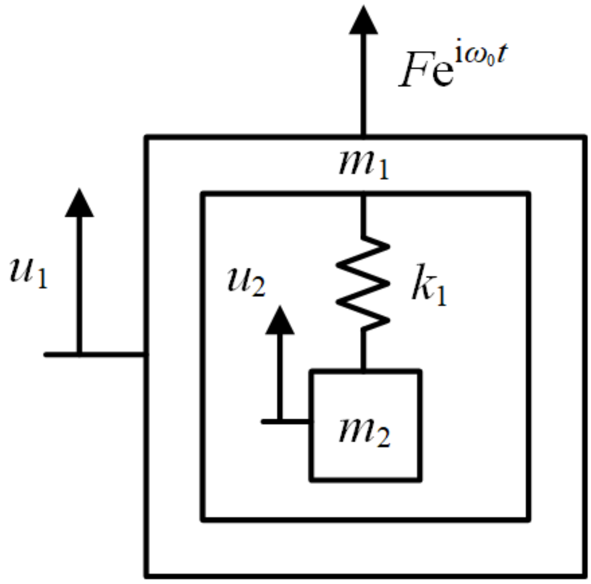

Figure 3.1: Mass-in-mass 2-DoF system

The equations of motion of this model can be derived:

$$m_1\ddot{u}_1 + k_1(u_1 - u_2) = F\mathrm{e}^{\mathrm{i}\omega_0 t}; \tag{3.1a}$$

$$m_2\ddot{u}_2 + k_1(u_2 - u_1) = 0. \tag{3.1b}$$

Rearranging 3.1 and writing it in matrix form yields

$$\begin{bmatrix} m_1 & 0 \\ 0 & m_2 \end{bmatrix} \begin{Bmatrix} \ddot{u}_1 \\ \ddot{u}_2 \end{Bmatrix} + \begin{bmatrix} k_1 & -k_1 \\ -k_1 & k_1 \end{bmatrix} \begin{Bmatrix} u_1 \\ u_2 \end{Bmatrix} = \begin{Bmatrix} F\mathrm{e}^{\mathrm{i}\omega_0 t} \\ 0 \end{Bmatrix} \tag{3.2}$$

Assume the displacement solutions are $u_1 = a_1\mathrm{e}^{\mathrm{i}\omega_0 t}$, $u_2 = a_2\mathrm{e}^{\mathrm{i}\omega_0 t}$, where a_1 and a_2 are constant. Hence the accelerations of the masses can be presented as $\ddot{u}_1 = -\omega_0^2 a_1\mathrm{e}^{\mathrm{i}\omega_0 t}$, $\ddot{u}_2 = -\omega_0^2 a_2\mathrm{e}^{\mathrm{i}\omega_0 t}$. Eqs. (3.2) can be further developed as

$$\begin{bmatrix} m_1 & 0 \\ 0 & m_2 \end{bmatrix} \begin{Bmatrix} -\omega_0^2 a_1\mathrm{e}^{\mathrm{i}\omega_0 t} \\ -\omega_0^2 a_2\mathrm{e}^{\mathrm{i}\omega_0 t} \end{Bmatrix} + \begin{bmatrix} k_1 & -k_1 \\ -k_1 & k_1 \end{bmatrix} \begin{Bmatrix} a_1\mathrm{e}^{\mathrm{i}\omega_0 t} \\ a_2\mathrm{e}^{\mathrm{i}\omega_0 t} \end{Bmatrix} = \begin{Bmatrix} F\mathrm{e}^{\mathrm{i}\omega_0 t} \\ 0 \end{Bmatrix} \tag{3.3}$$

Re-arrange Eqs.(3.3) to derive

$$\begin{bmatrix} -\omega_0^2 m_1 + k_1 & -k_1 \\ -k_1 & -\omega_0^2 m_2 + k_1 \end{bmatrix} \begin{Bmatrix} a_1 \\ a_2 \end{Bmatrix} = \begin{Bmatrix} F \\ 0 \end{Bmatrix} \tag{3.4}$$

The frequency response functions $H_{i1}(\omega)(i = 1, 2)$ between the response $a_i(t)$ and the input harmonic force $F(t)$ can be derived based on 3.4 as

$$H_{11} = \frac{a_1}{F} = \frac{k_1 - m_2\omega_0^2}{(k_1 - m_1\omega_0^2)(k_1 - m_2\omega_0^2) - k_1^2}; \tag{3.5a}$$

$$H_{21} = \frac{a_2}{F} = \frac{k_1}{(k_1 - m_1\omega_0^2)(k_1 - m_2\omega_0^2) - k_1^2}. \tag{3.5b}$$

Assume that the internal structure of the system is unknown to the observer, which means assuming $u_2 = 0$. It can be assumed as an effective SDoF system rather than 2-DoF system, and the effective mass $\tilde{m}$ of the SDoF system can be derived:

$$\tilde{m} = \frac{F\mathrm{e}^{\mathrm{i}\omega_0 t}}{\ddot{u}_1} = \frac{F}{-\omega_0^2 a_1} = m_1 + \frac{m_2}{1 - \omega_0^2/\omega_2^2}, \tag{3.6}$$

where $\omega_2 = \sqrt{k_2/m_2}$ is the resonant frequency of m_2.

According to Eq. (3.6), it reveals that when $\omega_2 > \omega_0$, as ω_0 approaches ω_2, the effective mass $|\tilde{m}|$ tends to infinity and u_1 tends to 0. In this case, based on Eqs. (3.1a), it is shown that $F = -k_1 u_2$, i.e. internal spring and mass act as vibration absorber and the external force are offset. What's more, when $\omega_2 < \omega_0$, according to Eq. (3.6), if $m_2/(1-\omega_0^2/\omega_2) < -m_1$, the effective mass $\tilde{m}$ can be negative.

3.1.2 Unit cell negative effective stiffness

Using the same method, a two-DOF mass-spring system shown in Fig. 3.2 is studied. The mass of the upper shell is ignored and the lower shell is fixed so only the mass of the internal lumped mass, m_2, is considered. Besides, u_1 and u_2 are the displacements of the upper shell and the lumped mass. The two shells are connected by two same springs with stiffness $k_1/2$ separately. F is the external harmonic excitation force with excitation frequency ω_0 and time t. The equations of motion of this system can be derived:

$$k_1 u_1 + k_2(u_1 - u_2) = F\mathrm{e}^{\mathrm{i}\omega_0 t}; \tag{3.7a}$$

$$m_2 \ddot{u}_2 + k_2(u_2 - u_1) = 0. \tag{3.7b}$$

Rearranging Eq. (3.7) and writing it in matrix form, it yields

$$\begin{bmatrix} 0 & 0 \\ 0 & m_2 \end{bmatrix} \begin{Bmatrix} \ddot{u}_1 \\ \ddot{u}_2 \end{Bmatrix} + \begin{bmatrix} k_1 + k_2 & -k_2 \\ -k_2 & k_2 \end{bmatrix} \begin{Bmatrix} u_1 \\ u_2 \end{Bmatrix} = \begin{Bmatrix} F\mathrm{e}^{\mathrm{i}\omega_0 t} \\ 0 \end{Bmatrix} \tag{3.8}$$

where the displacement solutions are $u_1 = a_1\mathrm{e}^{\mathrm{i}\omega_0 t}$, $u_2 = a_2\mathrm{e}^{\mathrm{i}\omega_0 t}$, where

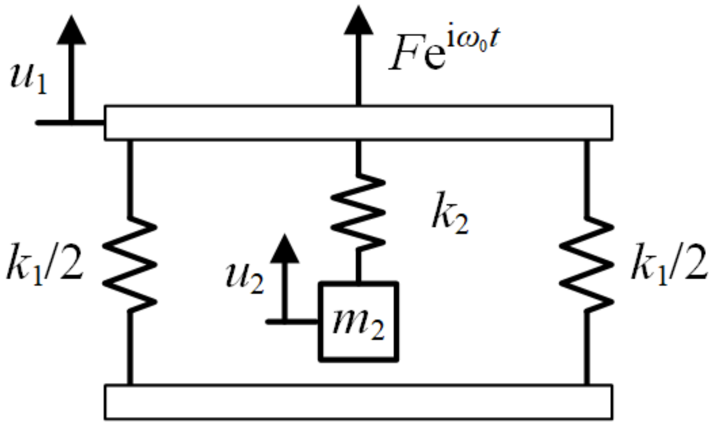

Figure 3.2: Mass-in-spring 2-DoF system

a_1 and a_2 are constant. Hence the corresponding accelerations can be presented as $\ddot{u}_1 = -\omega_0^2 a_1 \mathrm{e}^{\mathrm{i}\omega_0 t}$, $\ddot{u}_2 = -\omega_0^2 a_2 \mathrm{e}^{\mathrm{i}\omega_0 t}$. Eqs. (3.8) can be further developed and arranged as

$$\begin{bmatrix} k_1 + k_2 & -k_2 \\ -k_2 & -\omega_0^2 m_2 + k_2 \end{bmatrix} \begin{Bmatrix} a_1 \\ a_2 \end{Bmatrix} = \begin{Bmatrix} F \\ 0 \end{Bmatrix} \tag{3.9}$$

The frequency response functions $H_{i2}(\omega)(i = 1, 2)$ between the response $a_i(t)$ and the input harmonic force $F(t)$ can be derived as

$$H_{11} = \frac{a_1}{F} = \frac{k_2 - m_2\omega_0^2}{(k_1 + k_2)(k_2 - m_2\omega_0^2) - k_2^2}; \tag{3.10a}$$

$$H_{21} = \frac{a_2}{F} = \frac{k_2}{(k_1 + k_2)(k_2 - m_2\omega_0^2) - k_2^2}. \tag{3.10b}$$

Assume that the internal structure of the system is unknown to the observer. The system can also be treated as a one degree of freedom system, and the corresponding effective stiffness $\tilde{k}$ can be calculated:

$$\tilde{k} = \frac{F\mathrm{e}^{\mathrm{i}\omega_0 t}}{u_1} = \frac{F}{a_1} = k_1 + \frac{k_2}{1 - \omega_2^2/\omega_0^2}, \tag{3.11}$$

where $\omega_2 = \sqrt{k_2/m_2}$ is the resonant frequency of m_2.

According to Eq. (3.11), it shows that when $\omega_2 < \omega_0$, as ω_0 approaches ω_2, the effective stiffness $|\tilde{k}|$ tends to infinity and u_1 tends to 0. Based on Eqs. (3.7b), it can be derived that $F = -k_2 a_2$, which means that the internal force cancels out the external excitation force. Hence the displacement $u_1(t) = 0$. In this case, $a_2 = -F_0/k_2 = -F_0/(m_2\omega_2^2)$. a_2 will arise when m_2 drops. What's more, when $\omega_2 > \omega_0$, according to Eq. (3.11), if $k_1 < -k_2/(1-\omega_2^2/\omega_0^2)$), the effective stiffness $\tilde{k}$ could be negative.

It is novel that if the mass becomes negative, according to Newton's second law of motion, the acceleration will be opposite to the applied force, and the response amplitude will be decreased. And based on Hooke's law, if the stiffness is negative, the displacement will be opposite to the applied force, and the response amplitude will also be reduced.

3.2 Power flow analysis

Power flow analysis is a widely accepted method for displaying the dynamic characteristic of complex structures, which can provide a new perspective to understand and study the dynamic behaviour of the proposed system. PFA expresses the combined effect of the velocity amplitudes, forces, and their relative phase angles as a single quantity that can be used as a unified measure to directly evaluate the vibrational energy transfer between different components within a structure (Yang et al., 2013). The theory has been well developed and the time-averaged power flow variables have been used in many studies (Xing and Price, 1999; Xiong et al., 2003) as indices to evaluate the vibration dissipation for dynamic analysis.

The motion equations of the N-DoF system are written in the matrix form:

$$\mathbf{M}\ddot{\tilde{\mathbf{X}}} + \mathbf{C}\dot{\tilde{\mathbf{X}}} + \mathbf{K}\tilde{\mathbf{X}} = \tilde{\mathbf{F}}\mathrm{e}^{\mathrm{i}\Omega\tau}, \tag{3.12}$$

where $\mathbf{M}$, $\mathbf{C}$ and $\mathbf{K}$ are the mass, damping and stiffness matrices, respectively; $\ddot{\tilde{\mathbf{X}}}$, $\dot{\tilde{\mathbf{X}}}$ and $\tilde{\mathbf{X}}$ represent the acceleration, velocity and displacement vectors of the system, respectively; $\tilde{\mathbf{F}}$ is the vector for complex amplitudes of the external forces.

Pre-multiplying Eq. (3.12) by the velocity vector, the energy flow balance equation is derived

$$\dot{\tilde{\mathbf{X}}}^{\mathrm{H}}\mathbf{M}\ddot{\tilde{\mathbf{X}}} + \dot{\tilde{\mathbf{X}}}^{\mathrm{H}}\mathbf{C}\dot{\tilde{\mathbf{X}}} + \dot{\tilde{\mathbf{X}}}^{\mathrm{H}}\mathbf{K}\tilde{\mathbf{X}} = \dot{\tilde{\mathbf{X}}}^{\mathrm{H}}\tilde{\mathbf{F}}\mathrm{e}^{\mathrm{i}\Omega\tau}, \tag{3.13}$$

where the superscript $(\bullet)^{\mathrm{H}}$ indicates the conjugate, transposed matrix.

The total instantaneous power input into the system is the product of the excitation force and the corresponding velocity at the excitation point (Al Ba'ba'a and Nouh, 2017; Shi et al., 2019). Hence, the corresponding input power at time τ is given as:

$$P(\tau) = \Re\{\dot{\tilde{\mathbf{X}}}^{\mathrm{H}}\}\Re\{\tilde{\mathbf{F}}\mathrm{e}^{\mathrm{i}\Omega\tau}\} \tag{3.14}$$

The time averaged input power during one excitation cycle is denoted as follows (Xiong et al., 2001):

$$\begin{aligned} \overline{P} &= \frac{1}{\tau_{\mathrm{s}}}\int_{\tau_0}^{\tau_0+\tau_{\mathrm{s}}} \Re\{\dot{\tilde{\mathbf{X}}}^{\mathrm{H}}\}\Re\{\tilde{\mathbf{F}}\mathrm{e}^{\mathrm{i}\Omega\tau}\}\mathrm{d}\tau \\ &= \frac{1}{2}(\Re\{\dot{\tilde{\mathbf{X}}}^{\mathrm{H}}\}\Re\{\tilde{\mathbf{F}}\mathrm{e}^{\mathrm{i}\Omega\tau}\} + \Im\{\dot{\tilde{\mathbf{X}}}^{\mathrm{H}}\}\Im\{\tilde{\mathbf{F}}\mathrm{e}^{\mathrm{i}\Omega\tau}\}), \end{aligned} \tag{3.15}$$

where τ_0 is the averaging start operation time and $\tau_{\mathrm{s}} = 2\pi/\Omega$ is the excitation period.

3.3 Dynamic analysis for nonlinear system

Dynamic analysis for nonlinear systems involves studying the behavior and response of systems that exhibit nonlinear relationships between inputs and outputs. Unlike linear systems, where the superposition principle holds, nonlinear systems exhibit complex and often nonlinear responses that can include phenomena such as bilinearity, hysteresis, and chaotic behavior. To perform a dynamic analysis of a nonlinear system, several approaches can be employed.

3.3.1 Numerical Simulations

Numerical simulations are a powerful tool for analysing the behavior of nonlinear systems. They involve using computational methods and techniques to solve the mathematical equations that describe the system's dynamics. To simulate the system's behavior over time, numerical methods for time integration are employed. Commonly used methods include the Euler method (Hahn, 1991) and the Runge-Kutta methods (Butcher, 1996; Cockburn and Shu, 2001). These methods approximate the system's state at each time step based on the previous state and the system's dynamics as shown in Fig. 3.3. The accuracy of numerical simulations depends on various factors, such as the time step size, the spatial resolution, and the chosen numerical method. Smaller time step sizes and finer spatial resolutions generally lead to more accurate results, but they also increase computational costs.

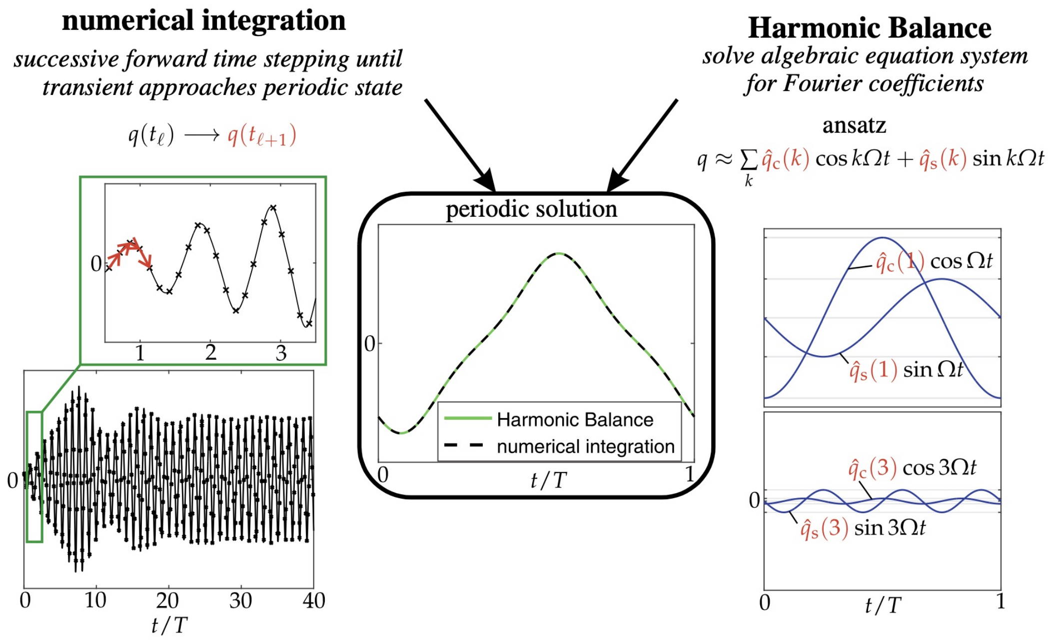

Figure 3.3: Two methods for calculating dynamic response, numerical integration and HB (Krack and Gross, 2019).

3.3.2 Analytical approximation

The Harmonic Balance (HB) Method in Fig. 3.3 is actually an analytical approximation method used to approximate the steady-state response of nonlinear systems subjected to periodic excitation. The method relies on the representation of time-periodic variables as Fourier series. By assuming a finite number of harmonic components, the governing equations of the system can be transformed into algebraic equations, which can then be solved analytically.

The periodic input and system response are represented in the frequency domain using Fourier series or Fourier transforms. The input is typically decomposed into a series of sinusoidal components. The governing equations of the system, typically differential equations, are transformed into algebraic equations using the frequency domain representation. This involves substituting the harmonic representation of the input and system response into the governing equations. The resulting algebraic equations are solved to obtain the values of the unknown harmonic components of the system response. This step typically involves algebraic manipulations and solution techniques such as polynomial root finding or matrix inversion. Once the unknown harmonic components are determined, the time domain response of the system can be reconstructed by summing the harmonics.

The main challenge of the HB approximation is to determine the Fourier coefficients, and one of the algorithms to solve generic nonlinear forces is the Alternating Frequency–Time (AFT) scheme (Cameron and Griffin, 1989; Cardona et al., 1998). The AFT scheme is the most common and versatile method to date for solving nonlinear force problems within the HB (Krack and Gross, 2019).

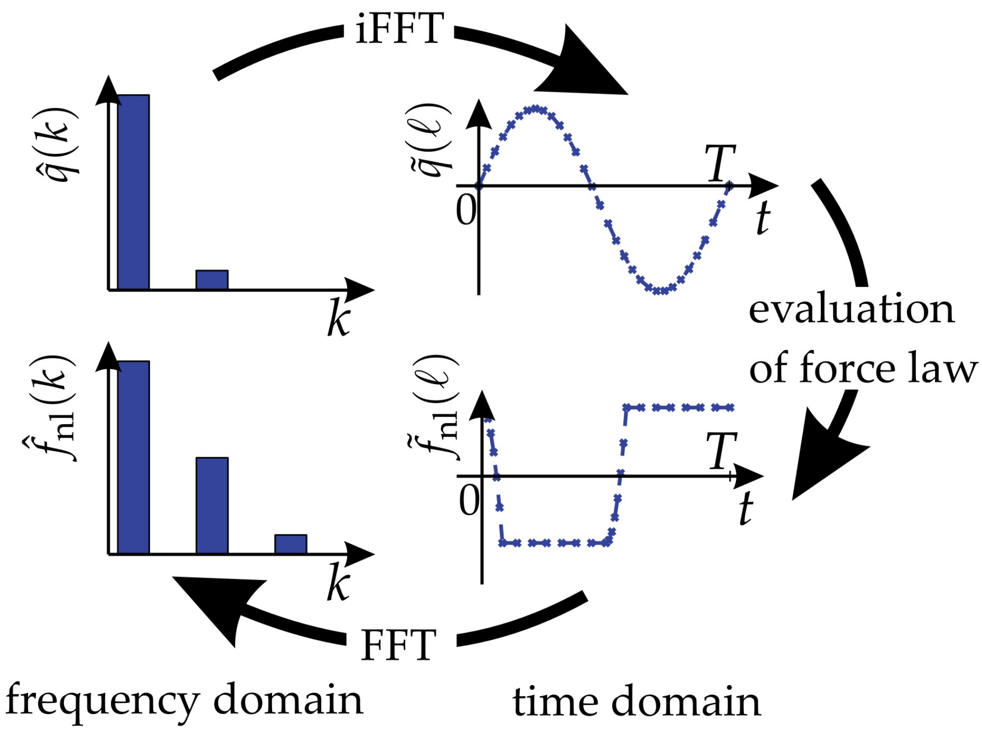

Figure 3.4: Graphical representation of the one-dimensional AFT scheme

As shown in Fig. 3.4, the generalised coordinates and velocities are sampled at equal time points within an oscillation period. The nonlinear forces are evaluated at these moments to obtain the samples. Finally, the Fourier coefficients of the approximate nonlinear forces are obtained by discrete Fourier transform. The AFT scheme is a fast and accurate method when computing nonlinear forces on polynomials (Woiwode et al., 2020), especially when using computationally efficient FFT. In contrast, non-polynomial nonlinear forces typically produce an infinite sequence of non-zero harmonics, even if the input is a truncated Fourier series. This unavoidably leads to aliasing when using an AFT scheme. At this point, a large number of time samples may be required to make the results sufficiently stable.

Chapter 4

Enhanced suppression of low-frequency vibration transmission in metamaterials with linear and nonlinear inerters

4.1 Introduction

In this study, a geometrical nonlinear inerter-based LRAM is analysed theoretically for its advantage for vibration suppression compared with that of linear configuration. Based on the Bloch's theorem, the dispersion relation of single and dual resonators attached linear configurations are calculated to observe the bandgap, and the relation of inerters and band characteristics is investigated by changing different inertance ratios. Then the band properties of a one-dimensional periodic mass-in-mass metamaterial beam with GNIM are studied. The nonlinear inertance force of this mechanism is approximated by Taylor expansion. With the HB method, the dispersion relations and bandgaps with different material parameters can be obtained. The effective inertance of GNIM can be adjusted to any desired value with better precision compared with linear inerter if the resonator displacement amplitude is suitable. The bandgap results are also validated by the wave transmittance and power flow diagrams of the finite unit cell system with different material parameters. For finite-unit-cell systems, the influence of cell number on wave suppression performance is also discussed.

The rest of the article is organised as follows. Two linear inerter-based single resonator attached LRAMs with in-parallel and in-series configurations are first introduced and their bandgap properties are presented in Sec. 4.2. In Sec. 4.3, the bandgap properties of LRAM with dual resonators in each unit attached are studied. The dispersion diagram is validated by comparing it with the wave transmittance diagram. In Sec. 4.4, the geometrical nonlinear inerter mechanism unit cell is presented and its use in the nonlinear inerter-based LRAM structure is examined. Results and discussions including dispersion relation diagrams, wave transmittance figures, and the influence of cell number on the attenuation effect are shown and discussed. Finally, conclusions are drawn in Sec. 4.5.

4.2 Linear inerter-based single-resonator LRAM

4.2.1 Mathematical modelling

Figure 4.1 shows three configurations of 1D chain LRAM systems. Figure 4.1(a) represents the benchmark configuration with N identical mass-in-mass unit cells and a spring-mass local resonator in each unit cell. Each unit cell has a lumped mass m_0 and an internal resonator mass m_1. The lumped masses m_0 are interconnected by linear springs with stiffness coefficient k_0 and dampers with damping coefficient c_0, while each internal resonator is attached to the corresponding individual lumped mass with a linear spring with stiffness coefficient k_1. The initial distance between main masses m_0 is L. The first lumped mass is attached to a harmonic excitation base with displacement amplitude d_0 and frequency ω_f . Figures 4.1(b) and (c) show two inerter-based LRAM configurations with different local resonator setups. In Fig. 4.1(b), the resonator in each unit cell is attached to the lumped mass with an in-parallel spring and inerter. In Fig. 4.1(c), the local resonator comprises a spring and an inerter, connecting in-series with mass m_0.

The equations of motion of the inerter-based in-parallel LRAM shown in Fig. 4.1(b) are

$$m_0\ddot{y}_j + c_0(2\dot{y}_j - \dot{y}_{j-1} - \dot{y}_{j+1}) + k_0(2y_j - y_{j-1} - y_{j+1}) + m_1\ddot{x}_j = 0; \quad (4.1a)$$

$$m_1\ddot{x}_j + k_1(x_j - y_j) + b_1(\ddot{x}_j - \ddot{y}_j) = 0, \quad (4.1b)$$

where y_j represent the displacement of lumped mass in the jth unit cell and x_j is the absolute displacement of the jth resonator. The equations of motion in Eq. (4.1) can be nondimensionalised to be

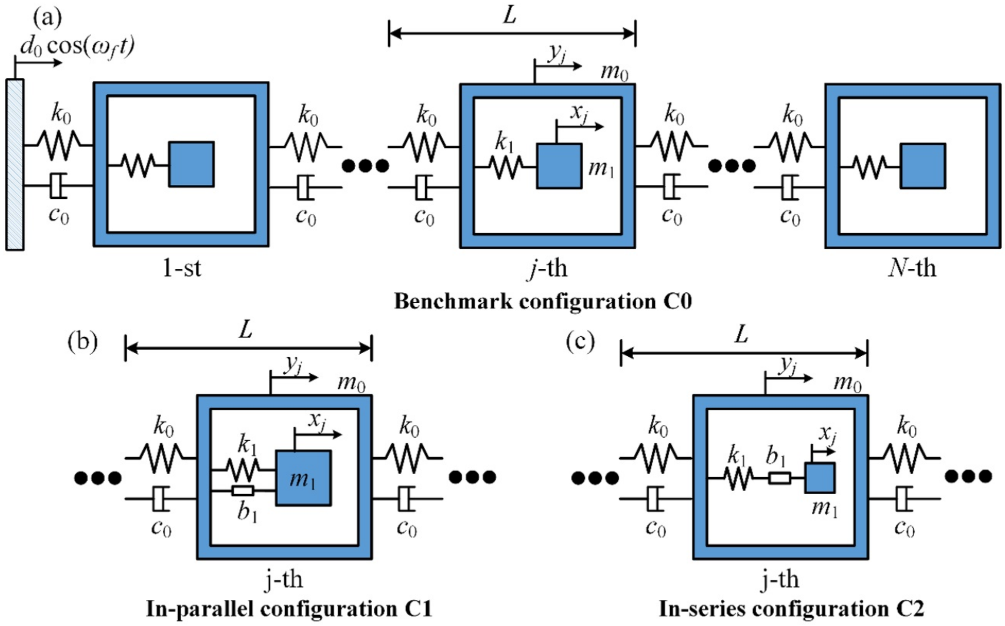

Figure 4.1: Locally resonant acoustic metamaterials configurations with N different identical mass-in-mass unit cells, which are interconnected by linear springs k_0 and dampers c_0. An excitation displacement $d_0 \cos \omega_f t$is applied to the first cell. (a) Benchmark model c_0. (b) Inerter-based model C1 with in-parallel spring k_1 and inerter b_1. (c) Inerter-based model C2 with in-series spring k_1 and inerter b_1.

$$Y_j'' + 2\zeta_0(2Y_j' - Y_{j-1}' - Y_{j+1}') + (2Y_j - Y_{j-1} - Y_{j+1}) + \mu_1 X_j'' = 0; \quad (4.2a)$$

$$\mu_1 X_j'' + \beta_1(X_j - Y_j) + \lambda_1(X_j'' - Y_j'') = 0. \quad (4.2b)$$

where the primes $(\bullet)'$ denote differentiation with respect to τ. The parameters and variables are introduced as

$$\begin{aligned} &Y_j = \frac{y_j}{L}, X_j = \frac{x_j}{L}, \omega_0 = \sqrt{\frac{k_0}{m_0}}, \omega_1 = \sqrt{\frac{k_1}{m_1}}, \tau = \omega_0 t, \\ &\Omega = \frac{\omega_f}{\omega_0}, \zeta_0 = \frac{c_0}{2m_0\omega_0} . \mu = \frac{m_1}{m_0}, \beta = \frac{k_1}{k_0}, \lambda = \frac{b_1}{m_0}, \end{aligned} \quad (4.3)$$

where Y_j and X_j represent the non-dimensional displacements; ω_0 and ω_1 are the natural frequencies of the lumped mass and the internal resonator, respectively; τ and Ω are the nondimensional time and excitation frequency, respectively; and ζ_0, μ_1, β_1, and λ_1 are the damping ratio, mass ratio, stiffness ratio, and the inertance-to-mass ratio, respectively.

4.2.2 Dispersion relation

For the jth unit cell in this system, the harmonic wave solutions are presented by

$$Y_j = \hat{Y}\mathrm{e}^{\mathrm{i}(jqL-\Omega\tau)}; \tag{4.4a}$$

$$X_j = \hat{X}\mathrm{e}^{\mathrm{i}(jqL-\Omega\tau)}, \tag{4.4b}$$

where q is the wave number and $\hat{Y}$ and $\hat{X}$ represent the response amplitudes for lumped mass and the internal resonator mass, respectively.

Based on the Bloch's theorem (Brillouin, 1953), if two adjacent masses vibrate with the same amplitude, there will be a phase difference. Therefore, the displacements of the $(j+1)$th and $(j-1)$th lumped masses can be written as

$$Y_{j+1} = \hat{Y}\mathrm{e}^{\mathrm{i}((j+1)qL-\Omega\tau)} = \hat{Y}\mathrm{e}^{\mathrm{i}(jqL-\Omega\tau)}\mathrm{e}^{\mathrm{i}qL}; \tag{4.5a}$$

$$Y_{j-1} = \hat{Y}\mathrm{e}^{\mathrm{i}((j-1)qL-\Omega\tau)} = \hat{Y}\mathrm{e}^{\mathrm{i}(jqL-\Omega\tau)}\mathrm{e}^{-\mathrm{i}qL}. \tag{4.5b}$$

Note that $\mathrm{e}^{\mathrm{i}qL} + \mathrm{e}^{-\mathrm{i}qL} = 2\cos(qL)$ and that in the calculation of dispersion relation, the damping effects are ignored in the current study. The damping will only have an influence on the response amplitude but not affect the bandgap frequency range. By substituting Eqs. (4.4) and (4.5) into Eq. (4.2) and ignoring the dampers, we have

$$\begin{bmatrix} 2-2\cos(qL)-\Omega^2 & -\mu_1\Omega^2 \\ -\beta_1+\lambda_1\Omega^2 & -\mu_1\Omega^2+\beta_1-\lambda_1\Omega^2 \end{bmatrix} \begin{Bmatrix} \hat{Y} \\ \hat{X} \end{Bmatrix} = \begin{Bmatrix} 0 \\ 0 \end{Bmatrix}. \tag{4.6}$$

If the determinant of the 2-by-2 matrix shown in Eq. 4.6 is null, there will be a set of trivial solutions. Therefore, the dispersion relation is

$$\begin{vmatrix} 2-2\cos(qL)-\Omega^2 & -\mu_1\Omega^2 \\ -\beta_1+\lambda_1\Omega^2 & -\mu_1\Omega^2+\beta_1-\lambda_1\Omega^2 \end{vmatrix} = 0. \tag{4.7}$$

Following the same derivation process, for the LRAM shown in Fig. 4.1(c), the equation governing the dispersion relation of the in-series inerter-based LRAM can be derived:

$$\begin{vmatrix} 2-2\cos(qL)-\Omega^2 & -\mu_1\Omega^2 \\ \lambda_1\gamma^2 & \lambda_1\Omega^2-\mu_1\gamma^2-\lambda_1\gamma^2 \end{vmatrix} = 0. \tag{4.8}$$

4.2.3 Wave transmission

The effective mass m_{eff} of the unit cell with a linear inerter-based resonator is obtained by considering the combined lumped mass and the internal resonator as a single equivalent mass that can be negative at some frequencies (Fang et al., 2006). Note that the nondimensional equation of motion is

$$M_{\text{eff}}Y_j'' + 2\zeta_0(2Y_j' - Y_{j_1}' - Y_{j+1}') + 2Y_j - Y_{j-1} - Y_{j+1} = 0, \tag{4.9}$$

where $M_{\text{eff}} = m_{\text{eff}}/m_0$.

For the in-parallel and the in-series configurations, by solving Eqs. (4.2), (4.8) and (4.9), the non-dimensional effective masses can be derived respectively as

$$M_{\text{eff\_p}} = 1 + \mu_1 + \frac{\mu_1^2 \Omega^2}{\beta_1 - \lambda_1 \Omega^2 - \mu_1 \Omega^2}; \tag{4.10a}$$

$$M_{\text{eff\_s}} = 1 + \frac{\lambda_1 \mu_1}{\mu_1 + \lambda_1 - \lambda_1 \Omega^2}. \tag{4.10b}$$

For an N-unit finite periodic effective mass lattice structure without damping, the wave transmission property is of interest (Meng et al., 2020). The equations of motion are shown below:

$$\begin{cases} M_{\text{eff}} Y_j'' + 2Y_j - Y_{j-1} - Y_{j+1} = 0, & \text{when} \quad j = 1, 2, ..., N-1; \\ M_{\text{eff}} Y_j'' + Y_j - Y_{j-1} = 0, & \text{when} \quad j = N. \end{cases} \tag{4.11}$$

Note that Y_0 represents the amplitude of motion excitation. Using Eqs. (4.4a) and (4.11), the following non-dimensional relations for a finite system are derived:

$$\begin{cases} (2 - \Omega^2 M_{\text{eff}}) \hat{Y}_j = \hat{Y}_{j+1} + \hat{Y}_{j-1}, & \text{when} \quad j = 1, 2, ..., N-1; \\ (1 - \Omega^2 M_{\text{eff}}) \hat{Y}_j = \hat{Y}_{j-1}, & \text{when} \quad j = N. \end{cases} \tag{4.12}$$

Based on Eq. (12), the wave transmittance $T = 20 \lg \mid \hat{Y}_j / \hat{Y}_0 \mid$ of the finite periodic lattice structure is

$$T = 20 \lg \left(\sum_{n=1}^{N} \mid T_{\text{a}} \mid \right). \tag{4.13}$$

where $T_{\mathrm{a}} = \hat{Y}_{\mathrm{a}}/\hat{Y}_{n-1}$ could be expressed in the form of

$$T_{\mathrm{a}} = \frac{1}{2 - T_{n+1} - M_{\mathrm{eff}}\Omega^2}, \tag{4.14}$$

when n=1, 2, ..., N, with $T_{N+1} = 1$.

4.2.4 Vibration power flow and transmission

The power flow analysis is also conducted for the design and application of the metamaterial system. The total instantaneous power input into the system is the product of the excitation force and the corresponding velocity at the excitation point (Al Ba'ba'a and Nouh, 2017; Shi et al., 2019). For the current metamaterial system, the first lumped mass is connected to a moving end of displacement, $D_0 \cos \omega_f t$, as the excitation displacement as shown in Fig. 4.1(b). By representing the effect of the local resonators in the outer mass as an effective mass, the metamaterial system is treated as a chain structure of effective masses connected by springs and dampers. The corresponding non-dimensional equation of motion of the system with N unit cells and the energy balance equation are

$$\mathbf{M}\mathbf{Y}'' + \mathbf{C}\mathbf{Y}' + \mathbf{K}\mathbf{Y} = \mathbf{F}; \tag{4.15a}$$

$$\mathbf{Y}'^{\mathrm{T}}\mathbf{M}\mathbf{Y}'' + \mathbf{Y}'^{\mathrm{T}}\mathbf{C}\mathbf{Y}' + \mathbf{Y}'^{\mathrm{T}}\mathbf{K}\mathbf{Y} = \mathbf{Y}'^{\mathrm{T}}\mathbf{F}. \tag{4.15b}$$

respectively, where

$$\mathbf{M} = M_{\text{eff}} \begin{bmatrix} 1 & 0 & \cdots & 0 \\ 0 & \ddots & \ddots & \vdots \\ \vdots & \ddots & \vdots & 0 \\ 0 & \cdots & 0 & 1 \end{bmatrix}; \tag{4.16a}$$

$$\mathbf{C} = 2\zeta_0 \begin{bmatrix} 2 & -1 & 0 & \cdots & 0 \\ -1 & 2 & -1 & \ddots & \vdots \\ 0 & \ddots & \ddots & \ddots & 0 \\ \vdots & \ddots & -1 & 2 & -1 \\ 0 & \cdots & 0 & -1 & 1 \end{bmatrix}; \tag{4.16b}$$

$$\mathbf{K} = \begin{bmatrix} 2 & -1 & 0 & \cdots & 0 \\ -1 & 2 & -1 & \ddots & \vdots \\ 0 & \ddots & \ddots & \ddots & 0 \\ \vdots & \ddots & -1 & 2 & -1 \\ 0 & \cdots & 0 & -1 & 1 \end{bmatrix}; \tag{4.16c}$$

$$\mathbf{F} = M_{\text{eff}} \begin{bmatrix} D_0 \cos \Omega\tau - 2\zeta_0 \Omega D_0 \sin \Omega\tau \\ 0 \\ \vdots \\ 0 \end{bmatrix} \tag{4.16d}$$

are the N by N total mass, damping and stiffness matrices, and the external force vector, respectively, and the symbol T stands for the transpose operation of a matrix. The displacement vector is calculated from the structural dynamics as

$$\mathbf{Y} = [\mathbf{K} + \mathrm{i}\Omega\mathbf{C} - \Omega^2\mathbf{M}]^{-1}\mathbf{F}. \tag{4.17}$$

The non-dimensional real power at time τ defined in the complex notation (Xing and Price, 1999) is given by

$$P(\tau) = \mathbf{F}(\tau)\mathbf{Y}'(\tau) = \Re\{\bar{\mathbf{F}}(\tau)\}\Re\{\bar{\mathbf{Y}}'(\tau)\}. \tag{4.18}$$

The non-dimensional time-averaging real power over an excitation cycle can be calculated and complex variable operated as follows:

$$\begin{aligned} P(\tau) &= \frac{1}{\tau_\mathrm{s}}\int_{\tau_0}^{\tau_0+\tau_\mathrm{s}} \Re\{\bar{\mathbf{F}}(\tau)\}\Re\{\bar{\mathbf{Y}}'(\tau)\}\mathrm{d}\tau \\ &= \frac{1}{2}(\Re\{\bar{\mathbf{F}}\}\Re\{\bar{\mathbf{Y}}'\} + \Im\{\bar{\mathbf{F}}\}\Im\{\bar{\mathbf{Y}}'\}). \end{aligned} \tag{4.19}$$

where τ_0 is the non-dimensional averaging operation beginning time and $\tau_\mathrm{s} = 2\pi/\omega_f$ is the non-dimensional excitation period.

Therefore, the excitation force is related to the difference of first lumped mass and excitation displacement $(D_0 \cos\Omega\tau - Y_1)$. For a N-unit finite metamaterial system, the total instantaneous output power is defined as the power transmitted to Nth lumped mass, which is the power of $(N-1)$-unit lumped mass. The force is related to the displacement difference of the last two lumped masses $(Y_{N-1} - Y_\mathrm{a})$. The non-dimensional steady-state time-averaged input and output powers are derived based on Eq. 4.19 as:

$$\begin{aligned} \bar{P}_\mathrm{in} = \frac{1}{\tau_\mathrm{s}}\int_{\tau_0}^{\tau_0+\tau_\mathrm{s}} & -D_0\Omega\sin\Omega\tau(Y_1 - D_0\cos\Omega\tau + 2\zeta_0 Y_1' + \\ & 2\zeta_0 D_0 \sin\Omega\tau)\mathrm{d}\tau, \end{aligned} \tag{4.20a}$$

$$\bar{P}_\mathrm{out} = \frac{1}{\tau_\mathrm{s}}\int_{\tau_0}^{\tau_0+\tau_\mathrm{s}} Y_{N-1}'(Y_{N-1} - Y_\mathrm{a} + 2\zeta_0 Y_{N-1}' - 2\zeta_0 Y_\mathrm{a}')\mathrm{d}\tau \tag{4.20b}$$

respectively. The relative power flow analysis transmission can be evaluated by comparing the input and output powers.

4.2.5 Results and validation

Figures 4.2(a) and (b) show the dispersion relation and the wave transmittance characteristics for the inerter-based LRAM configuration C1. The wave transmittance is defined as the ratio of the displacement amplitude of the last cell mass and that of the first cell displacement and is shown in a decibel scale. For numerical validations, the non-dimensional material parameters are selected as $\mu_1 = 0.5$ and $\beta_1 = 0.5$. Figure 4.2(a) represents the dispersion diagram with different inertance ratios λ_1. The figure shows that in each case there will be a shadowed frequency gap where there is no real solution in Eq. (4.7) for wave propagation constant qL. It indicates that the wave transmission is attenuated in this frequency region, and it can be recognised as the bandgap. Note that $\lambda_1 = 0$ corresponds to the no inerter case, i.e., configuration c_0 as shown in Fig. 4.1(a). When λ_1 increases from 0 to 1, the bandgap shifts to the lower-frequency region while the bandgap width is narrowed. The in-parallel inerter-based mechanism provides benefits to the bandgap properties by achieving the low-frequency bandgap. Figure 4.2(b) shows the wave transmittance diagram for the in-parallel LRAM structure with finite unit cells, obtained by presenting in the form of effective mass as shown in Eq. (4.10a). When the transmittance is less than zero due to the local resonance as highlighted in Fig. 4.2(b), it means the wave is well suppressed in this range. Comparing Fig. 4.2(a) with (b), the blue shadow reveals that they have a good agreement regarding the bandgap location and width from 0.72 to 0.82, thereby verifying each other. Based on Eqs. (4.13) and (4.14), for the 6-cell in-parallel LRAM system with $\lambda_1 = 0.4$, the corresponding wave transmittance diagram shows a distinct frequency gap with low transmittance. Outside the gap, there are many peaks located at different frequencies. Figure 4.2(b) also reveals that there is better wave attenuation performance when the frequency is near the lower limit of the bandgap than that close to the upper limit. As for a continuous or multiple degrees of freedom system, the wave transmittance is complex because the resonator is coupled with all structural modes of the host system, so the peaks correspond to different resonant frequencies.

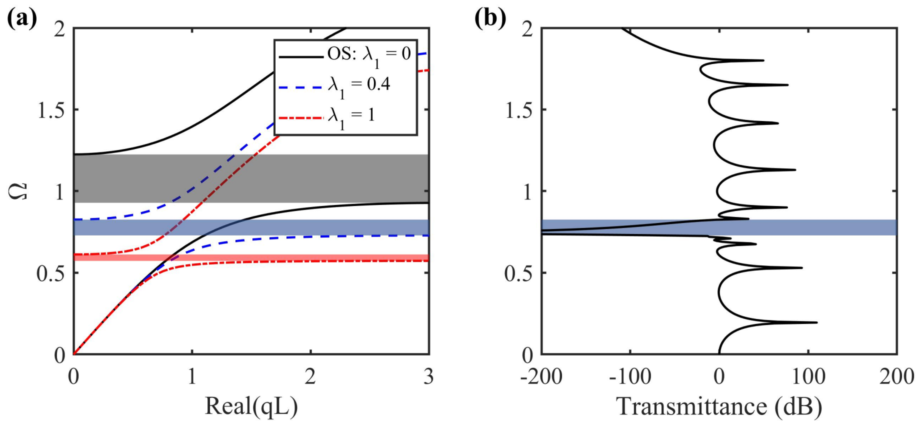

Figure 4.2: Theoretical results of inerter-based in-parallel LRAM configuration C1 of $\mu_1 = 0.5$, $\beta_1 = 0.5$ with different inertance ratios. (a) Dispersion diagram with different inertance ratios and (b) wave transmittance diagram. The gray, blue and red shadowed areas represent the bandgap locations with $\lambda_1 = 0$, 0.4, and 1, respectively. The case $\lambda_1 = 0$ can be recognised as the original system c_0.

Figure 4.3(a) shows the dispersion diagram for the in-series configuration C2. This structure becomes the benchmark configuration when λ_1 is set as infinite (solid curve). The figure reveals that when λ_1 is decreasing from infinity to a finite value of 0.4 and then 0.1, the bandgap is moving to a higher frequency with a broader width. This property is in contrast to the in-parallel configuration. Figure 4.3(b) shows the wave transmittance diagram when $\lambda_1 = 0.4$. There is one extra low-transmittance gap shadowed in blue, outside of which there are multiple small peaks resulting from the complex resonant frequencies. The bandgap shown in Fig. 4.3(b) is consistent with that shown in Fig. 4.3(a). Comparing Figs. 4.2 and

4.3, it is found that the in-parallel configuration may be desirable when low-frequency vibration suppression is sought.

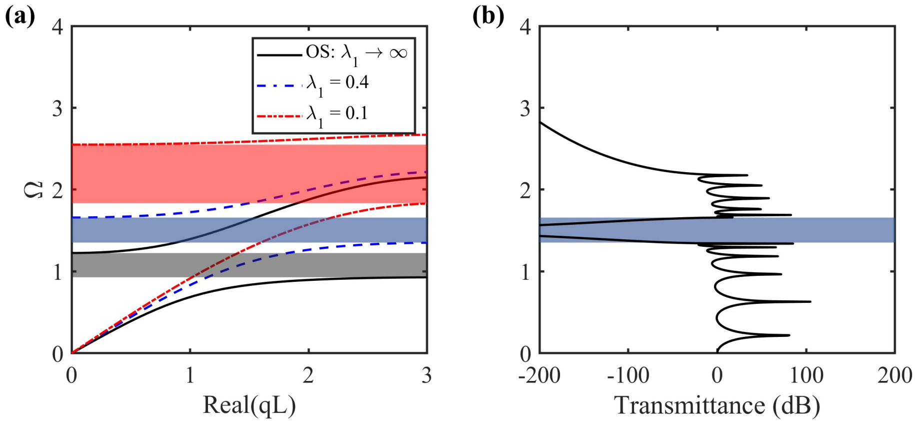

Figure 4.3: Theoretical results of inerter-based in-series LRAM configuration C2 with $\mu_1 = 0.5$, $\beta_1 = 0.5$ with different inertance ratios. (a) Dispersion diagram with different inertance ratios and (b) wave transmittance diagram. The gray, blue and red shadowed areas represent the bandgap locations with $\lambda_1 = 1$, 0.4, and 0.1, respectively. The case λ_1=1 can be recognised as the original system c_0.

In Fig. 4.4, the theoretical results of the time-averaging input and output power flow of the 100-unit in-parallel configuration C1 are plotted for comparing and deriving the power flow consumption. The non-dimensional parameters selected are $\mu_1 = 0.5$, $\beta_1 = 0.5$, $\lambda_1 = 0.4$, and $\zeta_0 = 0.005$. Figure 4.4(a) shows that the locations of power flow peaks and gap are similar, but the output power all over the frequency range is always smaller than the input power, especially the gap is much deeper. Figure 4.4(b) shows the difference between the input and output power flow, which is calculated by $(\lg \bar{P}_{\text{in}} - \lg \bar{P}_{\text{out}})$. The power consumption is extremely high in the range from 0.72 to 0.82, which is exactly the same as the bandgap location and width shown as the blue shadowed area in Fig. 4.3. It clearly indicates the bandgap power block effect. The output power will be much lower than the input power; thus, the vibration will be suppressed when the excitation frequency is within the bandgap. The power flow analysis can help with the LRAM configuration vibration suppression design.

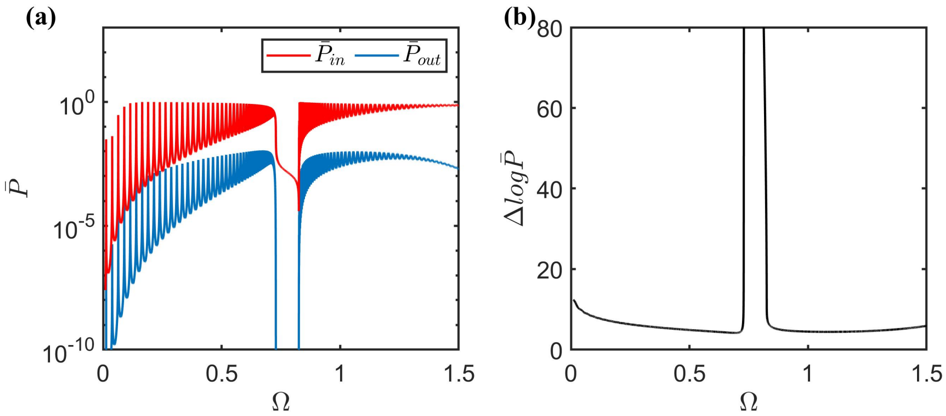

Figure 4.4: Theoretical results for the 100-unit in-parallel LRAM configuration C1 with $\mu_1 = 0.5$, $\beta_1 = 0.5$, $\lambda_1 = 0.4$ and $\zeta_0 = 0.005$. (a) The time-averaging power flow diagram. The red and blue curves are the input power of the first cell produced by excitation displacement and the output power of the last cell, respectively. (b) The power flow consumption in dB, which is the difference of the input and output power flow in the logarithmic scale.

4.3 Linear inerter-based dual-resonator LRAM

4.3.1 Modelling and governing equations

Multi-resonator LRAM will lead to the generation of the same number of bandgaps as that of the local resonators. Here, the use of the dual local resonators attached to a lumped mass m_0 is shown in Fig. 4.5. This configuration, labeled as C3, differs from the configuration C1 by the addition of another local resonator comprising mass m_2 connected to the lumped mass via a linear spring of stiffness k_2 and an inerter of inertance b_2. The absolute displacement of the jth resonator m_2 is defined as z_j.

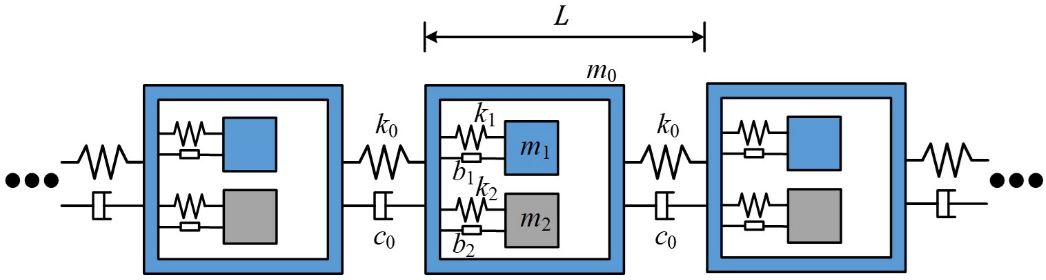

Figure 4.5: Linear inerter-based locally resonant acoustic metamaterials' configuration C3. The lumped masses are interconnected by identical springs k_0 and dampers c_0, while in each lumped mass dual local resonators are attached by in-parallel springs k_1, k_2 and inerters b_1, b_2.

The equations of motion for configuration C3 are

$$Y_j'' + 2\zeta_0(2Y_j' - Y_{j-1}' - Y_{j+1}') + (2Y_j - Y_{j-1} - Y_{j+1}) + \mu_1 X_j'' + \mu_2 Z_j'' = 0; \tag{4.21a}$$

$$\mu_1 X_j'' + \beta_1(X_j - Y_j) + \lambda_1(X_j'' - Y_j'') = 0; \tag{4.21b}$$

$$\mu_2 Z_j'' + \beta_2(Z_j - Y_j) + \lambda_2(Z_j'' - Y_j'') = 0, \tag{4.21c}$$

where the non-dimensional parameters are shown in Eq. (4.3), and new parameters have been introduced:

$$Z_j = \frac{z_j}{L}, \qquad \mu_2 = \frac{m_2}{m_0}, \qquad \beta_2 = \frac{k_2}{k_0}, \qquad \lambda_2 = \frac{b_2}{m_0}, \tag{4.22}$$

where Z_j represents the non-dimensional displacement and μ_2, β_2, and λ_2 are the damping ratio, mass ratio, stiffness ratio, and the inertance-to-mass ratio, respectively. The dispersion relation without damping for the dual resonator configuration can be derived as

$$\begin{vmatrix} 2(1-\cos(qL))-\Omega^2 & -\mu_1\Omega^2 & -\mu_2\Omega^2 \\ -\beta_1+\lambda_1\Omega^2 & -\mu_1\Omega^2+\beta_1-\lambda_1\Omega^2 & 0 \\ -\beta_2+\lambda_2\Omega^2 & 0 & -\mu_2\Omega^2+\beta_2-\lambda_2\Omega^2 \end{vmatrix} = 0 \tag{4.23}$$

Based on the Bloch theorem, the relations of displacement amplitude between the jth, $(j+1)$th, and $(j-1)$th lumped masses can be obtained by solving Eq. (4.21). Substituting the equations for connected lumped mass displacement amplitude into Eq. (4.9), the corresponding non-dimensional effective mass for the dual resonator configuration is derived to be

$$M_{\text{eff}}^{d} = 1+\mu_1+\mu_2+\frac{\mu_1^2\Omega^2}{\beta_1-\lambda_1\Omega^2-\mu_1\Omega^2}+\frac{\mu_2^2\Omega^2}{\beta_2-\lambda_2\Omega^2-\mu_2\Omega^2}. \tag{4.24}$$

The wave transmittance can also be obtained by inserting Eq. (4.24) into Eqs. (4.13) and (4.14).

4.3.2 Dispersion relation and validation

Figure 4.6 presents the bandgap characteristic diagrams of the LRAM configuration C3. The general material parameters are set as $\mu_1 = \mu_2 = 0.5$ and $\beta_1 = \beta_2 = 0.3$. When $\lambda_1 = 1$ and $\lambda_2 = 0.5$, the dispersion relation curve shows two separate bandgaps, which are caused by the presence of two local resonators. The bandgaps are located around the natural frequencies of the local resonators (El-Borgi et al., 2020). The wave transmittance diagram shown in Fig. 4.6(b) demonstrates that the low-transmittance gaps have good agreement with bandgap locations and widths, as shown in Fig. 4.6(a). The upper bandgap is relatively broader compared with the lower bandgap. To make full use of these two bandgaps, it is desirable to merge them into one complete gap. Material parameters such as the inertance ratio of the resonators can be tailor-designed to change the bandgap locations such that they can be merged.

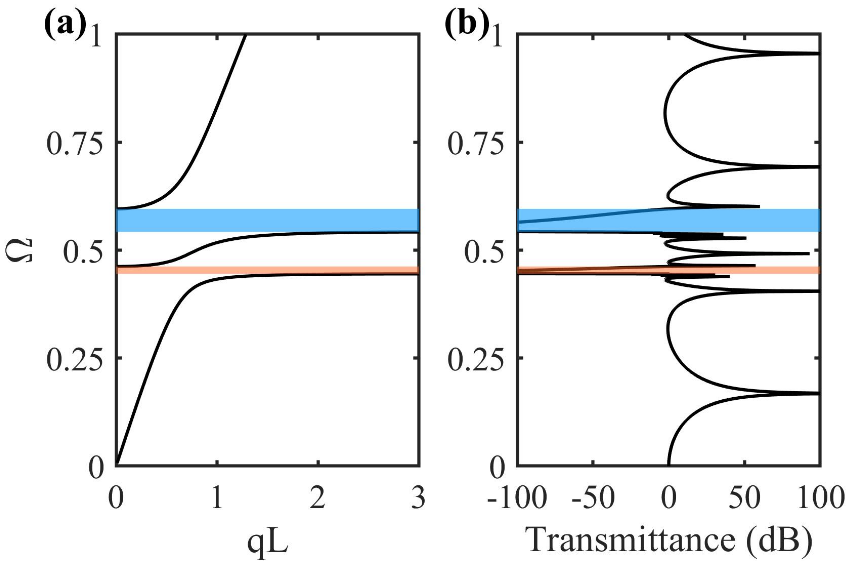

Figure 4.6: (a) Dispersion relations diagram and (b) wave transmittance diagram of the inerter-based dual-resonator LRAM configuration C3 with the parameters $\mu_1 = \mu_2 = 0.5$, $\beta_1 = \beta_2 = 0.3$, $\lambda_1 = 1$, and $\lambda_2 = 0.5$. The blue and orange shadowed areas are the dual produced bandgaps.

In Fig. 4.7(a), the inertance ratio λ_2 is set as a constant value of 0.5 while λ_1 increases from 0 to 1. It shows that at the two boundaries of $\lambda_1 = 0$ and $\lambda_1 = 1$, there are two bandgaps that are distinctly apart. The solid curve represents the total gap width of these two gaps. As λ_1 increases from 0 to 0.5, the bandgaps move toward each other and merge when $\lambda_1 = 0.5$. Therefore, in this case, $\lambda_1 = \lambda_2 = 0.5$ can lead to a complete bandgap located in the low-frequency region. The figure also shows that with increasing λ_1, the total bandwidth is reduced. Fig. 4.7(b) shows the bandgap characteristics when the inertance ratio λ_2 is set as a constant value of 0.8 while λ_1 increases from 0 to 1. It shows that two bandgaps merge when $\lambda_1 = \lambda_2 = 0.8$. Figs. 4.7(a) and (b) show that with larger

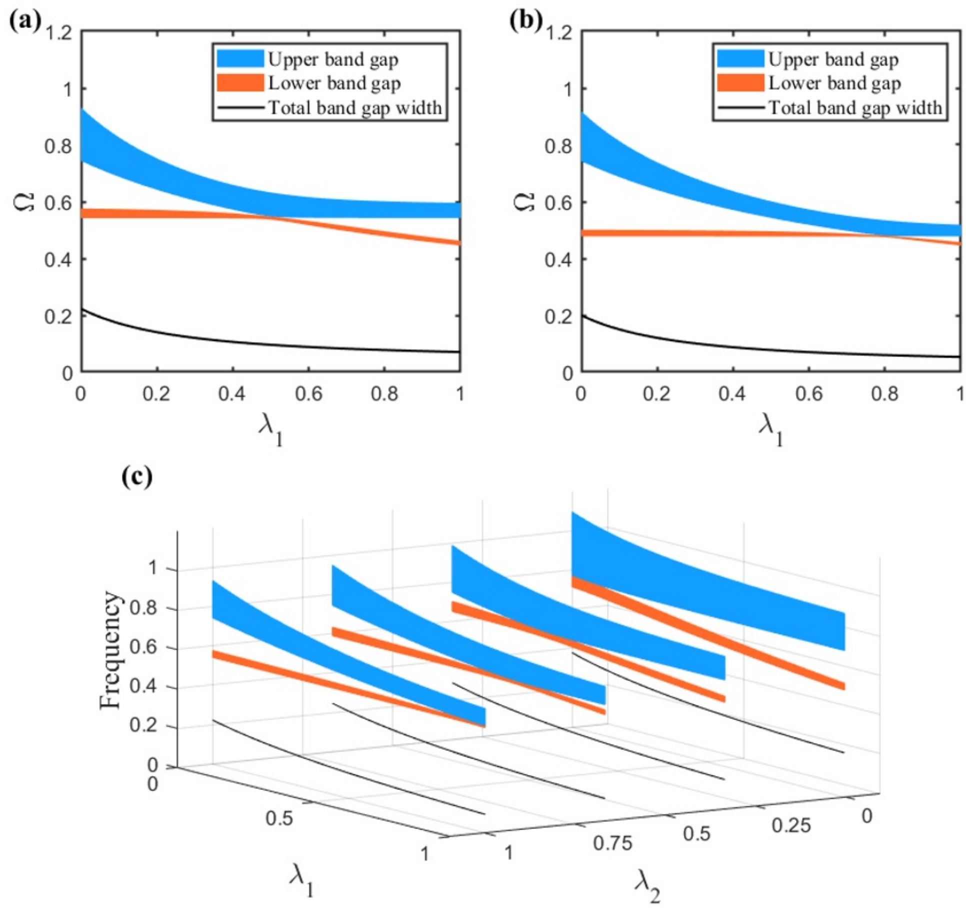

Figure 4.7: Influence of difference inertance ratios on dispersion diagrams for dual resonator configuration C3 with $\mu_1 = \mu_2 = 0.5$, $\beta_1 = \beta_2 = 0.3$. (a) $\lambda_1 = [0, 1]$, $\lambda_2 = 0.5$, (b) $\lambda_1 = [0, 1]$, $\lambda_2 = 0.8$, and (c) $\lambda_1 = [0, 1]$, $\lambda_2 = [0, 1]$. The blue and orange areas are the upper and lower bandgaps and the solid line represents the total bandgap width.

inertance ratios $\lambda_1 = \lambda_2$, the merged bandgap will be located at a lower frequency with a relatively narrower bandwidth. In Fig. 4.7(c), more cases with different parameters $\lambda_2(= 0, 1/3, 2/3, 1)$ are considered to verify the results shown in Figs. 4.7(a) and (b). Based on the results shown in these cases, it seems that when $\lambda_1 = \lambda_2$, the bandgaps can be merged into a single one. Comparing the dispersion relation of the dual-resonator structure and that of the single resonator structure, we can draw the conclusion that when the resonator-related parameters are the same, the dual-resonator structure can be recognised as a single-resonator structure, which will lead to a single bandgap dispersion relation. Fig. 4.7(c) shows that the setting of $\lambda_1 = \lambda_2 = 0$ leads to the broadest frequency range but with higher frequencies than the cases with nonzero values of λ_1 and λ_2. With the increasing of inertance ratios with $\lambda_1 = \lambda_2$, the gap bandwidth becomes narrower but located at lower frequency. In summary, for low-frequency vibration suppression using the configuration C3 with the same mass and stiffness ratios of the local resonators, the same inertance ratios are suggested for the merger of the bandgaps. There might be some limitations in applying the multi-resonator design due to possible space and weight constraints. Nevertheless, it will have more robustness against uncertainty compared with the single-resonator structure, as the system can still function even if one of the resonators does not work.

The theoretically calculated power flow for the 100-unit configuration C3 is shown in Fig. 4.8. The non-dimensional material parameters selected are $\mu_1 = \mu_2 = 0.5$, $\beta_1 = \beta_2 = 0.3$, $\lambda_1 = 1$, $\lambda_2 = 0.5$, and $\zeta_0 = 0.05$. Similar phenomenon is emerged compared with Fig. 4.4(a), but there are two much deeper gaps in dual-resonator configuration. The power flow consumption in Fig. 4.8(b) shows that there will be two frequency bands with extremely high power dissipation, which separately corresponds to the two bandgaps shown in Fig. 4.8. In these two excitation frequency ranges, the energy is blocked and vibration will be much reduced.

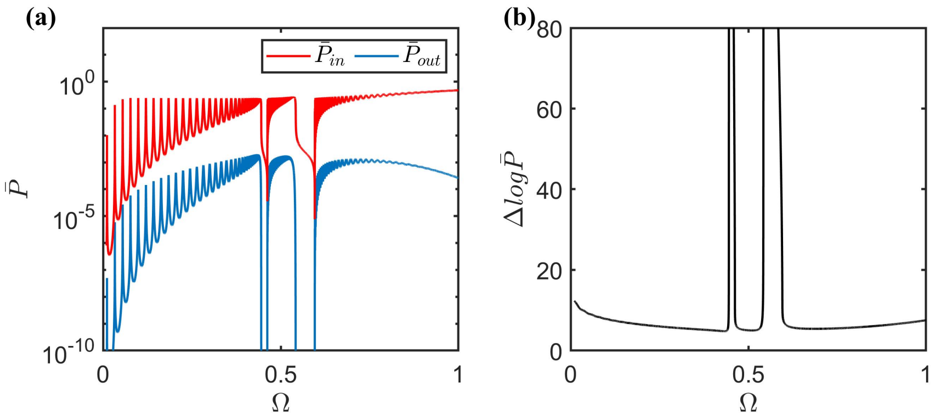

Figure 4.8: Theoretical results for the 20-unit dual configuration C3 with $\mu_1 = \mu_2 = 0.5$, $\beta_1 = \beta_2 = 0.3$, $\lambda_1 = 1$, $\lambda_2 = 0.5$, and $\zeta_0 = 0.005$. (a) The time-averaging power flow diagram. The red and blue curves are the input power of first cell produced by excitation displacement and the output power of the last cell, respectively. (b) The power flow consumption in dB, which is the difference of the input and output power flow in the logarithmic scale.

4.4 Nonlinear inerter-based single-resonator LRAM

The vibration absorber based on the nonlinear dynamics has attracted the attention of many researchers, but few of them have tried to do research in combination with the inerter, nonlinear dynamics, and LRAM. Continued with the above works related to the linear inerter, this section will focus on the study of the nonlinear inerter-based single resonator attached LRAM. The characteristics of a unit cell with nonlinear inerter will be introduced in the first section while the research will be extended to LRAM configuration in Sec. 4.4.1. Then the results and discussion will be stated in Sec. 4.4.2.

4.4.1 Unit cell comprising a nonlinear inerter

Figure 4.9(a) shows a schematic diagram of the geometrically nonlinear inertance mechanism (GNIM) proposed in our previous studies, which have shown the design and implementation feasibilities (Yang et al., 2020; Moraes et al., 2018; Wang et al., 2019c). In this mechanism, one pair of identical lateral inerters is hinged together at the point O while their other terminals are pinned to points A and B, to which the vertical distances from terminal O are the same and denoted as l. The two inerters are assumed to be of negligible physical mass and linear so that the inertial force of each inerter in the horizontal direction is proportional to the relative acceleration between the two ends. If the terminal O deviates from the static balance position along the horizontal direction, the lateral inerters will tilt and form a nonlinear inertance mechanism because of the geometrical nonlinearity. Due to symmetry, the terminal O moves only along the horizontal direction and the relative displacement is r.

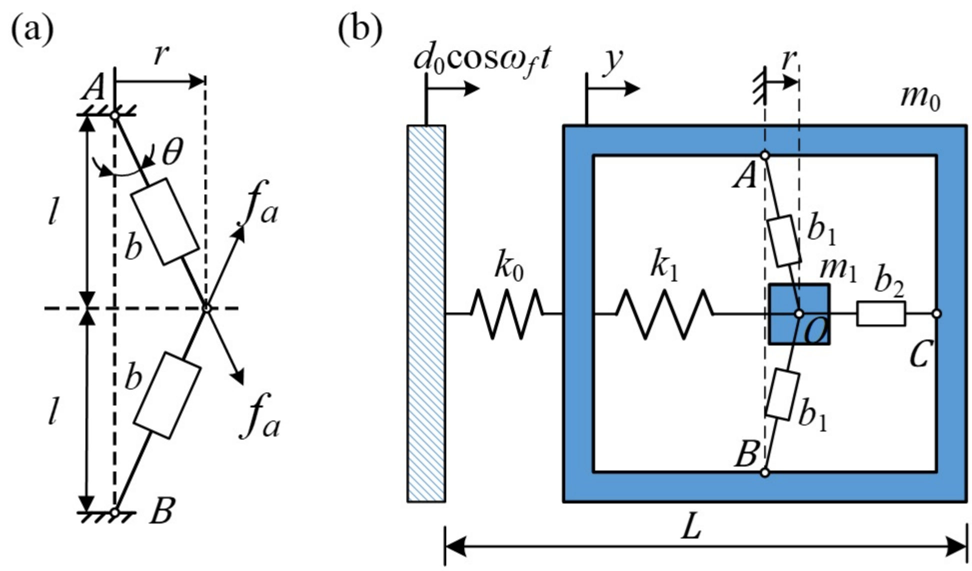

Figure 4.9: (a) Schematic diagrams of the geometrically nonlinear inertance mechanism. Two lateral inerters of b are hinged together at a terminal with displacement r. (b) 2-DoF GNIM based unit cell. The lumped mass is attached by a spring k_0 to a base of harmonic excitation displacement $d_0 \cos \omega_f t$. The resonator is connected to the lumped mass with longitudinal spring k_1, inerter b_2, and two lateral inerters b_1.

The force–response relationship of the GNIM has been analysed (Yang et al., 2020) and is revisited here. The velocity of the deviating terminal is $\dot{r}$, so the velocity along the axis of the inerter is $\dot{r}\sin\theta$, where $\sin\theta = r/\sqrt{r^2+l^2}$. The force along the inerter axis can be obtained as

$$f_{\mathrm{a}} = b_1 \frac{\mathrm{d}(\dot{r}\sin\theta)}{\mathrm{d}t} = b_1(\ddot{r}\sin\theta + \frac{\dot{r}^2 l^2}{(l^2+r^2)\sqrt{l^2+r^2}}). \tag{4.25}$$

Due to symmetry, the total nonlinear inertial force should be in the horizontal direction and is expressed by

$$f_{\mathrm{a}} = 2f_{\mathrm{a}}\sin\theta = 2b_1\left(\frac{r^2\ddot{r}}{l^2+r^2} + \frac{l^2 r\dot{r}^2}{(l^2+r^2)^2}\right) = f_{\mathrm{b1}} + f_{\mathrm{b2}}, \tag{4.26}$$

where $f_{\mathrm{b1}} = 2b_1 r^2\ddot{r}/(l^2+r^2)$ and $f_{\mathrm{b2}} = 2b_1 l^2 r\dot{r}^2/(l^2+r^2)^2$.

Figure 4.9(b) shows the schematic diagram of a unit cell comprising the GNIM. The outer lumped mass, m_0, is connected to a base by a spring of stiffness coefficient k_0. Inside the lumped mass, there is a local resonator comprising a mass, m_1, one horizontal spring with stiffness coefficient k_1, one horizontal inerter with inertance b_2, and the GNIM with two lateral inerters each with inertance b_1. The two lateral inerters are hinged together at the terminal O with the resonator mass while their other terminals A and B are fixed at the rigid lumped mass shell. The horizontal inerter is hinged at terminal O and pined at terminal C to the outer mass. The displacement of mass, m_0, is denoted by y and is connected to a moving end of displacement $d_0\cos\omega_f t$. The relative displacement between the resonator mass and the lumped mass is denoted as r, such that the inerters are oriented in the vertical direction when $r = 0$.

The equations of motion of the system shown in Fig. 4.9(b) are

$$m_0\ddot{y} + k_0(y - d_0\cos\omega_f t) - b_2\ddot{r} - k_1 r - f_\mathrm{a}(r,\dot{r},\ddot{r}) = 0; \tag{4.27a}$$

$$m_1(\ddot{r} + \ddot{y}) + b_2\ddot{r} + k_1 r + f_\mathrm{a}(r,\dot{r},\ddot{r}) = 0. \tag{4.27b}$$

By introducing the following parameters and variables:

$$Y = \frac{y}{L}, \quad R = \frac{r}{L}, \quad D_0 = \frac{d_0}{L}, \tag{4.28}$$

where Y and R represent the non-dimensional displacements and D_0 are the non-dimensional excitation amplitude, respectively. Referring to Eqs. (4.3), (4.22), and (4.28), the equations of motions in Eqs. (4.27) can be non-dimensionalised to be

$$(1+\mu_1)Y'' + \mu_1 R'' + Y = D_0\cos\Omega\tau; \tag{4.29a}$$

$$(\mu_1+\lambda_2)R'' + \mu_1 Y'' + \beta_1 R + G(R,R',R'') = 0, \tag{4.29b}$$

where the primes $(\bullet)'$ denote differentiation with respect to τ, and the non-dimensional nonlinear inertial force caused by the geometric nonlinearity is

$$G(R,R',R'') = \frac{f_\mathrm{a}(r,\dot{r},\ddot{r})}{m_0 L\omega_0^2} = 2\lambda_1\left(\frac{R^2R''}{1+R^2} + \frac{RR'^2}{(1+R^2)^2}\right). \tag{4.30}$$

It shows that the geometric nonlinear force is influenced by the relative displacement, velocity, and acceleration between masses m_0 and m_1.

When the relative displacement response R is small, the nonlinear term can be Taylor expanded at $R=0$ to obtain

$$G(R,R',R'') \approx 2\lambda_1 R^2R'' + 2\lambda_1(1-2R^2)RR'^2. \tag{4.31}$$

Substitute Eq. (4.31) into Eq. (4.29) to obtain the simplified non-dimensional equations

$$(1+\mu_1)Y'' + \mu_1 R'' + Y = D_0 \cos \Omega\tau; \tag{4.32a}$$

$$(\mu_1+\lambda_2)R'' + \mu_1 Y'' + \beta_1 R + 2\lambda_1 R^2 R'' + 2\lambda_1(1-2R^2)RR'^2 = 0. \tag{4.32b}$$

4.4.2 HB approximation and validation

The harmonic balance method (Von Groll and Ewins, 2001) is applied to solve nonlinear equations shown by Eqs. (4.32). Only considering the fundamental harmonic response, the non-dimensional steady-state displacement, the corresponding velocity and acceleration of the resonator mass can be written as

$$R = \hat{R}\cos(\Omega\tau+\phi); \tag{4.33a}$$

$$R' = -\hat{R}\Omega\sin(\Omega\tau+\phi); \tag{4.33b}$$

$$R'' = -\hat{R}\Omega^2\cos(\Omega\tau+\phi), \tag{4.33c}$$

where $\hat{R}$ and ϕ represent the response amplitude and the phase angle, respectively.

Substituting Eqs. (4.33) into Eq. (4.32b) and following the trigonometric sum-to-product identities, it can be derived that

$$\begin{aligned}\mu_1 Y'' &+ \left(-(\mu_1+\lambda_2)\Omega^2\hat{R} + \beta_1\hat{R} - \lambda_1\Omega^2\hat{R}^3 - \frac{\lambda_1\Omega^2\hat{R}^5}{2}\right)\cos(\Omega\tau+\phi)\\ &+ \left(-\lambda_1\Omega^2\hat{R}^3 + \frac{\lambda_1\Omega^2\hat{R}^5}{4}\right)\cos(3\Omega\tau+3\phi)\\ &+ \frac{\lambda_1\Omega^2\hat{R}^5}{4}\cos(5\Omega\tau+5\phi) = 0.\end{aligned} \tag{4.34}$$

Considering only the response component at the excitation frequency Ω and ignoring the terms with harmonics at 3Ω and 5Ω, the approximated displacement of the lumped mass is obtained as

$$\begin{aligned} Y &= \left(\frac{\beta_1 \hat{R}}{\mu_1 \Omega^2} - \frac{(\mu_1+\lambda_2)\hat{R}}{\mu_1} - \frac{\lambda_1 \hat{R}^3}{\mu_1} - \frac{\lambda_1 \hat{R}^5}{2\mu_1}\right)\cos(\Omega\tau+\phi) \\ &= \hat{Y}\cos(\Omega\tau+\phi). \end{aligned} \tag{4.35}$$

By using the approximate expressions of R and Y shown by Eqs. (4.33) and (4.35) to replace the corresponding terms in Eq. (4.32a), we obtain a simplified non-dimensional governing equation as

$$\begin{aligned} &-\Omega^2(1+\mu_1)\left(\frac{\beta_1 \hat{R}}{\mu_1 \Omega^2} - \frac{(\mu_1+\lambda_2)\hat{R}}{\mu_1} - \frac{\lambda_1 \hat{R}^3}{\mu_1} - \frac{\lambda_1 \hat{R}^5}{2\mu_1}\right)\cos(\Omega\tau+\phi) \\ &-\hat{R}\mu_1\Omega^2\cos(\Omega\tau+\phi) + \left(\frac{\beta_1 \hat{R}}{\mu_1 \Omega^2} - \frac{(\mu_1+\lambda_2)\hat{R}}{\mu_1} - \frac{\lambda_1 \hat{R}^3}{\mu_1} - \frac{\lambda_1 \hat{R}^5}{2\mu_1}\right) \\ &\cos(\Omega\tau+\phi) = D_0\cos\Omega\tau. \end{aligned} \tag{4.36}$$

According to the trigonometric identities, the right-hand side of Eq. (4.36) could be rewritten as

$$D_0\cos\Omega\tau = D_0\cos(\Omega\tau+\phi-\phi) \quad = D_0\cos\Omega\tau\cos\phi + D_0\sin\Omega\tau\sin\phi. \tag{4.37}$$

Insert Eq. (4.37) into Eq. (4.36), and there are no terms of $\sin(\Omega\tau+\phi)$ in the left-hand side, which means $\sin\phi = 0$ and $\cos\phi = 1$. Therefore, in this case, only the coefficients of $\cos(\Omega\tau+\phi)$ are needed to be balanced:

$$(1-\Omega^2-\mu_1\Omega^2)\left(\frac{\beta_1 \hat{R}}{\mu_1 \Omega^2} - \frac{(\mu_1+\lambda_2)\hat{R}}{\mu_1} - \frac{\lambda_1 \hat{R}^3}{\mu_1} - \frac{\lambda_1 \hat{R}^5}{2\mu_1}\right) - \hat{R}\mu_1\Omega^2 = D_0. \tag{4.38}$$

The displacement transmissibility is defined as the ratio of the displacement amplitude of the output and that of the input:

$$T_{\text{d\_unit}} = \frac{\hat{Y}}{D_0} = \frac{\left(\frac{\beta_1 \hat{R}}{\mu_1 \Omega^2} - \frac{(\mu_1+\lambda_2)\hat{R}}{\mu_1} - \frac{\lambda_1 \hat{R}^3}{\mu_1} - \frac{\lambda_1 \hat{R}^5}{2\mu_1}\right)}{D_0}. \tag{4.39}$$

It can be seen from Eq. (4.35) that μ_1, λ_1, λ_2, and β_1 are related to the material parameters. By sweeping the frequency Ω over a certain range, the response of the internal resonator can be derived. Then by substituting the response amplitude into Eq. (4.39), the corresponding displacement transmissibility of the lumped mass can be obtained based on analytical HB approximation.

To validate the frequency–response relationship obtained by HB approximation, here the fourth-order HB with alternating frequency- time (AFT) technique (Krack et al., 2013) and the Runge–Kutta (RK) method are used. In HB-AFT, the displacement responses of the lumped mass, R, R', and R'', are presented with an Nth order Fourier series with a fundamental frequency, Ω. The nonlinear term $G(R, R', R'')$ can be Fourier expanded and the coefficients of the harmonic terms are obtained by inserting in the harmonic expressions of R, R', and R''. When using the AFT scheme, the nonlinear term's continuous Fourier transforms are replaced by discrete Fourier transforms to obtain the nonlinear term sample at the equidistant moment of one oscillation period (Dai and Yang, 2021). After substituting the displacement responses and nonlinear term into Eq. (4.32) and balancing the coefficients of different harmonic terms, there will be a total number of $2(2N + 1)$ nonlinear algebraic equations, which can be solved by the Newton–Raphson method with a numerical continuation. Then the displacement response of lumped mass, R, is obtained.

Figure 4.10 shows the results obtained from the use of different methods for validation and comparison purpose. Figure 4.10(a) shows the transmittance diagram of the lumped mass in the 2-DoF GNIM-based system and the single-DoF (SDoF) system. The dashed line presents the wave transmittance for the SDoF system without the internal resonator. With the consideration of accuracy and computational cost, the dashed-dotted line represents the results obtained by the third-order HB-AFT method while the solid line denotes the results obtained using analytical first-order HB approximations. The pink circles are the results obtained by the RK time marching method. In these cases, the non-dimensional parameters are chosen as $\mu_1 = 1$, $\gamma_1 = 1$, $\lambda_1 = \lambda_2 = 0.1$, $\omega_0 = 1$, and $D_0 = 0.01$. The figure shows that the results obtained from analytical HB approximations agree well with those obtained using HB-AFT. There may be minor difference between the RK results and the HB approximations due to the absence of damping in the system. The figure shows that compared with the SDoF system, the system with the internal resonator will have two peaks and especially a frequency band in which there is low transmittance with the attached resonator working as a vibration absorber. Due to the nonlinear inertial force introduced by the GNIM, the right peak bends slightly to the left while the left peak remains almost unchanged. It also leads to the moving of the low-transmittance gap to lower-frequency region, which shows that the GNIM-based internal resonator has a good potential to control low-frequency vibration. Figure 4.10(b) shows the response characteristics of the internal resonator. There are two peaks in each curve, but there is no anti-peak, compared with the transmittances of the lumped mass shown in Fig. 4.10(a). In summary, with the addition of the internal resonator, the response amplitude of the lumped mass can be significantly reduced in a frequency band.

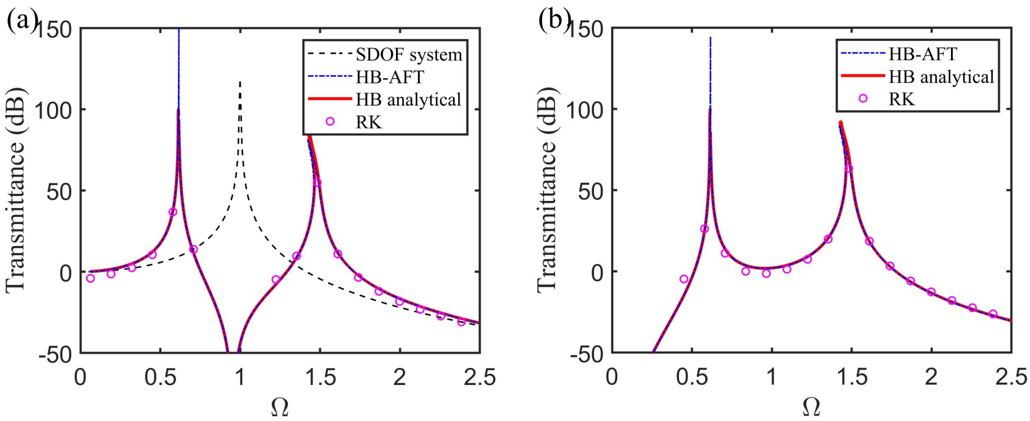

Figure 4.10: Wave transmittance diagrams gathered by analytical HB approximation, HB-AFT, and RK of (a) the lumped mass and (b) the internal resonator. The parameters selected are $\mu_1 = 1$, $\gamma_1 = 1$, $\lambda_1 = \lambda_2 = 0.1$, $\omega_0 = 1$, and $D_0 = 0.01$. The dashed line is the transmittance of the SDoF system. The dashed-dotted line, solid line, and circles are the results of the 2-DoF system obtained by HB-AFT, HB analytical, and RK methods, respectively.

The effective mass M_{eff} of the unit cell with an inerter-based resonator is obtained by considering this 2-DoF system as a SDoF equivalent mass subject to motion excitation. Note that the non-dimensionalised equation of motion could be expressed as

$$M_{\text{eff}} Y'' + Y - D_0 \cos \Omega\tau = 0, \tag{4.40}$$

where $M_{\text{eff}} = m_{\text{eff}}/m_0$. The non-dimensionalised effective mass can be derived by substituting Eqs. (4.35) and (4.38) into Eq. (4.40) to have

$$\begin{aligned} M_{\text{eff}} &= \frac{D_0 \cos \Omega\tau - Y}{Y''} \\ &= 1 + \mu_1 + \frac{2\mu_1^2\Omega^2}{2\beta_1 - 2\mu_1\Omega^2 - 2\lambda_2\Omega^2 - 2\lambda_1\Omega^2\hat{R}^2 - \lambda_1\Omega^2\hat{R}^4}. \end{aligned} \tag{4.41}$$

Figure 4.11 shows the variations of the effective mass M_{eff} of the combined mass m_0 and the nonlinear resonator against the excitation frequency considering the unit cell with and without adding inerters. The dashed line denotes the case when $\lambda_1 = \lambda_2 = 0.5$, $\hat{R}_2 = 0.05$ while the solid line represents the configuration C0 without inerters. It shows that there are two separate curves for each case. The effective mass associated with the first curve at low frequency keeps positive and the value increases fast as the frequency increases. The second curve starts at minus infinity and increases with the frequency to become greater than zero. However, the maximum value of M_{eff} is always smaller than the minimum value of the first left curve. The effective mass can be negative in the right-hand side curve when the excitation frequency is located in the respective shadowed frequency band. The figure shows that with the use of inerters in the local resonator, the frequency band of negative effective mass moves to the low-frequency band. The addition of inerters in the local resonator can affect the negative mass frequency range, providing potential benefits for low-frequency vibration control.

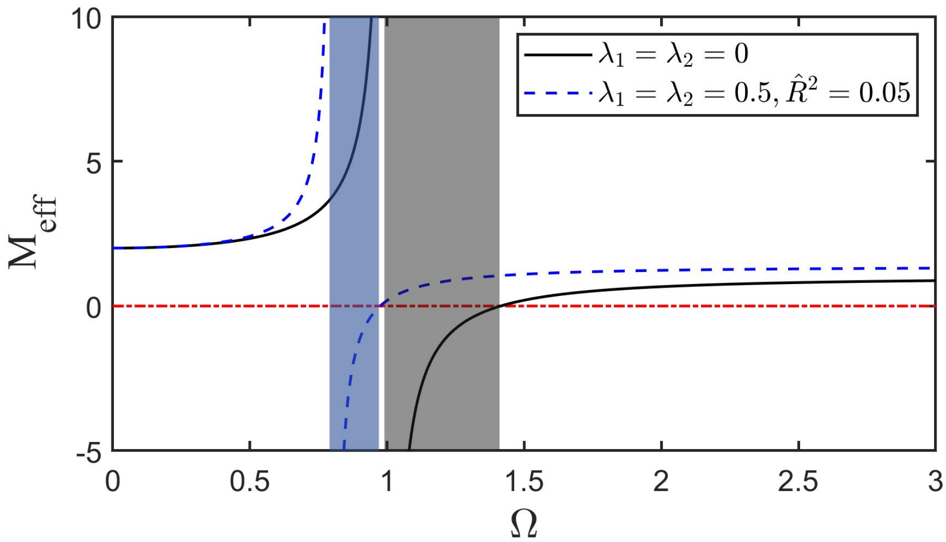

Figure 4.11: Effective mass of a unit cell with and without GNIM (configuration C1 and C0) in the local resonator ($\mu_1 = 1$, $\gamma_1 = 1$, and $\omega_0 = 1$). The solid line and dashed line are the effective mass curves for SDoF and 2-DoF systems while the corresponding gray and blue shadowed area represent the negative mass region.

4.4.3 Nonlinear inerter-based LRAM

Mathematical modelling

Figure 4.12 shows an inerter-based LRAM structure, which is the modified system developed from the structure shown in Fig. 4.1 by adding GNIM inside the rigid lumped mass shell between the local resonator mass and the lumped mass. The GNIM comprises a pair of identical vertical inerters of inertance b_1 and a linear horizontal inerter of inertance b_2.

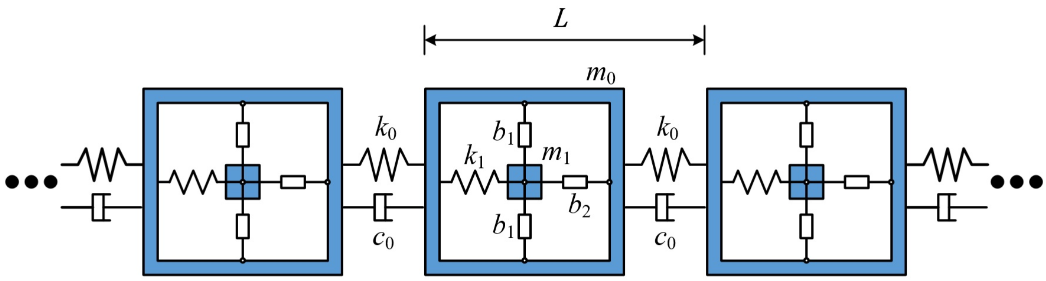

Figure 4.12: Geometrical nonlinear inerter mechanism-based locally resonant acoustic metamaterials configuration C4. The lumped masses m_0 are interconnected by spring k_0 and damper c_0 while each resonator m_1 is connected to the lumped mass with longitudinal spring k_1, inerter b_2, and two lateral inerters b_1.

The equations of motion of GNIM-LRAM can be derived and expressed as

$$m_0\ddot{y}_j + c_0(2\dot{y}_j - \dot{y}_{j-1} - \dot{y}_{j+1}) + k_0(2y_j - y_{j-1} - y_{j+1}) + m_1(\ddot{r}_j + \ddot{y}_j) = 0; \quad (4.42a)$$

$$m_1(\ddot{r}_j + \ddot{y}_j) + b_2\ddot{r}_j + k_1 r_j + 2b_1\left(\frac{r_j^2\ddot{r}_j}{l^2 + r_j^2} + \frac{l^2 r_j \dot{r}_j^2}{(l^2 + r_j^2)^2}\right) = 0, \quad (4.42b)$$

where y_j represents the displacement of lumped mass in the jth cell and r_j is the displacement of the jth resonator relative to the jth lumped mass. These two equations can be nondimensionalised by referring to the parameters defined in Eqs. (4.3), (4.22), and (4.28). Then, by approximating the inertial force caused by geometric nonlinearity via Taylor expansion at $R_j = 0$, we have

$$(1+\mu_1)Y_j'' + 2\zeta_0(2Y_j' - Y_{j-1}' - Y_{j+1}') + (2Y_j - Y_{j-1} - Y_{j+1}) + \mu_1 R_j'' = 0; \qquad (4.43a)$$

$$(\mu_1+\lambda_2)R_j'' + \mu_1 Y_j'' + \beta_1 R_j + 2\lambda_1 R_j^2 R_j'' + 2\lambda_1(1-2R_j^2)R_j R_j'^2 = 0. \qquad (4.43b)$$

Dispersion relation

For the GNIM-LRAM configuration, the HB method can also be applied to solve the nonlinearity in motion equations. Only the fundamental harmonic response is considered in this case. The non-dimensional steady state displacement, velocity, and acceleration of the jth resonator mass can be written as

$$R_j = \hat{R}_j \cos(\Omega\tau + \phi); \qquad (4.44a)$$

$$R_j' = -\hat{R}_j \Omega \sin(\Omega\tau + \phi); \qquad (4.44b)$$

$$R_j'' = -\hat{R}_j \Omega^2 \cos(\Omega\tau + \phi), \qquad (4.44c)$$

respectively. Substituting Eq. (4.44) into Eq. (4.43), following the trigonometric sum-to-product identities and considering only the response component at excitation frequency Ω, the approximated displacement of the jth, $(j+1)$th and $(j-1)$th lumped masses can be derived as

$$\begin{aligned} Y_j &= \left(\frac{\beta_1 \hat{R}_j}{\mu_1 \Omega^2} - \frac{(\mu_1 + \lambda_2)\hat{R}_j}{\mu_1} - \frac{\lambda_1 \hat{R}_j^3}{\mu_1} - \frac{\lambda_1 \hat{R}_j^5}{2\mu_1} \right) \cos(\Omega\tau + \phi) \\ &= \hat{Y}_j \cos(\Omega\tau + \phi); \end{aligned} \tag{4.45a}$$

$$Y_{j+1} = Y_j \mathrm{e}^{\mathrm{i}qL}; \tag{4.45b}$$

$$Y_{j-1} = Y_j \mathrm{e}^{-\mathrm{i}qL}. \tag{4.45c}$$

Note that $\mathrm{e}^{\mathrm{i}qL} + \mathrm{e}^{-\mathrm{i}qL} = 2\cos(qL)$. By substituting Eq. (4.45) into Eq. (4.43a), the governing equation for the dispersion curve of this configuration is obtained:

$$\begin{aligned} \cos(qL) =& 1 - \frac{\Omega^2(1+\mu_1)}{2} \\ &- \frac{\mu_1^2 \Omega^4}{2\beta_1 - 2\mu_1\Omega^2 - 2\lambda_2\Omega^2 - 2\lambda_1\Omega^2\hat{R}_j^2 - \lambda_1\Omega^2\hat{R}_j^4}. \end{aligned} \tag{4.46}$$

The dispersion equation can also be obtained in another way. The non-dimensional steady-state displacement of the jth resonator mass can also be presented in the form of complex Fourier series:

$$R_j = \hat{A}_{1.j}\mathrm{e}^{\mathrm{i}\Omega\tau} + \hat{A}_{2.j}\mathrm{e}^{-\mathrm{i}\Omega\tau}. \tag{4.47}$$

Using the same method, by substituting Eq. (4.47) into Eq. (4.43b), integrating twice with respect to τ and only keeping the form of $\mathrm{e}^{-\mathrm{i}\Omega\tau}$, the approximated displacement of the jth lumped mass is derived:

$$Y_j = \left(-(\mu_1 + \lambda_2)\hat{A}_{1.j} + \frac{\beta_1}{\Omega^2}\hat{A}_{1.j} - 4\lambda_1\hat{A}_{1.j}^2\hat{A}_{2.j} - 8\lambda_1\hat{A}_{1.j}^3\hat{A}_{2.j}^2 \right)\mathrm{e}^{\mathrm{i}\Omega\tau}. \tag{4.48}$$

Inserting Eq. (4.48) and applying the Bloch theorem, the equation governing the dispersion property can be obtained

$$\begin{aligned}\cos(qL) =& 1 - \frac{\Omega^2(1+\mu_1)}{2} \\ & - \frac{\mu_1^2\Omega^4}{2\beta_1 - 2\mu_1\Omega^2 - 2\lambda_2\Omega^2 - 8\lambda_1\hat{A}_{1.j}^2\hat{A}_{2.j} - 16\lambda_1\hat{A}_{1.j}^3\hat{A}_{2.j}^2}.\end{aligned} \tag{4.49}$$

As it is easy to prove that $\hat{R}_j^2 = 4\hat{A}_{1.j}\hat{A}_{2.j}$ based on these different displacement forms in Eqs. (4.44a) and (4.47), the two presentations of the dispersion relation as shown in Eqs. (4.46) and (4.49) are exactly the same.

4.4.4 Results and discussions

In this section, the effects of adding inerters on the low-frequency bandgap properties of LRAM are analysed. The dispersion relations with different material parameters are shown to examine the bandgap characteristics of the proposed nonlinear structure. Then the wave attenuation behavior is studied for the validation of the bandgap. The wave suppression effect of the proposed resonator in a finite unit cell structure is analysed. The influence of unit cell number on longitudinal wave attenuation in the GNI-LRAM is investigated.

Dispersion characteristics

Here, the dispersion characteristics of the inerter-based LRAM are derived by using Eqs. (4.46) and (4.49). The former equation is used for numerical validation. Equation (4.46) shows that the corresponding dispersion curve is independent of the number of lumped mass j. However, it will be influenced by the resonator displacement amplitude $\hat{R}_j$, the mass ratio μ_1, the stiffness ratio β_1, and inertance ratios λ_1 and λ_2. In other words, the bandgaps can be controlled by adjusting these parameter values. With the given range of frequency Ω, the wave propagation constant qL could be obtained. The material parameters are selected as $\mu_1 = \beta_1 = 0.3$, $\omega_0^2 = 1 \times 10^5(\text{rad/s})^2$. In order to express the characteristic change more clearly, in the subsequent results, the non-dimensional frequency Ω is processed to be dimensional frequency, $f = \Omega \times \omega_0/2\pi$.

Figure 4.13 shows the influence of the nonlinear inerter-based mechanism on the bandgaps. In Fig. 4.13(a), the effects of the inertance ratio λ_1 are studied. The horizontal linear inerter is not considered so the inertance ratio λ_2 is set to be 0. The resonator displacement amplitude square $\hat{R}_j^2$ is set constant as 0.01 while the inertance ratio λ_1 of the GNIM increases from 0 to 80. For the purpose of comparison, the case with $\lambda_1 = 0$ (solid curve) is regarded as the corresponding results of the benchmark LRAM structure without any inerters. Its bandgap location is from 48.0 to 57.4 Hz and the bandwidth is 9.4 Hz. When $\lambda_1 = 5$, the use of the nonlinear inerter-based resonator moves bandgap to the low-frequency region. The dispersion diagram reveals that the lower boundary of the bandgap reduces by approximately 3.0 Hz, and the total bandwidth decreases from 2.4 to 7.0 Hz. When $\lambda_1 = 20$, the bandgap moves to the area of 38.3–42.0 Hz. Its corresponding bandwidth decreases to 3.7 Hz. If λ_1 increases to 80, the bandgap location drops significantly to a band of 26.2–27.1 Hz. The bandwidth also drops to 0.9 Hz. In general, the figure shows that the bandgap location is successfully moved to the lower frequency area by the use of the GNIM at the expense of the slight narrowing of the bandwidth of the gap as the inertance ratio λ_1 increases. Figure 4.13(b) shows the dispersion curves for a fixed inertance ratio $\lambda_1 = 2$ while the resonator displacement amplitude R increases from 0 to 0.25. It also shows that the bandgaps move slowly to a lower frequency region. The solid line is for the system without GNIM for comparison. When $\hat{R}_j^2 = 0.01$, the gap shifts to the range of 46.8–55.0 Hz. The corresponding bandwidth reduces to 8.2 Hz. When $\hat{R}_j^2 = 0.05$ (the dashed-dotted curve), the location of the frequency region is relatively low from 42.4 to 47.8 Hz with a sufficient bandwidth of 5.4 Hz. The lower boundary of the bandgap drops to 29.3 Hz, and its bandwidth is 1.7 Hz when $\hat{R}_j^2$ increases to 0.25. With the increasing displacement amplitude of the local resonator, the location of the bandgap also moves to the low-frequency region and its width becomes narrower. These two subfigures show similar trends in the variation of the bandgap, i.e., the increases in the values of λ_1 and $\hat{R}_j$ of the GNIM lead to the shift of the relatively narrower bandgap to the lower frequency region. The results also show that if the oscillation amplitude increases, the geometrical nonlinearity of the GNIM becomes more significant.

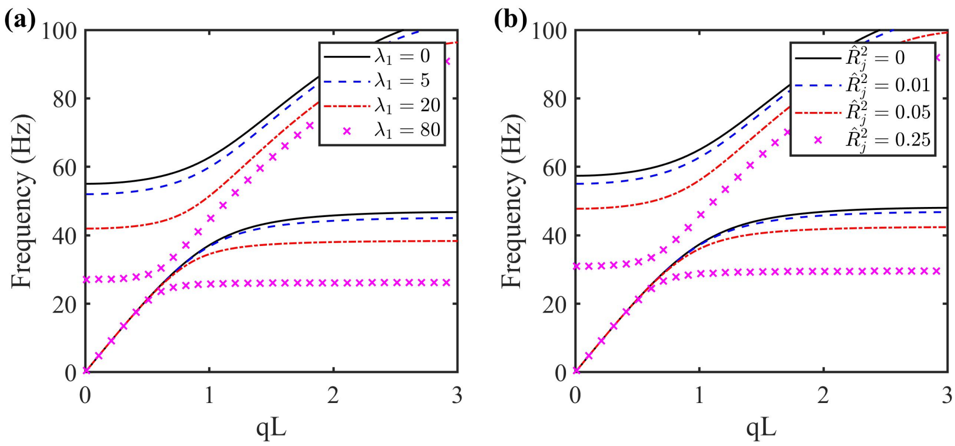

Figure 4.13: Dispersion diagrams of the nonlinear configuration C4 with parameters selected as $\mu_1 = \beta_1 = 0.3$ and $\omega_0^2 = 1 \times 10^5$. (a) The nonlinear parameters are $\lambda_2 = 0$ and $\hat{R}_j^2 = 0.01$. The solid line, dashed line, dashed-dotted line, and cross are the results with $\lambda_1 = 0$, 5, 20, and 80, respectively. (b) The nonlinear parameters are $\lambda_1 = 2$ and $\lambda_2 = 0$. The solid line, dashed line, dashed-dotted line, and cross are the results with $\hat{R}_j^2 = 0$, 0.01, 0.05, and 0.25, respectively.

Figure 4.14 presents the effects of the inertance ratio λ_2 on the properties of the bandgap. For the case in Fig. 4.14(a), each local resonator mass is attached to the lumped mass by the horizontal linear spring and the horizontal inerter, and no geometrical nonlinear lateral inerters is applied, which is achieved by setting the material parameters as $\lambda_1 = \hat{R}_j^2 = 0$. The inertance ratio λ_2 increases from 0 to 0.1 to 0.4 and then to 1. The solid line represents the benchmark case with the inerter for comparison. When λ_2 is set as 0.1, the bandgap is located at lower frequencies compared to the reference case shown by the solid line. With $\lambda_2 = 0.1$, the lower and upper boundaries of the bandgap are 40.3 and 44.7 Hz, respectively. When λ_2 is set at 0.4 and then 1, the bandgaps' lower boundary reduces to 31.6 and 23.7 Hz, respectively. Meanwhile, the corresponding bandwidths are 1.8 and 0.7 Hz, respectively. The figure shows that the increase in λ_2 will contribute to the moving of bandgap location and its width. Compared with the influence of the lateral inerters λ_1, the bandgap properties are more sensitive to the variations of the inertance λ_2 of the horizontal inerter. This is demonstrated by the stronger effects created by a small increase in λ_2 from 0 to 1, compared to those resulting from large variations of λ_1 from 0 to 80. Figure 4.14(b) has shown the effect of increases in λ_2 on the bandgap characteristics of the metamaterial configuration with nonlinear inerters. The related nonlinear parameters are set as $\lambda_1 = 10$ and $\hat{R}_j^2 = 0.01$. Compared with Fig. 4.14(a), the bandgaps have moved to a lower-frequency location. For instance, in the case shown by the dashed-dotted line ($\lambda_2 = 0.4$), the bandgap is from 30.6 to 32.2 Hz with a bandwidth of 1.6 Hz. The figure demonstrates the importance of taking full advantage of both linear and nonlinear inerters. The results show that the inerter-based mechanism yields a substantial and beneficial influence on the bandgap characteristics. This property can be applied to achieve a low-frequency bandgap at the cost of decreases in the associated bandwidth. It is necessary to create a bandgap in the low-frequency range while maintaining sufficient bandwidth. The results show that a small value of inertance for the linear inerter with $\lambda_2 = 1$ can lead to a relatively small bandwidth. It is worth exploring the use of a geometrical nonlinear inerter in LRAM for low-frequency vibration suppression.

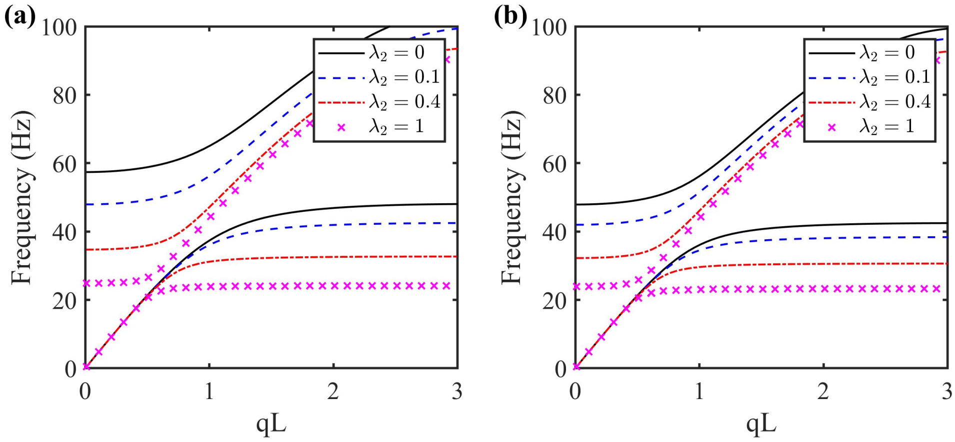

Figure 4.14: Dispersion diagrams of the nonlinear configuration C4 with parameters selected as $\mu_1 = \beta_1 = 0.3$ and $\omega_0^2 = 1 \times 10^5$. (a) The nonlinear parameters are $\lambda_1 = 0$ and $\hat{R}_j^2 = 0$. The solid line, dashed line, dashed-dotted line, and cross are the results with $\lambda_2 = 0$, 0.1, 0.4, and 1, respectively. (b) The nonlinear parameters are $\lambda_1 = 10$ and $\hat{R}_j^2 = 0.01$. The solid line, dashed line, dashed-dotted line, and cross are the results with $\lambda_2 = 0$, 0.1, 0.4, and 1, respectively.

Figure 4.15 shows the individual dispersion relation feature and the band structure of the inerter-based LRAM. Figure 4.15(a) presents the results associated with the case with $\lambda_1 = \lambda_2 = 0$, which is the benchmark configuration C0 as shown in Fig. 4.1. The constant qL is a complex number providing the propagation solution. The real part of qL decides the direction of propagation, which is the phase constant shown in the right-hand side of the figure. The lefthand side area is the imaginary part of qL, the attenuation constant, deciding the wave attenuation. A larger absolute value of the imaginary component will lead to a better wave attenuation effect. The bandgaps are highlighted in blue shadow between 48.0 and

57.4 Hz where there no real solutions exist for qL. The imaginary part is larger when it is close to the lower bandgap boundary, which means in the bandgap the wave suppression performance is even better at low excitation frequencies. Figure 4.15(b) shows the cases with $\lambda_1 = 0$ and $\lambda_2 = 0.1$. With the addition of the horizontal inerter, the bandgap moves to a lower frequency range between 42.5 and 47.9 Hz while the bandwidth decreases by 4.0 Hz. In Fig. 4.15(c), lateral inerters with $\lambda_1 = 20$ are attached to the system with no horizontal inerter. The bandgap is located at a lower frequency between 38.3 and 42.0 Hz compared to the system shown in Fig. 4.15(a). Figure 4.15(d) presents the case with $\lambda_1 = 20$, $\lambda_2 = 0.1$, $\hat{R}_j^2 = 0.01$. By the combined effects of both horizontal and lateral inerters, the bandgap moves to the region between 35.2 and 37.8 Hz, and the corresponding bandwidth reduces to 2.6 Hz. It is noted that with the protection of the geometry nonlinear structure, it is possible to have a heavier resonator mass and a softer stiffness in comparison to the benchmark configuration C0.

In Figs. 4.16 and 4.17, the effects of the variations of the mass ratio μ_1, the spring stiffness ratio β_1, and their combined changes on the dispersion behavior of the inerter-based LRAM are examined, respectively. Figure 4.16 shows that the increasing mass ratio will lead to a wider bandgap located at a lower frequency. In Fig. 4.16(a) with $\lambda_1 = 5$, $\lambda_2 = 0.1$, $\hat{R}_j^2 = 0.01$, when $\beta_1 = 0.5$ and $\mu_1 = 0.3$, the bandgap locates between 51.1 and 57.7 Hz. When μ_1 increases to 0.5, the bandgap moves down to the range from 42.2 to 51.2 Hz, while the bandwidth even increases by 2.4 Hz. When $\mu_1 = 0.7$, the lower bound of the band decreases by 5.4 Hz and the width rises to 10.7 Hz. Figures 4.16(b–d) show the influence of the mass ratio μ_1 on the dispersion relations while considering different values

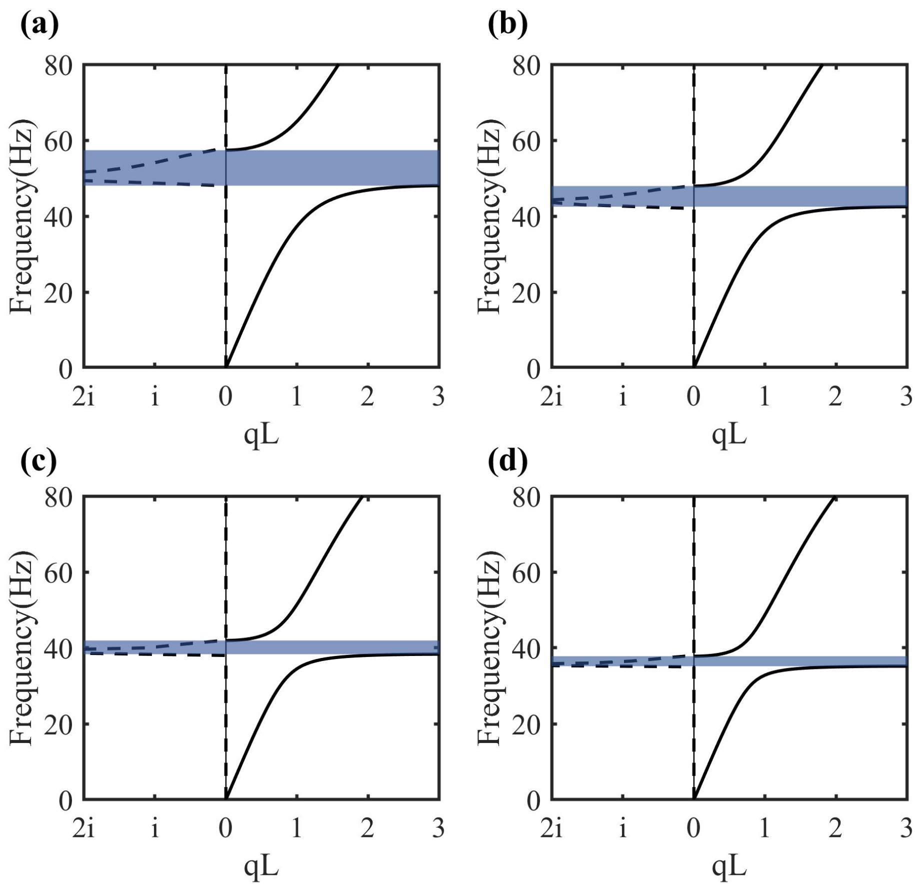

Figure 4.15: Dispersion relation diagram of the nonlinear structure with parameters selected as $\mu_1 = \beta_1 = 0.3$, $\omega_0^2 = 1 \times 10^5$ with different nonlinear parameters. (a) $\lambda_1 = \lambda_2 = 0$, (b) $\lambda_1 = 0$, $\lambda_2 = 0.1$, (c) $\lambda_1 = 20$, $\lambda_2 = 0$, $\hat{R}_j^2 = 0.01$, and (d) $\lambda_1 = 20$, $\lambda_2 = 0.1$, $\hat{R}_j^2 = 0.01$. The shadowed areas show the bandgap location and width.

of the amplitude $\hat{R}_j^2$ and the inertance ratios λ_1 and λ_2. It shows that the addition of parameters λ_1, λ_2, and $\hat{R}_j$ will lead to the reductions in both bandgap location frequency and also in the bandwidth. For instance, with same mass ratio $\mu_1 = 0.3$, the lower boundary of the bandgap in Fig. 4.16(b) decreases by 6.1 Hz while the bandwidth decreases to 3.8 Hz compared with the corresponding values shown in Fig. 4.16(a). For the cases in Figs. 4.16(c) and 4.16(d), the bandgaps are located at 40.6–43.1 Hz and 43.2–46.4 Hz, respectively. Their bandwidth decreases by 4.1 Hz and 3.4 Hz, respectively. The figure shows that for low frequency vibration suppression, within the manufacturing limit, larger inerter ratios λ_1, λ_2, and amplitude $\hat{R}_j$ are preferred for reducing the bandgap frequency, and greater mass ratio μ_1 is desirable as it enlarges the bandwidth.

In Fig. 4.17, the influence of β_1 and μ_1 on the bandgap is studied with $\hat{R}_j^2 = 0.01$, inertance ratios $\lambda_1 = 5$ and $\lambda_2 = 0.1$. Figure 4.17(a) reveals that a larger stiffness ratio β_1 can move the bandgap to a higher frequency range with a broader width. When $\beta_1 = 0.3$, $\mu_1 = 0.5$ (shown by the solid line), the lower boundary of the bandgap is 33.3 Hz while the upper boundary is 39.6 Hz, and the corresponding bandwidth is 6.3 Hz. As β_1 increases to 0.5, the bandgap moves up to be from 42.2 Hz to 51.2 Hz, with its width increasing by 2.7 Hz. When $\beta_1 = 0.7$, the band locates from 48.9 to 60.6 Hz with a bandwidth of 11.7 Hz. The figure demonstrates that as the stiffness ratio β_1 reduces from 0.7 to 0.3, the resonant frequency of the internal resonator also reduces, leading to the moving down of the bandgap frequency range and the narrowing of the bandwidth. In Fig. 4.17(b), the values of β_1 and μ_1 are kept the same for each case. It shows that with the parameter setting, the bandgap can have a much broader width spreading out to both sides. So a larger mass and stiffness with the same ratio is preferred in the LRAM design. When compared with the basic linear inerterbased structure, the geometrical nonlinear mechanism will play a protective role, and it is achievable to extend the material parameters' limitation for better wave attenuation performance. In summary, the nonlinear inerter-based mechanism could induce a low-frequency range with broader bandwidth compared with the common linear inerter-based LRAM.

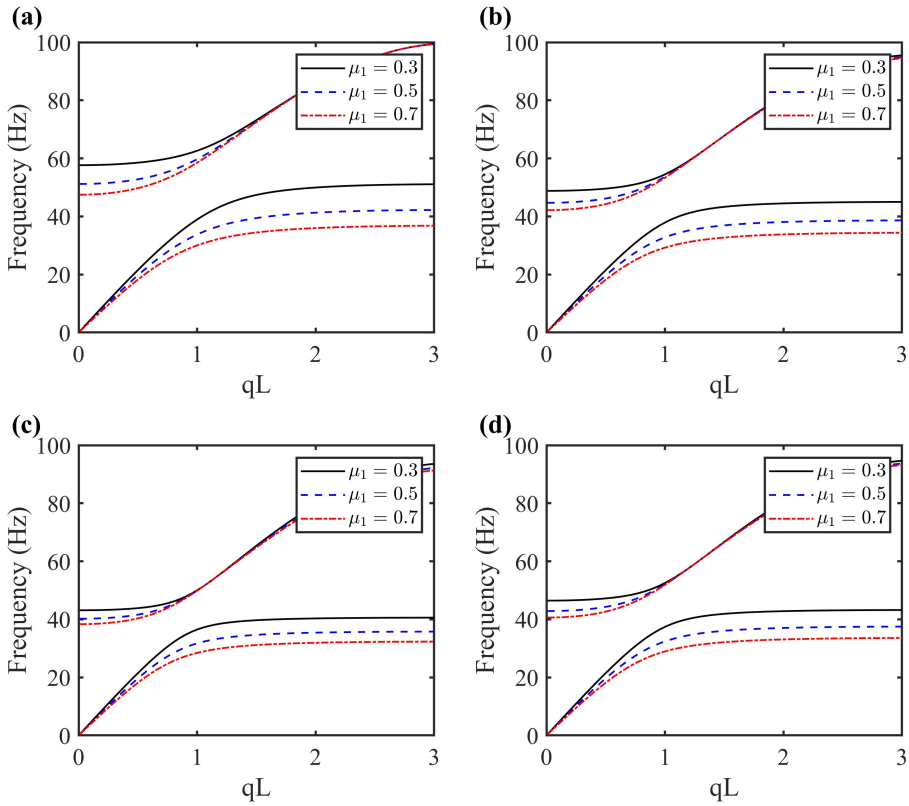

Figure 4.16: Dispersion relation diagram of the system when μ_1 is increasing with parameters selected as (a) $\lambda_1 = 5$, $\lambda_2 = 0.1$, $\hat{R}_j^2 = 0.01$, (b) $\lambda_1 = 20$, $\lambda_2 = 0.1$, $\hat{R}_j^2 = 0.01$, (c) $\lambda_1 = 5$, $\lambda_2 = 1$, $\hat{R}_j^2 = 0.01$, and (d) $\lambda_1 = 5$, $\lambda_2 = 0.1$, $\hat{R}_j^2 = 0.05$. The solid line, dashed line, and dashed-dotted line represent the cases that $\mu_1 = 0.3$, 0.5, and 0.7, respectively.

Wave transmittance

For the purpose of validation, the wave transmittance diagram for GNI-LRAM of finite unit cells is obtained by presenting in the form of effective mass as shown above. Figure 4.18 shows the dispersion and wave transmittance diagrams for the benchmark configuration C0. Based on the effective mass in Eq. (4.40) and transmittance equations in Eqs. (13) and (14), if there are six unit cells in the system, the wave transmittance diagram for the case without a nonlinear mechanism is illustrated in Fig. 4.18(b). It shows that there is a distinct frequency gap and many peaks located at

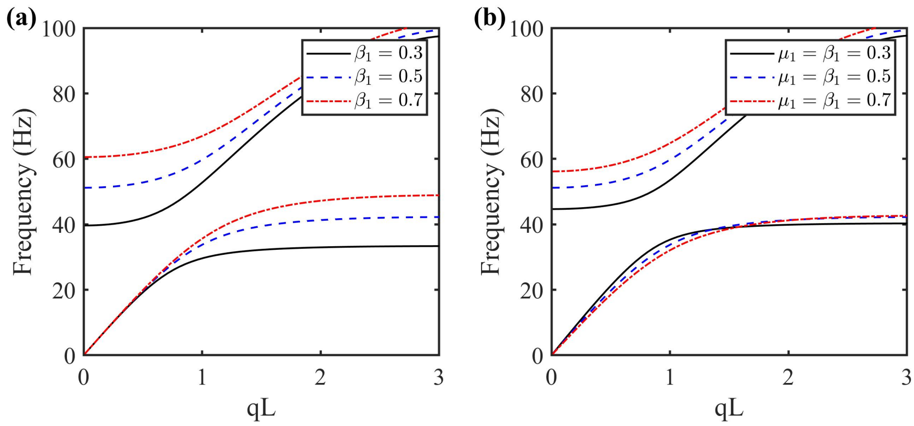

Figure 4.17: Dispersion relation diagrams of the system when parameters selected as $\lambda_1 = 5$, $\lambda_2 = 0.1$, $\hat{R}_j^2 = 0.01$. (a) Constant mass ratio $\mu_1 = 0.5$ and different stiffness ratios β_1. The solid line, dashed line, and dashed-dotted line represent the results of $\beta_1 = 0.3$, 0.5, and 0.7, respectively. (b) Different mass and stiffness ratios. The solid line, dashed line, and dashed-dotted line represent the results of $\mu_1 = \beta_1 = 0.3$, 0.5, and 0.7, respectively.

different frequencies. As for a continuous or multiple degrees of freedom system, the wave transmittance is complex because the resonator is coupled with all structural modes of the host system. The peaks are the different resonant frequencies. When the wave transmittance is less than zero as highlighted in blue shadow, it means the excitation frequency is located in the bandgap. Therefore, in this diagram, the bandgap is determined by searching a range where the wave transmittances are smaller than zero at higher and lower boundaries. Based on the definition of transmittance, the displacement amplitude of the last unit lumped mass is smaller than that of the first lumped mass that is applied by excitation force, which means in this case, the wave is suppressed. It shows that the lower and upper boundaries of the wave transmittance gap are 48.0 Hz and 57.4 Hz. Compared with the dispersion diagram shown in Fig. 4.18(a), the blue shadow reveals that they have good agreement with bandgap location and width. The corresponding wave transmittance figure also reveals that the wave attenuation effect within the bandgap area close to the lower edge is better than that close to the higher edge. For lower boundary, the wave transmittance in dB drops from 0 dB to -100 dB by the difference of just 0.5 Hz, while for the upper boundary, it costs 2.9 Hz to decrease the same value. This result also proves the correctness of the dispersion relation whose curve in the imaginary part shows the same characteristic in wave attenuation ability.

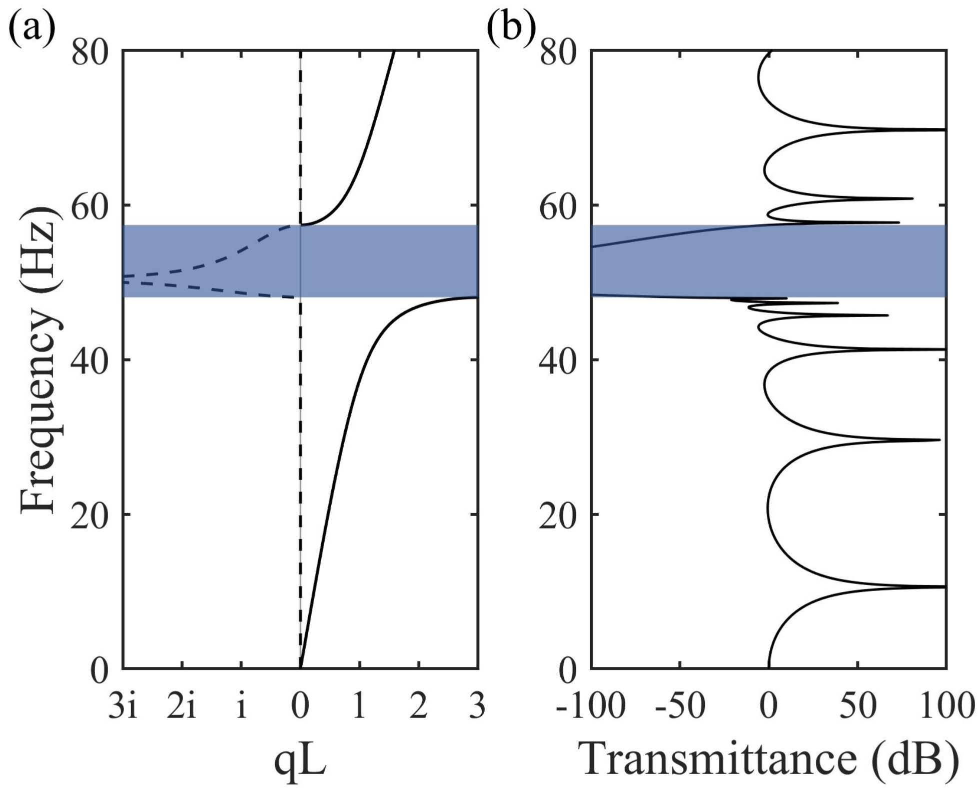

Figure 4.18: Theoretical results of the benchmark configuration C0 with parameters selected as $\mu_1 = \beta_1 = 0.3$, $\omega_0^2 = 1 \times 10^5$, $\lambda_1 = \lambda_2 = 0$. (a) Dispersion relation diagram. (b) Wave transmittance diagram. The shadowed area represents the bandgap and the low transmittance range.

Figure 4.19 shows the dispersion relation and transmittance property for a system consisted of six unit cells when $\lambda_1 = 5$, $\lambda_2 = 0.1$, $\hat{R}_j^2 = 0.01$. Its bandgap is located at the range from 42.2 to 51.2 Hz, which matches the result from the dispersion diagram. Figures 4.19(b-d) are, respectively, the transmittance diagrams for a system consisting of six unit cells when $\lambda_1 = 20$, $\lambda_2 = 0.1$, $\hat{R}_j^2 = 0.01$; $\lambda_1 = 5$, $\lambda_2 = 0.4$, $\hat{R}_j^2 = 0.01$; and $\lambda_1 = 5$, $\lambda_2 = 0.1$,

$\hat{R}_j^2 = 0.05$. Their bandgaps are located at the ranges from 38.6 to 44.7 Hz, from 35.8 to 40.2 Hz, and from 37.5 to 42.9 Hz. It seems that with different material parameters, the bandgaps in corresponding dispersion curves and wave transmittance diagrams are always almost the same. Therefore, these two types of diagrams are obtained by two different methods, and with the coincident bandgaps, they can verify each other.

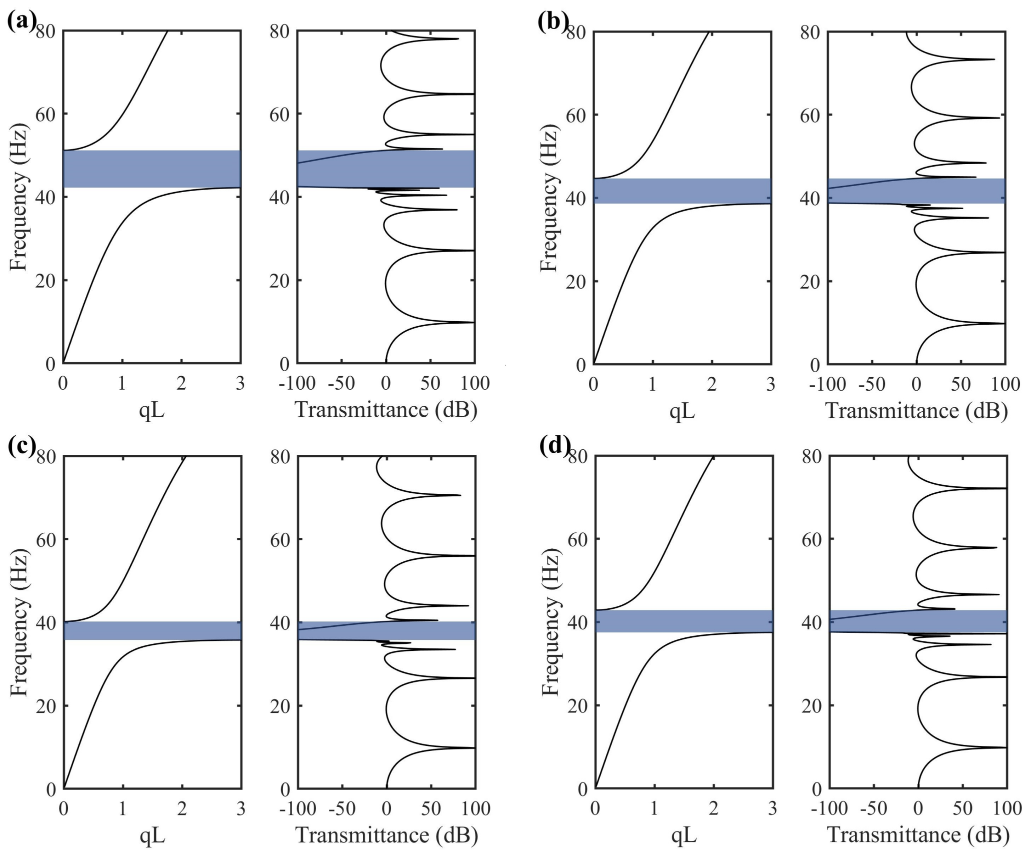

Figure 4.19: Dispersion and wave transmittance diagrams (six unit cells) of the nonlinear structure when parameters selected as (a) $\lambda_1 = 5$, $\lambda_2 = 0.1$, $\hat{R}_j^2 = 0.01$, (b) $\lambda_1 = 20$, $\lambda_2 = 0.1$, $\hat{R}_j^2 = 0.01$, (c) $\lambda_1 = 5$, $\lambda_2 = 0.4$, $\hat{R}_j^2 = 0.01$, and (d) $\lambda_1 = 5$, $\lambda_2 = 0.1$, $\hat{R}_j^2 = 0.05$. The shadowed area represents the bandgap and the low transmittance range.

Power flow analysis

The theoretically calculated input and output power flow and the power consumption for the proposed 100-unit nonlinear LRAM configuration C4 are shown in Fig. 4.20. The parameters selected are $\mu_1 = \beta_1 = 0.5$, $\lambda_1 = 5$, $\lambda_2 = 0.1$, $\hat{R}_j^2 = 0.01$, and $\zeta_0 = 0.005$. In Fig. 4.20(a), the corresponding peaks and gap locations are similar for both time-averaged power flow variables. The output power flow is lower than the input power due to damping especially within the gap. Fig. 4.20(b) shows that the power consumption is more than 20 dB between 42.2 and 51.2 Hz, which locates the same range as the bandgap shown in Fig. 4.19(a). It can be explained by the effect of the bandgap and the energy is almost blocked in this range.

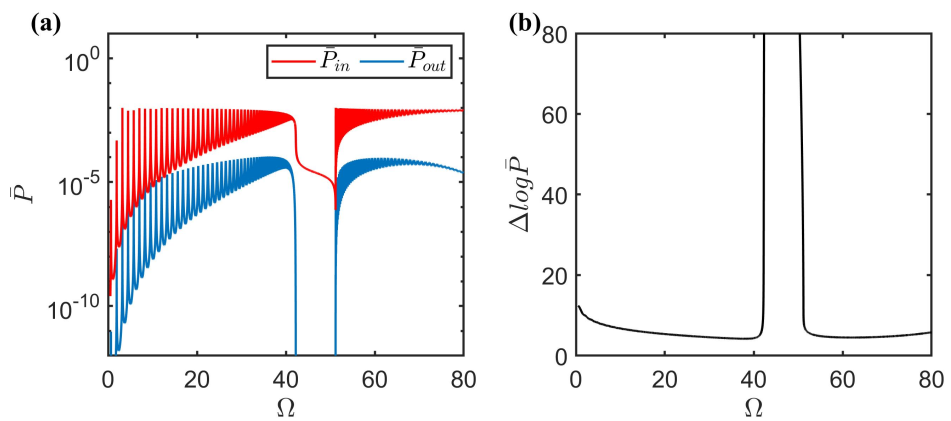

Figure 4.20: Theoretical results for the 100-unit nonlinear configuration C4 with $\mu_1 = \beta_1 = 0.5$, $\lambda_1 = 5$, $\lambda_2 = 0.1$, $\hat{R}_j^2 = 0.01$, and $\zeta_0 = 0.005$. (a) The time-averaging power flow diagram. The red and blue curves are the input power of the first cell produced by excitation displacement and the output power of the last cell, respectively. (b) The power flow consumption in dB, which is the difference of the input and output power flow in the logarithmic scale.

The effect of increasing the damping ratio on the output power flow is studied in Fig. 4.21. It shows that with different damping ratios, the peaks and gap locations remain the same. When the damping ratio is increasing, the peak amplitudes are reduced. When ζ_0 rises from 0.001 to 0.005, the power flow average amplitude along the frequency lower than the bandgap is about 6 times smaller, and it is about 2.5 times smaller when $\zeta_0 = 0.01$ compared with that of 0.05. Larger damper can reduce the power flow amplitude and reduce volatility. When $\zeta_0 = 0.02$, the power flow shows similar varying trend, but on the right-hand-side of the bandgap, the power reduces a lot more as the excitation frequency increases. The difference in these four cases is small at low frequency while it generally increases as frequency rises, which means that the large damper has better vibration suppression ability at higher frequency while it plays a little role in energy dissipation in low frequency.

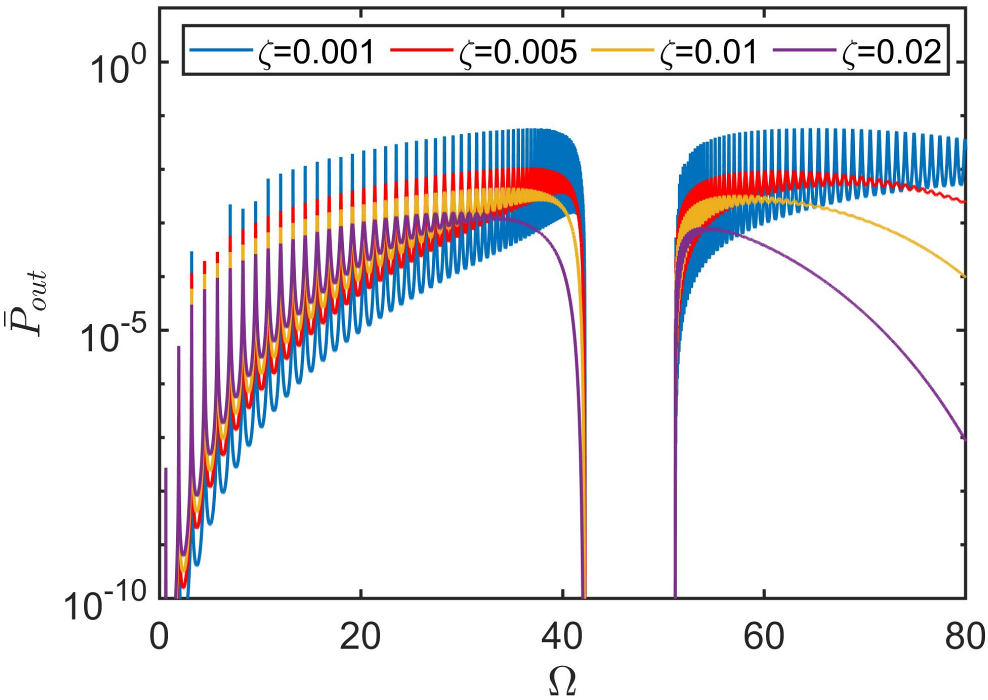

Figure 4.21: Effect of damping ratio on the 100th lumped mass for the 100-unit nonlinear configuration C4 with parameters selected as $\mu_1 = \mu_2 = 0.5$, $\beta_1 = \beta_2 = 0.3$, $\lambda_1 = 1$, and $\lambda_2 = 0.5$. The blue, red, yellow, and purple curves represent the results with $\zeta_0 = 0.001$, 0.005, 0.01, and 0.02, respectively.

Figure 4.22 shows power transmission along the 100-unit nonlinear configuration C4, which is defined as the ratio of the jth lumped mass power over the input power. Generally, over the whole frequency range, the power transmission is reduced as the cell position number increases. A gap with the same frequency range as bandgap is shown to have low transmission, and the extremely low transmission range (blue area) extends to fill the whole bandgap in the first few cells. The gap is generated by the bandgap effect while the low transmission at high frequency and large cell position number is influenced by the dampers. The dampers will dissipate more energy as the cell position number is larger, but the low-frequency vibration is hardly affected, which also indicates the challenges of controlling low-frequency vibrations. However, with the proposed nonlinear LRAM configuration, the bandgap can be designed to control the extremely low-frequency vibration.

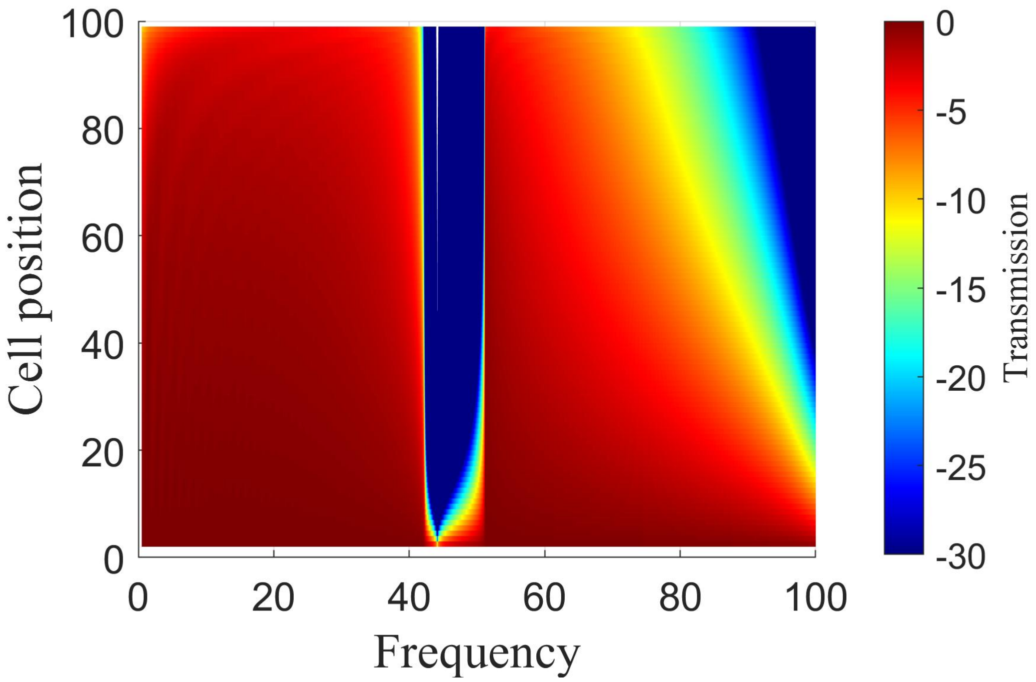

Figure 4.22: Power transmission map along the cell position for the 100-unit nonlinear configuration C4 with parameters selected as $\mu_1 = \mu_2 = 0.5$, $\beta_1 = \beta_2 = 0.3$, $\lambda_1 = 1$, and $\lambda_2 = 0.5$. The colorbar represents different wave transmittances in dB.

Influence of the unit cell number

As in practice it is not possible to build an infinite-unit LRAM, it is necessary to investigate the influence of the number of unit cells on the wave attenuation performance. The fast Fourier transform (FFT) is applied for analysing the lumped mass frequency spectra. As depicted in Fig. 4.23, the frequency spectra diagrams of the lumped masses in the nonlinear LRAM system are shown. Figure 4.23(a) shows the frequency spectra for different cell positions Y_j in a 20-unit-cell system. The horizontal axis is the cell position, representing Y_j, $j = 1, 2, ..., 20$. The non-dimensional excitation frequency $\Omega = 1$ is selected for example. It shows that with different cell positions, the frequency component remains similar, which means it will not be affected by the propagation distance. The frequency components (peaks) are located at two broad frequency bands. The frequency spectra diagram of the last cell response in the jth cell number nonlinear system is shown in Fig. 4.23(b). The horizontal axis represents the total cell number j for the systems, and only the last unit cell response of each system is focused and recorded. It can be seem that the variation trend of frequency spectra against unit cell number is similar with that against the propagation position in Fig. 4.23(a). The increase in the unit cell number will not influence the frequency components' location.

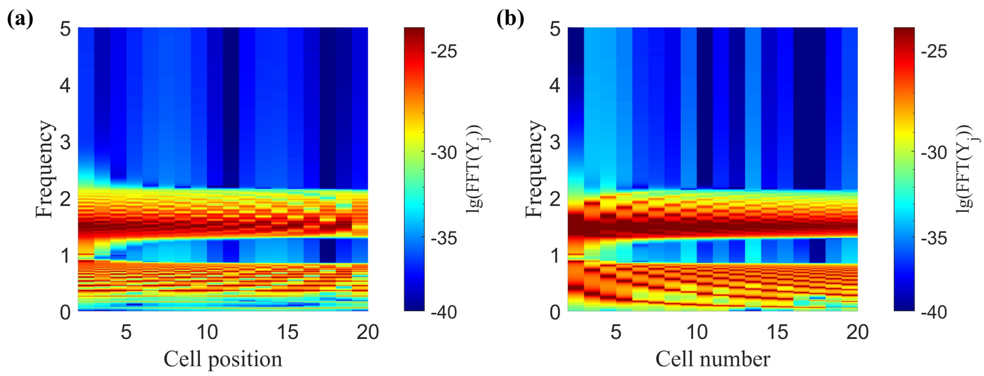

Figure 4.23: Frequency spectra of (a) different cell positions of Y_j in the 20-cell nonlinear configuration C4 and (b) the last cell response Y_j in different cell number nonlinear systems for the input non-dimensional frequency with parameters selected as $\lambda_1 = 1$, $\lambda_2 = 0.1$, $\hat{R}_j^2 = 0.01$. The colorbar represents different amplitude spectra.

Figure 4.24(a) shows the dispersion relation diagram of an infinite-unit LRAM. Figures 4.24(b) and (c) show two wave transmittance diagrams of finite systems with 6 and 30 unit cells, respectively. The parameters and variables are set as $\lambda_1 = 5$, $\lambda_2 = 0.1$, $\hat{R}_j^2 = 0.01$. It reveals that for these two different cases with same material parameters, the location and width of bandgaps are still the same. Some differences in wave suppression performance are exhibited. The figure shows that there are more peaks in wave transmittance for the 30-unit system than that for the 6-unit system. It is because that the former system has a much larger number of degrees of freedom. The figure also shows that the curve close to the upper boundary of the bandgap for the 30-unit system is flatter compared with that of the 6-unit system. The former is beneficial for vibration suppression. As shown in Fig. 4.24(b) for the six-cell system, at the upper boundary of the bandgap, the wave transmittance drops from 0 dB at 51.2 Hz to -100 dB at 48.1 Hz, demonstrating that the frequency variation is 3.1 Hz for the change in wave transmittance 0 to -100 dB. In comparison, for the 30-cell case, the wave transmittance drops from 0 to -100 dB with a variation in frequency being 0.3 Hz. At the lower bond of the bandgap, the difference in the attenuation performance of the two structures is found to be relatively small.

Figure 4.25(a) presents a 3D isometric view of the wave transmittance showing the influence of the unit cell number on wave attenuation when $\lambda_1 = 5$, $\lambda_2 = 0.1$, $\hat{R}_j^2 = 0.01$. The number of cells changes from 0 to 30 while the frequency range between 0 and 100 Hz is shown. The figure shows that there is a plane with many peaks distributed and a gap located in the neighborhood of 50 Hz. The bandgap shows low wave transmittance at this range of frequency. The suppression performance is enhanced because the transmittance in the bandgap becomes smaller as the number of unit cells increases. As the number of unit cells increases from 5 to 30, more

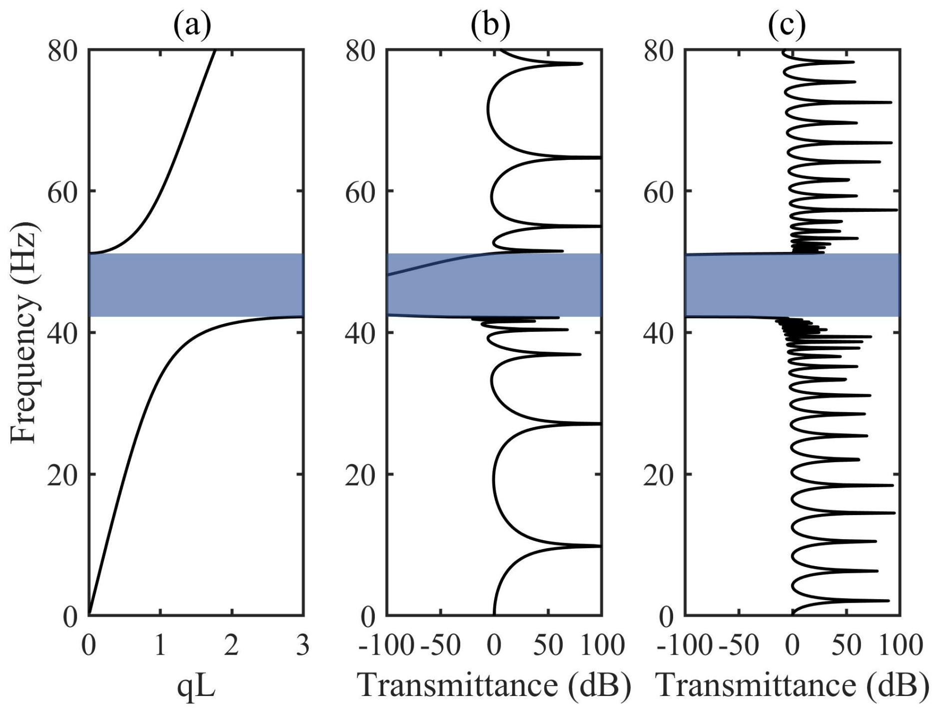

Figure 4.24: (a) Dispersion relation for the infinite system and (b) and (c) wave transmittances of 6-unit and 30-unit LRAM, respectively. Parameters are set as $\lambda_1 = 5$, $\lambda_2 = 0.1$, $\hat{R}_j^2 = 0.01$. The shadowed area represents the bandgap and low transmittance range.

amplitude peaks appear due to the increasing number of DoFs. Figure 4.25(b) is the top view of the 3D wave transmittance model. It shows that the bandgap width (defined as the frequency bandwidth within which the transmittance is below 0 dB) is almost not changed by the changes in the number of unit cells. However, the frequency range of the extreme low transmittance is widened as the cell number increases. It shows that the wave attenuation performance is better at the left boundary of the bandgap than at the right boundary. In summary, an increased number of unit cells can lead to better wave attenuation performance of the system.

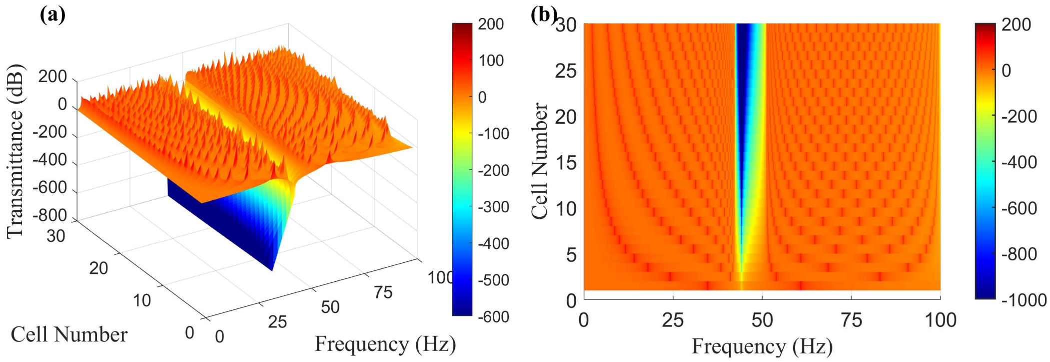

Figure 4.25: (a) 3D isometric view and (b) top view of the wave transmittance of the proposed nonlinear metamaterials for different numbers of unit cells with parameters selected as $\lambda_1 = 5$, $\lambda_2 = 0.1$, $\hat{R}_j^2 = 0.01$. The colorbar represents different wave transmittances.

4.5 Summary

This article investigated the performance of four different configurations of linear and nonlinear inerter-based locally resonant acoustic metamaterials (LRAM). For the linear inerter-based LRAMs, single in-parallel, in-series, and dual in-parallel structures were investigated. The geometrical nonlinear inerter mechanism (GNIM) was introduced to the proposed nonlinear inerter-based LRAM design. For the single resonator LRAM, the in-parallel configuration shows more potential for low-frequency vibration control compared with the in-series configuration. For the dual resonator LRAM, there are two bandgaps in the dispersion relation, and they can be combined to one complete broader bandgap. Moreover, the increasing inertance ratios will make the bandgap move to the lower frequency region with narrower width. For the proposed nonlinear inerter-based LRAM, it has been found that:

- The bandgap exists around the local resonant frequency. Compared with the linear inerter-based LRAM, nonlinear inerter-based LRAM, can induce a low-frequency range with a broader bandwidth, which is much less sensitive to the inertance changes of the GNIM.

- The bandgaps in the wave transmittance diagram for finite systems and dispersion diagram for infinite systems have good agreement with bandgap location and width.

- The power flow analysis shows that the power flow is blocked within the bandgap and the power transmission is lower as the cell position number increases.

- An adequate number of unit cells is preferred to gain better wave attenuation performance, especially around the upper band boundary.

In summary, the proposed nonlinear LRAM configuration can provide a lower-frequency bandgap with sufficient bandwidth. These findings can enhance the understanding of the effects and performance benefits of using geometrically nonlinear inerter mechanisms in LRAMs.

Chapter 5

Enhanced vibration suppression using diatomic acoustic metamaterial with negative stiffness mechanism

5.1 Introduction

The current chapter seeks to explore the combined use of the diatomic configuration and negative stiffness mechanism for enhanced performance of vibration suppression. Also, the dynamic properties of the proposed LRAMs are investigated from both the wave transmittance and the vibration power flow viewpoints. Multiple bandgaps can be created and the lower bound of the locally resonant bandgap can be reduced to quasi-zero value to achieve ultra low frequency wave attenuation. The local resonators were connected to the adjacent lumped masses in the proposed diatomic configuration. The bandgap characteristics of the monatomic configuration with similar parameters were compared to present additional Bragg scattering bandgaps. Wave transmittance and PFA methods were applied to investigate the wave control ability of the bandgaps. Based on the new perspective of analysis, the diatomic LRAM configuration is improved by applying NSM to connect each lumped mass and corresponding resonator to achieve a constant effective negative-stiffness coefficient. With a critical value of effective negative stiffness, the locally resonant bandgap can be effective from zero frequency, thus achieving ultralow frequency vibration control, while the upper band-folding-induced bandgap exhibits good performance.

The remainder of this study is organised as follows. Section 5.2 briefly presents the mathematical modelling of the diatomic-configuration LRAM. The corresponding governing equations for the dispersion relation are obtained together with an explanation of the wave transmittance and PFA methods. In Section 5.3, an NSM-based diatomic LRAM configuration is presented. The nonlinear characteristics of the NSM are presented in the SDoF and 4-DoF systems. Subsequently, the proposed LRAM with constant negative stiffness is analysed with the use of dispersion relations, wave transmittance, and PFA. The influence of material parameters was also studied. The conclusions of this study are presented in the last section.

5.2 Diatomic mass-spring chain model

5.2.1 Mathematical modelling

Fig. 5.1 depicts two 1-D mass-spring configurations representing the LRAMs. Fig. 5.1(a) shows a monatomic configuration C1 with N identical mass-spring unit cells. Each unit cell comprises one lumped mass m_1 and one resonator mass m_0. The lumped masses m_1 are interconnected by dampers of damping coefficient c and linear springs of stiffness coefficient k_0, and the initial distances between the lumped masses m_0 are L, which are the same as the lattice spacing. In each unit cell, resonator m_1 is connected to one lumped mass with a spring of stiffness coefficient k_2 and a fore-lumped mass with a spring of stiffness coefficient k_1. The first lumped mass is attached to a moving base of displacement, $d_0 \cos \omega t$, as motion excitation. Fig. 5.1(b) shows the proposed diatomic LRAM configuration C2. The only difference between configurations C1 and C2 is that the lumped masses in C2 are not all identical, with mass couples of m_1 and m_2 alternately distributed along the system.

The equations of motion for the diatomic LRAM depicted in Fig. 5.1(b) can be obtained as:

$$m_1\ddot{x}_i + c(2\dot{x}_i - \dot{x}_{j-1} - \dot{x}_j) + k_0(2x_i - x_{j-1} - x_j) + \\ k_1(x_i - y_j) + k_2(x_i - y_i) = 0; \tag{5.1a}$$

$$m_0\ddot{y}_i + k_1(y_j - x_{j-1}) + k_2(y_i - x_i) = 0, \tag{5.1b}$$

$$m_2\ddot{x}_j + c(2\dot{x}_j - \dot{x}_i - \dot{x}_{i+1}) + k_0(2x_j - x_i - x_{i+1}) + \\ k_1(x_j - y_{i+1}) + k_2(x_j - y_j) = 0; \tag{5.1c}$$

$$m_0\ddot{y}_j + k_1(y_j - x_i) + k_2(y_j - x_j) = 0, \tag{5.1d}$$

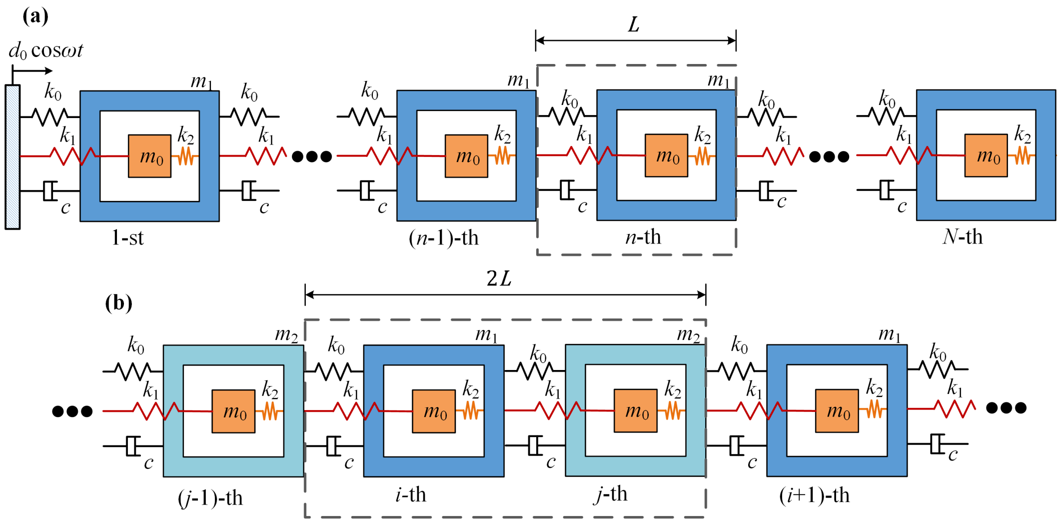

Figure 5.1: Mass-spring chain structure LRAMs with N identical mass-spring unit cells of (a) monatomic configuration C1 with cell spacing L and (b) diatomic configuration C2 with cell spacing $2L$.

where x, y are the displacements of the lumped mass and resonator, respectively, and the subscripts i and j represent the i-th and j-th cell positions, respectively.

5.2.2 Dispersion relation

For an infinite LRAM of diatomic configuration, the harmonic wave solutions are presented by:

$$x_i = X_i \cos(\omega t + \phi); \tag{5.2a}$$

$$x_j = X_j \cos(\omega t + \phi); \tag{5.2b}$$

$$y_i = Y_i \cos(\omega t + \phi); \tag{5.2c}$$

$$y_j = Y_j \cos(\omega t + \phi), \tag{5.2d}$$

where ϕ is the phase angle and X and Y are the response amplitudes of the lumped mass and resonator, respectively. Considering the i-th resonator as an example, the steady-state velocity and acceleration can be written as

$$\dot{x}_i = -X_i \omega \sin(\omega t + \phi); \tag{5.3a}$$

$$\ddot{x}_i = -X_i \omega^2 \cos(\omega t + \phi), \tag{5.3b}$$

respectively. According to the Bloch's theorem (Brillouin, 1953), a phase difference occurs when the amplitudes of two adjacent vibrating masses are identical. Hence, the motion of adjacent masses can be expressed as:

$$x_{j-1} = x_j \mathrm{e}^{-2\mathrm{i}qL}; \tag{5.4a}$$

$$x_{i+1} = x_i \mathrm{e}^{2\mathrm{i}qL}; \tag{5.4b}$$

$$y_{i+1} = y_i \mathrm{e}^{2\mathrm{i}qL}, \tag{5.4c}$$

where q is the Bloch wave number, and L is the lattice constant.

It is noted that previous studies have often used the corresponding undamped structures to determine the dispersion properties of LRAMs, which in reality are weakly damped. Similarly, the dispersion analysis carried out in the current study is based on the absence of damping. However, it is noted that in the wave transmittance and power flow analysis in the next sections, damping effects are taking into consideration as there is associated energy dissipation. By substituting Eqs. (5.2)– (5.4) into Eqs. (5.1b) and (5.1d), the displacements of the i-th and j-th resonators can be derived:

$$Y_i = \frac{k_1 \mathrm{e}^{-2\mathrm{i}qL} X_j + k_2 X_i}{-m_0 \omega^2 + k_1 + k_2}; \tag{5.5a}$$

$$Y_j = \frac{k_1 X_i + k_2 X_j}{-m_0 \omega^2 + k_1 + k_2}. \tag{5.5b}$$

Eqs. (5.5a) and (5.5b) can be substituted into Eqs. (5.1a) and (5.1c) to eliminate the responses of the internal resonators. By combining the terms $(-\omega^2 X_i)$, $(2X_i - \mathrm{e}^{-2\mathrm{i}qL} X_j - X_j)$, $(-\omega^2 X_j)$ and $(2X_j - X_i - \mathrm{e}^{2\mathrm{i}qL} X_i)$, the following equations are obtained:

$$\left(m_1 + \frac{m_0(k_1+k_2)}{k_1+k_2-m_0\omega^2}\right)(-\omega^2 X_i) + \left(k_0 + \frac{k_1k_2}{k_1+k_2-m_0\omega^2}\right)(2X_i - \mathrm{e}^{2\mathrm{i}qL}X_j - X_j) = 0; \quad (5.6a)$$

$$\left(m_2 + \frac{m_0(k_1+k_2)}{k_1+k_2-m_0\omega^2}\right)(-\omega^2 X_j) + \left(k_0 + \frac{k_1k_2}{k_1+k_2-m_0\omega^2}\right)(2X_i - \mathrm{e}^{2\mathrm{i}qL}X_j - X_j) = 0. \quad (5.6b)$$

Based on the effective mass concept (Huang et al., 2009; Alamri et al., 2018; Sugino et al., 2017; Tan et al., 2012; Zhu et al., 2014), the system can be effectively considered as a chain structure with alternating distributed effective masses mi eff and mj eff , connected by identical effective stiffness springs Keff . The equations of motion can be written as:

$$m_{\mathrm{eff}}^{\mathrm{i}}\ddot{x}_i + k_{\mathrm{eff}}(2x_i - x_{j-1} - x_j) = 0; \quad (5.7a)$$

$$m_{\mathrm{eff}}^{\mathrm{j}}\ddot{x}_j + k_{\mathrm{eff}}(2x_j - x_i - x_{i+1}) = 0. \quad (5.7b)$$

where

$$m_{\mathrm{eff}}^{\mathrm{i}} = m_1 + \frac{m_0(k_1+k_2)}{k_1+k_2-m_0\omega^2}; \quad (5.8a)$$

$$m_{\mathrm{eff}}^{\mathrm{j}} = m_2 + \frac{m_0(k_1+k_2)}{k_1+k_2-m_0\omega^2}; \quad (5.8b)$$

$$k_{\mathrm{eff}} = k_0 + \frac{k_1k_2}{k_1+k_2-m_0\omega^2}. \quad (5.8c)$$

Eq. (5.7) can be further written in a matrix form as:

$$\begin{bmatrix} 2k_{\text{eff}} - m^{\text{i}}_{\text{eff}}\omega^2 & -(1+\mathrm{e}^{-2\mathrm{i}qL})k_{\text{eff}} \\ -(1+\mathrm{e}^{2\mathrm{i}qL})k_{\text{eff}} & 2k_{\text{eff}} - m^{\text{j}}_{\text{eff}}\omega^2 \end{bmatrix} \begin{Bmatrix} X_i \\ X_j \end{Bmatrix} = \begin{Bmatrix} 0 \\ 0 \end{Bmatrix}. \tag{5.9}$$

A set of trivial solutions to Eq. (5.9) are obtained when the matrix determinant is zero. Hence, the equation for the dispersion relation is:

$$\begin{vmatrix} 2k_{\text{eff}} - m^{\text{i}}_{\text{eff}}\omega^2 & -(1+\mathrm{e}^{-2\mathrm{i}qL})k_{\text{eff}} \\ -(1+\mathrm{e}^{2\mathrm{i}qL})k_{\text{eff}} & 2k_{\text{eff}} - m^{\text{j}}_{\text{eff}}\omega^2 \end{vmatrix} = 0. \tag{5.10}$$

Eq. (5.10) can be rewritten as

$$(2k_{\text{eff}} - m^{\text{i}}_{\text{eff}}\omega^2)(2k_{\text{eff}} - m^{\text{j}}_{\text{eff}}\omega^2) - (1+\mathrm{e}^{-2\mathrm{i}qL})(1+\mathrm{e}^{2\mathrm{i}qL})k^2_{\text{eff}} = 0. \tag{5.11}$$

Note that $\mathrm{e}^{2\mathrm{i}qL} + \mathrm{e}^{-2\mathrm{i}qL} = 2\cos(2qL)$, so Eq. (5.11) can be further written as

$$\cos(2qL) = 1 + \frac{m^{\text{i}}_{\text{eff}} m^{\text{j}}_{\text{eff}}\omega^4 - 2k_{\text{eff}} m^{\text{i}}_{\text{eff}}\omega^2 - 2k_{\text{eff}} m^{\text{j}}_{\text{eff}}\omega^2}{2k^2_{\text{eff}}}. \tag{5.12}$$

Similarly, the dispersion relation of the monatomic configuration C1 can be obtained:

$$\cos(qL) = 1 - \frac{m^{\text{n}}_{\text{eff}}\omega^2}{2k^n_{\text{eff}}}. \tag{5.13}$$

where $m^{\text{n}}_{\text{eff}} = m_1 + m_0(k_1+k_2)/(k_1+k_2-m_0\omega^2)$ and $k^n_{\text{eff}} = k_1k_2/(k_1+k_2-m_0\omega^2)$.

The dispersion diagrams of the monatomic and diatomic configurations can be obtained using Eqs. (5.12) and (5.13). Fig. 5.2(a) and (b) show the corresponding dispersion relation curves for configurations C1 and C2, respectively, with the set parameter. The mass parameters in C2 were selected as $m_1 = m_2 = 1$ kg, such that configurations C1 and C2 were the

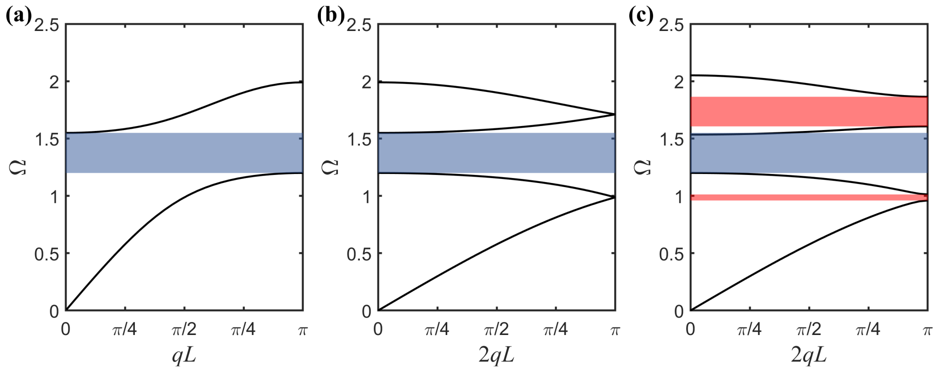

Figure 5.2: Dispersion relation diagrams for (a) monatomic configuration C1, (b) diatomic configuration C2 with $m_1 = m_2 = 1$ kg, and (c) diatomic configuration with $m_1 = 1.2$ kg, $m_2 = 0.8$ kg.

same. The other parameters are selected as $m_0 = 0.6$ kg, $\omega_1 = 30$ rad/s, $k_0 = (m_1 + m_2)\omega_1^2/2$, $k_1/k_0 = 0.4$ and $k_2/k_0 = 0.8$, $\omega_2 = \sqrt{k_2/m_2}$. The solid curves are associated with the real part of qL and the non-dimensional frequency Ω is defined as ω/ω_2. The figure shows the bandgap indicated by a blue-shadowed frequency range, in which there is no real solution. When $m_1 = m_2$, the bandgaps for the two configurations are the same. The dispersion curve shown in Fig. 5.2(b) was obtained by folding the curve by the midline ($qL = \pi/2$), as shown in Fig. 5.2(a). Fig. 5.2(c) shows the dispersion relation diagram of the system with $m_1 = 1.2$ kg, $m_2 = 0.8$ kg while the remaining parameters are set the same as those used in Fig. 5.2(a) and (b). Fig. 5.2(c) shows the dispersion relation diagram of the system with $m_1 = 1.2$ kg, $m_2 = 0.8$ kg. The figure shows three different bandgaps, with the one shaded in blue being the same as the ones shown in Fig. 5.2(a) and (b). Two additional bandgaps emerge at the two band-folding points, shaded in red. The local resonant gaps remain constant because the total mass remains the same. From a macro perspective, configurations C1 and C2 should exhibit similar performance. However, the staggered distribution of different lumped masses leads to more band-folding-induced bandgaps, which have beneficial dynamic characteristics and can yield better vibration suppression performance.

5.2.3 Wave transmittance and power flow analysis

The methods of wave transmittance and PFA are briefly discussed in this section. If the 2-DoF mass-resonator unit is converted into a SDoF system by using the effective mass, the LRAM structure can be considered as a system comprising effective masses connected by dampers and springs of effective stiffness. The motion equations of N-DoF chain oscillator corresponding to the LRAM configuration C2 are written in the matrix form as:

$$\mathbf{M}\ddot{\widetilde{\mathbf{X}}} + \mathbf{C}\dot{\widetilde{\mathbf{X}}} + \mathbf{K}\widetilde{\mathbf{X}} = \widetilde{\mathbf{F}}_e \mathrm{e}^{\mathrm{i}\omega t}, \tag{5.14}$$

where

$$\mathbf{M} = \begin{bmatrix} m_{\text{eff}}^{\text{i}} & 0 & \cdots & 0 & 0 \\ 0 & m_{\text{eff}}^{\text{j}} & \ddots & \ddots & 0 \\ \vdots & \ddots & \ddots & \ddots & \vdots \\ 0 & \ddots & \vdots & m_{\text{eff}}^{\text{i}} & 0 \\ 0 & 0 & \cdots & 0 & m_{\text{eff}}^{\text{j}} \end{bmatrix}; \tag{5.15a}$$

$$\mathbf{C} = c \begin{bmatrix} 2 & -1 & 0 & \cdots & 0 \\ -1 & 2 & -1 & \ddots & \vdots \\ 0 & \ddots & \ddots & \ddots & 0 \\ \vdots & \ddots & -1 & 2 & -1 \\ 0 & \cdots & 0 & -1 & 1 \end{bmatrix}; \tag{5.15b}$$

$$\mathbf{K} = k_{\text{eff}} \begin{bmatrix} 2 & -1 & 0 & \cdots & 0 \\ -1 & 2 & -1 & \ddots & \vdots \\ 0 & \ddots & \ddots & \ddots & 0 \\ \vdots & \ddots & -1 & 2 & -1 \\ 0 & \cdots & 0 & -1 & 1 \end{bmatrix}; \tag{5.15c}$$

$$\widetilde{\mathbf{F}}_e = \begin{bmatrix} \widetilde{F}_1 \\ \widetilde{F}_2 \\ \vdots \\ \widetilde{F}_{N-1} \\ \widetilde{f}_{\mathrm{n}} \end{bmatrix}; \tag{5.15d}$$

$$\widetilde{\mathbf{X}} = \begin{bmatrix} \widetilde{X}_1 \\ \widetilde{X}_2 \\ \vdots \\ \widetilde{X}_{N-1} \\ \widetilde{X}_N \end{bmatrix} \mathrm{e}^{\mathrm{i}\omega t}. \tag{5.15e}$$

Note that $\mathbf{M}$, $\mathbf{C}$ and $\mathbf{K}$ present the $N \times N$ total mass, damping, stiffness matrices, respectively; $\widetilde{\mathbf{F}}_e$ is the vector for complex amplitudes of the external forces; $\widetilde{\mathbf{X}}$, $\dot{\widetilde{\mathbf{X}}}$ and $\ddot{\widetilde{\mathbf{X}}}$ denote the displacement, velocity, and acceleration vectors of the system, respectively. The solution to Eq. (5.14) has the form $\dot{\widetilde{\mathbf{X}}} = \widetilde{\mathbf{V}}\mathrm{e}^{\mathrm{i}\omega t}$, with $\widetilde{\mathbf{V}}$ being the complex amplitudes of velocities. Therefore, Eq. (5.14) takes the form

$$\widetilde{\mathbf{F}}_e = \left(\mathrm{i}\omega\mathbf{M} + \mathbf{C} + \frac{\mathbf{K}}{\mathrm{i}\omega}\right)\widetilde{\mathbf{V}}, \tag{5.16}$$

and we have the vector for velocity amplitudes:

$$\widetilde{\mathbf{V}} = \left[\mathrm{i}\omega\mathbf{M} + \mathbf{C} + \frac{\mathbf{K}}{\mathrm{i}\omega}\right]^{-1}\widetilde{\mathbf{F}}_e. \tag{5.17}$$

The transmittance is defined as the logarithmic ratio of the response amplitude of the N-th effective mass to the first effective mass:

$$T = 20\lg\left(\left|\frac{\widetilde{\mathbf{X}}_N}{\widetilde{\mathbf{X}}_1}\right|\right). \tag{5.18}$$

PFA can also provide a new perspective for LRAM design and application. The energy flow balance equation was obtained by premultiplying Eq. (5.14) by the velocity vector

$$\dot{\widetilde{\mathbf{X}}}^{\mathrm{H}}\mathbf{M}\ddot{\widetilde{\mathbf{X}}} + \dot{\widetilde{\mathbf{X}}}^{\mathrm{H}}\mathbf{C}\dot{\widetilde{\mathbf{X}}} + \dot{\widetilde{\mathbf{X}}}^{\mathrm{H}}\mathbf{K}\widetilde{\mathbf{X}} = \dot{\widetilde{\mathbf{X}}}^{\mathrm{H}}\widetilde{\mathbf{F}}_e\mathrm{e}^{\mathrm{i}\omega t}, \tag{5.19}$$

where the superscript $(\bullet)^{\mathrm{H}}$ denotes a conjugate, transpose matrix. The total input instantaneous power of the system is the product of the excitation point velocity and the excitation force (Shi et al., 2019). The real power at time t is given as:

$$P(t) = \Re\left\{\dot{\widetilde{\mathbf{X}}}^{\mathrm{H}}\right\}\Re\left\{\widetilde{\mathbf{F}}_e\mathrm{e}^{\mathrm{i}\omega t}\right\}. \tag{5.20}$$

The time-averaged power over one excitation cycle is expressed as follows:

$$\begin{aligned}\overline{P} &= \frac{1}{t_{\mathrm{s}}}\int_{t_0}^{t_0+t_{\mathrm{s}}}\Re\left\{\dot{\widetilde{\mathbf{X}}}^{\mathrm{H}}\right\}\Re\left\{\widetilde{\mathbf{F}}_e\mathrm{e}^{\mathrm{i}\omega t}\right\}\mathrm{d}t \\ &= \frac{1}{2}\left(\Re\left\{\dot{\widetilde{\mathbf{X}}}^{\mathrm{H}}\right\}\Re\left\{\widetilde{\mathbf{F}}_e\mathrm{e}^{\mathrm{i}\omega t}\right\} + \Im\left\{\dot{\widetilde{\mathbf{X}}}^{\mathrm{H}}\right\}\Im\left\{\widetilde{\mathbf{F}}_e\mathrm{e}^{\mathrm{i}\omega t}\right\}\right),\end{aligned} \tag{5.21}$$

where t_0 is the start time of the averaging operation and $t_{\mathrm{s}} = 2\pi/\Omega$ is the excitation period.

The differences in the output and input power can be compared to identify the energy dissipation. The force applied to each cell is associated with the difference in displacements and velocity responses between the adjacent effective masses. For an N-unit LRAM configuration, the input power is defined as the power transmitted to the first effective mass from the motion excitation, whereas the output power is the power transmitted to the N-th effective mass from the $(N-1)$-th effective mass. Therefore, the time-averaged input and output powers for the LRAM configuration C2 attached to a moving base left-hand-side end of displacement, $d_0\mathrm{e}^{\mathrm{i}\omega t}$, by the spring and damper can be obtained:

$$\overline{P}_{\mathrm{in}} = \frac{1}{t_{\mathrm{s}}}\int_{t_0}^{t_0+t_{\mathrm{s}}} \Re\left\{(\mathrm{i}\omega c + k_{\mathrm{eff}})(\widetilde{X}_1 - d_0)\mathrm{e}^{\mathrm{i}\omega t}\right\}\Re\left\{\mathrm{i}\omega d_0 \mathrm{e}^{\mathrm{i}\omega t}\right\}\mathrm{d}t; \tag{5.22a}$$

$$\overline{P}_{\mathrm{out}} = \frac{1}{t_{\mathrm{s}}}\int_{t_0}^{t_0+t_{\mathrm{s}}} \Re\left\{(\mathrm{i}\omega c + k_{\mathrm{eff}})(\widetilde{X}_N - \widetilde{X}_{N-1})\mathrm{e}^{\mathrm{i}\omega t}\right\}\Re\left\{\mathrm{i}\omega \widetilde{X}_{N-1}\mathrm{e}^{\mathrm{i}\omega t}\right\}\mathrm{d}t. \tag{5.22b}$$

Fig. 5.3(a) and (b) present the displacement transmittance of the proposed diatomic-chain LRAM structures with 10-and 50-unit cells, respectively. The excitation displacement amplitude was set to be $d_0 = 0.1$ m, and the damping coefficient $c = 0.001$. Frequency ranges with transmittances lower than -20 dB are defined as regions of low wave transmittance. Fig. 5.3(a) shows that for the 10-unit cell structure, there will be a clear low transmittance gap from $\Omega = 1.20$ to 1.55 within the locally resonant bandgap. At the same time, the wave attenuation performance is not compromised within the upper band-folding-induced bandgap and within the lower band-folding-induced bandgap from $\Omega = 0.96$ to 1.01. Fig. 5.3(b) presents the corresponding transmittance for the configuration of 50-unit cell. In this case, the upper bandgap induced by band folding demonstrates a lower transmittance, and the lower bandgap around $\Omega = 1$ also validates the existence of a lower bandfolding- induced bandgap. With enough unit cells, the upper bandgap can provide good wave attenuation performance as a locally resonant bandgap, which is better than that of the lower bandgap.

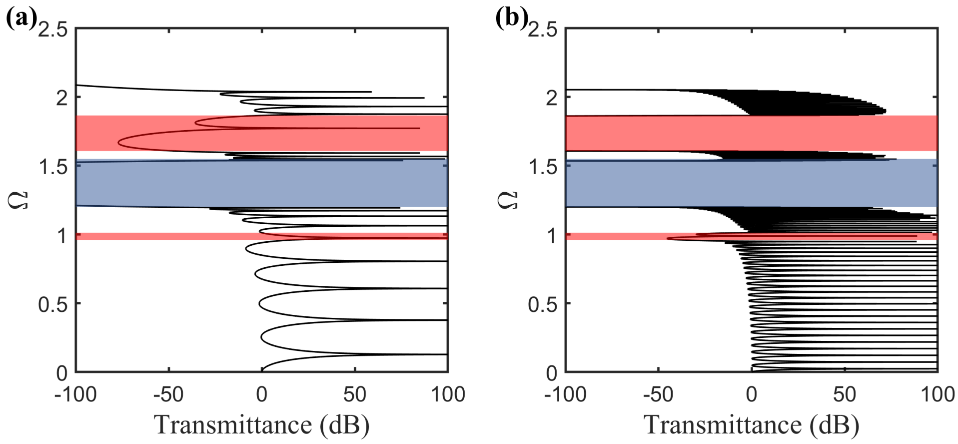

Figure 5.3: Wave transmittance diagrams for diatomic configuration C2 with m_1 = 1.2 kg, m_2 = 0.8 kg and of (a) 10 unit cells and (b) 50 unit cells.

The use of PFA to investigate the system can lead to improved understanding and reveal the structural wave suppression behaviour from another viewpoint. Fig. 5.4 shows the vibration power flow characteristics of the monatomic and diatomic configurations. The time-averaged power flows for monatomic configuration C2 are shown in Fig. 5.4(a), with the red and blue solid lines representing the input and output powers, respectively. The material parameters remained unchanged, as applied in the case study in Fig. 5.2 and the lumped mass number is 50. The input power was always larger than the output power, and a gap was induced in the output power flow curve. Fig. 5.4(b) shows the power transmittance in dB, which is defined as the logarithmic ratio of the output and input powers ($\lg(P_{\text{out}}/P_{\text{in}})$). Compared with Fig. 5.2(b), within the locally resonant bandgap frequency, the power transmittance is lower, suggesting that the energy of the waves with the excitation frequency located in the bandgap is blocked. Fig. 5.4(c) and (d) depict the time-averaged power flow and power transmittance, respectively, for diatomic configuration C2.

In contrast to configuration C1, there are two more gaps induced by band folding, as shaded in red, which represents the power-blocking ability. The lower frequency band has a weaker power consumption ability, which may be due to the use of a small cell number. The results show that the energy is almost blocked in the upper two bandgaps, and the performance is better at higher frequencies.

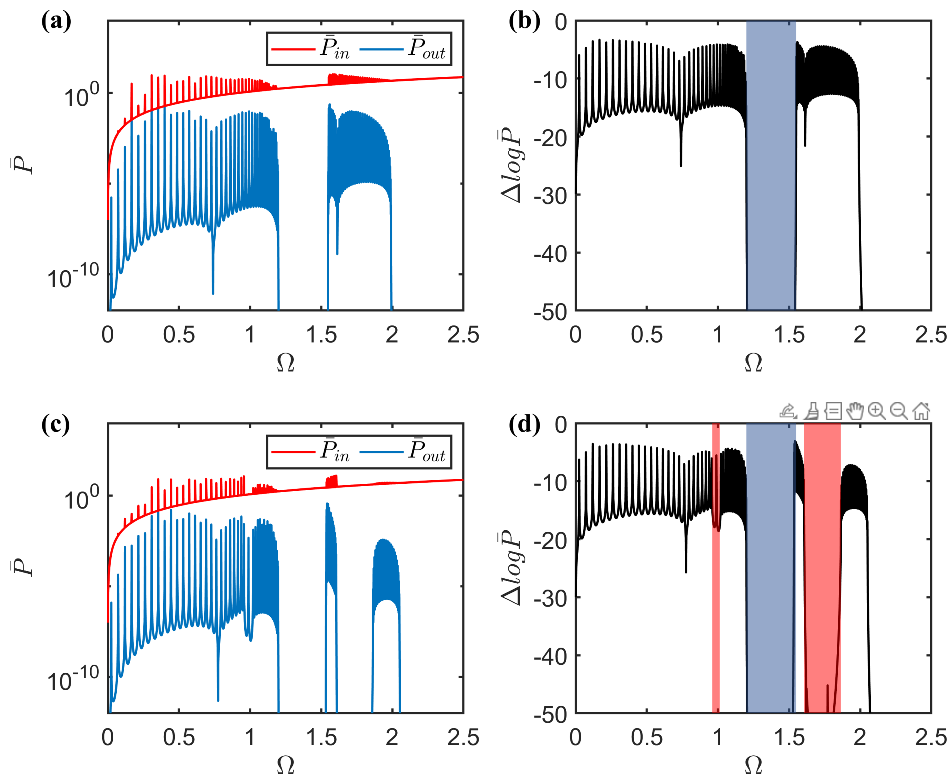

Figure 5.4: Power flow behaviour of monatomic and diatomic LRAM configurations with 50-unit cells. (a) Time-averaged input and output powers and (b) power consumption for monatomic configuration C1. (c)Time-averaged input and output powers and (d) power consumption for diatomic configuration C2.

In Fig. 5.5, the influence of the number of unit cells on the bandgap characteristics is investigated further. The power transmission maps in the 3D view and top view are shown in Fig. 5.5(a) and (b), respectively. The labelled axes represent the non-dimensional frequency, unit cell number,

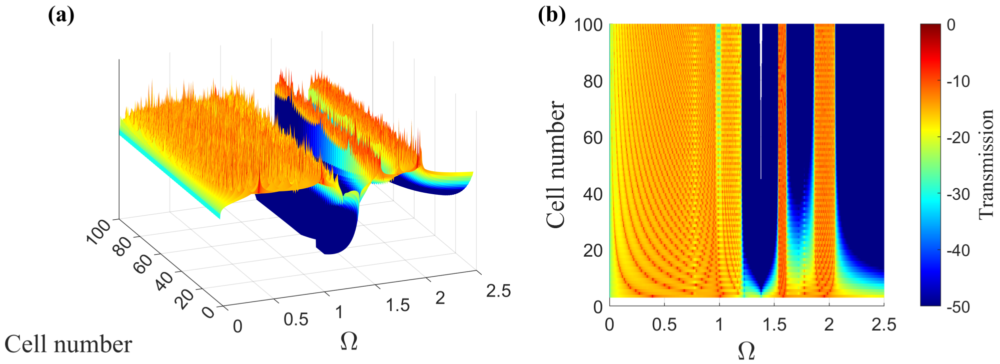

Figure 5.5: The influence of the number of unit cells on power flow of LRAM structures. (a) 3D view and (b) top view.

and power transmission, respectively. Fig. 5.5(b) shows that the bandgap induced by local resonance with frequencies between 1.20 and 1.55 can block the energy even with just a few cells, while the power transmission within the upper band-folding-induced bandgap is relatively higher but still has a good ability to block the vibration power transmission. It is noted that for the lower band-folding-induced bandgap, at least 40 cells were required to achieve the desirable energy dissipation.

5.3 Diatomic configuration with negative stiffness

Low-frequency vibrations need to be suppressed in many engineering systems. In this section, an improved spring-bar mechanism with constant negative stiffness is applied to the diatomic-configuration LRAM for low-frequency wave suppression. As shown in Fig. 5.5, the width of the lower bandgap was not as broad as that of the other two bandgaps even with a relatively large number of cells. In this section, the application of negative stiffness to enhance benefits is explored.

5.3.1 Negative-stiffness-based diatomic LRAM

The diatomic LRAM applied with spring-bar mechanisms is depicted in Fig. 5.6, while the springs and dampers, except k_2, are equivalent to those in Fig. 5.1(b). The spring-bar mechanism coloured in green can be represented by an effective spring with stiffness k_n. The influence of NSM-based configuration can be modelled by replacing k_1 with k_n in the original diatomic configuration.

The corresponding equations of motion of the system are:

$$m_1\ddot{x}_i + c(2\dot{x}_i - \dot{x}_{j-1} - \dot{x}_j) + k_0(2x_i - x_{j-1} - x_j) + k_1(x_i - y_j) + k_\mathrm{n}(x_i - y_i) = 0; \quad (5.23a)$$

$$m_0\ddot{y}_i + k_1(y_j - x_{j-1}) + k_\mathrm{n}(y_i - x_i) = 0; \quad (5.23b)$$

$$m_2\ddot{x}_j + c(2\dot{x}_j - \dot{x}_i - \dot{x}_{i+1}) + k_0(2x_j - x_i - x_{i+1}) + k_1(x_j - y_{i+1}) + k_\mathrm{n}(x_j - y_j) = 0; \quad (5.23c)$$

$$m_0\ddot{y}_j + k_1(y_j - x_i) + k_\mathrm{n}(y_j - x_j) = 0. \quad (5.23d)$$

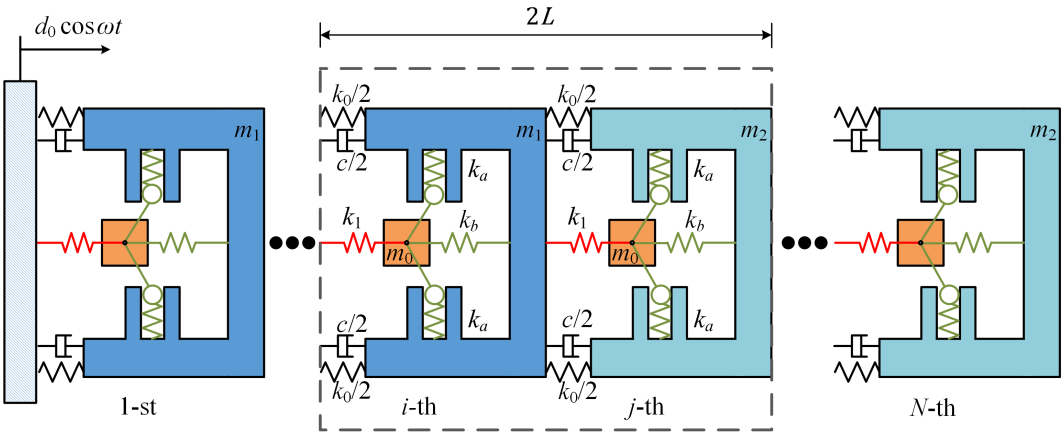

Figure 5.6: The model of proposed diatomic LRAM configuration C3 with spring-bar mechanism colored in green whose dynamic stiffness can be represented by k_n.

5.3.2 Spring-bar mechanism with negative stiffness

There have been a few physical realisations of NSMs, and their potential benefits in vibration isolation systems have been reviewed (Li et al., 2020a). In this model, a spring-bar mechanism NSM based on our previous study (Shi et al., 2021), as shown in Fig. 5.7(a), is applied for the performance enhancement of a diatomic LRAM. Two identical vertical springs of stiffness k_a are guided by the blocks, with one of the terminals pinned to the fixed wall and the other attached to joints A and B. The two joints are connected to terminal O with mass m by separate rigid bars of fixed length l and can only move vertically owing to the restraint of the frictionless slide guide blocks. The mass at terminal O is also attached to a point C with a spring stiffness coefficient k_b and a damper of damping coefficient c. A harmonic motion excitation $d(t)$ is applied to terminal C, leading to the horizontal motion of the mass denoted as $z(t)$. The static equilibrium position of the mass was considered as the reference position of $z = 0$, where the bars were horizontal. The masses of the springs, joints, and bars described above were considered negligible in this study. The two bars tilt at an angle of θ and constitute a potentially geometrical nonlinear mechanism. To achieve negative stiffness characteristics, the springs were initially compressed by δ_0 at the static equilibrium position.

According to the structure geometrical relations, we have:

$$\tan\theta = \frac{z}{\sqrt{l^2 - z^2}}. \tag{5.24}$$

Therefore, the combined horizontal force related to k_a and k_b can be

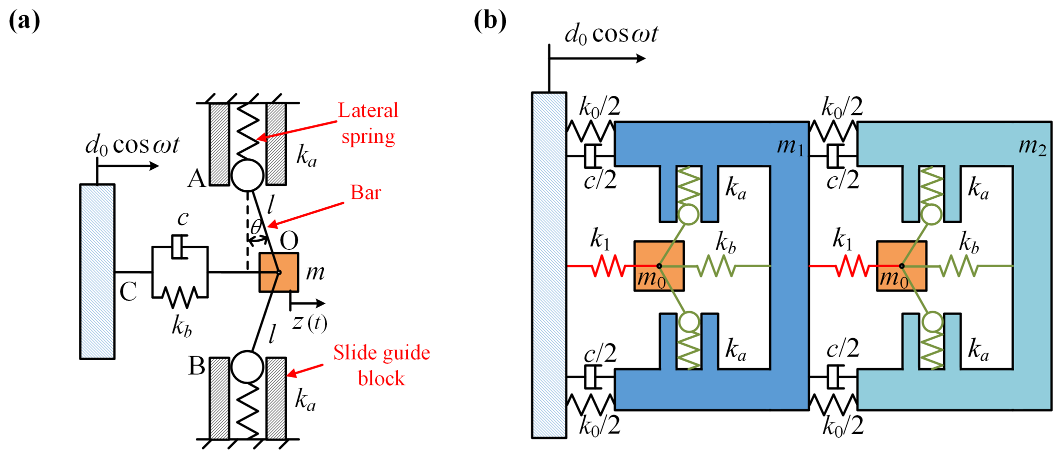

Figure 5.7: Schematic diagrams of (a) a SDoF spring-bar NSM-based system and (b) a 4-DoF diatomic spring-bar NSM-based system with harmonic motion excitation.

obtained by replacing the trigonometric terms as:

$$f_\mathrm{n} = \left(k_\mathrm{b} + 2k_\mathrm{a}\frac{l - \sqrt{l^2 - z^2} - \delta_0}{\sqrt{l^2 - z^2}}\right)z = k_\mathrm{n}z, \tag{5.25}$$

where $k_\mathrm{n} = k_\mathrm{b} + 2k_\mathrm{a}(l - \sqrt{l^2 - z^2} - \delta_0)/(\sqrt{l^2 - z^2})$.

Based on Eq. (5.25), if $\delta_0 = l$, which means that the initial compression of the horizontal springs is the same as the length of the bars, the combined restoring force will be:

$$f_\mathrm{n} = (k_\mathrm{n} - 2k_\mathrm{a})z = k_\mathrm{n1}z, \tag{5.26}$$

where $k_\mathrm{n1} = k_\mathrm{b} - 2k_\mathrm{a}$. Eq. (5.26) shows that, under suitable material parameters, the restoring force varies linearly with the displacement, and the effective stiffness of this spring-bar mechanism can be a negative constant. Compared with the NSM formed by a pair of oblique springs, the dynamic stiffness of this mechanism does not introduce nonlinearity.

The equation of motion of the SDoF mechanism depicted in Fig. 5.7(a) is:

$$m\ddot{z} + c\dot{z} + \left(k_{\mathrm{b}} + 2k_{\mathrm{a}}\frac{l - \sqrt{l^2 - z^2} - \delta_0}{\sqrt{l^2 - z^2}}\right)z = d_0 \cos\omega t + cd_0\omega\cos\omega t. \quad (5.27)$$

Fig. 5.8 shows the frequency–response curve of the lumped mass m under different parameter settings of the NSM. With the given parameters, Eq. (5.27) can be solved using the HB-AFT technique and the numerical time-marching Runge–Kutta (RK) method. The results in lines are obtained by HB-AFT, while those represented by the markers are obtained from the RK method, and the colours represent cases with different nonlinearity related parameters. The linear parameters are selected as $m = 1$ kg, $c = 0.02$ N/(m/s), $k_{\mathrm{b}}/k_0 = 1$. The solid black line is a linear case with no lateral springs k_{a}. The blue, red, and pink dash-dotted lines are the results with $k_{\mathrm{a}}/k_0 = 0.1$ and $\lambda = 0.5$, 1, 1.5, respectively, where $\lambda = \delta_0/l$. The marks obtained from the RK method seem to agree well with the results of the HB-AFT; therefore, the results can be verified. This shows that the resonant peak is bent into the high-frequency range when $\lambda = 0.5$, and conversely, the peak is bent into the low-frequency range when $\lambda = 1.5$. When $\lambda = 1$ as expressed in Eq. (5.26), the curve shows no nonlinear characteristics, and the effective stiffness of the NSM is a constant.

A 4-DoF diatomic system with NSM is shown in Fig. 5.7(b), which can be recognised as one unit of the proposed LRAM, as shown in Fig. 5.6 with harmonic motion excitation. For nonlinear systems, the harmonic orders, and number and size of time steps per period should be considered when using HB-AFT and RK methods, respectively. The dynamics of this diatomic unit structure can be studied first before analysing the multi- DoF system.

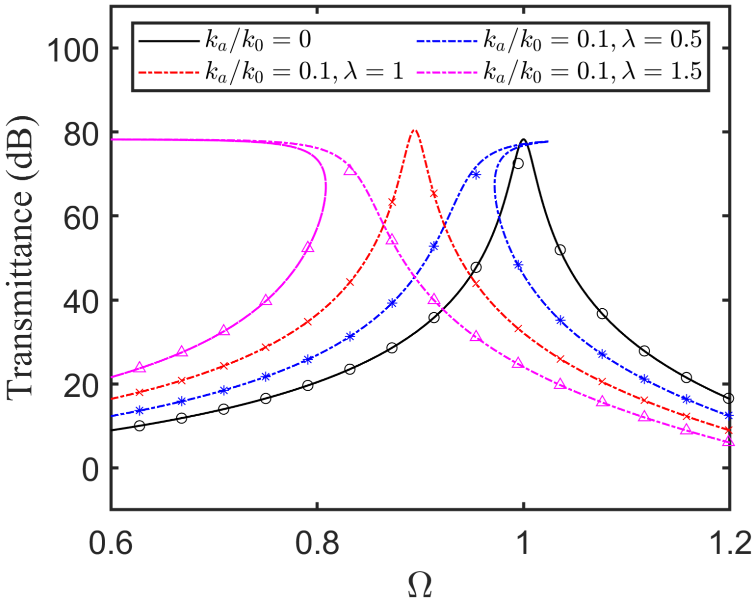

Figure 5.8: Transmissibility diagram of the lumped mass m in a SDoF spring-bar NSM-based system obtained by HB-AFT technique (lines) and RK method (markers) with different geometrical nonlinearity related parameters.

The equations of motion of the 4-DoF configuration depicted in Fig. 5.7 (b) are:

$$\begin{bmatrix} m_1 & 0 & 0 & 0 \\ 0 & m_0 & 0 & 0 \\ 0 & 0 & m_2 & 0 \\ 0 & 0 & 0 & m_0 \end{bmatrix} \begin{bmatrix} \ddot{x}_1 \\ \ddot{y}_1 \\ \ddot{x}_2 \\ \ddot{y}_2 \end{bmatrix} \begin{bmatrix} 2c & 0 & -c & 0 \\ 0 & 0 & 0 & 0 \\ -c & 0 & c & 0 \\ 0 & 0 & 0 & 0 \end{bmatrix} \begin{bmatrix} \dot{x}_1 \\ \dot{y}_1 \\ \dot{x}_2 \\ \dot{y}_2 \end{bmatrix} +$$
$$\begin{bmatrix} 2k_0 + k_1 + k_\mathrm{n} & -k_\mathrm{n} & -k_0 & -k_1 \\ -k_\mathrm{n} & k_1 + k_\mathrm{n} & 0 & 0 \\ -k_0 & 0 & k_0 + k_\mathrm{n} & -k_\mathrm{n} \\ -k_1 & 0 & -k_\mathrm{n} & k_1 + k_\mathrm{n} \end{bmatrix} \begin{bmatrix} x_1 \\ y_1 \\ x_2 \\ y_2 \end{bmatrix} = \begin{bmatrix} cd_0\omega \sin \omega t + k_0 d_0 \cos \omega t \\ k_1 d_0 \cos \omega t \\ 0 \\ 0 \end{bmatrix}. \tag{5.28}$$

The displacement transmissibility diagrams for masses m_1 and m_2 in 4-DoF are presented in Fig. 5.9(a) and (b), respectively. The blue dashed line, red dash-dotted line, and pink dotted line represent the results with geometrical parameter λ being 0.5, 1 and 1.5, respectively. Because it is a 4-DoF system, four resonant peaks exist in each curve. The nonlinearity is influenced by the mass displacements; therefore, only the first two peaks with relatively high amplitudes exhibit strong bending characteristics with the selected parameters. Similar to Fig. 5.8, the peaks are bent into the high and low frequency ranges with λ=0.5 and 1.5, respectively. When λ= 1, the system can be considered linear. It shows that the NSM can provide a constant negative stiffness when λ=1 without the need for nonlinear analysis. NSM can be applied to diatomic LRAM to achieve a stable constant negative stiffness avoiding the introduction of nonlinearity into the system.

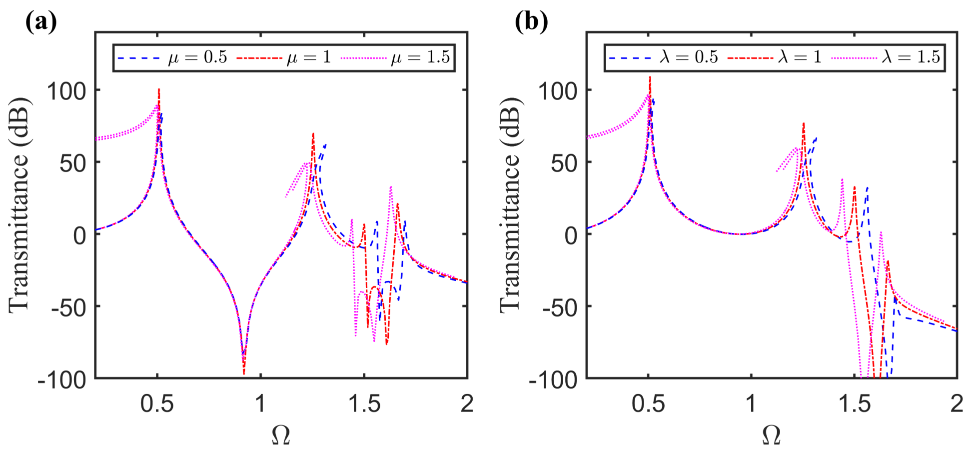

Figure 5.9: Transmissibility diagrams of (a) lumped mass m_1 and (b) lumped mass m_2 in a 4-DoF spring-bar NSM-based system obtained by HB-AFT technique with different geometrical nonlinearity related parameters.

5.3.3 Critical value for negative stiffness

Based on the governing equations for the dispersion relation, the boundaries of the bandgaps can be calculated by setting $\cos(2qL)$ $=\pm1$ in Eq. (5.12). Because the locally resonant bandgap and band-folding bandgaps cannot be merged, and the lower bandgap becomes narrower as it moves to a low frequency, the optimal case is that the lower boundary of the locally resonant bandgap reaches 0. In this case, a bandgap covering a low-frequency range and an additional bandgap covering a high-frequency range were obtained. The ranges of the locally resonant bandgap in the monatomic and diatomic structures are the same, which means that the upper and lower bounds of the locally resonant bandgap can also be obtained by setting $\cos(qL) = \pm 1$ in Eq.(5.13):

$$\omega_{\mathrm{U}} = \sqrt{(k_1 + k_2)(\frac{1}{m_0} + \frac{1}{m_1})}, \tag{5.29}$$

$$\omega_{\mathrm{L}} = \frac{-B - \sqrt{B^2 - 4AC}}{2A}, \tag{5.30}$$

where $A = m_0 m_1$, $B = -(m_0 + m_1)(k_{\mathrm{n}} + k_2) - 4k_0 m_0$, $C = 4k_0(k_{\mathrm{n}} + k_2) + 4k_1 k_2$, ω_{U} and ω_{L} are the frequencies of the upper and lower bounds of the locally resonant bandgap, respectively.

For a linear system, the bandgap location is not affected by external excitation, but only by the material parameters. When ω_{L}, as shown in Eq. (5.30) with ω_{L} being zero, the critical value of the stiffness for the optimal low-frequency bandgap can be calculated. With the same parameters set as $m_1 = 1$ kg,$m_0 = 0.6$ kg, $k_0 = m_1\omega_1^2$, $k_2/k_0 = 0.8$, ω_{L} =0 Hz, the critical value of the effective stiffness ratio can be obtained as $\beta_{\mathrm{n}} = k_{\mathrm{n}}/k_0 = -4/9$.

5.3.4 Wave transmittance and power flow

In Fig. 5.10, the influence of NSM on the dispersion relations is investigated with different values of $\beta_{\mathrm{n}} = -0.2$, -4/9, -0.6 being considered. When $\beta_{\mathrm{n}} = -4/9$, the locally resonant bandgap is located in an ultra-low frequency region, starting from $\Omega = 0$ to $\Omega = 0.84$. The upper band-folding-induced bandgap appears at relatively higher frequencies with the band from 1.38 to 1.68 while the lower band is narrow at approximately $\Omega = 0.59$. With a smaller absolute value of negative stiffness, as shown in Fig. 5.10(a), the locally resonant bandgap moves to a higher-frequency region with a narrower bandwidth, and there are two band-folding bandgaps. The upper one moves slightly higher with almost no variations in width, and the lower one is narrow. If the value of β_{n} increases to -0.6 as presented in Fig. 5.10(c), the locally resonant bandgap will still start from $\Omega = 0$ but the upper bound will be reduced, yielding a narrower bandwidth. The upper bandgap also shifted slightly toward a lower frequency, with a slight change in the width. Overall, the dispersion relation diagrams show that a specific value of effective negative stiffness exists at which the wave attenuation performance of the proposed LRAM configuration is optimal. Therefore, the NSM-based configuration with the optimal stiffness value will be analysed further.

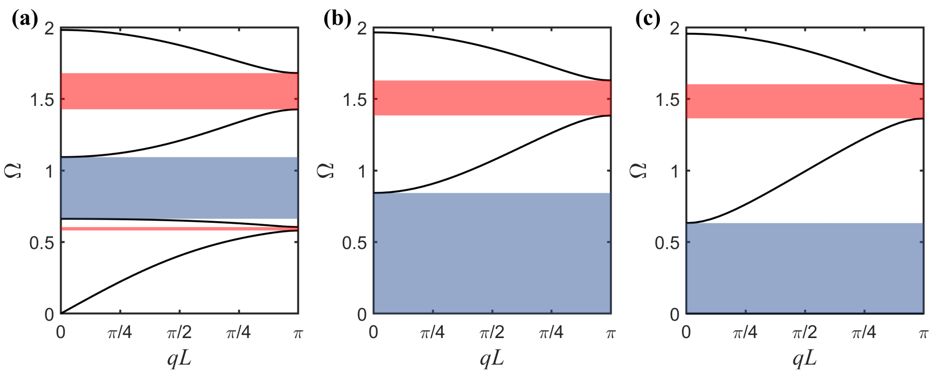

Figure 5.10: Dispersion diagrams of negative stiffness mechanism based diatomic configuration with (a)$\beta_{\mathrm{n}} = -0.2$, (b)$\beta_{\mathrm{n}} = -4/9$, (c)$\beta_{\mathrm{n}} = -0.6$.

In Fig. 5.11, the wave transmittance diagrams of the proposed LRAM with 20- and 50-unit cells with critical negative stiffnesses are depicted. The two clear low transmittance bands were in good agreement with the bandgaps shown in Fig. 5.10. The transmittance is low and stable within the locally resonant bandgap, whereas the vibration suppression performance associated with the upper bandgap improves with an increase in the unit cell number. The results exhibit good potential performance benefits for the inclusion of an NSM in LRAMs to control ultra-lowfrequency waves because the bandgap can theoretically cover frequencies starting from zero.

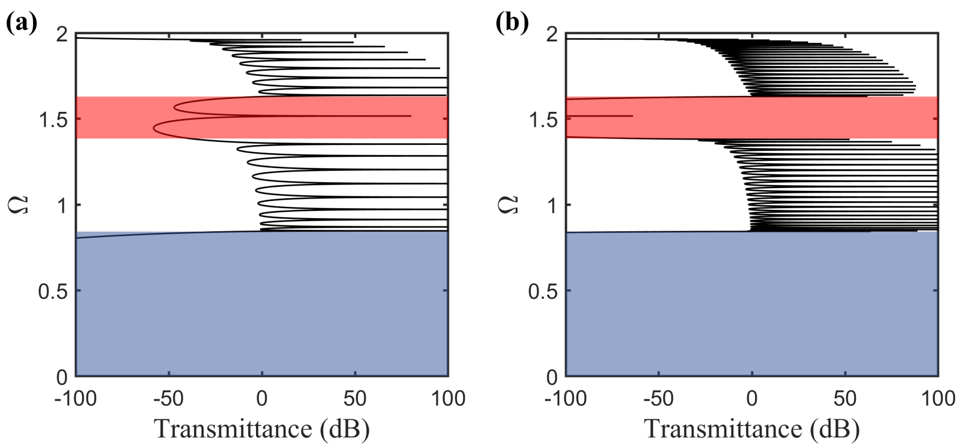

Figure 5.11: Wave transmittance diagram for proposed negative stiffness based diatomic configuration LRAM with (a) 20 unit cells and (b) 50 unit cells.

To examine the effects of the number of unit cells and cell position on the bandgap characteristics, results were obtained and power transmittance diagrams were constructed. In Fig. 5.12(a), the power transmittance, or power transmission ratio is the logarithmic ratio of the time-averaged transmitted power into the last cell to the time-averaged power input into the first cell. The number of cells increases from 0 to 100. This shows that the number of peaks for the power flow increases with the number of cells, which correspondingly leads to an increase in the number of DoFs and resonant frequencies. For comparison, the power transmittance in Fig. 5.12(b) shows the logarithmic ratio of the time-averaged power transmission to different cell positions in a 100-cell structure to the time-averaged power of the first cell. For the power transmittances of the cell positions along the 100-cell system, the peak numbers are almost the same, which is different from the power transmittance of the cell numbers shown in Fig. 5.12(a). Fig. 5.12(a) and (b) are similar to the two bands of blocked power transmission located within the bandgaps shown in the dispersion diagrams. The power transmittance decreased as the number of unit cells and the cell position increased. Fig. 5.12 also shows that it is more difficult to suppress the low-frequency wave, even within the locally resonant bandgap. With approximately 20-unit cells, the proposed LRAM can block most of the energy transmission within the bandgaps with transmittance being lower than - 20 dB.

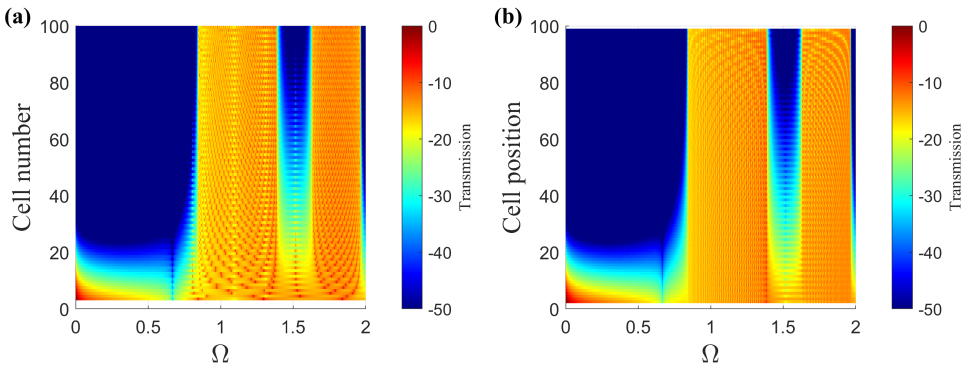

Figure 5.12: Top view of a surface plot of power flow transmittance of the proposed LRAM with critical negative stiffness coefficient investigating the effects of (a) cell number and (b) cell position on bandgap characteristics.

Several studies on LRAMs have not considered the effects of damping. However, physical systems and structures exhibit inherent damping. Here, PFA was conducted to examine the effects of damping on energy transmission and dissipation. Fig. 5.13 shows the time-averaged output power flow and wave transmittances of the proposed diatomic LRAM with damping coefficients varying from 0.002 to 0.05 N/(m/s), respectively. In Fig. 5.13(a), the curves for the three cases have similar varying trends and the frequency locations of peaks and gaps for the cases are the same. When the damping coefficient increased from 0.001 to 0.05 N/(m/s), the peak amplitudes of the time-averaged transmitted power to the last cell were reduced, while there were fewer fluctuations. At low frequencies, small differences existed in the amplitudes of the time-averaged output power of these three cases. The differences become larger with an increase in frequency, suggesting that damping has a greater impact on energy transmission at higher frequencies. The wave transmittance diagram as shown in Fig. 5.13(b) indicates identical bandgaps. As damping coefficients increase, the peak amplitudes are reduced substantially with fewer fluctuations. The effect of damping was significant at high frequencies, where the overall transmittance is evidently decreased. In general, a larger damping coefficient can lead to fewer local variations in the power flow curve without much influence on its overall average power, while it will decrease the overall wave transmittance significantly.

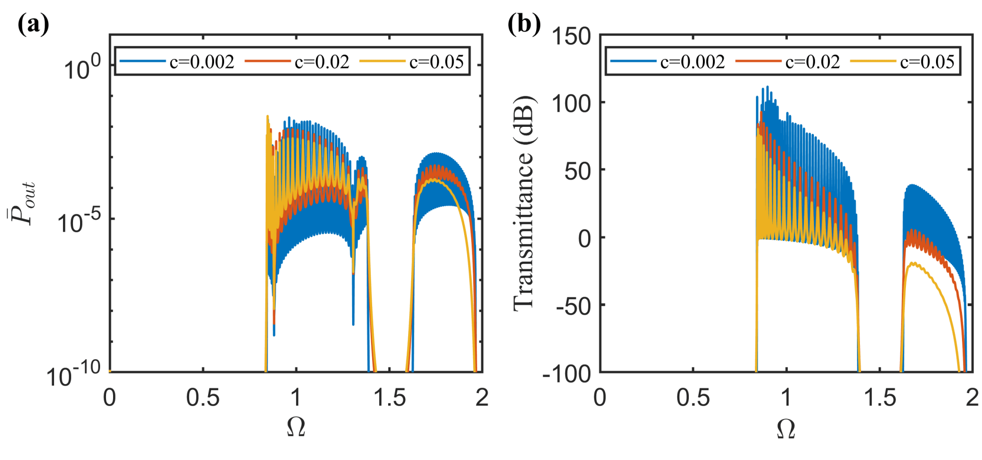

Figure 5.13: Effects of damping coefficients, $c = 0.002$, 0.02, 0.05 N/(m/s), on (a) the time averaged output power flow and (b) the wave transmittances of the proposed LRAM with 50 unit cells.

5.3.5 Influence of material parameters

Here, the influence of the parameters of the diatomic LRAMs on the performance was investigated. A lumped mass distribution in a diatomic configuration induces a band-folding bandgap, and the material parameters are related to the bandgap characteristics. In this section, the total mass of m_1 and m_2 is kept constant. The mass ratio is defined as the proportion of m_1 against the total mass, $\mu = m_1/(m_1 + m_2)$. The influence of the mass ratio on the diatomic LRAM bandgap characteristics is investigated, and the dispersion relation diagrams with $\mu = 0.55$, 0.6, 0.65 are shown in Fig. 5.14(a-c). For these three cases, the ranges of the lower locally resonant bandgaps were the same, from 0 to 0.843. The bandgaps induced by band folding became broader as the mass ratio increased, and the boundaries extended in both directions with corresponding band ranges of 1.432 - 1.552, 1.384 - 1.629 and 1.343 - 1.723, respectively. Therefore, the mass ratio preference for configuration C3 is relatively high mass ratio that does not exceed the limit preferred for diatomic structure designs.

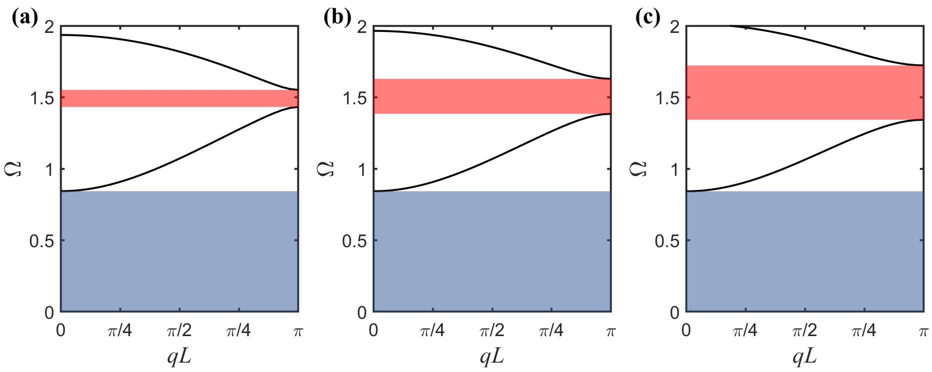

Figure 5.14: The dispersion diagram for the proposed LRAM with critical values of negative stiffness with (a)$\mu = 0.55$, (b)$\mu = 0.6$, and (c)$\mu = 0.65$.

Fig. 5.15 shows the influence of variations in the spring stiffness k_2. Based on Eq. (5.30), stiffness k_2 is related to the lower bound of the locally resonant bandgap. Here, we will keep the lower bound always located at $\omega = 0$ so that the critical value of stiffness β_{n} will be changed simultaneously with $\beta_2 = k_2/k_0$. Fig. 5.15(a-c) show the dispersion relation diagrams for three cases when $\beta_2 = 0.5$, β_{n} =- 0.3333 for Case one, $\beta_2 = 0.8$, β_{n} =- 0.4444 for Case two and $\beta_2 = 1.1$, β_{n} =- 0.5238 for Case three, respectively. The locally resonant bandgap becomes broader with the increase in the absolute values of the stiffness ratios β_2 and β_{n}. Meanwhile, the bandgap induced by upper band folding is shifted to a lower frequency range, but with a narrower bandwidth. The total bandwidths of the two gaps for Cases one, two, and three were 1.042, 1.088, and 1.122, respectively, indicating that the total bandwidth increased with the absolute stiffness ratios.

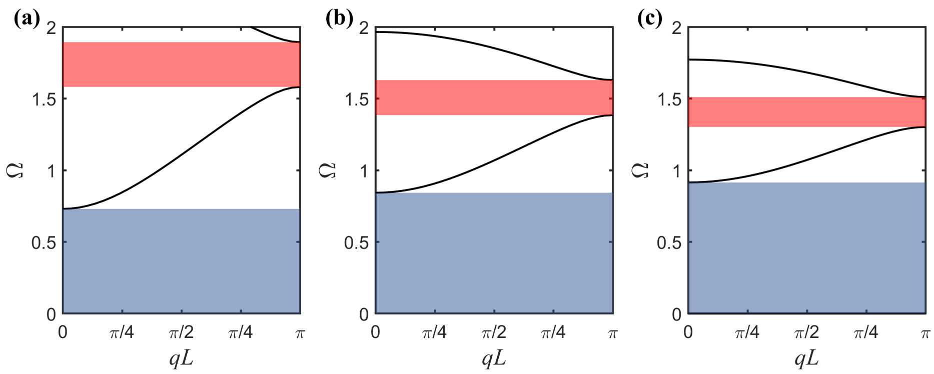

Figure 5.15: The dispersion diagram for the proposed LRAM with critical value of negative stiffness with (a)$\beta_2 = 0.5$, β_{n} = - 0.3333, (b)$\beta_2 = 0.8$, β_{n} =- 0.4444 and (c)$\beta_2 = 1.1$, β_{n} = - 0.5238.

Further investigation of the effects of the stiffness ratios is carried out with results depicted in Fig. 5.16, which shows the top views of the wave transmittance and power flow maps of the proposed diatomic LRAM based on an NSM with 20 unit cells and 50 evenly distributed values of the stiffness ratio β_2 from 0.5 to 2. The two subfigures clearly show low transmittance and bands of blocked power flow. The results matched well with the bandgaps in the case study, as shown in Fig. 5.15. In Fig. 5.16 (a), the transmittance within the locally resonant bandgap is shown in deep blue, whereas that within the upper bandgap is in a slightly lighter blue gradient. With an increase in the absolute value of the stiffness ratio β_2, the lower bandgaps became broader, and the upper band gradually moved toward lower frequencies with a narrower width and better wave attenuation performance. The power flow in Fig. 5.16(b) presents similar bandgaps, while the lower band is in gradient blue and the upper band is in gradient yellow, owing to the difference in the colour map limits. In general, relatively higher absolute stiffness ratios are preferred for diatomic configuration design as the bandgaps are shifted to a lower frequency region with a broader total bandwidth.

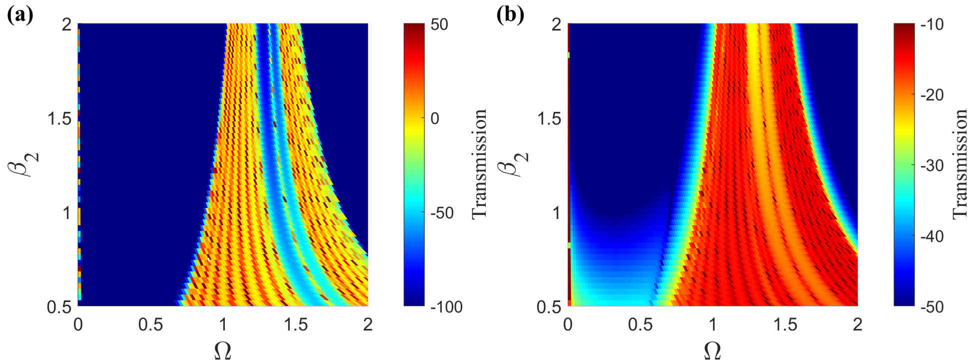

Figure 5.16: The top views of wave transmittance and power flow maps of the proposed NSM-based diatomic LRAM with increasing stiffness ratio β_2 from 0.5 to 2.

5.4 Summary

This study investigated the vibration suppression performance of diatomic LRAMs with negative stiffness mechanisms by using wave transmittance and vibration power flow indices. For the foundational diatomic configuration with the same average mass of the lumped masses, a better wave attenuation ability can be achieved as shown by two additional bandgaps induced by band folding. These bandgaps are located on both sides of the typical locally resonant bandgap. Based on the power flow and wave transmittance analyses, the results show that the vibration attenuation performance of the higher band-foldinginduced bandgap is better than that of the lower band. A satisfactory performance can be obtained by increasing the number of unit cells. Because the locally resonant bandgap is related to the resonant frequency of the resonator, it can be shifted to an ultralow frequency with the use of NSMs. For the proposed NSM-based diatomic LRAM configuration, the following conclusions are drawn:

- The diatomic LRAM configuration can be beneficial by creating two additional Bragg scattering bandgaps located on both sides of the locally resonant bandgap.
- With the application of NSMs on diatomic LRAMs, the lower bound of the locally resonant bandgap can reach zero. The upper bandfolding induced bandgap exists with good wave attenuation performance.
- Based on the power flow analysis, the upper bandgap presents good power blocking ability with a small number of requisite unit cells, which means that the proposed LRAM configuration can yield another low-frequency bandgap compared to the monatomic configuration with little cost.
- Investigations on the influence of material parameters show that a relatively higher diatomic mass ratio and absolute stiffness ratio are preferred for designs, and a relatively larger damping ratio benefits energy dissipation.

This study suggested a new perspective of power flow to analyse the wave attenuation performance, leading to anenhanced understanding of bandgap characteristics. Meanwhile, a diatomic LRAM configuration with negative stiffness was proposed to achieve broadband ultra-lowfrequency vibrations. The PFA method can be used to reveal the performance benefits of introducing negative stiffness or other auxiliary mechanisms to LRAM designs.

Chapter 6

Flexnertia: A novel dissipation mechanism for structural vibration reduction through coupling of flexural motion with an inerter

6.1 Introduction

This chapter focuses on the experimental demonstration of Flexnertia, which is a novel structure for coupling structural flexural motion with an inerter device. Here an arc-shaped metastructure with an integrated inerter device is proposed for the reduction of structural vibration, with an emphasis on flexural motion. The proposed structures have potential applications in vibration suppression of engineering structures such as bridges, buildings, as well as aircraft wings for enhancing the dynamic performance by coupling inerters with a particular vibration mode of structures. According to the D'Alembert's principle, the theoretical inertance of the designed inerter device can be derived and the effective rotational inertia can be calculated based on the inertia equation of classical mechanics of coupled gear systems. The numerical modelling of the Flexnertia structure is verified by finite element (FE) software while a corresponding experimental assembly is firstly designed for testing. The predictions are in excellent agreement with the experimental measurements.

6.2 Arc beam

The schematic diagram for illustrating a finite element in a semicircle beam is shown in Fig. 6.1. Analytical formulation of the equation of motion of the arc beam structure is available and can be used to determine the natural frequencies and mode shapes for forced vibration analysis (Henrych, 1981; Yang et al., 2018). The beam is considered infinitely stiff in shear. The element studied is defined with a small radius angle of θ and the shear, stress and bending moment are presented as V, N, M, respectively. We assume $u(\theta, t)$ and $w(\theta, t)$ as the axial and transverse motion deflection.

The strain of any circumferential fibre in the analysed finite element is shown as

$$\epsilon = \frac{(\mathrm{d}s' - \mathrm{d}s)}{\mathrm{d}s} \approx \frac{1}{R}[w + \frac{\partial u}{\partial \theta} + \frac{z}{R}(\frac{\partial u}{\partial \theta} - \frac{\partial^2 w}{\partial \theta^2}), \tag{6.1}$$

where z is the height of the fibre from the element's central line.

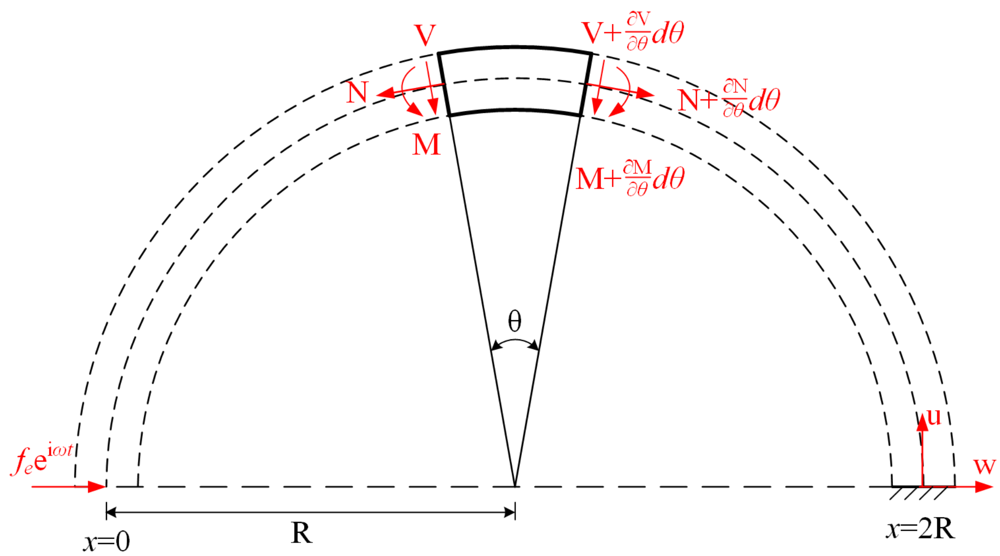

Figure 6.1: Schematic diagram for a finite element of the arc beam.

The stress and bending moment can be presented based on the strain in Eq. (6.1) as

$$N = \int \epsilon E \, \mathrm{d}A = \frac{EA}{R}(w + \frac{\partial u}{\partial \theta}); M = -\int \epsilon E z \, \mathrm{d}A = -\frac{EI}{R^2(\frac{\partial u}{\partial \theta} - \frac{\partial^2 w}{\partial \theta^2})}, \tag{6.2}$$

where E is the Youngs' modulus, A is the cross-section area, I is the second moment of area.

The force balance equation in the circumferential direction is

$$\rho A R \, \mathrm{d}\theta \frac{\partial^2 u}{\partial t^2} = N + \frac{\partial N}{\partial \theta}\mathrm{d}\theta - N + V\frac{\mathrm{d}\theta}{2} + (V + \frac{\partial V}{\partial \theta}\mathrm{d}\theta)\frac{\mathrm{d}\theta}{2}, \tag{6.3}$$

where ρA represents mass per unit length and $R \, \mathrm{d}\theta$ is the small length of the element. It can be simplified to

$$\rho A R \frac{\partial^2 u}{\partial t^2} = \frac{\partial N}{\partial \theta} + V. \tag{6.4}$$

The force balance equation in the radial direction is

$$\rho AR\,\mathrm{d}\theta\frac{\partial^2 w}{\partial t^2} = V + \frac{\partial V}{\partial \theta}\mathrm{d}\theta - V - N\frac{\mathrm{d}\theta}{2} + (N + \frac{\partial N}{\partial \theta}\mathrm{d}\theta)\frac{\mathrm{d}\theta}{2}, \tag{6.5}$$

which can be simplified to

$$\rho AR\frac{\partial^2 w}{\partial t^2} = \frac{\partial V}{\partial \theta} - N. \tag{6.6}$$

Based on the rotational dynamics balance, it can be obtained that

$$M - (M + \frac{\partial M}{\partial \theta}d\theta) - VR\mathrm{d}\theta = 0, \tag{6.7}$$

which can be simplified to

$$V = -\frac{1}{R}\frac{\partial M}{\partial \theta}. \tag{6.8}$$

Substituting Eqs.(6.2) and (6.8) to Eqs.(6.4) and (6.6), the equations of motion of the arc beam can be obtained

$$\rho AR\frac{\partial^2 u}{\partial t^2} = \frac{EA}{R}(\frac{\partial w}{\partial \theta} + \frac{\partial^2 u}{\partial \theta^2}) + \frac{EI}{R^3}(\frac{\partial^2 u}{\partial \theta^2} - \frac{\partial^3 w}{\partial \theta^3}), \tag{6.9a}$$
$$\rho AR\frac{\partial^2 w}{\partial t^2} = -\frac{EA}{R}(w + \frac{\partial u}{\partial \theta}) + \frac{EI}{R^3}(\frac{\partial^3 u}{\partial \theta^3} - \frac{\partial^4 w}{\partial \theta^4}), \tag{6.9b}$$

Based on the boundary conditions, the mode shapes and natural frequencies can be obtained.

6.3 Design of the prestressed metastructure with an integrated inerter

The principal objective of this work is to design and assemble a metastructure which would exhibit high effective inertia for targeted modes of vibration. This pronounced effective inertia should be achieved through minimum added extra mass, thus employing an inerter able to provide a large effective translational inertia through coupling the motion to small rotating masses would seem to be an ideal engineering choice. In this study, gear-based inerters are applied and the friction and backlash problem may occur. We prestress the free end of the arc structure to reduce the influence of backlash. The flexinertia structure allows the use of any type of inerters, such as ballscrew inerter, helical fluid inerter and hydraulic inerter, which are free from backlash problems.

The advantages of employing an inerter for damping out flexural motion in civil structures have been theoretically discussed (Lazar et al., 2014; Giaralis and Petrini, 2017), and it has already been noted that one of the main challenges of employing an inerter is coupling a structural position of low global displacement to a structural position of large global displacement through physical links (e.g. prestressed cables). Structures such as arches and cylindrical panels seem to be ideal for the application of such a design concept as they can provide relatively high displacement between the ends. Pretensioned flat panels can also be appropriate under certain circumstances, while the design could well include a rotating damping device to further enhance motion dissipation. An arc structure (Fig. 6.2) is hereby chosen to demonstrate the proposed Flexnertia structure with the inerter device placed opposite the constrained edge of the structure which implies that the targeted vibrating modes are the ones involving large levels of antidiametrical displacements. It is also of interest to note that by simultaneously physically coupling several structural positions to the inerter, a wider range of structural vibration modes can be damped.

The semi-circle arc structure is made of Aluminium through extrusion and drawing processes with a radius of $r_\mathrm{s} = 45$ cm, a width of $t_\mathrm{s} = 5$ cm and a thickness of $h_\mathrm{s} = 2.3$ mm. The experimental design of the proposed inerter device is shown in Fig. 6.3 while the free body diagram of the proposed arc structure and the schematic diagram of the inerter device are depicted in Fig. 6.4. The housing of the inerter is additively manufactured on a fusion deposition modelling system using Acrylonitrile butadiene styrene (ABS) material. The housing is bonded to one side of the arc structure. The two Φ 6 mm rods are mounted through the housing and their lateral movement is constrained through the use of shaft collars (see Fig. 6.3). The threaded prestressed rod is made of brass. One end of this rod is connected to the free side of the arc structure while the other end is connected to the Φ 6 mm shaft. When motion is induced on the input side of the arc structure, where the prestressed rod is connected, the motion will be transferred through the rod to the inerter mechanism contained within the housing. The gears will then be allowed to move and absorb this motion; performing better than an equivalent attached lumped mass which merely acts in a translational vibration mode.

The calculation of the nominal inertance properties of the designed inerter device (Smith, 2020) can be carried out based on the schematic diagram presented in Fig. 6.4. Assume the mass of long prestressed rod and fixation assembly is m_r, the mass of bracket is m_b, the mass of Φ 60 mm gears is m_g and radius is r_g, the mass of Φ 10 mm pinion is m_p

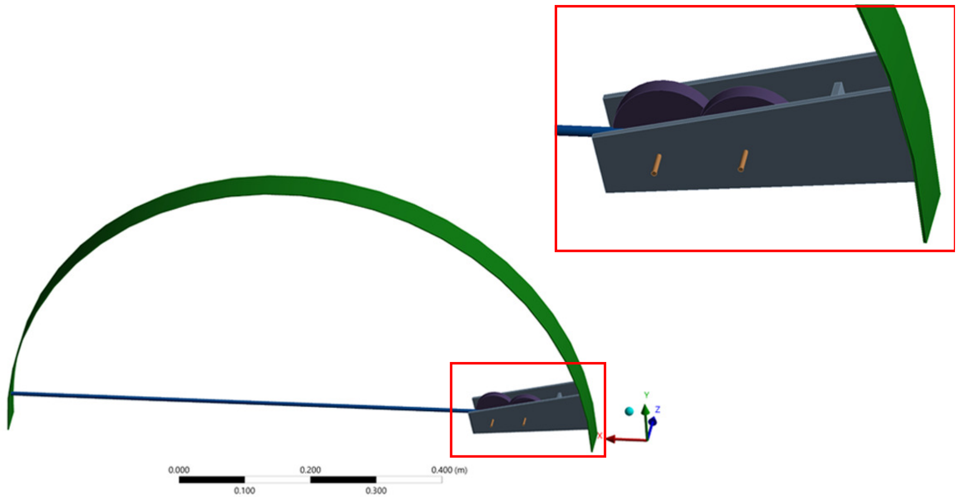

Figure 6.2: Global illustrative of the Flexnertia structure presenting the structure investigation and focusing on the inerter mechanism.

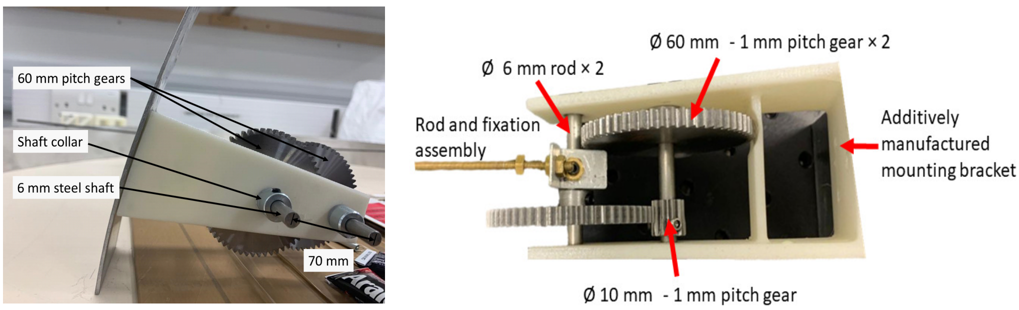

Figure 6.3: Design of the inerter mechanism comprising an assembly of shafts and gears. The ABS housing is bonded to one side of the arc structure while the two rods are mounted through the housing and their lateral movement is constrained through the use of shaft collars. One end of this rod is connected to the free side of the arc structure while the other end is connected to the shaft.

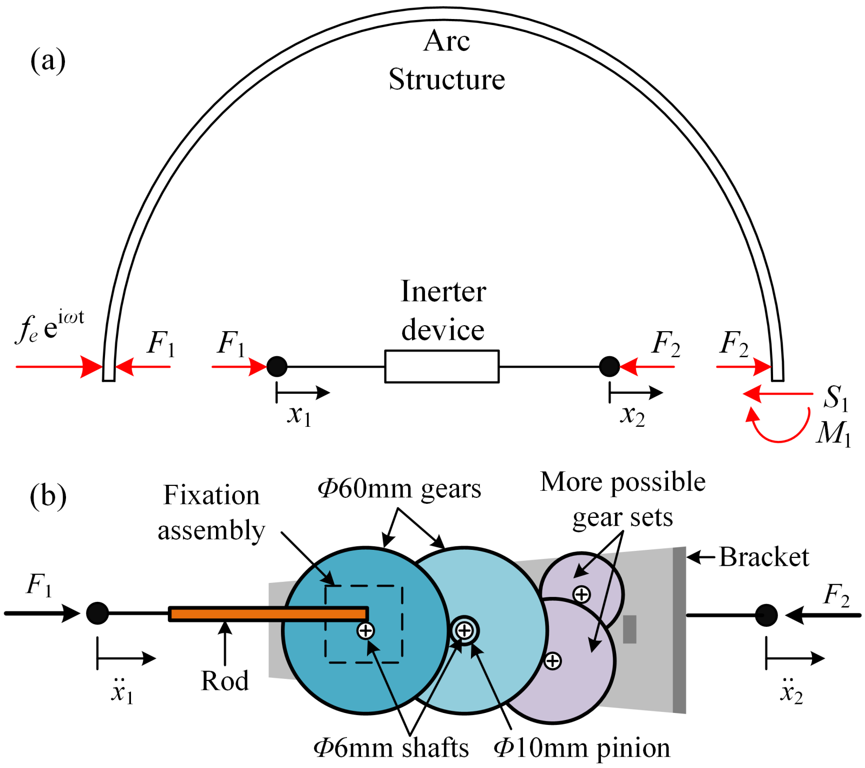

Figure 6.4: (a) The free body diagrams for the arc structure and inerter device. (b) Schematic diagram for the designed inerter device.

and radius r_{p} and the rotational Φ 6 mm shafts have mass m_{s} and radius r_{s}. The angle of rotation θ_0 of the gear assembled with prestressed rod satisfies $\theta_0 r_{\mathrm{s}} = x_2 - x_1$, where x_1, x_2 are the displacements of the left terminal and right terminal, respectively. The Φ 10mm pinion rotates with angle of rotation θ_1 satisfying $\theta_1 r_{\mathrm{p}} = \theta_0 r_{\mathrm{g}}$. The moment of inertia of the gears, pinion and shaft are J_{g}, J_{p} and J_{s}, respectively. If coupled gear systems containing N sets of gears are considered, we define $J_0 = J_{\mathrm{g}} + J_{\mathrm{s}}$ as the total inertia of the components directly activated by the physical connection to the structure and their mass are $m_0 = m_{\mathrm{g}} + m_{\mathrm{s}}$, J_n as the total moment of inertia of the connected components n steps away from the first set of gears (here $J_1 = J_{\mathrm{g}} + J_{\mathrm{p}} + J_{\mathrm{s}}$) and their mass are m_n (here $m_1 = m_{\mathrm{g}} + m_{\mathrm{p}} + m_{\mathrm{s}}$) angle of rotation are θ_n. τ_n is the effective gear ratio of the n_{th} gear set to the first gear set. The influence of the rod fixation assembly and the eccentricity between the rod and the axle of the first gear is small compared with the whole mechanism, so they are neglected in the mathematical formulation. Based on the D'Alembert's principle, assuming infinitesimal displacements δx_1, δx_2, $\delta\theta_1$, $\delta\theta_2$ and $\delta\theta_n$, we can derive the moment balance equation

$$\begin{aligned}
0 &= (F_1 - m_\mathrm{r}\ddot{x}_1)\delta x_1 + (-F_2 - (m_\mathrm{b} + 2m_\mathrm{g} + m_\mathrm{p} + 2m_\mathrm{s} + \sum_{n=2}^{N} m_n)\ddot{x}_2)\delta x_2 \\
&\quad - (J_\mathrm{g} + J_\mathrm{s})\ddot{\theta}_0\delta\theta_0 - (J_\mathrm{g} + J_\mathrm{p} + J_\mathrm{s})\ddot{\theta}_1\delta\theta_1 - \sum_{n=2}^{N} J_n\ddot{\theta}_n\delta\theta_n \\
&= (F_1 - m_\mathrm{r}\ddot{x}_1)\delta x_1 + (-F_2 - (m_\mathrm{b} + m_0 + \sum_{n=1}^{N} m_n)\ddot{x}_2)\delta x_2 \\
&\quad - \frac{1}{{r_\mathrm{s}}^2}(J_0 + \sum_{n=1}^{N}\frac{J_n}{\tau_n^2})(\ddot{x}_2 - \ddot{x}_1)(\delta x_2 - \delta x_1).
\end{aligned} \tag{6.10}$$

Since δx_1 and δx_2 are independent, it can be sorted as

$$F_1 = b(\ddot{x}_2 - \ddot{x}_1) + m_\mathrm{r}\ddot{x}_1, \tag{6.11a}$$

$$F_2 = b(\ddot{x}_2 - \ddot{x}_1) - M\ddot{x}_2, \tag{6.11b}$$

where the inertance $b = (J_0 + \sum_{n=1}^{N} J_n/\tau_n^2)/{r_\mathrm{s}}^2$ and the total mass of the inerter device $M = m_\mathrm{b} + m_0 + \sum_{n=1}^{N} m_n$. The terms $m_\mathrm{r}\ddot{x}_1$ and $M\ddot{x}_2$ in Eqs 6.11(a) and (b) can be considered as two masses m_1 and M directly connected to terminals 1 and 2, respectively, while the remaining inertance part can generate extra ideal inertial force in addition to the physical mass of the device, which is related to the acceleration difference between the two terminals.

It is therefore shown that the inertance is closely related to the total rotational inertia of the gear system, and it can be further expressed as

$$b = \frac{J_{\text{eq}}}{{r_{\text{s}}}^2}, \tag{6.12}$$

in which $J_{\text{eq}} = J_0 + \sum_{n=1}^{N} J_n/(\eta\tau_n^2)$ represents the equivalent total rotational inertia of the system with the consideration of the gear efficiency η. The merit of employing an inerter device is evident out of the expression of J_{eq} which suggests that the effectiveness of a rotational inertia can be multiplied by several orders through such a mechanism.

In our demonstration case study, a single stage referred inertia system is employed with a gear ratio $\tau_1 = r_{\text{p}}/r_{\text{g}} = 1/6$. With the consideration of gear, the total physical mass of the inerter mechanism including the bracket is $M = 0.477$ kg. The inerter arrangement and gear dimensions are shown in Fig. 6.4 with the total inertia of the first set of gears being equal to $J_0 = 7.13 \times 10^{-5}$ kg·m^2 and the equivalent combined total rotational inertia of the inerter being $J_{\text{eq}} = 2.93 \times 10^{-3}$ kg·m^2, thus close to two orders of magnitude higher than the single gear. Then the corresponding theoretical additional inertance can be calculated to be equal to $b = 0.326$ kg, which can yield an effective translational inertia of 0.803 kg.

6.4 Mathematical model analysis

Fig. 6.5(a) shows the structural model comprising a semi-circular arc beam ABC coupled with a horizontal inerter with its two ends attached to points A and C. The initial shape of the beam is a half circle with a radius of R and with point O being the center. The arc beam, made of Aluminium, is with a cross section width of W and a thickness of h . The beam is fixed at the end point C while the other end, point A, is subjected to a horizontal external force of amplitude f_e and frequency ω.

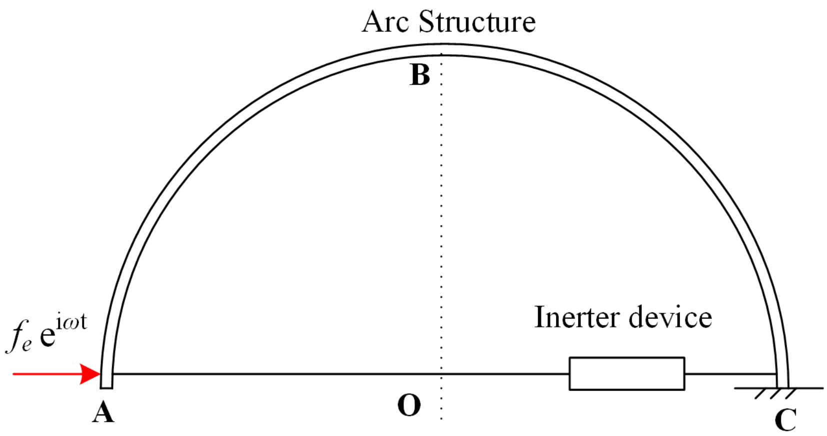

Figure 6.5: Schematic diagram for a semi-circular arc structure model with horizontal inerter mechanism connecting both ends. The beam is fixed at the end point C while the other end, point A, is subjected to a horizontal external force of amplitude f_e and frequency ω.

6.4.1 Power flow analysis and dynamic properties of individual components

Power flow analysis (PFA) is a widely accepted method to study vibration describing the dynamic behaviour of coupled systems and complex structures (Xing and Price, 1999; Xiong et al., 2003). PFA, which provides a new perspective for dynamic analysis and new indices to evaluate structural dynamic characteristics performance (Liu et al., 2022c). The instantaneous input power p_{in} is defined as the product of the excitation force $\tilde{f}_e$ and the velocity $\tilde{v}_{\text{A}} = \mathrm{i}\omega\tilde{u}_{\text{A}}\mathrm{e}^{\mathrm{i}\omega t}$ of the excitation point A. Then the time averaged input power flow can be further derived as (Goyder and White, 1980; Xiong et al., 2001; Yang et al., 2016):

$$\overline{p}_{\text{in}} = \frac{1}{2}\Re(\tilde{f}_e\tilde{v}_{\text{A}}^*) = \frac{1}{2}\Re(\tilde{f}_{\text{e}}^*\tilde{v}_{\text{A}}) \tag{6.13}$$

where $(\bullet)^*$ denotes the operation of taking complex conjugate.

The point receptance function, $\tilde{\beta}$, relating the complex amplitude of the horizontal displacement of the excited point A of the arc beam to the amplitude of a harmonic excitation is (Zhu et al., 2021b)

$$\tilde{\beta} = \sum_{j=1}^{N} \frac{(\phi_j)_e(\phi_j)_r}{m_j(\omega_j^2 - \omega^2)} \tag{6.14}$$

where j stands for the j-th mode; ϕ_j and ω_j represent the mode shape and the corresponding natural frequency, respectively, which can be calculated based on Appendix 6.2; N denotes the highest mode taken into consideration; m_j is the modal mass; the subscript e and r denote the excitation point and the response point, respectively. Note that for simple structure, it may be possible to obtain the mode shapes and natural frequencies analytically. For complex structures, the finite element analysis is performed to obtain the receptance function. For the current system, the excitation point and the interested response point are both taken as point A and thus they coincide.

For the horizontally embedded inerter of inertance b, we have the following relationship between the applied force by the arc beam with complex amplitude $\tilde{f}_{\mathrm{b}}$ and the relative acceleration $\tilde{u}_{\mathrm{A}}$

$$f_{\mathrm{b}}(t) = \tilde{f}_{\mathrm{b}}\mathrm{e}^{\mathrm{i}\omega\mathrm{t}} = b\frac{\mathrm{d}^2(\tilde{u}_{\mathrm{A}}\mathrm{e}^{\mathrm{i}\omega t})}{\mathrm{d}t^2} = -\omega^2 b\tilde{u}_{\mathrm{A}}\mathrm{e}^{\mathrm{i}\omega t}, \tag{6.15}$$

from which we have $\tilde{f}_{\mathrm{b}} = -\omega^2 b\tilde{u}_{\mathrm{A}}$, where $\tilde{f}_{\mathrm{b}}$ and $\tilde{u}_{\mathrm{A}}$ are positive pointing to the right.

6.4.2 Vibration analysis based on a substructure method

Obtaining a complete analytical solution of the dynamic response is challenging for complex structures. The finite element method (FEM) is a widely used method for analysing vibration properties, but its computational cost is often much higher than that associated with analytical or theoretical methods for complex structures, especially for an inerter mechanism-based model. The substructure method can keep the advantages of both FEM and theoretical methods, and it has been applied for investigating the dynamic characteristics of integrated systems (Zhu et al., 2021b; Wang et al., 2002b,a). The main idea of the substructure method is to divide a complete system into two or more subsystems, each of which can be solved using an appropriate analytical method, including experimental, analytical and numerical methods. Based on the force balance and displacement continuity conditions, the coupling force and displacements can be solved to further investigate the dynamic characteristics of the integrated structure.

Here the substructure method is used to investigate inerter based arc beam structure. For this, the system is divided into two substructures. Substructure I is the arc beam structure and substructure II is the inerter device. For the inerter device, the relationship between the interaction forces and the relative acceleration between two terminals can be expressed analytically as shown by Eq. (6.15).

For the arc beam without the inerter, the receptance function shown by Eq. (6.14) can be firstly obtained using FE analysis. The complex amplitude of the total applied at point A of the arc beam is

$$\tilde{f}_1 = \tilde{f}_e - \tilde{f}_{\mathrm{b}} = \beta \tilde{u}_{\mathrm{A}}, \tag{6.16}$$

where $\tilde{f}_{\rm b}$ is the complex amplitude of the force applied by the inerter to the arc beam. By using Eqs.(6.15) and (6.16), the following relationship is established:

$$\tilde{f}_e = (\beta - b\omega^2)\tilde{u}_{\rm A}. \tag{6.17}$$

Therefore, the complex amplitude of the displacement response at point A is

$$\tilde{u}_{\rm A} = \frac{\tilde{f}_e}{(\beta - b\omega^2)}. \tag{6.18}$$

For comparison and method verification, a more complex device can be considered, replacing the inerter device in Fig.1. For this complex device, a spring with stiffness coefficient k and a damper with damping coefficent c are configured in parallel with the inerter. Following the substructure method, the response at point A would become

$$\tilde{u}_{\rm A} = \frac{\tilde{f}_e}{(\beta + k + {\rm i}\omega c - b\omega^2)}. \tag{6.19}$$

6.4.3 Results and discussion

Here parameter studies are carried out to demonstrate the use of the theoretical and numerical analysis methods. A sine excitation force of amplitude 3 N and frequency ranging from 0 Hz to 450Hz is applied horizontally to the free end. The 2-node Beam 188 linear element based on Timoshenko beam theory, which is a first-order shear-deformation theory, is used in ANSYS FEM with a shear correction factor of 5/6. The shear locking phenomenon may occur when the Timoshenko beam is applied to very thin beam structures (Rakowski, 1990; Hernández and Vellojin, 2021). The reduced integration technique is one of the most commonly used methods to solve the shear locking problem (Heyliger and Reddy, 1988). In this study, the proposed structure is a Aluminium semi-circle arch with the radius of $r_\mathrm{s} = 45$ cm, the width of $t_\mathrm{s} = 5$ cm and the thickness of $h_\mathrm{s} = 2.3$ mm. As the thickness to the length ratio of the arc beam is not too small, no shear locking phenomenon is observed in numerical FE simulations. The arc structure is discretised into a total number of 50 elements.

By FEM modelling, the response of a spring-based arc structure without inerter can be obtained with relatively low computational cost. The response results obtained by analytical calculation and FEM can be compared to verify the substructure method. The free end horizontal displacements of the arc structure with and without spring connecting both ends obtained by analytical calculation in Eq. (6.19) and FEM are plotted in Fig. 6.6, and here no inerter is considered. The black solid line indicates the response of the arc structure without spring obtained by FEM, while the dash-dotted lines and circles are the results of spring attached structures obtained by FEM and analytical calculation, respectively. Different colours represent the cases with different stiffness coefficients, where blue, red and pink are k=5,20,50 N/mm. It can be seen from the results that the results of the theoretical calculation based on the substructure method are consistent with the results obtained from using a full finite element model, which verifies the correctness of the substructure method.

The responses of arc structure with inerter device can be further obtained by substructure method based on Eq. (6.18), which are plotted in Fig. 6.7(a). It shows that as inertance increases, the peaks move to lower frequencies while the gap frequencies remain the same. Especially with a large inertance, the peak amplitude is reduced, and the frequency range is narrower. Moreover, the dynamic response is much reduced, indicating good vibration control performance of the inerter device-based arc

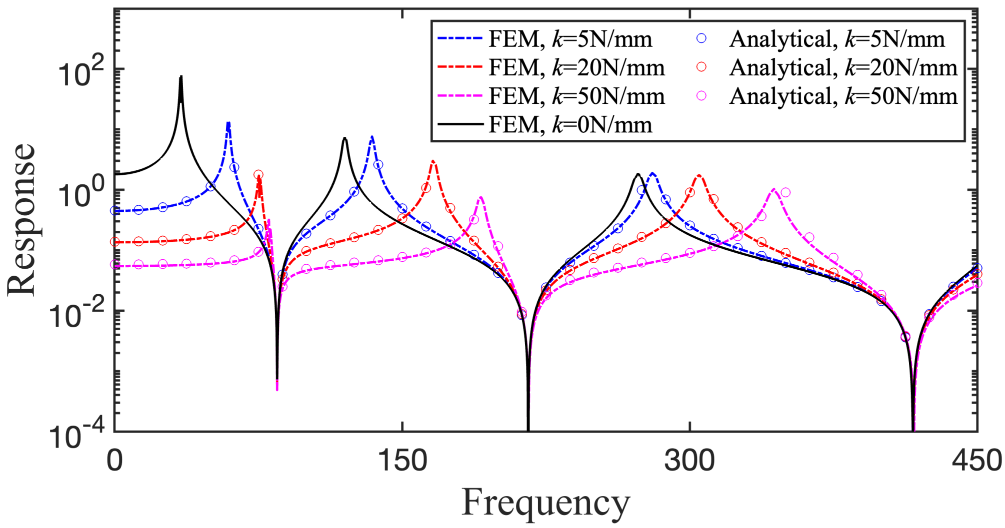

Figure 6.6: Responses of arc structure obtained by analytical calculation and FEM. The black solid line indicates the response of the arc structure without spring obtained by FEM, while the dash-dotted lines and circles are the results of spring attached structures obtained by FEM and analytical calculation, respectively.

structure.

The response diagram for the spring-inerter-based arc structure is plotted in Fig. 6.7(b). The blue, red and pink dash-dotted lines represent the cases with different stiffness coefficients $k = 5, 20, 20$ N/mm and inertance $b = 0.001, 0.001, 0.005$ kg. It shows that the increase of k can move the peaks to higher frequencies and reduce the peak amplitude but the effect decreases as the excitation frequency rises. The response at quais-zero frequency is also reduced while the change of inertance will not influence the zero-frequency response. As observed from Figs. 6.7(a-b) and a lot of other research (Dai et al., 2022b; Wagg, 2021) also showed that, a larger inertance can shift the peaks to lower frequencies with lower amplitudes. The attached spring-inerter device can provide excellent vibration suppression performance to the host arc structure.

The damper is a vital element for providing energy dissipation mech-

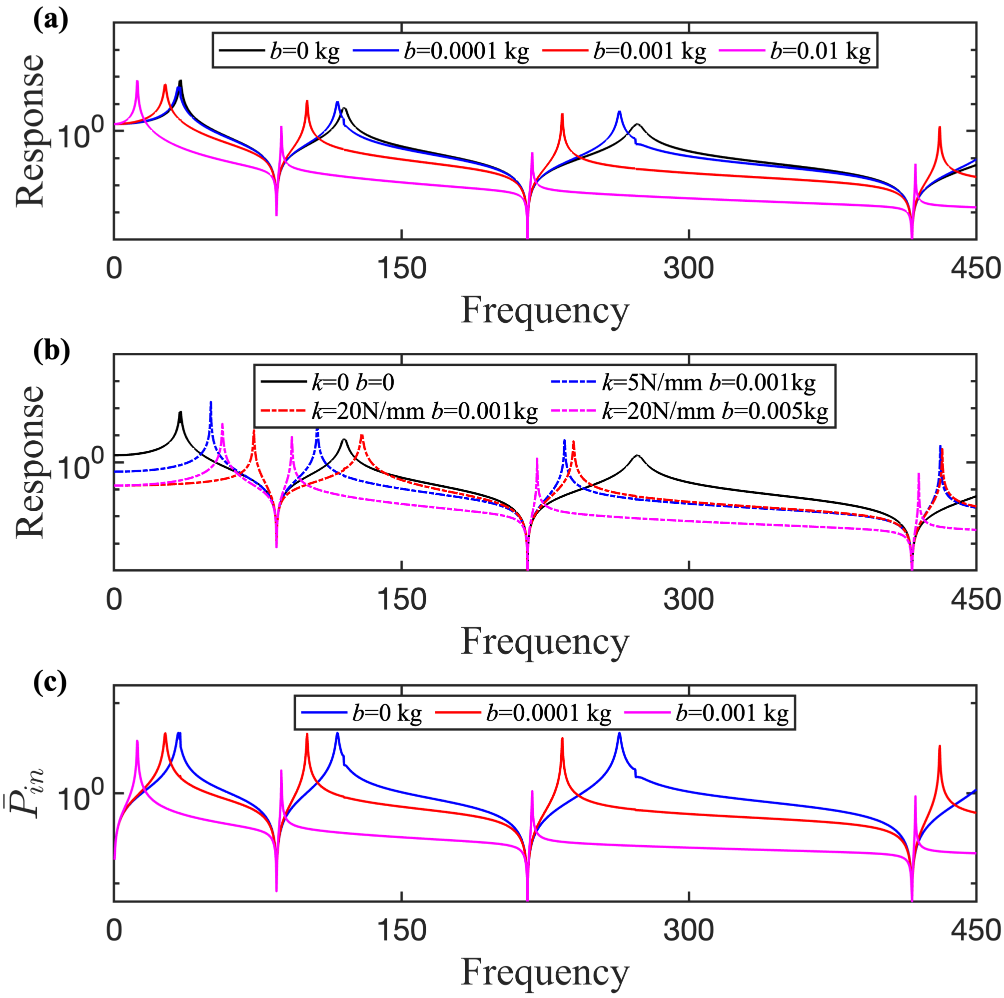

Figure 6.7: (a)Responses of arc structure with and without an inerter device calculated by substructure method. The black, blue, red and pink solid lines represent the cases with inertance of 0, 0.0001, 0.001 and 0.01 kg, respectively. (b)Responses of arc structure with a spring and an inerter device calculated by substructure method. The black solid line represent the inerter deactivated case while the blue, red and pink dash-dotted lines represent the cases with different stiffness coefficient $k = 5, 20, 20$ N/mm and inertance $b = 0.001, 0.001, 0.005$ kg. (c)Power flow of the arc structure with the spring-damper-inerter device. The blue, red and pink solid lines represent the cases with inertance of 0, 0.0001 and 0.001 kg, respectively.

anism and its effects can be demonstrated directly using power flow analysis. Here a damper of damping coefficient $c = 2$ N/(mm/s) and spring of stiffness coefficient of $k = 5$ N/mm is considered in the spring-damper-inerter-based arc structure, whose power flow is shown in Fig. 6.7(c). It indicates that, under the same excitation, the integrated structure with a larger inertance has less energy flowing in, which means there is an energy block band for vibration control.

6.5 Manufacturing, assembly and test setup

The experimental assembly of the arc-shaped metastructure of the Flexnertia structure with energy absorption mechanism is shown in Fig. 6.8. An optical table is used to mount the dynamic shaker and the arc structure. The end of the arc structure with the inerter mechanism is clamped to the table while the other end is allowed to move freely. The dynamic shaker (Modal Shop 2050) is connected to the free side of the arc structure to induce horizontal movement. An impedance head (PCB model 288D01) is introduced between the shaker and the arc mechanism to measure the force at the input side of the setup. The impedance head has a range between 1 Hz to 5000 Hz and a sensitivity of 22.4 mV/N. An accelerometer (PCB 352C65) is attached to the middle top of the arc mechanism. The accelerometer has a frequency range from 0.5 Hz to 10 kHz and a sensitivity of 10.2 mV/(m/s^2). A chirp wave was generated for each test using a proprietary computer software while triggering and data collection was done through a Polytec VIB-E-400 junction box.

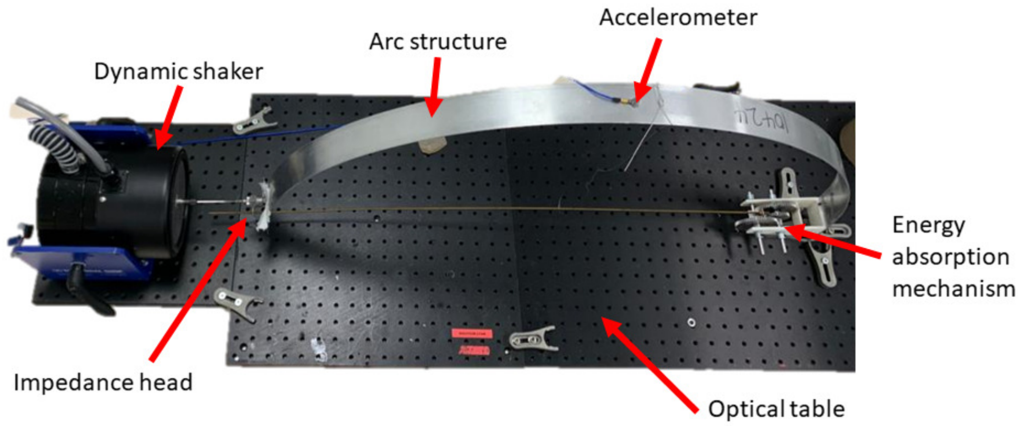

Figure 6.8: Experimental assembly of the arc metastructure comprising the integrated inerter device. The end of the arc structure with the inerter mechanism is clamped while the other end is free. The shaker is connected to the free side to induce horizontal movement

6.6 Discussion on experimental and numerical results

Numerical modelling of the proposed design of the Flexnertia structure was performed through a full finite element approach using the ANSYS© software. As with the experimental study, the case where the inerter is decoupled from the vibrating end of the arch (labelled as 'No mechanism' in Fig. 6.9) is compared against the case where the rotational inertia is activated and coupled to the flexural motion of the structure. A nonlinear analysis is done for the prestressed structure in two stages. A pretensioning load is initially applied in 100 steps of equal displacement to prestress the free end of the master structure from its initial position to $d_{\text{prest}} = 12$ mm (as done in the experimental study). Then the steady-state harmonic analysis is performed in steps of $f_{\text{resol}} = 1$ Hz with the imposed displacement applied on the free end of the arc with an amplitude of $A_{\text{oscil}} = 3$ mm around the prestressed equilibrium point. A total of 20 loading cycles is imposed on the structure in order to ensure that it reaches its steady state before the frequency response is computed using Welch's approach by taking into account the steady-state range of the transient signature at each input frequency.

Diagrams of experimental and numerical acceleration-to-force ratio versus frequency are presented in Fig. 6.9, expressed on a logarithmic scale while the y-axis represents the degrees. The experimental results are shown with black and red solid lines indicating the activated and deactivated inerter device, respectively. The deactivated system still carries the inerter device so it has the same mass as the activated system. When the inerter device is deactivated, the acceleration over force increases with the excitation frequency and it is relatively stable at around a response value of 2 between 10 Hz to 100 Hz. Some peaks with low amplitude are observed around 10 Hz, 18 Hz, 27 Hz, 60 Hz and 80 Hz. These are usually associated with resonance modes of the arc structure. The results of the activated inerter have an average overall response value far below 2. Some resonances shown at 20 Hz, 38 Hz, and 80 Hz took the response to above 2. The 10 Hz resonance of the deactivated system is damped out in the activated mechanism. The most noticeable behaviour of the activated mechanism is its extreme attenuation capabilities below 20 Hz in comparison to the deactivated mechanism. This indicates that the inerter device can achieve good vibration suppression performance, covering multiple modes of the arc metastructure.

The activated mechanism can suppress waves of different frequencies with different effects. Excellent vibration control ability is shown at frequencies between 50 Hz and 70 Hz while weak effects are observed in some narrow frequency bands near 20 Hz and 40 Hz. More importantly, the wave in the frequency band from 5 Hz to 20 Hz is clearly attenuated, which indi-

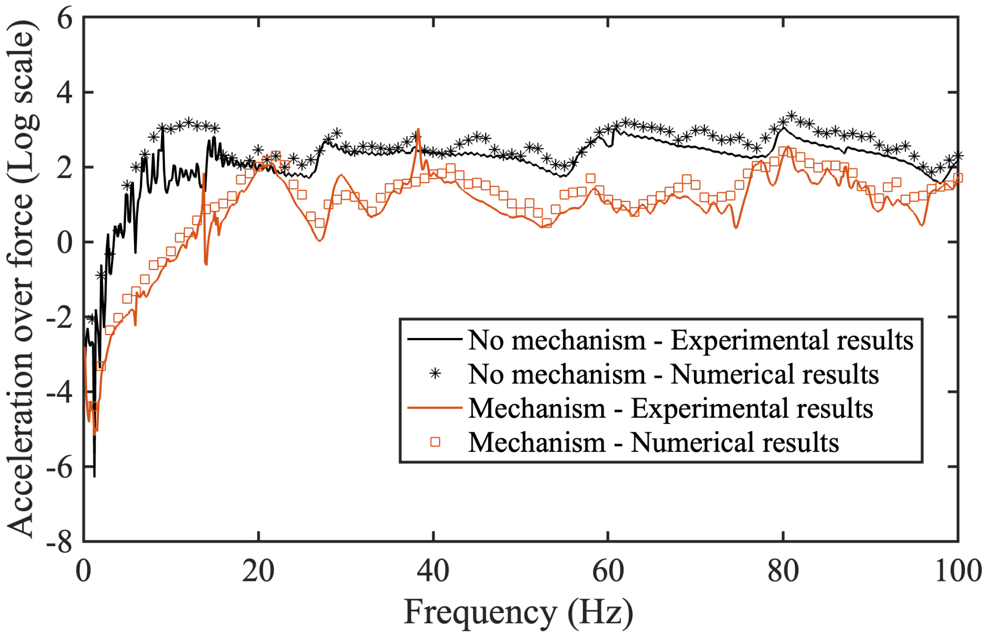

Figure 6.9: Logarithmic experimental and numerical results for the metastructure having the inerter deactivated (black) and activated (red). The activated and deactivated systems have exactly the same mass. The solid lines are the experimental results while the black asterisks and the red squares are the numerical results calculated through a nonlinear finite element analysis for the prestressed structure. The steady-state harmonic analysis is performed in steps of $f_{\text{resol}} = 1$ Hz with the imposed displacement applied on the free end with an amplitude of $A_{\text{oscil}} = 3$ mm.

Table 6.1: Amplitude percentage reduction of the numerical results between the deactivated and activated inerter based structures for specific frequencies.

Frequency (Hz)	10	20	30	40	50	60	70	80	90	100
No mechanism	20.3	11.7	12.8	11.0	9.9	20.3	19.5	24.5	16.6	10.0
Mechanism	0.8	7.4	3.5	6.0	2.2	3.1	4.6	11.2	4.0	5.5
Amplitude reduction(%)	96.2	36.7	73.0	45.0	77.8	84.8	76.5	54.3	76.0	44.5

cates its effect is not weakened in the low-frequency band. The amplitude percentage reduction of the numerical results between the deactivated and activated inerter based structures for specific frequencies is listed in Table 6.1. The activated inerter device shows a good amplitude reduction performance. In general, the application of the inerter device reduces the acceleration-to-force ratio of the proposed arc metastructure by 0.5 on a logarithmic scale, demonstrating the potential for application in vibration control.

The numerical results are depicted in Fig. 6.9 and the black asterisks and the red squares represent the systems with activated and deactivated inerter device, respectively. The acceleration and force are measured horizontally at the moving end of the structure where the shaker is attached. Although the excitation settings for experimental and numerical analysis are slightly different, which are swept sines and multiple sines, a good agreement can be observed from the comparisons between the results depicted. For the experimental result with inerter device, a small peak and drop can be observed, which is not shown in numerical results. This may be resulted from a more complex set-up in the experiment than in the numerical model. Error may also originate from the effect of friction and backlash of inerter device influencing the experimental result. The numerical results are more intuitive to show the wave attenuation ability of inerter device by smooth curve. It presents the effects over almost all frequencies except for a narrow band around 18 Hz and it is remarkable at the lower frequencies. This attenuation performance is even better than that shown between 40 Hz to 100 Hz. For the proposed inerter based arc metastructure, the experimental and numerical results analysis can be mutually verified, suggesting that the inerter has good prospects for vibration control in theory and exhibits excellent performance in practical applications.

The proposed Flexertia structural concept has the potential to be applied to the design of engineering structures, such as bridges and aircraft wings, by coupling inerter with one of the interested modes of vibration.

With further advances in manufacturing technologies, particularly additive manufacturing, these interer devices can made in smaller macroscales to fit within various mechanical systems, which is also potential for the periodical metamaterial design.

6.7 Summary

This study investigated the advantages and limitations of the Flexnertia design structure, which involves coupling the structural flexural motion of a structure to an integrated inerter device. The theoretical analysis based on the substructure method exhibits the vibration suppression performance of inerter based arc structure. The research on inerters is mature so the inertance and effective rotational inertia of the rod-and-pinion device can be deduced in a straightforward manner. The experimental test is carried out to demonstrate the vibration attenuation performance of this structure. The experimental work shows very similar results compared to the numerical results obtained from the nonlinear FE modeling, indicating that the numerical and experimental results are in good agreement and can be verified against each other. The most obvious finding to emerge from this study is that the average overall response of the metastructure is much lower with the activated inerter device than that of the deactivated system. Moreover, the beneficial effect is predominant in the low-frequency band, demonstrating good potential for practical application in cases where constrained damping layers are inactive and tuned mass dampers are too heavy. With further development of manufacturing technologies especially additive manufacturing, inerter devices of smaller scales and customised properties and packaging can be fabricated to fit a large variety of mechanical systems.

Chapter 7

Enhanced suppression of vibration response and power transfer by tailoring contact hysteresis friction

7.1 Introduction

This study explores enhanced vibration transfer suppression and power dissipation based on a coupled structure employing a nonlinear friction damper. The main difference of this study compared to previous studies on friction dampers is the tailoring of vibration energy transfer by exploiting hysteresis friction properties. The dynamical characteristics of the proposed structure are investigated from a new perspective of considering vibration power flow as a performance index, not restricted to displacement response and force transfer.

A bilinear hysteresis model based on Jenkins element is considered for the friction damper model. The study starts by describing the theoretical calculations and linearization methods on the basis of an SDoF system, and then develops a 2-DoF coupled structure. Combining phase diagrams, time and frequency domain responses to analyse the nonlinear vibration and the effect of maximum displacement versus critical slip displacement on the dynamic behaviour of the system. The effect of the parameters of the friction damper on the vibration attenuation is also discussed. The results show the friction damper dissipates energy only in the frequency band around the natural frequency of the system, resulting in high amplitude vibration attenuation. The friction damper based coupled systems are flexible and the capacity can be modified for different vibration control purposes. The rest of the article is organised as follows. Section 7.2 describes the hysteresis friction damper. The SDoF system with a bilinear hysteresis friction damper and its mathematical model is shown in Sec. 7.3, together with the linearization of the hysteresis and theoretical calculation. In Sec. 7.4, the 2-DoF coupled structure with friction damper is studied assisted by power flow and wave transmittance analysis. The conclusions of the present study are given in the last section.

7.2 Hysteresis friction damper

Figure 7.1 depicts the schematic diagram of a hysteresis friction damper and the corresponding force-displacement relationship. The friction damper is presented by a macro-slip element with static stiffness, k_{s}, and an element comprising a spring of kinetic stiffness, k_{n}, and a dry friction element with slip force, $\mu_{\mathrm{f}} f_{\mathrm{n}}$, in series. When the dry friction damper starts to move from rest, the pre-sliding stiffness is (k_s+k_n). Assuming it is anticipated to begin slipping when the relative displacement between interfaces in a particular direction surpasses a critical threshold, which is associated with the slip force of the Coulomb slider, then only static stiffness, k_s, is involved. Sticking occurs when the direction of relative motion is reversed, during which time the pre-sliding stiffness is $(k_s + k_n)$. Repeating the above movement, i.e. the relative displacement exceeds a specific sliding threshold, sliding starts again, during which only static stiffness, k_s, is engaged.

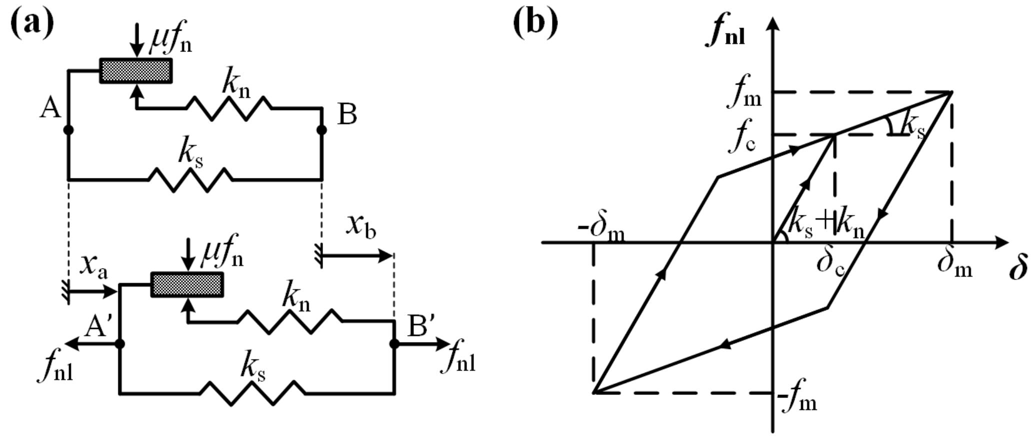

Figure 7.1: (a) Schematic diagram of the nonlinear hysteresis friction damper. (b) Bilinear hysteretic force-displacement relationship of the dry friction damper.

The corresponding restoring force is mathematically expressed as (Huang et al., 2018)

$$f_{\mathrm{nl}}(\delta,\dot{\delta}) = \begin{cases} (k_{\mathrm{s}}+k_{\mathrm{n}})\delta + \mathrm{sgn}(\dot{\delta})k_{\mathrm{n}}(\delta_{\mathrm{m}}-\delta_{\mathrm{c}}), \\ \text{when} \quad \delta_{\mathrm{m}} - 2\delta_{\mathrm{c}} \leq -\mathrm{sgn}(\dot{\delta})\delta < \delta_{\mathrm{m}}; \\ k_{\mathrm{s}}\delta + \mathrm{sgn}(\dot{\delta})k_{\mathrm{n}}\delta_{\mathrm{c}}, \\ \text{when} \quad -\mathrm{sgn}(\dot{\delta})\delta \leq \delta_{\mathrm{m}} - 2\delta_{\mathrm{c}}, \end{cases} \tag{7.1}$$

where f_{nl} denotes the restoring force of the friction damper, $\delta = x_{\mathrm{b}} - x_{\mathrm{a}}$ denotes the relative displacement between interfaces, δ_{m} is the maximum displacement, δ_c is the critical slip displacement, $\delta_c = \mu_f f_n / k_n$, μ_f is the coefficient of friction, f_n is the normal force applied, and $\mathrm{sgn}(\bullet)$ represents the sign function.

7.3 SDoF system with nonlinear hysteresis friction damper

In this section, the influence of the inclusion of a hysteresis friction element in a Single-DoF system is investigated. Figure 7.2 provides a schematic diagram of an SDoF system with a viscous damper describing the inherent viscous damping of the mechanical system and a grey box representing the hysteresis nonlinear friction damper as shown in Fig. 7.1. The implementations of different friction dampers have been presented in different research (Paronesso and Lignos, 2021; Qiu et al., 2022; Lee et al., 2016). Based on the conventional friction damper, piezoelectric actuators can be assembled with bolts to control the normal force applied to it.

The investigated system is a mechanical system so the harmonic force excitation is considered. The lumped mass m subjected to an external force with amplitude f and frequency ω, is connected to the left fixed base by a viscous damper of damping coefficient c and a hysteresis friction damper. The lumped masses move horizontally without considering the friction with the horizontal base. The absolute displacement of lumped mass is x and $x = 0$ is considered to be the static equilibrium position.

The equation of motion for the corresponding model is

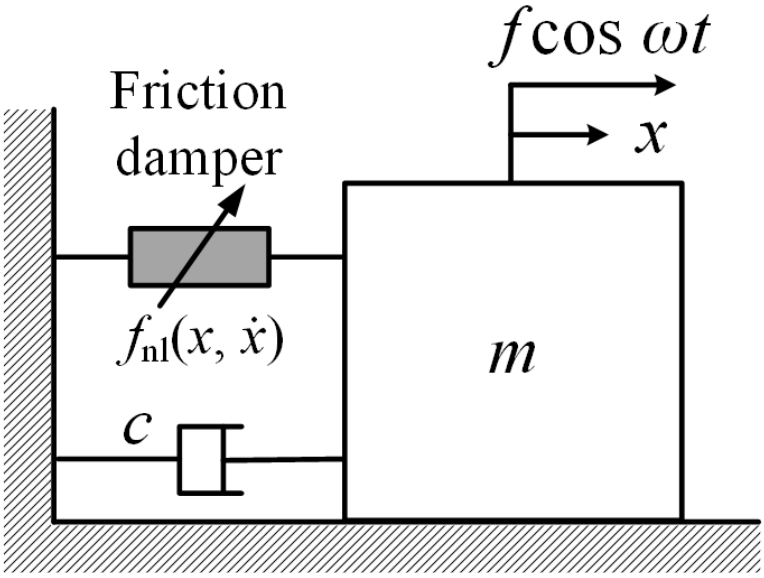

Figure 7.2: Schematic diagram of the SDoF structure with a nonlinear hysteresis friction damper and a viscous damper.

$$m\ddot{x} + c\dot{x} + f_{\mathrm{nl}}(x, \dot{x}) = f\cos\omega t, \tag{7.2}$$

where the overdot $(\dot{\bullet})$ is the derivative with respect to time and the f_{nl} denotes the nonlinear dry friction force.

To better analyse the model, non-dimensional variables and parameters are introduced as

$$\begin{aligned} &X = \frac{x}{l}, X_{\mathrm{m}} = \frac{x_{\mathrm{m}}}{l}, X_{\mathrm{c}} = \frac{x_{\mathrm{c}}}{l}, F_0 = \frac{f}{k_{\mathrm{s}} l}, \omega_0 = \sqrt{\frac{k_{\mathrm{s}}}{m}}, \\ &\Omega = \frac{\omega}{\omega_0}, \tau = \omega_0 t, \zeta = \frac{c}{2m\omega_0}, \beta = \frac{k_{\mathrm{n}}}{k_{\mathrm{s}}}, \end{aligned} \tag{7.3}$$

where X, X_{m} and X_{c} represent the nondimensional absolute, maximum and critical slip displacement of lumped mass m; F_0 denotes the nondimensional amplitude of excitation force; ω_0 is the undamped natural frequency of the system; Ω and τ are the nondimensional excitation frequency and time, respectively; ζ and β are the nondimensional damping ratio and stiffness ratio, respectively.

The equation of motion in Eq. (7.2) can be further nondimensionalised as

$$X'' + 2\zeta X' + F_{\mathrm{nl}}(X, \dot{X}) = F_0 \cos \Omega\tau, \tag{7.4}$$

where the primes $(\bullet)'$ denote differentiation with respect to τ and the nondimensional restoring force updated from Eq. (7.1) is

$$F_{\mathrm{nl}}(X, X') = \begin{cases} (1+\beta)X + \mathrm{sgn}(X')\beta(X_{\mathrm{m}} - X_{\mathrm{c}}), \\ \text{when} \quad X - 2X_{\mathrm{c}} \le -\mathrm{sgn}(X')X < X_{\mathrm{m}}; \\ X + \mathrm{sgn}(X')\beta X_{\mathrm{c}}, \\ \text{when} \quad -\mathrm{sgn}(X')X \le X_{\mathrm{m}} - 2X_{\mathrm{c}} \end{cases}, \tag{7.5}$$

7.3.1 Dynamic response analysis

For the nonlinear hysteresis system, analytical and numerical methods are used to obtain the steady-state response. The harmonic balance method is used to obtain the response analytically. The fourth-order Runge-Kutta method based on numerical integration is also employed. The former method has the advantage of relatively low computational cost. The latter method, i.e., the numerical integration method, has the merit of providing accurate results but is more expensive computationally.

The periodic solution of the displacement of lumped mass m can be approximated by

$$X = \hat{X} \sin(\Omega\tau + \tau_0) = \hat{X} \sin\theta, \tag{7.6}$$

where $\hat{X}$ represents the relative response amplitudes of m, which means the maximum displacement X_{m} can be presented by $\hat{X}$, and $\Omega\tau \equiv \theta$. Eq.

(7.5) can be further written as

$$F_{\mathrm{nl}}(\hat{X},\theta)=\begin{cases}(1+\beta)\hat{X}\sin\theta+\mathrm{sgn}(\cos\theta)\beta(\hat{X}-X_{\mathrm{c}}),\\ \text{when}\quad \theta\in[\theta_A,\theta_B)\cup[\theta_{\mathrm{c}},\theta_D)\\ \hat{X}\sin\theta+\mathrm{sgn}(\cos\theta)\beta X_{\mathrm{c}},\\ \text{otherwise}\end{cases},\tag{7.7}$$

where

$$\begin{aligned}&\theta_A=\frac{\pi}{2},\theta_B=\pi-\sin^{-1}(1-\frac{2X_{\mathrm{c}}}{\hat{X}}),\theta_{\mathrm{c}}=\frac{3\pi}{2},\\ &\theta_D=2\pi-\sin^{-1}(1-\frac{2X_{\mathrm{c}}}{\hat{X}}).\end{aligned}\tag{7.8}$$

The approximation of the restoring force of the nonlinear friction damper is obtained by considering the fundamental harmonic component of its Fourier series expansion, represented as

$$F_{\mathrm{nl}}(X,X')\approx\hat{F}_{\mathrm{nl}}\sin(\theta+\phi)=\hat{F}_{\mathrm{a}}\sin\theta+\hat{F}_{\mathrm{b}}\cos\theta,\tag{7.9}$$

where the symbols $\hat{F}_{\mathrm{nl}}$ and ϕ denote the nondimensional amplitude and phase shift, respectively, of the restoring force. $\hat{F}_{\mathrm{a}}$ and $\hat{F}_{\mathrm{b}}$ represent the Fourier coefficients involved in the analysis:

$$\hat{F}_{\mathrm{a}}=\frac{1}{\pi}\int_0^{2\pi}F_{\mathrm{nl}}(\hat{X},\theta)\sin\theta\,\mathrm{d}\theta,\tag{7.10a}$$

$$\hat{F}_{\mathrm{b}}=\frac{1}{\pi}\int_0^{2\pi}F_{\mathrm{nl}}(\hat{X},\theta)\cos\theta\,\mathrm{d}\theta.\tag{7.10b}$$

As the restoring force can be written as (Liu et al., 2021)

$$F_{\mathrm{nl}}(X,X')=\hat{K}X+\hat{C}X'=\hat{K}\hat{X}\sin\theta+\hat{C}\Omega\hat{X}\cos\theta,\tag{7.11}$$

where $\hat{K}$ and $\hat{C}$ denote the effective stiffness coefficient and damping coefficient of the hysteresis system. Based on Eqs. (7.9) and (7.11), it shows that

$$\hat{K} = \frac{\hat{F}_1}{\hat{X}}, \tag{7.12a}$$

$$\hat{C} = \frac{\hat{F}_2}{\Omega \hat{X}}. \tag{7.12b}$$

Based on Eqs. (7.10) and (7.12), it can be derived that

$$\hat{K}(\hat{X}) = \begin{cases} 1+\beta, & \hat{X} \le X_\mathrm{c} \\ \frac{2+\beta}{2} - \frac{\beta}{\pi}[\sin^{-1}(1-\frac{2X_\mathrm{c}}{\hat{X}})+ & \\ \frac{2X_\mathrm{c}}{\hat{X}}(1-\frac{2X_\mathrm{c}}{\hat{X}})\sqrt{\frac{\hat{X}}{X_\mathrm{c}}-1}], & \hat{X} > X_\mathrm{c} \end{cases}, \tag{7.13}$$

and

$$\hat{C}(\hat{X}) = \begin{cases} 0, & \hat{X} \le X_\mathrm{c} \\ \frac{4\beta}{\pi\Omega}\frac{X_\mathrm{c}}{\hat{X}}(1-\frac{X_\mathrm{c}}{\hat{X}}), & \hat{X} > X_\mathrm{c} \end{cases}. \tag{7.14}$$

According to Eq. (7.14), the hysteresis model's effective stiffness coefficient depends on the displacement amplitude $\hat{X}$, while the effective damping coefficient is affected by both the frequency Ω and the displacement amplitude $\hat{X}$.

For the proposed SDoF model, the instantaneous input power P_in is

$$P_\mathrm{in} = \Re(X')\Re(F_0 \cos \Omega\tau), \tag{7.15}$$

and the corresponding time averaged input power is

$$\overline{P}_\mathrm{in} = \frac{1}{\tau_\mathrm{s}} \int_{\tau_0}^{\tau_0+\tau_\mathrm{s}} P_\mathrm{in} \mathrm{d}\tau. \tag{7.16}$$

The instantaneous dissipated power P_d and P_df by the damper and the friction damper are respectively written as

$$P_\mathrm{d} = 2\zeta(\Re(X'))^2, P_\mathrm{df} = \Re(X')\Re(F_\mathrm{nl}), \tag{7.17}$$

and the corresponding time averaged dissipated power are

$$\overline{P}_\mathrm{d} = \frac{1}{\tau_\mathrm{s}}\int_{\tau_0}^{\tau_0+\tau_\mathrm{s}} P_\mathrm{d}\mathrm{d}\tau, \overline{P}_\mathrm{df} = \frac{1}{\tau_\mathrm{s}}\int_{\tau_0}^{\tau_0+\tau_\mathrm{s}} P_\mathrm{df}\mathrm{d}\tau. \tag{7.18}$$

The numerical time-marching Runge–Kutta (RK) method can be used for obtaining the forced response of the above SDoF system, which is a common method for solving the nonlinear problem. As the dry friction damper behaves hysteretic nonlinear force-displacement relationship, the equation of motion is different when the displacement and movement direction change as shown in Eq. (7.5). Therefore, the calculation follows the flow chart logic as shown in Fig. 7.3. The critical slip displacement X_c is a constant as long as the slip force $\mu_\mathrm{f} f_\mathrm{n}$ remains unchanged, while the maximum displacement X_m varies after each circle. Depending on the direction of movement and the current position of the object in the corresponding hysteresis force-displacement relationship, the lumped mass m_1 is subjected to different nonlinear forces.

7.3.2 Results and discussion

With the non-dimensional parameters selected as $\omega_0 = 141$ rad/s, $\zeta = 0.03$, $F_0 = 5 \times 10^{-4}$ and $\beta = 0.5$, the figures for nondimensional forced response and the ratio of maximum and critical slip displacement are depicted in Fig.

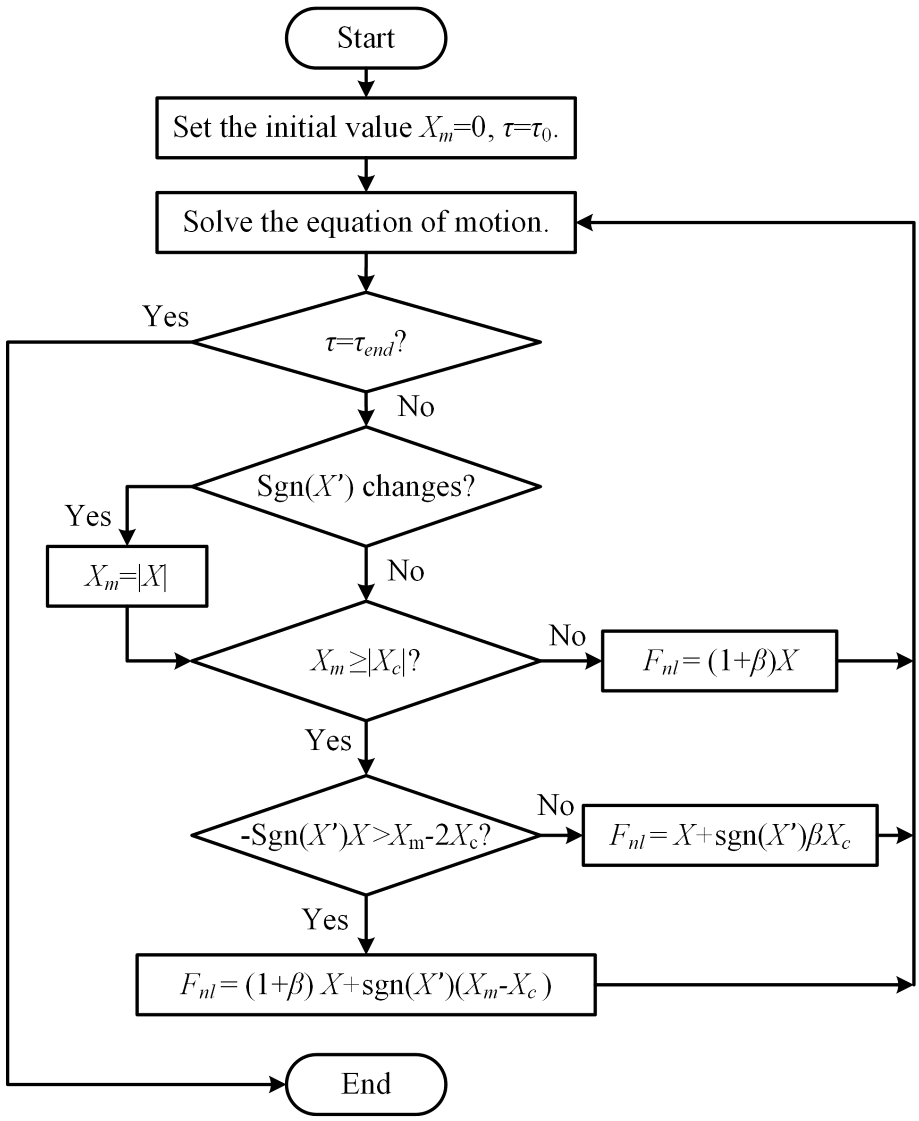

Figure 7.3: Flow chart of the solving process of the hysteresis nonlinear system based model.

7.4. The solid lines represent the results obtained from the linearization calculation and the star markers are the results from the RK method. Since the critical slip displacement x_c leads a significant role in the nonlinear hysteresis force-displacement relationship, the normal force applied to the dry friction damper, f_n, is controlled for analysis with the friction factor μ_f keeping constant.

When the normal force infinitely approaches 0, which is the same as the case with no dry friction damper attached, the response shows a very

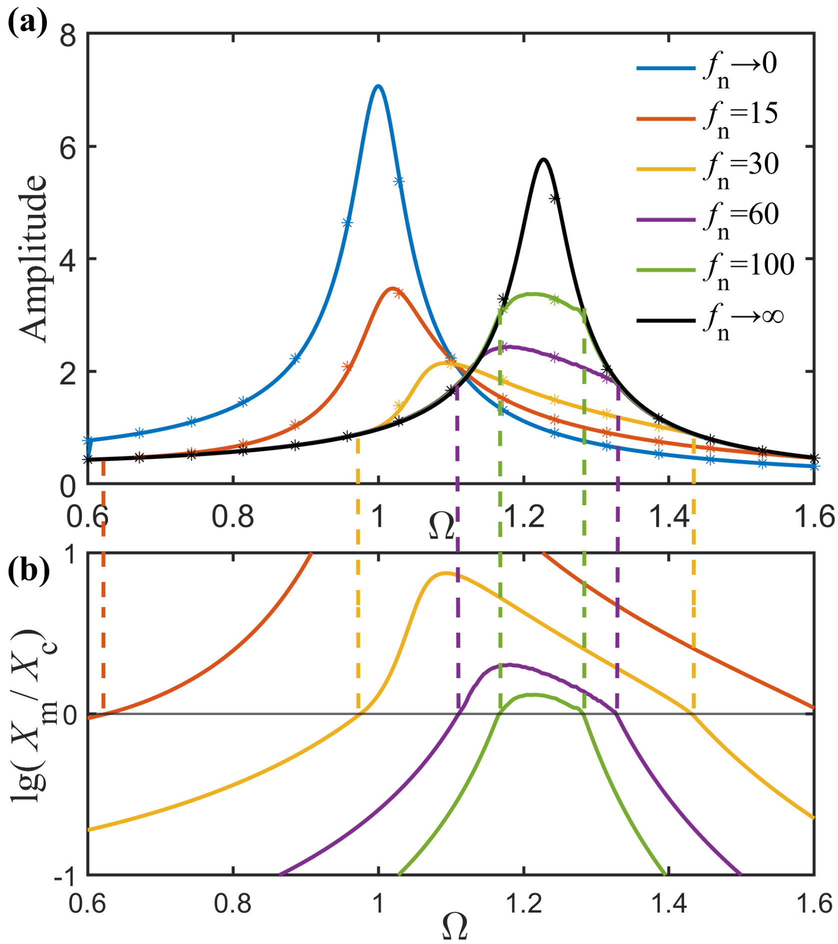

Figure 7.4: (a) Nondimensional response of the lumped mass with harmonic excitation. The colours of the lines represent the cases with different normal forces, and the markers indicate the results obtained by the RK method. (b) The ratio of maximum and critical slip displacement. The black solid line $\lg(X_{\mathrm{m}}/X_{\mathrm{c}}) = 0$ is the reference line.

high peak with frequency $\Omega = 1$. And the case where normal force approaches infinity can be regarded as a linear model without a frictional element, but with both springs of static stiffness of k_{s} and k_{n}, which also has a high response amplitude with frequency $\Omega = (\omega_0\sqrt{1+\beta})/\omega_0 = 1.22$. As the normal force increases, the peak frequency moves from $\Omega = 1.00$ towards higher frequency $\Omega = 1.22$, and the peak amplitude exhibits an initially decreasing and then increasing trend. For instance, the amplitude for the case with no dry friction damper is 7.06 while that for $f_{\mathrm{n}} = 30$ is 2.15, which is a reduction of 69.55%, indicating excellent wave attenuation performance and demonstrating the potential of applying hysteresis models for vibration suppression. What's more, it can be observed that some parts of different cases share the same curve. Based on the logic of the dry friction model, the response of the lumped mass with the same excitation amplitude will be the same if the maximum displacement is less than the critical slip displacement. The corresponding ratios of X_{m} and X_{c} in Fig. 7.4(b) give a clear indication of the transition points between the linear and nonlinear regions. When $\lg(X_{\mathrm{m}}/X_{\mathrm{c}})$ is below the black zero reference line, which means the maximum displacement of the lumped mass is lower than the critical slip displacement and therefore there is no nonlinear behaviour involved, the curve follows the trend of the linear damper model. We find that each set of boundary points under different parameters has the same amplitude, as shown by the dashed lines of the corresponding colours in the figure. Among all shown cases, when the normal force is equal to 60N and 100N, the peak amplitudes are substantially reduced compared to the linear damper case, while the response in the other frequency regions is almost unaffected. It demonstrates that the friction damper can not only significantly reduce the forced response of the system but can even simultaneously maintain or modulate the peak frequency when the appropriate parameters are selected.

An in-depth study of the specific time-domain response and its corresponding force-displacement relationship when different frequency excitations are applied can assist in understanding the role of friction dampers in this system. The responses are shown in Fig. 7.5(a,c) and the black dashed lines indicate the critical slip displacements in both directions. The force-displacement relationships are shown in Fig. 7.5(b,d) and the red lines represent their force-displacement relationship in the steady states. When the excitation frequency $\Omega = 0.7$, as the response amplitude of the lumped mass does not exceed the value of the critical slip displacement until the relative steady state is reached, the friction damper is linear as seen from the force-displacement diagram. When $\Omega = 1.1$, the response amplitude exceeds the critical slip displacement and remains above it until it reaches the relative steady state. The corresponding force-displacement curve also exhibits a hysteresis curve similar to that of Fig. 7.1. As the maximum displacement changes, its shape also changes and tends to stabilise in the end.

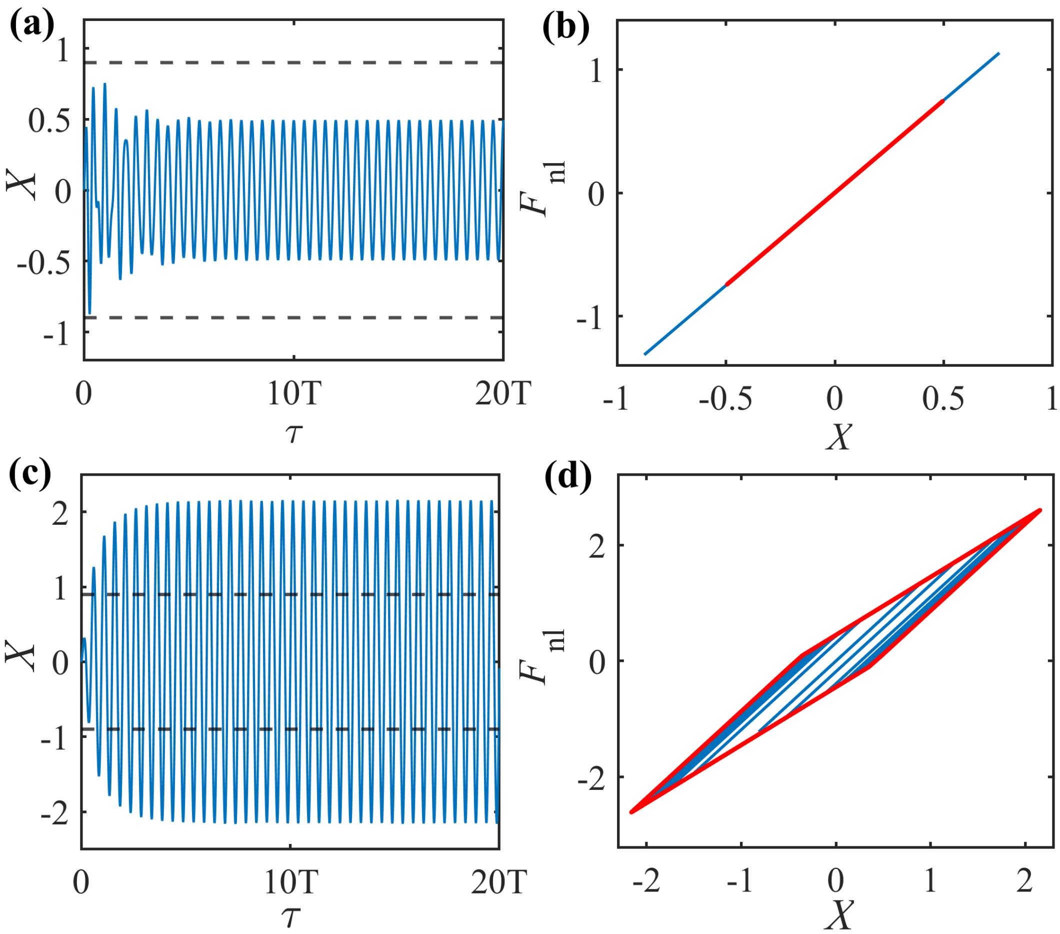

Figure 7.5: (a,c) The time domain response and (b,d) corresponding force-displacement relationship of the SDoF system for a normal force $f_{\mathrm{n}} = 30$ applied on the friction damper at different harmonic excitation frequencies (a,b) $\Omega = 0.7$ and (c,d) $\Omega = 1.1$. The red lines indicate the force-displacement relationship in the steady states.

The investigation of the system using PFA can deepen the understanding and reveal the behaviour of structural vibration control from a different perspective. Figure 7.6 presents the time averaged vibration power flow characteristics of the SDoF structure with varying normal force on the friction damper. In each subplot, the black solid line and yellow dashed line represent the input power and the power dissipated by the damper, respectively, while the red solid line represents the power dissipated by the friction damper. The figures show that there is almost no energy dissipation by the friction damper in the two extreme cases where the normal force is close to 0 and infinity. With appropriate force values, such as 30N and 60N, the friction damper is involved in energy dissipation in certain frequency bands, which indicates that the friction damper participates in energy dissipation only when it begins to slip. The boundaries are also determined by the ratio of the maximum slip displacement to the critical slip displacement. The working frequency bands all cover the peaks of the response, providing a softening effect.

7.4 2DOF model with dry friction damper

7.4.1 Mathematical modelling

The coupled structure can be characterised by two SDoF systems connected, each representing a dominant mode of a substructure (Dai et al., 2022c; Shi et al., 2019). The schematic diagram of a coupled mechanical structure connected by a hysteresis nonlinear friction damper is depicted in Fig. 7.7. In subsystem I, the lumped mass m_1 subjected to an external force with amplitude f and frequency ω, is connected to the left fixed base

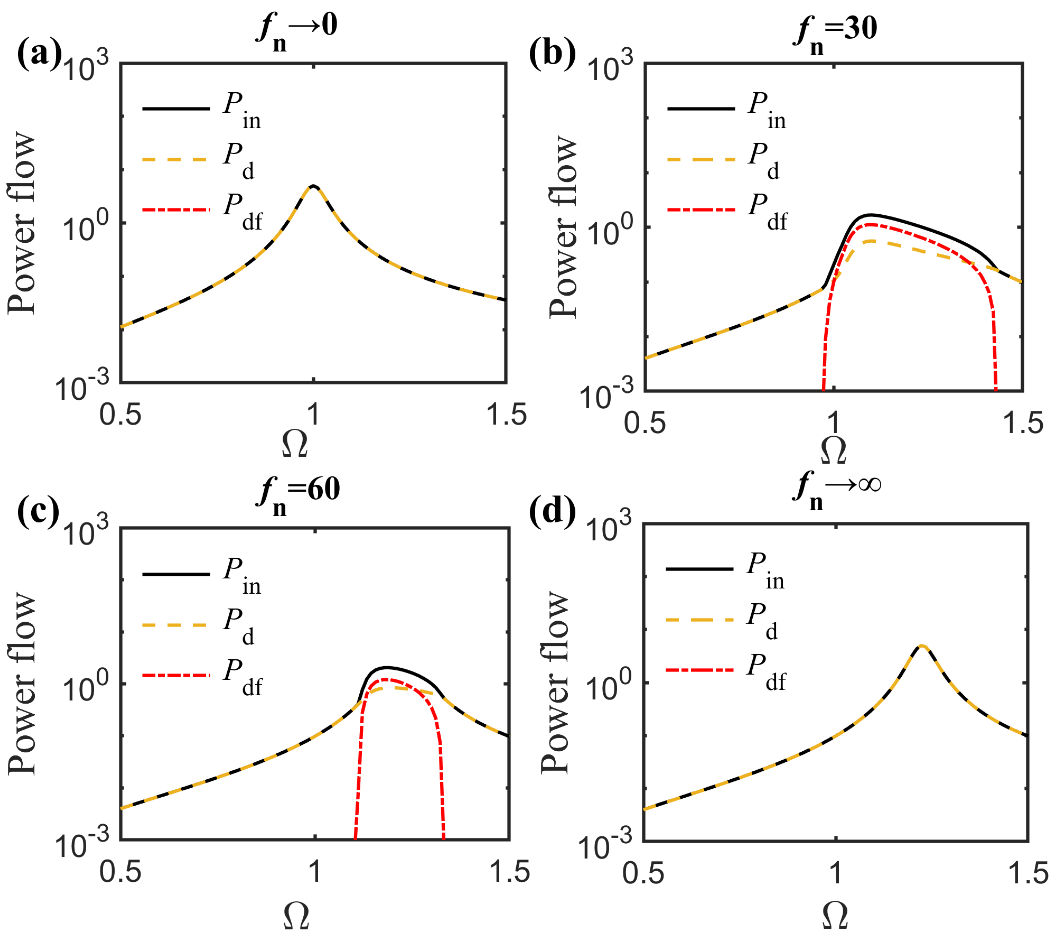

Figure 7.6: Power flow behaviour of the SDoF structure with hysteresis nonlinear friction damper. Figures (a-d) represent the four cases when the normal force applied to the friction damper tends to 0, equals 30, 60 and tends to infinity, respectively. P_{in}, P_{d} and P_{df} represent the input power, the power dissipated by the viscous damper and the friction damper, respectively.

by a damper of damping coefficient c_1 and a spring of stiffness k_1. While subsystem II is composed of mass m_2 connected to the right fixed base by a damper of damping coefficient c_2 and a spring of linear stiffness k_2. The hysteresis friction damper between the two subsystems is presented by a macro-slip element with static stiffness k_{s}, kinetic stiffness k_{n}, and the slip force $\mu_{\mathrm{f}} f_{\mathrm{n}}$. The lumped masses move horizontally without considering the friction with the horizontal base. The absolute displacements of masses are x and y and the relative displacement of m_2 is $\delta = y - x$. Displacements

$x = y = 0$ are considered to be the static equilibrium position.

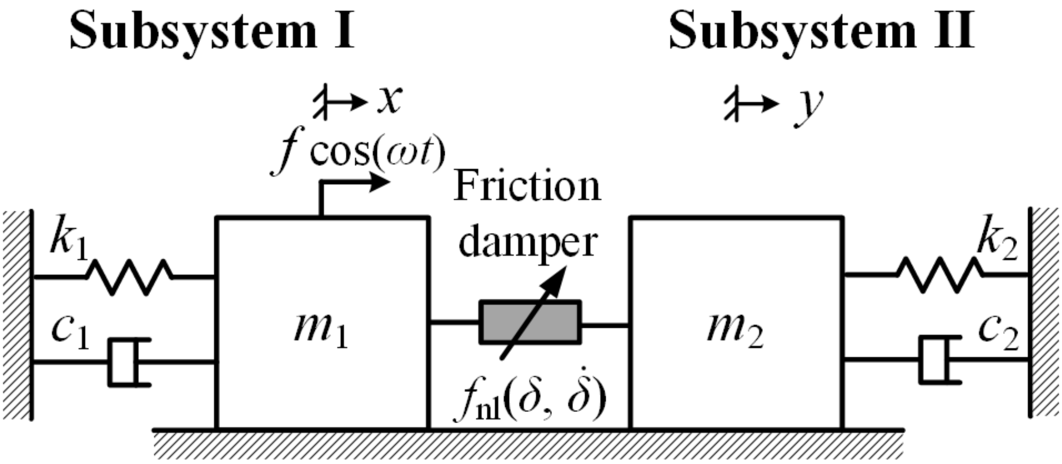

Figure 7.7: Schematic diagram for a coupled structure with a nonlinear hysteresis friction damper.

The equations of motion for this model are

$$\begin{bmatrix} m_1 & 0 \\ 0 & m_2 \end{bmatrix} \begin{Bmatrix} \ddot{x} \\ \ddot{y} \end{Bmatrix} + \begin{bmatrix} c_1 & 0 \\ 0 & c_2 \end{bmatrix} \begin{Bmatrix} \dot{x} \\ \dot{y} \end{Bmatrix} + \begin{bmatrix} k_1 & 0 \\ 0 & k_2 \end{bmatrix} \begin{Bmatrix} x \\ y \end{Bmatrix} + \begin{Bmatrix} -f_{\mathrm{nl}}(\delta, \dot{\delta}) \\ f_{\mathrm{nl}}(\delta, \dot{\delta}) \end{Bmatrix} = \begin{Bmatrix} f \cos \omega t \\ 0 \end{Bmatrix} \tag{7.19}$$

where the overdot $\dot{(\bullet)}$ is the derivative with respect to time and the f_{nl} is the nonlinear dry friction force.

To better analyse the model, nondimensional variables and parameters are introduced as

$$\begin{aligned} &Y = \frac{y}{l}, \Delta = \frac{\delta}{l}, \Delta_{\mathrm{m}} = \frac{\delta_{\mathrm{m}}}{l}, \Delta_{\mathrm{c}} = \frac{\delta_{\mathrm{c}}}{l}, F = \frac{f}{k_1 l}, \\ &\omega_0 = \sqrt{\frac{k_1}{m_1}}, \zeta_1 = \frac{c_1}{2m_1\omega_0}, \zeta_2 = \frac{c_2}{2m_1\omega_0}, \alpha = \frac{m_2}{m_1}, \\ &\beta_1 = \frac{k_2}{k_1}, \beta_{\mathrm{s}} = \frac{k_{\mathrm{s}}}{k_1}, \beta_{\mathrm{n}} = \frac{k_{\mathrm{n}}}{k_1}, \end{aligned} \tag{7.20}$$

where Y and Δ denote the nondimensional absolute and relative displacement of the lumped mass m_2; Δ_m and Δ_c are the nondimensional maximum and critical slip displacement of m_2; F denotes the nondimensional amplitude of excitation force; ω_0 is the natural frequencies of the lumped mass m_1; ζ_1 and ζ_2 are the nondimensional damping ratio; α is the mass ratios; β_1, β_s and β_n are the stiffness ratios.

The equations of motion in Eq. (7.19) can be further nondimensionalised as

$$\begin{bmatrix} 1 & 0 \\ 0 & \alpha \end{bmatrix} \begin{Bmatrix} X'' \\ Y'' \end{Bmatrix} + \begin{bmatrix} 2\zeta_1 & 0 \\ 0 & 2\zeta_2 \end{bmatrix} \begin{Bmatrix} X' \\ Y' \end{Bmatrix} + \begin{bmatrix} 1 & 0 \\ 0 & \beta \end{bmatrix} \begin{Bmatrix} X \\ Y \end{Bmatrix} + \begin{Bmatrix} -F_\mathrm{nl}(\Delta, \Delta') \\ F_\mathrm{nl}(\Delta, \Delta') \end{Bmatrix} = \begin{Bmatrix} F\cos\Omega\tau \\ 0 \end{Bmatrix} \tag{7.21}$$

where the primes $(\bullet)'$ represent differentiation with respect to τ and the nondimensional restoring force updated from Eq. (7.1) is

$$F_\mathrm{nl}(\Delta, \Delta') = \begin{cases} (\beta_\mathrm{s} + \beta_\mathrm{n})\Delta + \mathrm{sgn}(\Delta')\beta_\mathrm{n}(\Delta_\mathrm{m} - \Delta_\mathrm{c}), \\ \text{when} \quad \Delta - 2\Delta_\mathrm{c} \le -\mathrm{sgn}(\Delta')\Delta < \Delta_\mathrm{m} \\ \beta_\mathrm{s}\Delta + \mathrm{sgn}(\Delta')\beta_\mathrm{n}\Delta_\mathrm{c}, \\ \text{when} \quad -\mathrm{sgn}(\Delta')\Delta \le \Delta_\mathrm{m} - 2\Delta_\mathrm{c} \end{cases}, \tag{7.22}$$

7.4.2 Forced response and power flow analysis

Based on the same approach as introduced in Sec. 7.3.1, the approximation of the restoring force of the nonlinear friction damper in Eq. (7.22) can be presented by the effective stiffness coefficient and damping coefficient. The forced response of the proposed 2DoF coupled system and the corresponding ratio of maximum and critical slip displacements can be further derived. Following the same process in Sec. 3.2, the instantaneous input power P_{in}, dissipated power P_{d} and P_{df} by the dampers and the friction damper are respectively written as

$$\begin{aligned}
P_{\mathrm{in}} &= \Re(X')\Re(F\cos\Omega\tau);\\
P_{\mathrm{d}} &= 2\zeta_1(\Re(X'))^2 + 2\zeta_2(\Re(Y'))^2;\\
P_{\mathrm{df}} &= \Re(\Delta')\Re(F_{\mathrm{nl}}).
\end{aligned} \tag{7.23}$$

The corresponding time averaged power during one excitation cycle are

$$\begin{bmatrix} \overline{P}_{\mathrm{in}} \\ \overline{P}_{\mathrm{d}} \\ \overline{P}_{\mathrm{df}} \end{bmatrix} = \frac{1}{\tau_{\mathrm{s}}}\int_{\tau_0}^{\tau_0+\tau_{\mathrm{s}}} \begin{bmatrix} P_{\mathrm{in}} \\ P_{\mathrm{d}} \\ P_{\mathrm{df}} \end{bmatrix} \mathrm{d}\tau. \tag{7.24}$$

Here the nondimensional parameters for the equations of motion in Eqs. (7.21) and (7.22) are stated in Table 7.1, with partially selected parameters refer to references (Huang et al., 2018; Wu et al., 2019).

Table 7.1: Model parameters of the coupled structures with hysteresis nonlinear friction damper.

Parameter	Value	Parameter	Value
F	0.5	ω_0	141 Hz
ζ_1	0.0035	ζ_2	0.0035
α	0.5	β_1	0.5
β_{s}	0.5	β_{n}	0.5

The plot Fig. 7.8(a) shows the nondimensional forced response of the lumped mass m_2 when varying normal forces are applied to the dry friction damper connecting the two subsystems. The solid line and the markers indicate the results from the theoretical calculations and the RK method, respectively, and the results match very well. The first peak near $\Omega = 1$ is almost unaffected by the applied normal force, which is related to the fact that the natural frequency of subsystem I remains almost constant. It is

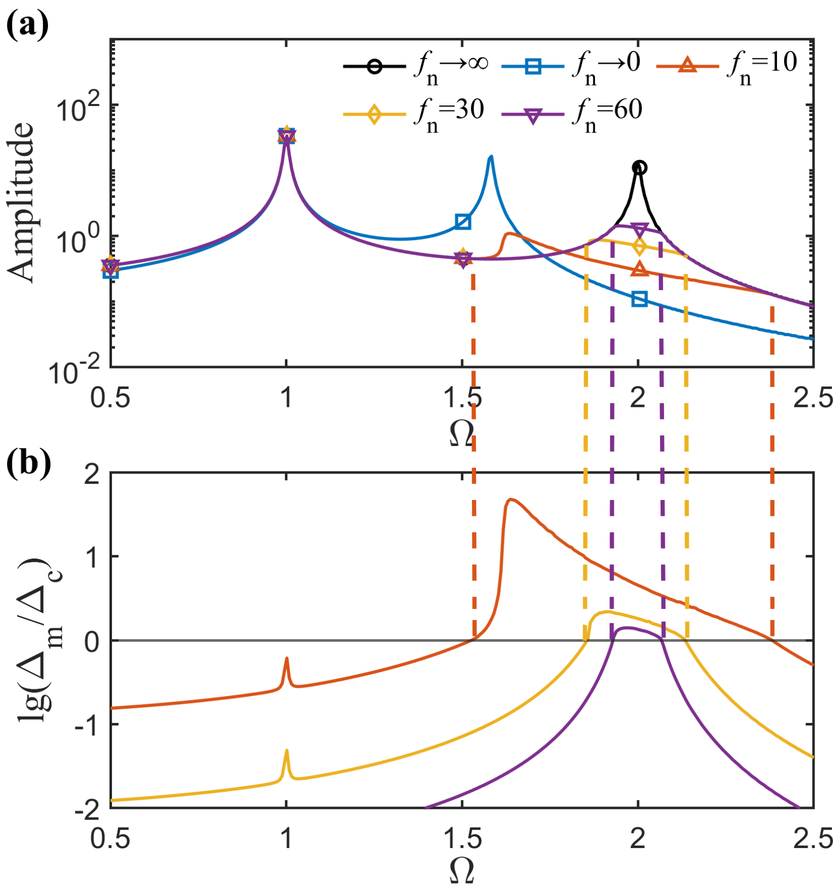

Figure 7.8: (a) Response of the coupled system with different normal forces represented by colours, and the markers indicate the results obtained by RK method. (b) The ratio of maximum and critical slip displacements. The black solid line is the zero reference line.

evident that the second peak on the right is affected by the friction damper. As the normal force increases, the resonance peak moves to higher frequencies and the peak amplitude shows a decreasing and then increasing trend, which is similar to the SDoF system. Figure 7.8(b) shows the relationship between maximum and critical slip displacements. It can also be found that in the frequency band where the maximum displacement is greater than the critical slip displacement, the response is varied by the influence of the friction damper, which in general serves to soften the response amplitude and reduce the frequency of the response. However, unlike single-degree-of-freedom systems, the response amplitudes at the boundary points where the change occurs are not the same, due to the fact that the change in the parameters of the friction damper is determined by the relative displacement of the two subsystems. Meanwhile there is a small peak in the displacement ratio curve at $\Omega = 1$, which is also due to the resonance at the natural frequency of subsystem I.

To examine the effects of the normal force on the response of the lumped mass m_2 in the proposed system, the top view of a surface plot of its response with varying normal force from 0 to 50 is shown in Fig. 7.9. The first peak around $\Omega = 1$ is almost not influenced while the other peak is controlled by the normal force. For normal forces less than 10, the response has a very high amplitude at around $\Omega = 1.58$, and it quickly decreases and moves to a higher frequency after the force continues to increase. When the normal force is around 25, the friction damper exerts better dynamic performance in wave suppression. Its advantages are the absence of high amplitude peaks compared to the two extreme linear conditions, in which the friction damper acts as a high amplitude filter. More importantly, compared to the infinitely normal force case, the softening effect occurs only in the frequency band where the peak is located and does not affect the response at other frequencies, demonstrating excellent vibration control performance in specific frequency bands covering the resonance frequency.

In Fig. 7.10, the nondimensional forced response of the lumped mass m_1 with varying normal force applied to the dry friction damper is shown with the dynamic information including force-displacement relationships in steady states, phase diagrams and the time domain input power of two specific excitation frequencies. Figure 7.10(b-d) and (e-f) presents the dynamic behaviour of two cases with excitation frequency $\Omega = 1.65$ and $\Omega = 2.00$

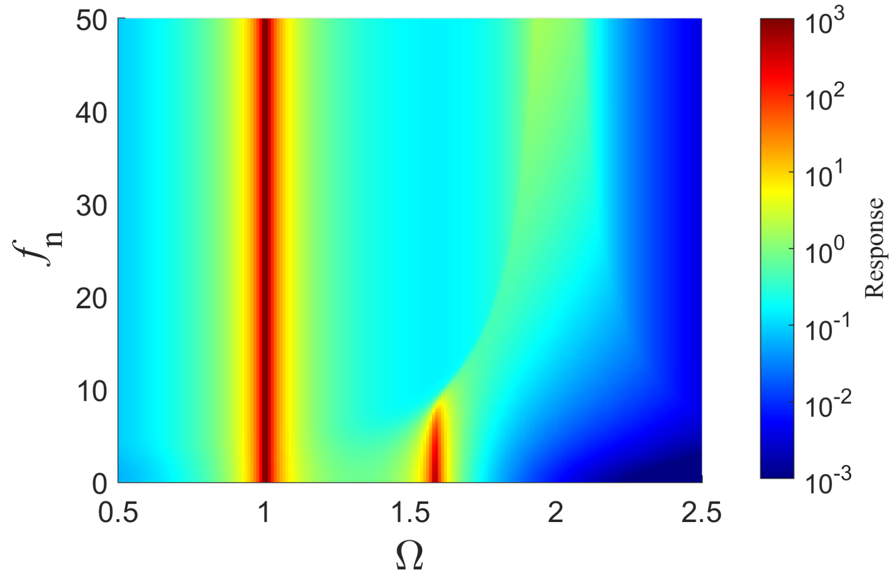

Figure 7.9: Top view of a surface plot of response of m_2 with varying normal force from 0 to 50.

when the normal force is equal to 10 and 60, which are represented by orange and purple lines, respectively. The force-displacement relationships indicate that the slipping of friction damper will influence the responses. When $\Omega = 1.65$ and $f_\mathrm{n} = 60$, the response amplitudes of the relative displacement between two masses Δ don't exceed the critical slip displacement, thus indicating an absence of expected hysteresis. Meanwhile, when $f_\mathrm{n} = 10$, as the amplitude exceeds the critical slip displacement, a clear hysteresis curve can be observed, which results in a nonlinear effect. When $\Omega = 2$, it can be noted that both cases exhibit hysteresis, but have different shapes due to their different values of critical slip displacements, which in turn has different effects on the dynamics of the systems. Similar properties can also be observed in the phase and time-domain power flow diagrams, where at $\Omega = 1.65$, the $f_\mathrm{n} = 10$ case has greater velocity and displacement amplitude and variations, and correspondingly greater power flow, whereas these are reversed at $\Omega = 2$.

The detailed time domain responses of the relative displacement Δ

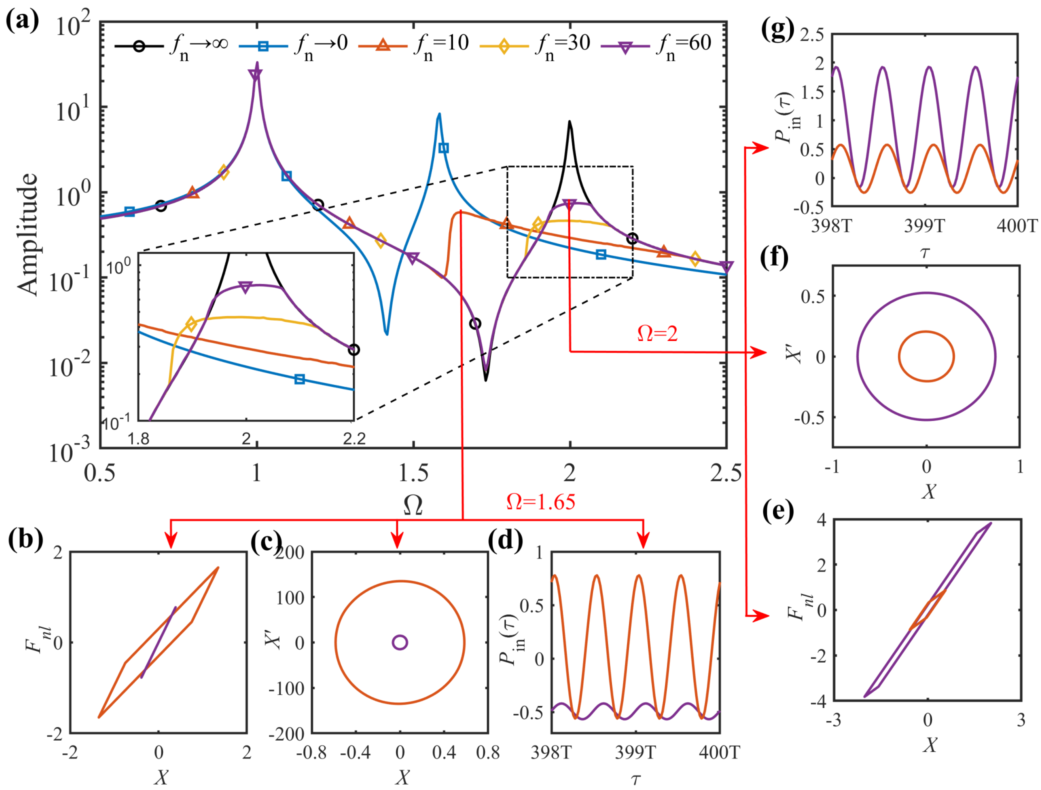

Figure 7.10: (a) Forced response of the lumped mass, m_1, with different normal force applied to the friction damper. Lines: Theoretical calculation; Markers: RK method. Force-displacement relationships, phase diagrams and time domain responses of the input power with (b-d) $\Omega = 1.65$ and (e-g) $\Omega = 2.00$.

with applied normal force f_n close to 0, $f_n = 30$ and $f_n = 60$ for a harmonic excitation frequency of $\Omega = 2$ are shown in Fig. 7.11. The plot (a) shows its response in the period from $\tau = 0$ to τ=100 T while the panel (b) is a zoomed-in view of its response at times 0 to 12 T, which has been marked with a dotted box. As it can be seen from the above figure, since one of the resonant frequencies of the system is $\Omega = 2$ as f_n approaches infinity, the result represented by the black line keeps getting larger and takes more time to reach the steady state with a large amplitude. While the friction damper acts, for instance, when $f_n = 30$ and 60, it reaches the steady state faster with a smaller amplitude. In the enlarged figure below, the corresponding critical slip displacements are also marked with dashed lines of the respective colours. It demonstrates clearly that when the response amplitude does not exceed the critical slip displacement, the responses are exactly the same for all three cases. However, once the response exceeds the critical slip displacement, the friction damper is involved in influencing the system dynamics and a stable state is quickly reached.

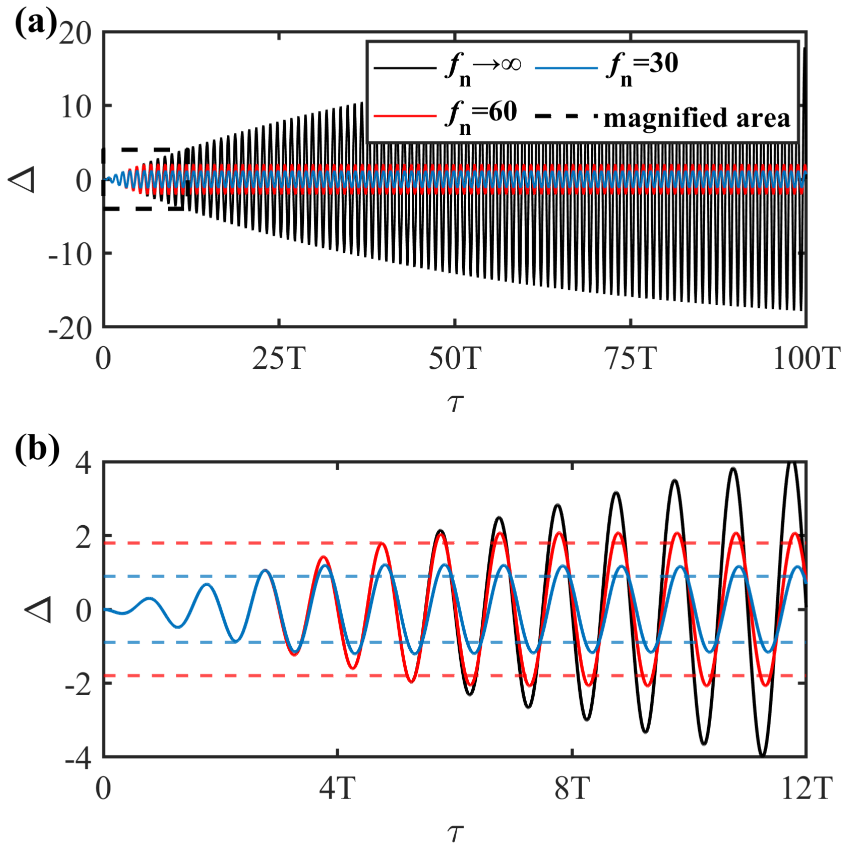

Figure 7.11: (a) Time domain result of the response of the relative displacement Δ for the cases of different normal force applied in the period from $\tau = 0$ to $\tau = 100$ T. (b) Partial enlarged detail of the response of Δ of m_2 in the period from $\tau = 0$ to $\tau = 12$ T.

The steady-state friction behaviours are shown in Fig. 7.12. Subplot (a) shows the corresponding force-displacement relationship when the normal force is 10, where the blue curve represents all the nonlinear forces in the friction damper, including both kinetic and static friction induced by k_n and k_s and the orange curve represents the kinetic friction induced by k_n. Subplot (b) shows the time histories of the friction force with the corresponding colours marked. Subplots (c) and (d) show similar force-displacement plots and time-domain plots, respectively, for a normal force $f_\mathrm{nl} = 60$. When the relative displacement exceeds the critical slip displacement, slip occurs and the kinetic friction remains constant while the total friction continues to increase. When the relative displacement reaches its maximum value, which means the relative velocity goes to 0 and the direction of the velocity is about to change, the sticking effect occurs. The normal force applied to the friction damper changes the magnitude of critical slip displacement, which in turn affects the shape of the force-displacement hysteresis curve. It can be observed in the figures that at the same harmonic excitation frequency $\Omega = 2$, the friction can be controlled by simply changing the magnitude of the normal force f_n, thus affecting the system response.

The figures in Fig. 7.13 depict the time averaged power flow behaviour of the proposed system. The black solid lines and yellow dashed lines represent the input power and the power dissipated by the viscous damper, and the red dash-dotted lines indicate the power dissipated by the friction damper. It can also be observed that the proposed model can be considered as a linear model under two boundary conditions when the normal force is close to zero and infinite. When the friction damper has suitable parameters, such as $f_\mathrm{n} = 8$ and 20, it will show energy dissipation characteristics in a specific frequency band that is related to the relative displacement of the two ends of the friction damper. And it works when the relative displacement is large, effectively reducing the amplitude and frequency of the resonance peaks of the system. By comparing the two examples with $f_\mathrm{n} = 8$ and 20, it is found that the width of the frequency band in which the

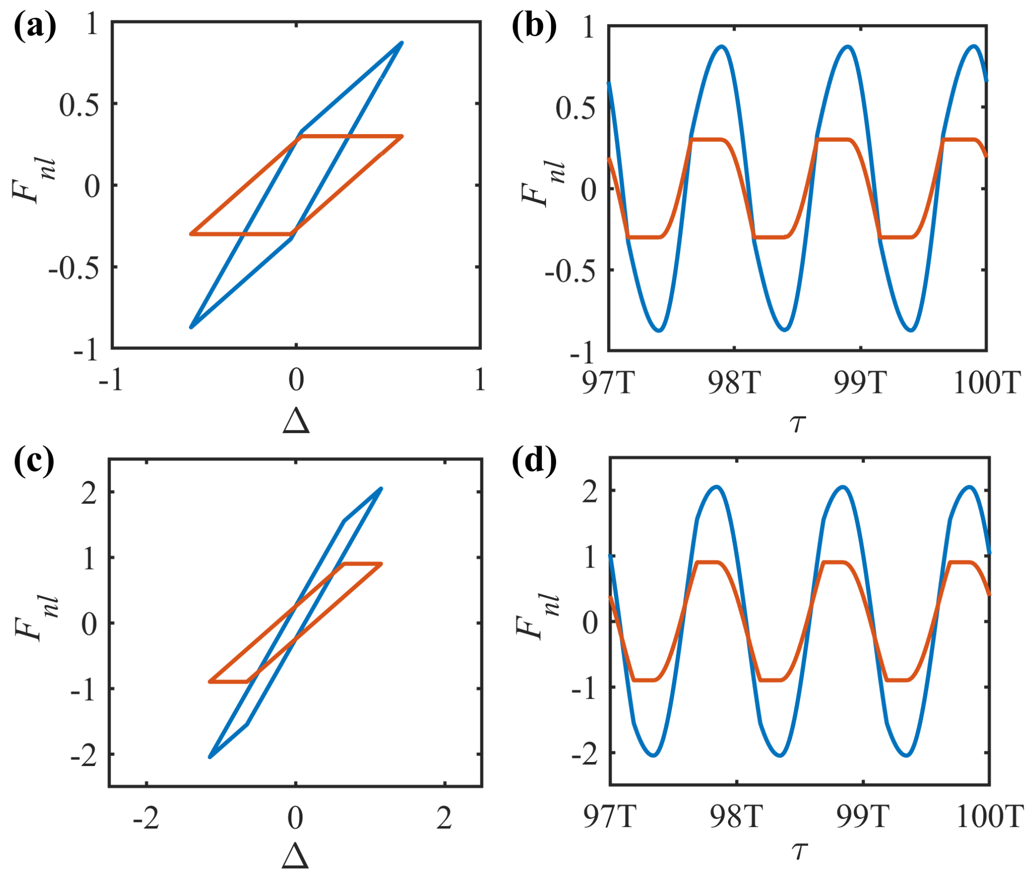

Figure 7.12: Steady state force-displacement relationship diagrams with (a) $f_\mathrm{n} = 10$ and (c) $f_\mathrm{n} = 60$. Steady state time history of friction force with (b) $f_\mathrm{n} = 10$ and (d) $f_\mathrm{n} = 60$. The excitation frequency $\Omega = 2$. The blue curves indicate the static and kinetic friction of the whole friction damper including k_s and k_n while the orange curves indicate the kinetic friction, which is only related to k_n.

friction damper acts is adjustable, but the damping effect is not uniform across the frequencies in the wide band. The results have demonstrated its advantages in energy dissipation as well as vibration control, proving its potential for adjustable damping bands.

To further investigate the effect of the parameter of the normal force applied to the friction damper on its energy dissipation performance in the proposed coupled system, Figure 7.14(b) exhibits a top view of the time averaged power consumed by the friction damper for normal forces from

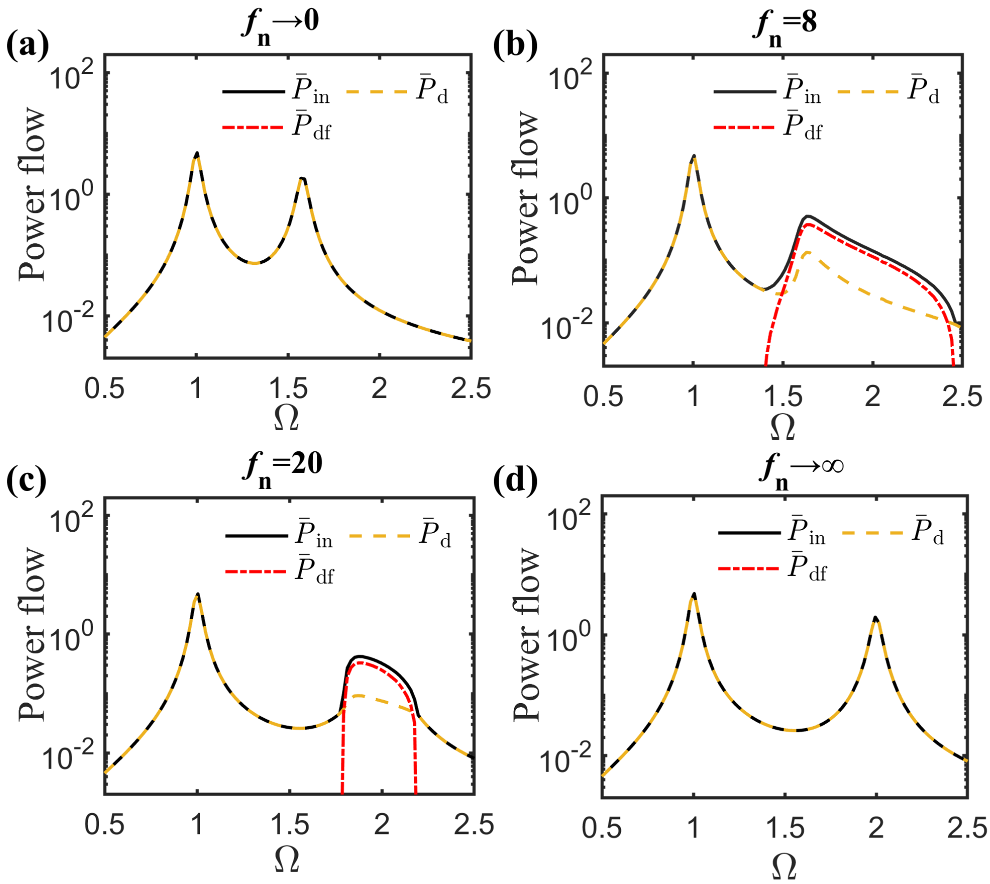

Figure 7.13: Time averaged power flow with different normal force applied to the friction damper, (a) f_n approaching zero, (b) $f_n = 8$, (c) $f_n = 20$ and (d) f_n approaching infinite. The black solid lines and yellow dashed lines represent the input power and the power dissipated by the viscous damper, and the red dash-dotted lines indicate the power dissipated by the friction damper.

0 to 50. It can be found that as the normal force grows from 0 to about 10, the width of the band in which the friction damper is active gradually increases, but its peak frequency remains almost the same and maintains a large amplitude. As the normal force grows a little more, the peak suddenly drops and shifts to higher frequencies, and while it continues to increase, the bandwidth gradually decreases and the peak shows a gentle trend of decreasing and then increasing. Based on the current top view plot and Fig. 7.13, it can be predicted that as the force continues to increase beyond 50, the bandwidth will become narrower and narrower until it disappears.

Figure 7.14(a) exhibits a top view of the time averaged input power flow over the same normal force range. It can be seen that the first peak of the input power is also virtually unaffected, while the second peak has a similar trend to the response, with the difference that there is a gap at the lower frequency of the second peak. This gap is also shallower and narrower at a normal force of about 10. Summarising the above results, a normal force of around 20 is optimal for the friction damper as a high amplitude filter to reduce the response of the proposed coupled system.

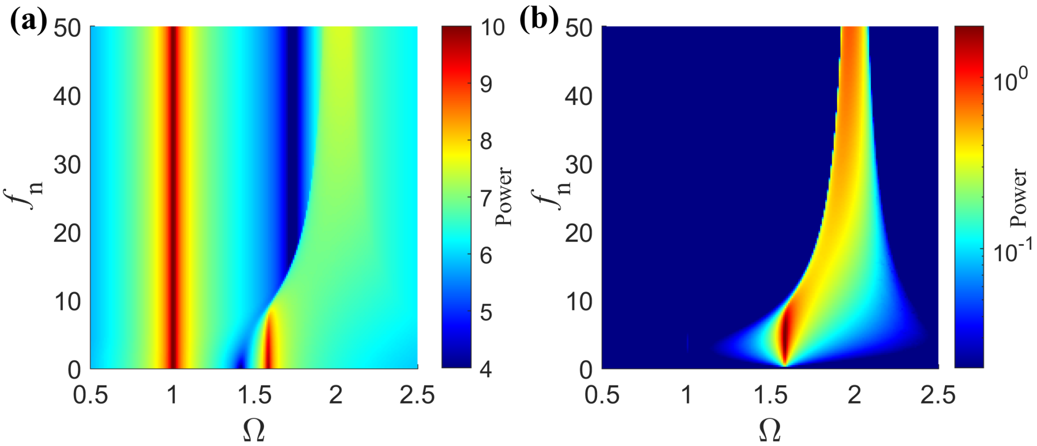

Figure 7.14: Top view of a surface plot of time averaged (a) input power and (b)power dissipated by friction damper with varying normal force from 0 to 50.

The wave transmission within the coupled system provides another perspective for analysing the dynamic performance of the proposed structure. The different coloured solid lines in Fig. 7.15 indicate cases where the normal force applied to the dry friction damper is different. The top view of a surface plot of wave transmission for the proposed coupled system with varying normal force from 0 to 50 is drawn in Fig. 7.15 the detailed and clear effects of parameter changes. All the curves show only a single peak, and the peak frequency is correlated to the gap frequency between the two peaks in the forced response curve. As the normal force increases from 0 to

16, the peak frequency increases from $\Omega = 1.41$ and the amplitude shows a similar decrease and then increase trend as the forced responses. Approximately after a normal force greater than 8, there is a sharp drop in the trough after the peak and a levelling off after a short period of frequency. As the normal force continues to increase beyond 17, the results show that the peak remains constant after the frequency reaches $\Omega = 1.73$ and the normal force will only influence the drop position. Meanwhile, compared with the boundary case coloured in black, the width of the transmittance drop gap becomes narrower and shallower around Ω=2, which means that the effectiveness of friction damping in reducing the transmissibility is decreasing. From this we can conclude that a more desirable low transmittance can be achieved in the proposed coupled system at a normal force of 10.

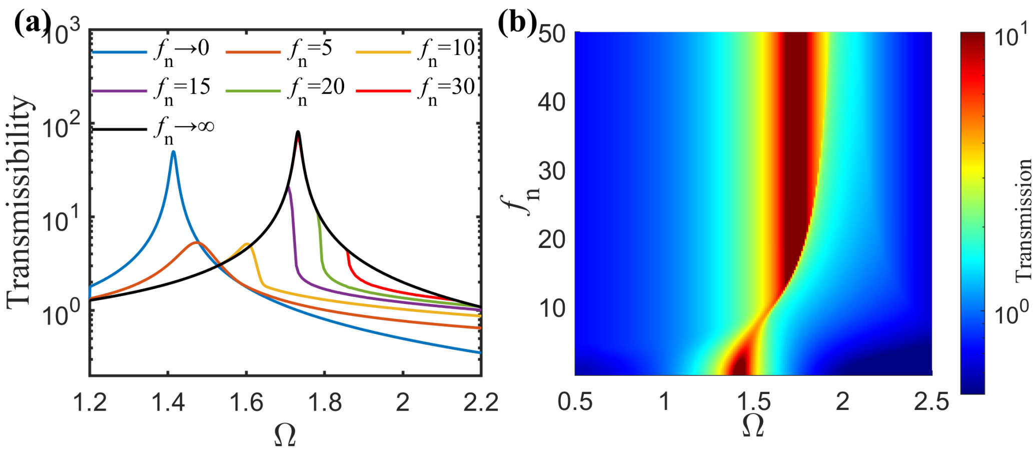

Figure 7.15: (a) Wave transmission diagram for the proposed coupled system with varying normal force. (b) Top view of a surface plot of wave transmission for the proposed coupled system with varying normal force from 0 to 50.

The mass ratio between the two substructures of the investigated coupled structure also has an effect on its response and vibration power flow. The forced response amplitudes of the lumped masses of two substructures are shown in Fig. 7.16, where the solid lines in different colours indicate the cases with different mass ratios $\alpha = 0.6$, 0.5, 0.4 and 0.3, respectively. It can be observed that as the mass ratio decreases, the first peak of the lumped mass m_1 response amplitude shifts slightly towards higher frequencies and its peak also rises a bit, while the second peak is substantially shifted to higher frequencies and its peak is considerably lower and flatter. At the same time, the gap moves to higher frequencies and becomes deeper. For the response amplitude of the lumped mass m_2 of substructure II, both of its peaks move towards the high-frequency region as the mass ratio decreases, as the response of m_1, but with the difference that the peak of the first peak shows a slight downward trend and, as described above, there is no gap between the two peaks.

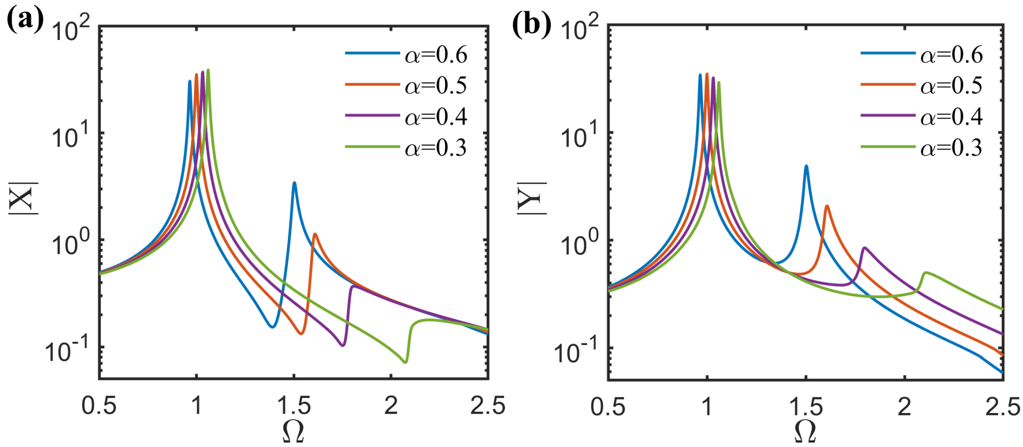

Figure 7.16: Forced response amplitude of lumped masses (a) m_1 and (b) m_2 with different mass ratio α. The blue, red, purple and green solid lines indicate the cases with $\alpha = 0.6, 0.5, 0.4$ and 0.3, respectively.

As the response varies as a result of the mass ratio, it can be surmised that its power flow varies accordingly, and thus an attempt can be made to explain the effect caused by the mass ratio on it. The time averaged power flow of the proposed coupled structure with different mass ratios are shown in Fig. 7.17. The solid and dashed lines in Fig. 7.17(a) represent the input power and the power dissipated by the linear damper, respectively, while the power dissipated by the friction damper is presented in (b). As α

decreases, from 0.6 to 0.3 as shown in the figure, it is observed that the first peak is slightly shifted towards higher frequencies and the peak becomes a little larger. At the same time, the second peak moves substantially towards the high frequency region and the peak decreases and becomes less sharp. The power dissipated by the friction damper is mainly around two peaks, where it should be noted that at alpha = 0.5, the friction damper dissipates almost no power in the first peak. The power dissipated by the friction damper reaches its peak at the peak of the input power at the same time. Although the amplitude of the power dissipation increases in the first peak and decreases considerably in the second peak as α decreases, the ratios of the dissipated power relative to the input power provide more information, as can be seen in Fig. 7.17(c). In the vicinity of the second peak, the power consumed by the friction damper can reach more than 90% of the input power. Around the first peak, the percentage is smaller in all cases except for $\alpha = 0.6$, where the two parts merge.

A more detailed variation of the power flow dissipated by friction damping due to the mass ratio α is shown in Fig. 7.18. Fig. 7.18(a) and (b) indicate the power dissipated by the friction damper and its percentage to the input power, respectively. At $\alpha = 0.5$, it dissipates almost no power at the first peak, its band broadens and the proportion of consumption increases as α moves away from 0.5. Around the second peak, the ratio is maintained over 90% as long as the friction damper is involved in the power dissipation. At α greater than 0.6, the two components involved in power consumption show a tendency to merge.

The dynamic behaviour of the investigated coupled system is controlled by the friction damper. It is apparent that in addition to the normal force acting on the damper, the sliding stiffness also affects the hysteresis

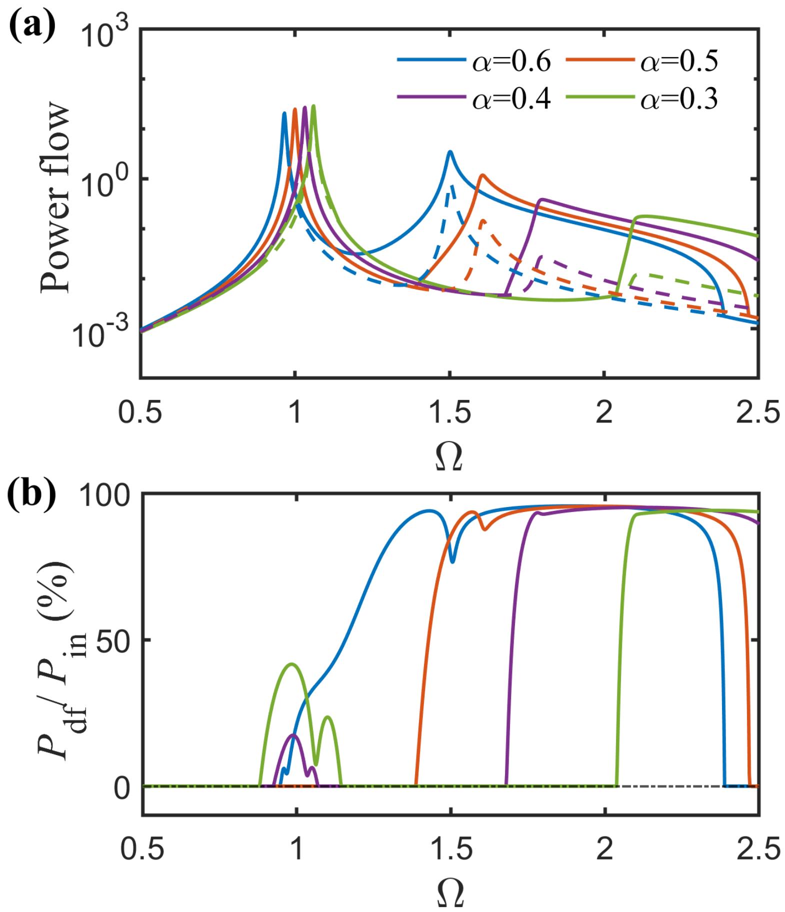

Figure 7.17: (a) Time averaged power flow where the solid and dashed lines represent the input power and the power dissipated by the linear damper, respectively. (b) Time averaged power dissipated by the nonlinear friction damper. (c) The percentage of power dissipated by the nonlinear friction damper in the input power.

loop, which is related to the sliding force and can be varied by changing the friction coefficient μ_f. The influence of varying the stiffness ratio β_n from 0.5 to 1.5 on the forced response of the lumped masses m_1 and m_2 is shown in Fig. 7.19. It can be found that the first peak frequency of the two concentrated masses does not change with the stiffness ratio β_n, which is similar to the parametric study based on the normal force in Fig. 7.9. The frequencies of the second peaks shift continuously to higher frequencies as β_n increases, while its width increases and its amplitude decreases. As distinct from the above results based on normal force f_n and mass ratio

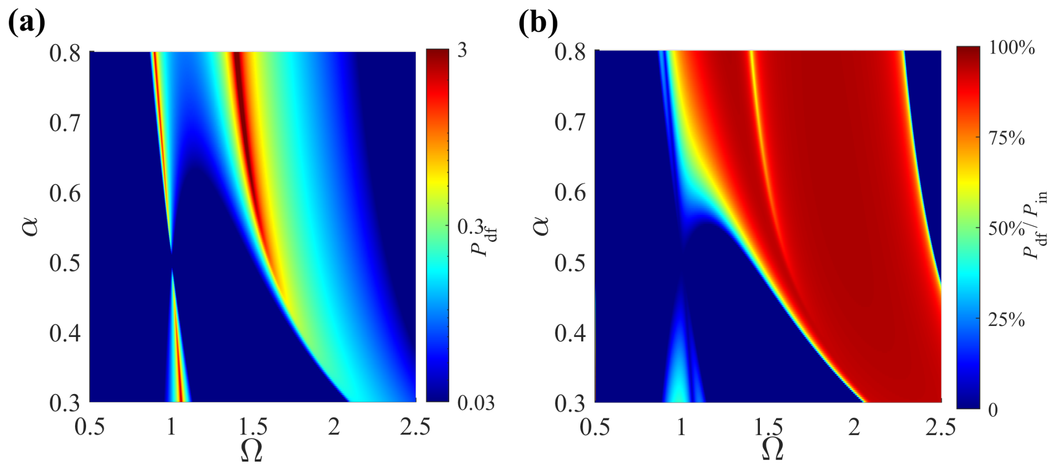

Figure 7.18: (a) Power flow map of the time averaged power dissipated by the nonlinear friction damper. (b) Power flow map of the percentage of time averaged power dissipated by the nonlinear friction damper in the input power.

α, the frequency shift and width change of the second peak in the current result follows a linear-like trend.

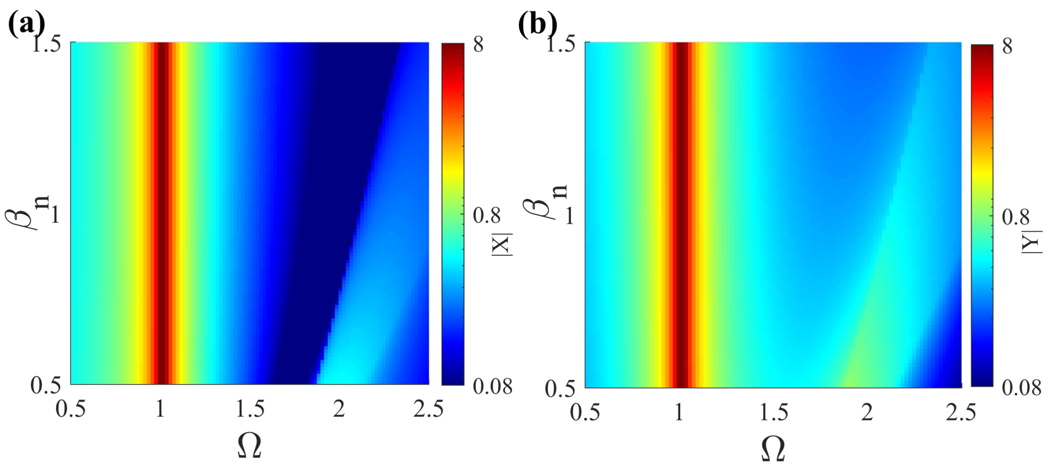

Figure 7.19: Forced response amplitude map of lumped masses (a) m_1 and (b) m_2 with different stiffness ratios β_n from 0.5 to 1.5.

7.5 Summary

This study investigated the vibration control performance of the dry friction damper based systems. By using the harmonic balance method and the

Runge–Kutta method, the hysteretic nonlinearity of the friction damper is described. Based on the forced response and vibration power flow analysis, the friction damper applied to a single-degree-of-freedom system demonstrated the ability to significantly reduce vibration amplitude and control resonant frequency, showing potential as a high-amplitude vibration filter. For further research about the proposed friction damper based coupled structure, the following conclusions are drawn:

- The forced response amplitude of subsystem II is well controlled by choosing the appropriate parameters of the normal force applied to the dry friction damper. The peak frequency is tunable within a certain range, which is between the resonance frequencies of the two boundary cases.
- Based on the power flow analysis, the friction damper exhibits energy dissipation in the frequency band controlled by the normal force, and this frequency band surrounds the natural frequency of substructure II, which achieves high-amplitude vibration filtering.
- The transmission analyses show that the parameters chosen for the normal force in order to realise low transmittance between the subsystems are distinct from the objective of high amplitude filtering. The friction dampers are flexible and can be adapted to alter capacity for different vibration control purposes.

The dry friction damper based coupled structure is investigated and the vibration power flow analysis is utilised to explain and deepen the understanding of the vibration suppression effect of the device from the energy transfer and dissipation perspective. In addition, while the normal force is conventionally designed as a constant force, this study has demonstrated that it has the potential to be designed to be adjustable to suppress peaks in vibration response and to reduce vibration energy transfer.

Chapter 8

Conclusions and further work

8.1 Conclusions

In conclusion, this project has explored various aspects of mechanical vibration control and presented novel linear and nonlinear advanced mechanisms for mitigating vibrations in mechanical systems. It aimed to enhance the understanding of vibration phenomena, develop innovative control strategies, and optimise the design of vibration control devices, based on the forced response, vibration transfer and power flow analysis. The study began by exploring the synergistic effects of combining inerters and LRAMs and proposes linear and geometrical nonlinear inerter based LRAM configurations, which extend the original material parameter restrictions, leading to lower-frequency bandgap. Then a diatomic LRAM configuration was investigated to obtain extra bandgaps compared with the monatomic configuration, and the application of NSM induces an ultralow frequency bandgap effective from zero frequency. In addition, this study proposed a novel Flexnertia metastructure concept to perform vibration suppression through coupling rotational inertia to structural flexural motion. The experimental and numerical results were in good agreement, both confirming that the average overall response of the metastructure is significantly reduced. At last, a coupled structure based on a nonlinear hysteresis friction damper subjected to harmonic forces for vibration suppression was studied. The results indicated that the friction damper participates in the energy dissipation in the frequency band around the resonance frequency, thereby enabling high-amplitude vibration filtering, and they have the potential to be designed to be adjustable and respond to different vibration control objectives.

Through a comprehensive investigation and analysis, several key findings and contributions have been made:

- The potential of metamaterials in low-frequency vibration control is demonstrated. The unique properties of metamaterials, such as negative effective mass and bandgap characteristics, were leveraged to design and develop novel devices capable of attenuating vibrations. The research highlighted the importance of structural design and optimisation techniques to maximise the effectiveness of metamaterial-based vibration control systems.

- The application of inerters is explored in mechanical vibration control. The design and optimisation of inerter-based systems were investigated to achieve enhanced vibration isolation and damping capabilities. The findings emphasised the significance of proper configuration and control strategies to leverage the inertial force of inerters for effective vibration control.

- The investigation into friction dampers revealed their potential for enhanced suppression of vibration response and power transfer. The nonlinear hysteresis behavior and preload mechanisms were analysed to improve the energy dissipation capabilities of friction dampers. The research highlighted the importance of advanced friction damper designs to effectively attenuate vibration amplitude by tailoring contact hysteresis friction.

- As artificial periodic structures, due to their excellent customizability, metamaterials can be well combined with other advanced elements and mechanisms, such as inerters and nonlinear mechanisms, to offer improved vibration control performance compared to traditional passive systems.

- These advanced vibration control mechanisms exhibit broad frequency ranges of operation. Inerters, for example, can provide effective control across a wide frequency spectrum, including low-frequency vibrations that are challenging to address with conventional approaches. Nonlinear mechanism-based metamaterials can also exhibit frequency-dependent properties, allowing for tailored vibration control across different frequency bands. The friction damper can also be controlled to affect hysteresis behavior and thus adjust the amplitude suppression band.

- The proposed advanced mechanisms offer flexibility and versatility in their application. The inerter, as a mechanical element, has been proven to have a wide range of applications. One of the biggest advantages of metamaterials is that the bandgap can be customised. The nonlinear mechanisms can extend the original material parameter restrictions. While their synergistic effects show the ability to be tailored and optimised for specific vibration control requirements, enabling adaptability to different applications and environments.

8.2 Recommendations for future research

While this thesis has made significant contributions to the field of mechanical vibration control through the exploration of linear and nonlinear advanced mechanisms, there are several areas that warrant further investigation. These avenues for further work can provide a foundation for future research and advancements in this field. The following suggestions outline potential directions for future investigations:

- optimisation of Design Parameters: The optimisation of design parameters for inerters or nonlinear mechanism-based metamaterials can be further explored. This can involve the development and application of advanced optimisation algorithms to determine the optimal design configurations and parameters for improved vibration control performance. Additionally, considering different constraints, such as weight, size, and cost, can help develop practical design guidelines for the implementation of these control mechanisms in real-world applications.

- Combined with Semi-active Control: Current research and designs can be incorporated into semi-active control systems, allowing for further enhancement of vibration control capabilities. By combining their inherent passive characteristics with semi-active control strategies, these mechanisms can adaptively respond to changing vibration conditions in real time, providing optimal control performance.

- Experimental Validation and Verification: Conducting extensive experimental studies to validate and verify the performance of inerters or nonlinear mechanism-based metamaterials is crucial. Laboratory-scale experiments can be designed to investigate the vibration attenuation capabilities under various excitation conditions. Field-scale experiments can be conducted to assess the effectiveness of these control mechanisms in real-world applications. The results obtained from such experiments will provide empirical evidence and further validate the theoretical findings presented in this thesis.

- Comparative Studies: Conducting comparative studies between inerters or nonlinear mechanism-based metamaterials and other vibration control techniques will provide valuable insights into their relative advantages and limitations. Comparisons with traditional passive systems, semi-active control approaches, or other emerging vibration control technologies will help in understanding the trade-offs and selecting the most suitable solutions for specific applications. These comparative studies can be conducted based on performance metrics such as vibration reduction, energy consumption, and cost-effectiveness.

By pursuing these avenues for further work, researchers can extend the findings presented in this thesis and contribute to the advancement of the field of mechanical vibration control. Addressing these research directions will enable the development of more efficient, reliable, and practical solutions based on linear and nonlinear advanced mechanisms, ultimately benefiting various industries and improving the performance and longevity of mechanical systems.

Bibliography

Akay, A. (2002). Acoustics of friction. *The Journal of the Acoustical Society of America*, 111(4):1525–1548.

Al Ba'ba'a, H. B. and Nouh, M. (2017). Mechanics of longitudinal and flexural locally resonant elastic metamaterials using a structural power flow approach. *International Journal of Mechanical Sciences*, 122:341–354.

Al-Bender, F., Lampaert, V., and Swevers, J. (2005). The generalized maxwell-slip model: a novel model for friction simulation and compensation. *IEEE Transactions on Automatic Control*, 50(11):1883–1887.

Alamri, S., Li, B., Mchugh, G., Garafolo, N., and Tan, K. (2019). Dissipative diatomic acoustic metamaterials for broadband asymmetric elastic-wave transmission. *Journal of Sound and Vibration*, 451:120–137.

Alamri, S., Li, B., and Tan, K. (2018). Dynamic load mitigation using dissipative elastic metamaterials with multiple maxwell-type oscillators. *Journal of Applied Physics*, 123(9).

Antoniadis, I., Chronopoulos, D., Spitas, V., and Koulocheris, D. (2015). Hyper-damping properties of a stiff and stable linear oscillator with a negative stiffness element. *Journal of Sound and Vibration*, 346:37–52.

Arunkumar, M., Pitchaimani, J., Gangadharan, K., and Lenin Babu, M. (2017). Sound transmission loss characteristics of sandwich aircraft panels: Influence of nature of core. *Journal of Sandwich Structures & Materials*, 19(1):26–48.

Attarzadeh, M., Al Ba'ba'a, H., and Nouh, M. (2018). On the wave dispersion and non-reciprocal power flow in space-time traveling acoustic metamaterials. *Applied Acoustics*, 133:210–214.

Bae, M. H. and Oh, J. H. (2020). Amplitude-induced bandgap: New type of bandgap for nonlinear elastic metamaterials. *Journal of the Mechanics and Physics of Solids*, 139:103930.

Bae, M. H. and Oh, J. H. (2022). Nonlinear elastic metamaterial for tunable bandgap at quasi-static frequency. *Mechanical Systems and Signal Processing*, 170:108832.

Banhart, J. (2001). Manufacture, characterisation and application of cellular metals and metal foams. *Progress in Materials Science*, 46(6):559–632.

Bao, H., Wu, C., Wang, K., and Yan, B. (2021). An enhanced dual-resonator metamaterial beam for low-frequency vibration suppression. *Journal of Applied Physics*, 129(9).

Berger, E. (2002). Friction modeling for dynamic system simulation. *Applied Mechanics Reviews*, 55(6):535–577.

Berman, A. D., Ducker, W. A., and Israelachvili, J. N. (1996). Origin and characterization of different stick- slip friction mechanisms. *Langmuir*, 12(19):4559–4563.

Bograd, S., Reuss, P., Schmidt, A., Gaul, L., and Mayer, M. (2011). Modeling the dynamics of mechanical joints. *Mechanical Systems and Signal Processing*, 25(8):2801–2826.

Brillouin, L. (1953). *Wave propagation in periodic structures: Electric filters and Crystal Lattices*. Dover.

Brzeski, P., Lazarek, M., and Perlikowski, P. (2017). Experimental study of the novel tuned mass damper with inerter which enables changes of inertance. *Journal of Sound and Vibration*, 404:47–57.

Butcher, J. C. (1996). A history of runge-kutta methods. *Applied numerical mathematics*, 20(3):247–260.

Cameron, T. M. and Griffin, J. H. (1989). An alternating frequency/time domain method for calculating the steady-state response of nonlinear dynamic systems. *Journal of Applied Mechanics*, 56(1):149–154.

Cardona, A., Lerusse, A., and Géradin, M. (1998). Fast fourier nonlinear vibration analysis. *Computational Mechanics*, 22(2):128–142.

Casini, P. and Vestroni, F. (2022). The role of the hysteretic restoring force on modal interactions in nonlinear dynamics. *International Journal of Non-Linear Mechanics*, 143:104029.

Ceglarek, D., Colledani, M., Váncza, J., Kim, D.-Y., Marine, C., Kogel-Hollacher, M., Mistry, A., and Bolognese, L. (2015). Rapid deployment of remote laser welding processes in automotive assembly systems. *CIRP Annals*, 64(1):389–394.

Chang, I.-L., Liang, Z.-X., Kao, H.-W., Chang, S.-H., and Yang, C.-Y. (2018). The wave attenuation mechanism of the periodic local resonant metamaterial. *Journal of Sound and Vibration*, 412:349–359.

Chao, C., Shi, B., Dai, W., and Yang, J. (2023). Performance analysis of frictional inerter-based vibration isolator. *Journal of Vibration Engineering & Technologies*, 11(6):2793–2817.

Chaunsali, R., Chen, C.-W., and Yang, J. (2018). Experimental demonstration of topological waveguiding in elastic plates with local resonators. *New Journal of Physics*, 20(11):113036.

Chen, C., Chen, T., Wang, Y., Wu, J., and Zhu, J. (2019). Observation of topological locally resonate and bragg edge modes in a two-dimensional slit-typed sonic crystal. *Applied Physics Express*, 12(9):097001.

Chen, H., Zeng, H., Ding, C., Luo, C., and Zhao, X. (2013). Double-negative acoustic metamaterial based on hollow steel tube meta-atom. *Journal of Applied Physics*, 113(10).

Chen, H.-Y., Mao, X.-Y., Ding, H., and Chen, L.-Q. (2020a). Elimination of multimode resonances of composite plate by inertial nonlinear energy sinks. *Mechanical Systems and Signal Processing*, 135:106383.

Chen, M. Z., Hu, Y., Huang, L., and Chen, G. (2014). Influence of inerter on natural frequencies of vibration systems. *Journal of Sound and Vibration*, 333(7):1874–1887.

Chen, Z., Zhou, W., and Lim, C. (2020b). Active control for acoustic wave propagation in nonlinear diatomic acoustic metamaterials. *International Journal of Non-Linear Mechanics*, 125:103535.

Cheng, Y., Xu, J., and Liu, X. (2008). One-dimensional structured ultrasonic metamaterials with simultaneously negative dynamic density and modulus. *Physical Review B*, 77(4):045134.

Ciğeroğlu, E. and Özgüven, H. N. (2006). Nonlinear vibration analysis of bladed disks with dry friction dampers. *Journal of Sound and Vibration*, 295(3-5):1028–1043.

Cockburn, B. and Shu, C.-W. (2001). Runge–kutta discontinuous galerkin methods for convection-dominated problems. *Journal of scientific computing*, 16:173–261.

Cummer, S. A., Christensen, J., and Alù, A. (2016). Controlling sound with acoustic metamaterials. *Nature Reviews Materials*, 1(3):1–13.

Dahl, P. R. (1976). Solid friction damping of mechanical vibrations. *AIAA Journal*, 14(12):1675–1682.

Dai, J., Xu, Z.-D., and Gai, P.-P. (2019). Tuned mass-damper-inerter control of wind-induced vibration of flexible structures based on inerter location. *Engineering Structures*, 199:109585.

Dai, W., Li, T., and Yang, J. (2022a). Energy flow and performance of a nonlinear vibration isolator exploiting geometric nonlinearity by embedding springs in linkages. *Acta Mechanica*, 233(4):1663–1687.

Dai, W., Shi, B., and Yang, J. (2024). Vibration isolation performance enhancement using hybrid nonlinear inerter and negative stiffness based on linkage mechanism. *Journal of Vibration Engineering & Technologies*, 12(1):837–855.

Dai, W., Shi, B., Yang, J., Zhu, X., and Li, T. (2022b). Enhanced suppression of longitudinal vibration transmission in propulsion shaft system using nonlinear tuned mass damper inerter. *Journal of Vibration and Control*, page 10775463221081183.

Dai, W. and Yang, J. (2021). Vibration transmission and energy flow of impact oscillators with nonlinear motion constraints created by diamond-shaped linkage mechanism. *International Journal of Mechanical Sciences*, 194:106212.

Dai, W., Yang, J., and Shi, B. (2020). Vibration transmission and power flow in impact oscillators with linear and nonlinear constraints. *International Journal of Mechanical Sciences*, 168:105234.

Dai, W., Yang, J., and Wiercigroch, M. (2022c). Vibration energy flow transmission in systems with coulomb friction. *International Journal of Mechanical Sciences*, 214:106932.

Dano, M.-L., Kamal, E., and Gendron, G. (2007). Analysis of bolted joints in composite laminates: Strains and bearing stiffness predictions. *Composite Structures*, 79(4):562–570.

De Domenico, D., Deastra, P., Ricciardi, G., Sims, N. D., and Wagg, D. J. (2019). Novel fluid inerter based tuned mass dampers for optimised structural control of base-isolated buildings. *Journal of the Franklin Institute*, 356(14):7626–7649.

Dehkordi, M. K., Osguei, A. T., Khamoushi, I., Pavlovskaia, E., and Wiercigroch, M. (2022). Internal mechanics of anti stick–slip tool. *International Journal of Mechanical Sciences*, 221:107188.

DePauw, D., Singh, T., Nouh, M., et al. (2018). Dispersion transitions and pole-zero characteristics of finite inertially amplified acoustic metamaterials. *Journal of Applied Physics*, 123(10).

Deymier, P. A. (2013). *Acoustic metamaterials and phononic crystals*, volume 173. Springer Science & Business Media.

Dezfuli, F. H., Li, S., Alam, M. S., and Wang, J.-Q. (2017). Effect of constitutive models on the seismic response of an sma-lrb isolated highway bridge. *Engineering Structures*, 148:113–125.

Ding, Y., Liu, Z., Qiu, C., and Shi, J. (2007). Metamaterial with simultaneously negative bulk modulus and mass density. *Physical review letters*, 99(9):093904.

Dong, Z., Chronopoulos, D., and Yang, J. (2021). Enhancement of wave damping for metamaterial beam structures with embedded inerter-based configurations. *Applied Acoustics*, 178:108013.

Dong, Z., Shi, B., Yang, J., and Li, T. (2022). Suppression of vibration transmission in coupled systems with an inerter-based nonlinear joint. *Nonlinear Dynamics*, 107(2):1637–1662.

Donmez, A., Cigeroglu, E., and Ozgen, G. O. (2020). An improved quasi-zero stiffness vibration isolation system utilizing dry friction damping. *Nonlinear Dynamics*, 101:107–121.

El-Borgi, S., Fernandes, R., Rajendran, P., Yazbeck, R., Boyd, J., and Lagoudas, D. (2020). Multiple bandgap formation in a locally resonant linear metamaterial beam: Theory and experiments. *Journal of Sound and Vibration*, 488:115647.

Fabro, A. T., Meng, H., and Chronopoulos, D. (2020). Uncertainties in the attenuation performance of a multi-frequency metastructure from additive manufacturing. *Mechanical Systems and Signal Processing*, 138:106557.

Fan, L., He, Y., Zhao, X., and Chen, X.-a. (2020a). Subwavelength and broadband tunable topological interface state for flexural wave in one-dimensional locally resonant phononic crystal. *Journal of Applied Physics*, 127(23).

Fan, R., Xiong, B., Peng, R., and Wang, M. (2020b). Constructing metastructures with broadband electromagnetic functionality. *Advanced Materials*, 32(27):1904646.

Fang, N., Xi, D., Xu, J., Ambati, M., Srituravanich, W., Sun, C., and Zhang, X. (2006). Ultrasonic metamaterials with negative modulus. *Nature materials*, 5(6):452–456.

Fang, X., Wen, J., Yin, J., Yu, D., and Xiao, Y. (2016). Broadband and tunable one-dimensional strongly nonlinear acoustic metamaterials: theoretical study. *Physical Review E*, 94(5):052206.

Ferri, A. A. (1995). Friction damping and isolation systems. *Journal of Vibration and Acoustics*, 117(B):196–206.

Filiatrault, A. and Cherry, S. (1987). Performance evaluation of friction damped braced steel frames under simulated earthquake loads. *Earthquake spectra*, 3(1):57–78.

Fitzgerald, T., Anagnos, T., Goodson, M., and Zsutty, T. (1989). Slotted bolted connections in aseismic design for concentrically braced connections. *Earthquake spectra*, 5(2):383–391.

Fok, L., Ambati, M., and Zhang, X. (2008). Acoustic metamaterials. *MRS bulletin*, 33(10):931–934.

Gao, C., Kuhlmann-Wilsdorf, D., and Makel, D. D. (1993). Fundamentals of stick-slip. *Wear*, 162:1139–1149.

Gao, N., Zhang, Z., Deng, J., Guo, X., Cheng, B., and Hou, H. (2022).

Acoustic metamaterials for noise reduction: a review. *Advanced Materials Technologies*, 7(6):2100698.

Garcia-Chocano, V. M., Graciá-Salgado, R., Torrent, D., Cervera, F., and Sanchez-Dehesa, J. (2012). Quasi-two-dimensional acoustic metamaterial with negative bulk modulus. *Physical Review B*, 85(18):184102.

Gaul, L. and Lenz, J. (1997). Nonlinear dynamics of structures assembled by bolted joints. *Acta Mechanica*, 125(1-4):169–181.

Gaul, L. and Nitsche, R. (2001). The role of friction in mechanical joints. *Applied Mechanics Reviews*, 54(2):93–106.

Giaralis, A. and Petrini, F. (2017). Wind-induced vibration mitigation in tall buildings using the tuned mass-damper-inerter. *Journal of Structural Engineering*, 143(9):04017127.

Gonzalez-Buelga, A., Lazar, I. F., Jiang, J. Z., Neild, S. A., and Inman, D. J. (2017). Assessing the effect of nonlinearities on the performance of a tuned inerter damper. *Structural Control and Health Monitoring*, 24(3):e1879.

Gonzalez-Buelga, A., Clare, L., Neild, S., Burrow, S., and Inman, D. (2015). An electromagnetic vibration absorber with harvesting and tuning capabilities. *Structural Control and Health Monitoring*, 22(11):1359–1372.

Goyder, H. and White, R. (1980). Vibrational power flow from machines into built-up structures, part i: introduction and approximate analyses of beam and plate-like foundations. *Journal of Sound and Vibration*, 68(1):59–75.

Grigorian, C. E. (1994). *Energy dissipation with slotted bolted connections*. University of California, Berkeley.

Grigorian, C. E., Yang, T.-S., and Popov, E. P. (1993). Slotted bolted connection energy dissipators. *Earthquake Spectra*, 9(3):491–504.

Haberman, M. R. and Guild, M. D. (2016). Acoustic metamaterials. *Physics Today*, 69(6):42–48.

Hahn, G. (1991). A modified euler method for dynamic analyses. *International Journal for Numerical Methods in Engineering*, 32(5):943–955.

Halling, J. and Burton, R. A. (1977). Principles of tribology. *Journal of Lubrication Technology*, 99(2):305–306.

He, X. (2011). A review of finite element analysis of adhesively bonded joints. *International Journal of Adhesion and Adhesives*, 31(4):248–264.

Henrych, J. (1981). *The dynamics of arches and frames*. Elsevier Scientific Pub. Co., Amsterdam New York.

Hernández, E. and Vellojin, J. (2021). A locking-free finite element formulation for a non-uniform linear viscoelastic timoshenko beam. *Computers & Mathematics with Applications*, 99:305–322.

Hessabi, R. M. and Mercan, O. (2016). Investigations of the application of gyro-mass dampers with various types of supplemental dampers for vibration control of building structures. *Engineering Structures*, 126:174–186.

Heyliger, P. and Reddy, J. (1988). A higher order beam finite element for bending and vibration problems. *Journal of sound and vibration*, 126(2):309–326.

Hu, G., Lan, C., Tang, L., and Yang, Y. (2022). Local resonator stimulated polarization transition in metamaterials and the formation of topological interface states. *Mechanical Systems and Signal Processing*, 165:108388.

Hua, X.-g., Tai, Y.-j., Huang, Z.-w., and Chen, Z.-q. (2021). Optimal design and performance evaluation of a novel hysteretic friction tuned inerter damper for vibration control systems. *Structural Control and Health Monitoring*, 28(8):e2775.

Huang, H. and Sun, C. (2011). Locally resonant acoustic metamaterials with 2d anisotropic effective mass density. *Philosophical Magazine*, 91(6):981–996.

Huang, H., Sun, C., and Huang, G. (2009). On the negative effective mass density in acoustic metamaterials. *International Journal of Engineering Science*, 47(4):610–617.

Huang, X.-R., Jézéquel, L., Besset, S., Li, L., and Sauvage, O. (2018). Nonlinear modal synthesis for analyzing structures with a frictional interface using a generalized masing model. *Journal of Sound and Vibration*, 434:166–191.

Hussein, M. I. and Frazier, M. J. (2013). Metadamping: An emergent phenomenon in dissipative metamaterials. *Journal of sound and vibration*, 332(20):4767–4774.

Hussein, M. I., Leamy, M. J., and Ruzzene, M. (2014). Dynamics of phononic materials and structures: Historical origins, recent progress, and future outlook. *Applied Mechanics Reviews*, 66(4):040802.

Hwang, J.-S., Kim, J., and Kim, Y.-M. (2007). Rotational inertia dampers with toggle bracing for vibration control of a building structure. *Engineering Structures*, 29(6):1201–1208.

Iwan, W. D. (1966). A distributed-element model for hysteresis and its steady-state dynamic response. *Journal of Applied Mechanics*, 33(4):893–900.

Iyama, J., Seo, C., Ricles, J., and Sause, R. (2009). Self-centering mrfs with bottom flange friction devices under earthquake loading. *Journal of Constructional Steel Research*, 65(2):314–325.

Jaisee, S., Yue, F., and Ooi, Y. H. (2021). A state-of-the-art review on passive friction dampers and their applications. *Engineering Structures*, 235:112022.

Javidialesaadi, A. and Wierschem, N. E. (2019). An inerter-enhanced nonlinear energy sink. *Mechanical Systems and Signal Processing*, 129:449–454.

Jensen, J. S. (2003). Phononic band gaps and vibrations in one-and two-dimensional mass–spring structures. *Journal of sound and Vibration*, 266(5):1053–1078.

Ji, J., Luo, Q., and Ye, K. (2021). Vibration control based metamaterials and origami structures: A state-of-the-art review. *Mechanical Systems and Signal Processing*, 161:107945.

Jia, Z., Chen, Y., Yang, H., and Wang, L. (2018). Designing phononic crystals with wide and robust band gaps. *Physical Review Applied*, 9(4):044021.

Jiang, S., Chen, H., Dai, L., Hu, H., and Laude, V. (2017). Multiple low-frequency broad band gaps generated by a phononic crystal of periodic circular cavity sandwich plates. *Composite Structures*, 176:294–303.

Johanastrom, K. and Canudas-De-Wit, C. (2008). Revisiting the lugre friction model. *IEEE Control Systems Magazine*, 28(6):101–114.

John, E. D. and Wagg, D. J. (2019). Design and testing of a frictionless mechanical inerter device using living-hinges. *Journal of the Franklin Institute*, 356(14):7650–7668.

Jung, J., Kim, H.-G., Goo, S., Chang, K.-J., and Wang, S. (2019). Realisation of a locally resonant metamaterial on the automobile panel structure to reduce noise radiation. *Mechanical Systems and Signal Processing*, 122:206–231.

Kashani, H. (2017). Analytical parametric study of bi-linear hysteretic model of dry friction under harmonic, impulse and random excitations. *Nonlinear Dynamics*, 89(1):267–279.

Kawamata, S., Yoneda, M., and Hangai, Y. (1973). Development of a vibration control system of structures by means of mass pumps. *Institute of Industrial Science, University of Tokyo: Tokyo, Japan.*

Khoo, H.-H., Clifton, C., MacRae, G., Zhou, H., and Ramhormozian, S. (2015). Proposed design models for the asymmetric friction connection. *Earthquake Engineering & Structural Dynamics*, 44(8):1309–1324.

Kim, H.-J. and Christopoulos, C. (2008). Friction damped posttensioned self-centering steel moment-resisting frames. *Journal of Structural Engineering*, 134(11):1768–1779.

Krack, M. and Gross, J. (2019). *Harmonic balance for nonlinear vibration problems*, volume 1. Springer.

Krack, M., Panning-von Scheidt, L., and Wallaschek, J. (2013). A method for nonlinear modal analysis and synthesis: Application to harmonically forced and self-excited mechanical systems. *Journal of Sound and Vibration*, 332(25):6798–6814.

Kulkarni, P. P. and Manimala, J. M. (2016). Longitudinal elastic wave propagation characteristics of inertant acoustic metamaterials. *Journal of Applied Physics*, 119(24).

Kumar, S., Bhushan, P., Prakash, O., and Bhattacharya, S. (2018). Double negative acoustic metastructure for attenuation of acoustic emissions. *Applied Physics Letters*, 112(10):101905.

Kumar, S. and Lee, H. P. (2020). Labyrinthine acoustic metastructures enabling broadband sound absorption and ventilation. *Applied Physics Letters*, 116(13):134103.

Lazar, I., Neild, S., and Wagg, D. (2014). Using an inerter-based device for structural vibration suppression. *Earthquake Engineering & Structural Dynamics*, 43(8):1129–1147.

Lazarov, B. S. and Jensen, J. S. (2007). Low-frequency band gaps in chains with attached non-linear oscillators. *International Journal of Non-Linear Mechanics*, 42(10):1186–1193.

Lee, C.-H., Ryu, J., Oh, J., Yoo, C.-H., and Ju, Y. K. (2016). Friction between a new low-steel composite material and milled steel for safe dampers. *Engineering Structures*, 122:279–295.

Lee, D., Ku, N., Kim, T.-W., Kim, J., Lee, K.-Y., and Son, Y.-S. (2011). Development and application of an intelligent welding robot system for shipbuilding. *Robotics and Computer-Integrated Manufacturing*, 27(2):377–388.

Li, B., Alamri, S., and Tan, K. (2017a). A diatomic elastic metamaterial for tunable asymmetric wave transmission in multiple frequency bands. *Scientific Reports*, 7(1):6226.

Li, C., Liang, M., Wang, Y., and Dong, Y. (2012). Vibration suppression using two-terminal flywheel. part i: Modeling and characterization. *Journal of Vibration and Control*, 18(8):1096–1105.

Li, D., Botto, D., Li, R., Xu, C., and Zhang, W. (2022). Experimental and theoretical studies on friction contact of bolted joint interfaces. *International Journal of Mechanical Sciences*, 236:107773.

Li, F., Zhang, C., and Liu, C. (2017b). Active tuning of vibration and wave propagation in elastic beams with periodically placed piezoelectric actuator/sensor pairs. *Journal of Sound and Vibration*, 393:14–29.

Li, H., Li, Y., and Li, J. (2020a). Negative stiffness devices for vibration isolation applications: a review. *Advances in Structural Engineering*, 23(8):1739–1755.

Li, J. and Chan, C. T. (2004). Double-negative acoustic metamaterial. *Physical Review E*, 70(5):055602.

Li, J., Yuan, Y., Wang, J., Bao, R., and Chen, W. (2021a). Propagation of nonlinear waves in graded flexible metamaterials. *International Journal of Impact Engineering*, 156:103924.

Li, Y., Li, H., Liu, X., and Yan, S. (2021b). Bandgap and wave propagation of spring–mass–truss elastic metamaterial with a scissor-like structure. *Journal of Physics D: Applied Physics*, 55(5):055303.

Li, Y., Shen, W., and Zhu, H. (2019a). Vibration mitigation of stay cables using electromagnetic inertial mass dampers: Full-scale experiment and analysis. *Engineering Structures*, 200:109693.

Li, Y., Wang, X., and Yan, G. (2021c). Configuration effect and bandgap mechanism of quasi-one-dimensional periodic lattice structure. *International Journal of Mechanical Sciences*, 190:106017.

Li, Y., Zhang, Y., and Xie, S. (2020b). A lightweight multilayer honeycomb membrane-type acoustic metamaterial. *Applied Acoustics*, 168:107427.

Li, Y., Zhou, Q., Zhou, L., Zhu, L., and Guo, K. (2019b). Flexural wave band gaps and vibration attenuation characteristics in periodic bi-directionally orthogonal stiffened plates. *Ocean Engineering*, 178:95–103.

Liang, Z. and Li, J. (2012). Extreme acoustic metamaterial by coiling up space. *Physical review letters*, 108(11):114301.

Lin, S., Zhang, Y., Liang, Y., Liu, Y., Liu, C., and Yang, Z. (2021). Bandgap characteristics and wave attenuation of metamaterials based on negative-stiffness dynamic vibration absorbers. *Journal of Sound and Vibration*, 502:116088.

Liu, F., Wang, L., Jin, D., Liu, X., and Lu, P. (2021). Equivalent beam model for spatial repetitive lattice structures with hysteretic nonlinear joints. *International Journal of Mechanical Sciences*, 200:106449.

Liu, Y., Shi, D., He, H., Liu, S., and Fan, H. (2022a). Double-resonator based metaconcrete composite slabs and vibration attenuation mechanism. *Engineering Structures*, 262:114392.

Liu, Y., Yang, J., Yi, X., and Chronopoulos, D. (2022b). Enhanced suppression of low-frequency vibration transmission in metamaterials with linear and nonlinear inerters. *Journal of Applied Physics*, 131(10).

Liu, Y., Yang, J., Yi, X., Guo, W., Feng, Q., and Chronopoulos, D. (2022c). Enhanced vibration suppression using diatomic acoustic metamaterial with negative stiffness mechanism. *Engineering Structures*, 271:114939.

Liu, Y., Yang, J., Zhou, C., Elmadih, W., Zhu, J., and Chronopoulos, D. (2023). Flexnertia: A novel dissipation mechanism for structural vibration reduction through coupling of flexural motion with an inerter. *Mechanics of Advanced Materials and Structures*, pages 1–10.

Liu, Y.-f., Huang, J.-k., Li, Y.-g., and Shi, Z.-f. (2019). Trees as large-scale natural metamaterials for low-frequency vibration reduction. *Construction and Building Materials*, 199:737–745.

Liu, Z., Chan, C. T., and Sheng, P. (2005). Analytic model of phononic crystals with local resonances. *Physical Review B*, 71(1):014103.

Liu, Z., Zhang, X., Mao, Y., Zhu, Y., Yang, Z., Chan, C. T., and Sheng, P. (2000). Locally resonant sonic materials. *science*, 289(5485):1734–1736.

Loo, W. Y., Quenneville, P., and Chouw, N. (2014). A new type of symmetric slip-friction connector. *Journal of Constructional Steel Research*, 94:11–22.

Lopez, I., Busturia, J., and Nijmeijer, H. (2004). Energy dissipation of a friction damper. *Journal of Sound and Vibration*, 278(3):539–561.

Lu, K., Wu, J. H., Guan, D., Gao, N., and Jing, L. (2016). A lightweight low-frequency sound insulation membrane-type acoustic metamaterial. *Aip Advances*, 6(2).

Luo, H., Shen, Y., Liao, Z., Yang, X., Gao, B., and He, B. (2022). Spidroin composite biomimetic multifunctional skin with meta-structure. *Advanced Materials Technologies*, page 2101097.

Ma, R., Bi, K., and Hao, H. (2021). Inerter-based structural vibration control: A state-of-the-art review. *Engineering Structures*, 243:112655.

MacRae, G. A., Clifton, G. C., Mackinven, H., Mago, N., Butterworth, J., and Pampanin, S. (2010). The sliding hinge joint moment connection. *Bulletin of the New Zealand Society for Earthquake Engineering*, 43(3):202–212.

Marino, L. and Cicirello, A. (2020). Experimental investigation of a single-degree-of-freedom system with coulomb friction. *Nonlinear Dynamics*, 99(3):1781–1799.

Mathis, A. T., Balaji, N. N., Kuether, R. J., Brink, A. R., Brake, M. R., and Quinn, D. D. (2020). A review of damping models for structures with mechanical joints. *Applied Mechanics Reviews*, 72(4):040802.

Meng, H., Chronopoulos, D., Fabro, A. T., Maskery, I., and Chen, Y. (2020). Optimal design of rainbow elastic metamaterials. *International Journal of Mechanical Sciences*, 165:105185.

Miguel, L. P., Teloli, R. d. O., and Silva, S. d. (2022). Bayesian model identification through harmonic balance method for hysteresis prediction in bolted joints. *Nonlinear Dynamics*, 107(1):77–98.

Milton, G. W. and Willis, J. R. (2007). On modifications of newton's second law and linear continuum elastodynamics. *Proceedings of the*

Royal Society A: Mathematical, Physical and Engineering Sciences, 463(2079):855–880.

Mohammadi Estakhri, N., Edwards, B., and Engheta, N. (2019). Inverse-designed metastructures that solve equations. *Science*, 363(6433):1333–1338.

Moraes, F. d. H., Silveira, M., and Gonçalves, P. J. P. (2018). On the dynamics of a vibration isolator with geometrically nonlinear inerter. *Nonlinear Dynamics*, 93:1325–1340.

Moscatelli, M., Ardito, R., Driemeier, L., and Comi, C. (2019). Band-gap structure in two-and three-dimensional cellular locally resonant materials. *Journal of Sound and Vibration*, 454:73–84.

Mosquera-Sánchez, J. A. and De Marqui Jr, C. (2021). Dynamics and wave propagation in nonlinear piezoelectric metastructures. *Nonlinear Dynamics*, 105(4):2995–3023.

Muhammad and Lim, C. W. (2021a). Phononic metastructures with ultrawide low frequency three-dimensional bandgaps as broadband low frequency filter. *Scientific Reports*, 11(1):7137.

Muhammad and Lim, C. W. (2021b). Ultrawide bandgap by 3d monolithic mechanical metastructure for vibration and noise control. *Archives of Civil and Mechanical Engineering*, 21(2):52.

Nagarajaiah, S. and Sen, D. (2020). Apparent-weakening by adaptive passive stiffness shaping along the height of multistory building using negative stiffness devices and dampers for seismic protection. *Engineering Structures*, 220:110754.

NBSPRC (2018). Classification of strategic emerging industries (2018). https://www.gov.cn/zhengce/zhengceku/2018-12/31/content_5433037.htm.

Nguyen, X. B., Komatsuzaki, T., and Truong, H. T. (2022). Adaptive parameter identification of bouc-wen hysteresis model for a vibration system using magnetorheological elastomer. *International Journal of Mechanical Sciences*, 213:106848.

NSFC and CAS (2012). *China's discipline development strategy in the next 10 years*. Beijing: Science Press.

Padthe, A. K., Drincic, B., Oh, J., Rizos, D. D., Fassois, S. D., and Bernstein, D. S. (2008). Duhem modeling of friction-induced hysteresis. *IEEE Control Systems Magazine*, 28(5):90–107.

Pai, P. F. (2010). Metamaterial-based broadband elastic wave absorber. *Journal of intelligent material systems and structures*, 21(5):517–528.

Pai, P. F., Peng, H., and Jiang, S. (2014). Acoustic metamaterial beams based on multi-frequency vibration absorbers. *International journal of mechanical sciences*, 79:195–205.

Pall, A. et al. (2004). Performance-based design using pall friction dampers-an economical design solution. In *13th World Conference on Earthquake Engineering, Vancouver, BC, Canada*, volume 71.

Pall, A. S. and Marsh, C. (1981). Friction-damped concrete shearwalls. In *Journal Proceedings*, volume 78, pages 187–193.

Pall, A. S. and Marsh, C. (1982). Response of friction damped braced frames. *Journal of the Structural Division*, 108(6):1313–1323.

Pall, A. S., Marsh, C., and Fazio, P. (1980). Friction joints for seismic control of large panel structures. *Journal of Prestressed Concrete Institute*, 25(6):38–61.

Pall, A. S. and Pall, R. (1996). Friction-dampers for seismic control of buildings–a canadian experience. In *Eleventh world conference on earthquake engineering, Acapulco, Mexico*.

Papageorgiou, C., Houghton, N. E., and Smith, M. C. (2009). Experimental testing and analysis of inerter devices. *Journal of Dynamic systems, Measurement, and Control*, 131(1).

Paronesso, M. and Lignos, D. G. (2021). Experimental study of sliding friction damper with composite materials for earthquake resistant structures. *Engineering Structures*, 248:113063.

Pendry, J. B. (2000). Negative refraction makes a perfect lens. *Physical review letters*, 85(18):3966.

Peris, E. et al. (2020). Environmental noise in europe: 2020. *Eur. Environ. Agency*, 1:104.

Persson, B. N. (2013). *Sliding friction: physical principles and applications*. Springer Science & Business Media.

Petrini, F., Giaralis, A., and Wang, Z. (2020). Optimal tuned mass-damper-inerter (tmdi) design in wind-excited tall buildings for occupants' comfort serviceability performance and energy harvesting. *Engineering Structures*, 204:109904.

Pietrosanti, D., De Angelis, M., and Giaralis, A. (2020). Experimental study and numerical modeling of nonlinear dynamic response of sdof system equipped with tuned mass damper inerter (tmdi) tested on shaking table under harmonic excitation. *International Journal of Mechanical Sciences*, 184:105762.

Porubov, A. and Andrianov, I. (2013). Nonlinear waves in diatomic crystals. *Wave Motion*, 50(7):1153–1160.

Providakis, C. (2008). Effect of lrb isolators and supplemental viscous dampers on seismic isolated buildings under near-fault excitations. *Engineering structures*, 30(5):1187–1198.

Qiu, C., Liu, J., and Du, X. (2022). Cyclic behavior of sma slip friction damper. *Engineering Structures*, 250:113407.

Raghavan, L. and Phani, A. S. (2013). Local resonance bandgaps in periodic media: Theory and experiment. *The Journal of the Acoustical Society of America*, 134(3):1950–1959.

Rakowski, J. (1990). The interpretation of the shear locking in beam elements. *Computers & Structures*, 37(5):769–776.

Rivin, E. (2004). Passive vibration isolation. *Applied Mechanics Reviews*, 57(6):B31–B32.

Royston, T. and Singh, R. (1996). Optimization of passive and active nonlinear vibration mounting systems based on vibratory power transmission. *Journal of Sound and Vibration*, 194(3):295–316.

Sachan, M. and Majetich, S. (2005). Darpa meta-materials program report.

Sainidou, R., Djafari-Rouhani, B., Pennec, Y., and Vasseur, J. O. (2006). Locally resonant phononic crystals made of hollow spheres or cylinders. *Physical Review B*, 73(2):024302.

Saito, K. (2007). Optimum response control of 1-dof system using linear viscous damper with inertial mass and its kelvin-type modeling. *Journal of Structural Construction Engineering Architectural Institute of Japan*, 53:53.

Saito, K. and Inoue, N. (2007). A study on optimum response control of passive control systems using viscous damper with inertial masssubstituting equivalent nonlinear viscous elements for linear viscous elements in optimum control systems. *AIJ Journal of Technology and Design*, 13(26).

Salvatore, A., Carboni, B., and Lacarbonara, W. (2022). Nonlinear dynamic response of an isolation system with superelastic hysteresis and negative stiffness. *Nonlinear Dynamics*, pages 1–26.

Sepehri, S., Mashhadi, M. M., and Fakhrabadi, M. M. S. (2021). Manipulation of wave motion in smart nonlinear phononic crystals made of shape memory alloys. *Physica Scripta*, 96(12):125527.

Sepehri, S., Mashhadi, M. M., and Fakhrabadi, M. M. S. (2022). Dispersion curves of electromagnetically actuated nonlinear monoatomic and mass-in-mass lattice chains. *International Journal of Mechanical Sciences*, 214:106896.

Settimi, V., Lepidi, M., and Bacigalupo, A. (2021). Nonlinear dispersion properties of one-dimensional mechanical metamaterials with inertia amplification. *International Journal of Mechanical Sciences*, 201:106461.

Sheng, P., Zhang, X., Liu, Z., and Chan, C. T. (2003). Locally resonant sonic materials. *Physica B: Condensed Matter*, 338(1-4):201–205.

Shi, B., Dai, W., and Yang, J. (2022a). Performance analysis of a nonlinear inerter-based vibration isolator with inerter embedded in a linkage mechanism. *Nonlinear Dynamics*, 109(2):419–442.

Shi, B., Dai, W., and Yang, J. (2024). Performance enhancement of vehicle suspension system with geometrically nonlinear inerters. *Archive of Applied Mechanics*, 94(1):39–55.

Shi, B., Yang, J., and Jiang, J. Z. (2022b). Tuning methods for tuned inerter dampers coupled to nonlinear primary systems. *Nonlinear Dynamics*, 107(2):1663–1685.

Shi, B., Yang, J., and Li, T. (2021). Enhancing vibration isolation performance by exploiting novel spring-bar mechanism. *Applied Sciences*, 11(19):8852.

Shi, B., Yang, J., and Rudd, C. (2019). On vibration transmission in oscillating systems incorporating bilinear stiffness and damping elements. *International Journal of Mechanical Sciences*, 150:458–470.

Shi, B., Yang, J., and Wiercigroch, M. (2023). Vibrational energy transfer in coupled mechanical systems with nonlinear joints. *International Journal of Mechanical Sciences*, 260:108612.

Sigalas, M. M. (1992). Elastic and acoustic wave band structure. *Journal of sound and vibration*, 158(2):377–382.

Singh, R., Nie, Y., Gao, M., Agarwal, A. M., and Anthony, B. W. (2021). Inverse design of photonic meta-structure for beam collimation in on-chip sensing. *Scientific Reports*, 11(1):1–11.

Smith, M. C. (2002). Synthesis of mechanical networks: the inerter. *IEEE Transactions on automatic control*, 47(10):1648–1662.

Smith, M. C. (2020). The inerter: A retrospective. *Annual Review of Control, Robotics, and Autonomous Systems*, 3(1):361–391.

Stein, A., Nouh, M., and Singh, T. (2022). Widening, transition and coalescence of local resonance band gaps in multi-resonator acoustic metamaterials: From unit cells to finite chains. *Journal of Sound and Vibration*, 523:116716.

Su, N., Xia, Y., and Peng, S. (2022). Filter-based inerter location dependence analysis approach of tuned mass damper inerter (tmdi) and optimal design. *Engineering Structures*, 250:113459.

Sugino, C., Xia, Y., Leadenham, S., Ruzzene, M., and Erturk, A. (2017). A general theory for bandgap estimation in locally resonant metastructures. *Journal of Sound and Vibration*, 406:104–123.

Sun, F.-F., Wang, M., and Nagarajaiah, S. (2021). Multi-objective optimal design and seismic performance of negative stiffness damped outrigger structures considering damping cost. *Engineering Structures*, 229:111615.

Sun, L., Hong, D., and Chen, L. (2017). Cables interconnected with tuned inerter damper for vibration mitigation. *Engineering Structures*, 151:57–67.

Symans, M. D., Charney, F. A., Whittaker, A., Constantinou, M. C., Kircher, C., Johnson, M. W., and McNamara, R. J. (2008). Energy dissipation systems for seismic applications: current practice and recent developments. *Journal of structural engineering*, 134(1):3–21.

Tan, K. T., Huang, H., and Sun, C. (2012). Optimizing the band gap of effective mass negativity in acoustic metamaterials. *Applied Physics Letters*, 101(24).

Tian, S., Ren, F., Wu, J., Mo, J., Zhang, X., Lai, M., and Bao, W. (2023). Axial compressive behavior of a novel assembled joint connecting fc-src columns and rc beams with pre-damage. *Engineering Structures*, 293:116647.

Tirca, L. (2015). Friction dampers for seismic protections of steel buildings subjected to earthquakes: Emphasis on structural design. *Encyclopedia of Earthquake Engineering, Springer, Berlin*, 1058:1070.

Torrent, D. and Sánchez-Dehesa, J. (2008). Acoustic cloaking in two dimensions: a feasible approach. *New Journal of Physics*, 10(6):063015.

Tsai, K.-C., Chou, C.-C., Lin, C.-L., Chen, P.-C., and Jhang, S.-J. (2008). Seismic self-centering steel beam-to-column moment connections using bolted friction devices. *Earthquake Engineering & Structural Dynamics*, 37(4):627–645.

Vezina, S., Proulx, P., Pall, R., and Pall, A. (1992). Friction-dampers for aseismic design of canadian space agency. In *10th World conference on earthquake engineering*, pages 4123–4128.

Von Groll, G. and Ewins, D. J. (2001). The harmonic balance method with arc-length continuation in rotor/stator contact problems. *Journal of sound and vibration*, 241(2):223–233.

Wagg, D. J. (2021). A review of the mechanical inerter: historical context, physical realisations and nonlinear applications. *Nonlinear Dynamics*, 104(1):13–34.

Walser, R. M. (2001). Electromagnetic metamaterials. In *Complex Mediums II: beyond linear isotropic dielectrics*, volume 4467, pages 1–15. SPIE.

Wang, D., Song, L., Zhu, R., and Cao, P. (2022a). Nonlinear dynamics and stability analysis of dry friction damper for supercritical transmission shaft. *Nonlinear Dynamics*, 110(4):3135–3149.

Wang, F.-C., Hong, M.-F., and Lin, T.-C. (2011). Designing and testing a hydraulic inerter. *Proceedings of the Institution of Mechanical Engineers, Part C: Journal of Mechanical Engineering Science*, 225(1):66–72.

Wang, J., Huang, H. W., Zhang, B., Menq, F.-Y., Nakshatrala, K. B., Mo, Y., and Stokoe, K. (2022b). Active isolation tests of metamaterial-based barriers and foundation. *Engineering Structures*, 260:114253.

Wang, K., Zhou, J., Xu, D., and Ouyang, H. (2019a). Lower band gaps of longitudinal wave in a one-dimensional periodic rod by exploiting geometrical nonlinearity. *Mechanical Systems and Signal Processing*, 124:664–678.

Wang, M., Sun, F.-f., and Jin, H.-j. (2018). Performance evaluation of existing isolated buildings with supplemental passive pseudo-negative stiffness devices. *Engineering Structures*, 177:30–46.

Wang, M., Sun, F.-f., Yang, J.-q., and Nagarajaiah, S. (2019b). Seismic protection of sdof systems with a negative stiffness amplifying damper. *Engineering Structures*, 190:128–141.

Wang, P., Casadei, F., Shan, S., Weaver, J. C., and Bertoldi, K. (2014). Harnessing buckling to design tunable locally resonant acoustic metamaterials. *Physical review letters*, 113(1):014301.

Wang, Y., Wang, R., Meng, H., and Zhang, B. (2019c). An investigation of the dynamic performance of lateral inerter-based vibration isolator with geometrical nonlinearity. *Archive of Applied Mechanics*, 89:1953–1972.

Wang, Y., Zhang, C., Chen, W., Li, Z., Golub, M. V., and Fomenko, S. I. (2021). Precise and target-oriented control of the low-frequency lamb wave bandgaps. *Journal of Sound and Vibration*, 511:116367.

Wang, Y.-F., Wang, Y.-Z., Wu, B., Chen, W., and Wang, Y.-S. (2020). Tunable and active phononic crystals and metamaterials. *Applied Mechanics Reviews*, 72(4):040801.

Wang, Y.-Z. and Wang, Y.-S. (2018). Active control of elastic wave propagation in nonlinear phononic crystals consisting of diatomic lattice chain. *Wave Motion*, 78:1–8.

Wang, Z., Xing, J., and Price, W. (2002a). An investigation of power flow characteristics of l-shaped plates adopting a substructure approach. *Journal of Sound and Vibration*, 250(4):627–648.

Wang, Z., Xing, J., and Price, W. (2002b). Power flow analysis of indeterminate rod/beam systems using a substructure method. *Journal of Sound and Vibration*, 249(1):3–22.

Wen, Y.-K. (1976). Method for random vibration of hysteretic systems. *Journal of the Engineering Mechanics Division*, 102(2):249–263.

Woiwode, L., Balaji, N. N., Kappauf, J., Tubita, F., Guillot, L., Vergez, C., Cochelin, B., Grolet, A., and Krack, M. (2020). Comparison of two algorithms for harmonic balance and path continuation. *Mechanical Systems and Signal Processing*, 136:106503.

Wu, B., Zhang, J., Williams, M., and Ou, J. (2005). Hysteretic behavior of improved pall-typed frictional dampers. *Engineering Structures*, 27(8):1258–1267.

Wu, J., Ma, F., Zhang, S., and Shen, L. (2016). Application of acoustic metamaterials in low-frequency vibration and noise reduction. *Journal of Mechanical Engineering*, 52(13):68–78.

Wu, W. and Tang, B. (2020). An approximate method for solving force and displacement transmissibility of a geometrically nonlinear isolation system. *International journal of non-linear mechanics*, 125:103512.

Wu, Y., Lai, Y., and Zhang, Z.-Q. (2007). Effective medium theory for elastic metamaterials in two dimensions. *Physical Review B*, 76(20):205313.

Wu, Y., Li, L., Fan, Y., Ma, H., Wang, W., Christen, J.-L., and Ichchou, M. (2019). Design of semi-active dry friction dampers for steady-state vibration: sensitivity analysis and experimental studies. *Journal of Sound and Vibration*, 459:114850.

Xia, Y., Ruzzene, M., and Erturk, A. (2020). Bistable attachments for wideband nonlinear vibration attenuation in a metamaterial beam. *Nonlinear Dynamics*, 102:1285–1296.

Xie, S., Yang, S., Yang, C., and Wang, D. (2020). Sound absorption performance of a filled honeycomb composite structure. *Applied Acoustics*, 162:107202.

Xin, L., Siyuan, Y., Harry, L., Minghui, L., and Yanfeng, C. (2020). Topological mechanical metamaterials: A brief review. *Current Opinion in Solid State and Materials Science*, 24(5):100853.

Xing, J.-T. and Price, W. (1999). A power–flow analysis based on continuum dynamics. *Proceedings of the Royal Society of London. Series A: Mathematical, Physical and Engineering Sciences*, 455(1982):401–436.

Xiong, Y., Xing, J., and Price, W. (2001). Power flow analysis of complex coupled systems by progressive approaches. *Journal of Sound and Vibration*, 239(2):275–295.

Xiong, Y., Xing, J., and Price, W. (2003). A general linear mathematical model of power flow analysis and control for integrated structure–control systems. *Journal of Sound and Vibration*, 267(2):301–334.

Xiong, Y., Xing, J., and Price, W. (2005). Interactive power flow characteristics of an integrated equipment—nonlinear isolator—travelling flexible ship excited by sea waves. *Journal of Sound and Vibration*, 287(1-2):245–276.

Xu, X., Barnhart, M. V., Fang, X., Wen, J., Chen, Y., and Huang, G. (2019). A nonlinear dissipative elastic metamaterial for broadband wave mitigation. *International Journal of Mechanical Sciences*, 164:105159.

Yang, B., Guo, K., and Sun, J. (2022). Towards metamaterial rods with amplitude-dependent band gaps: A superelastic alloy-based approach. *Mechanical Systems and Signal Processing*, 166:108459.

Yang, C., Xu, B., Xia, J., Chang, H., Chen, X., and Ma, R. (2023). Mechanical behaviors of inter-module connections and assembled joints in modular steel buildings: A comprehensive review. *Buildings*, 13(7):1727.

Yang, F., Sedaghati, R., and Esmailzadeh, E. (2018). Free in-plane vibration of curved beam structures: a tutorial and the state of the art. *Journal of Vibration and Control*, 24(12):2400–2417.

Yang, J., Jiang, J. Z., and Neild, S. A. (2020). Dynamic analysis and performance evaluation of nonlinear inerter-based vibration isolators. *Nonlinear Dynamics*, 99:1823–1839.

Yang, J., Xiong, Y., and Xing, J. (2013). Dynamics and power flow behaviour of a nonlinear vibration isolation system with a negative stiffness mechanism. *Journal of sound and vibration*, 332(1):167–183.

Yang, J., Xiong, Y., and Xing, J. (2016). Vibration power flow and force transmission behaviour of a nonlinear isolator mounted on a nonlinear base. *International Journal of Mechanical Sciences*, 115:238–252.

Yasar, C., Karuk, V., Cavdar, E., and Ozdemir, G. (2024). Modifications in both lead and rubber properties of lrbs at low temperatures considering the size effect. *Engineering Structures*, 307:117902.

Yu, J., Dong, X., Su, X., Tao, X., and Li, X. (2021a). Design and testing of a semi-active inerter with magneto-rheological fluid valve. *Smart Materials and Structures*, 30(10):105035.

Yu, M., Fang, X., and Yu, D. (2021b). Combinational design of linear and nonlinear elastic metamaterials. *International Journal of Mechanical Sciences*, 199:106422.

Zhang, L., Xue, S., Zhang, R., Hao, L., Pan, C., and Xie, L. (2022). A novel crank inerter with simple realization: Constitutive model, experimental investigation and effectiveness assessment. *Engineering Structures*, 262:114308.

Zhang, R.-f., Cao, Y.-r., and Pan, C. (2019a). Inerter system and its state-of-the-art. *Engineering Mechanics*, 36(10):8–27.

Zhang, X.-l., Gao, Q., and Nie, J. (2018). The mem-inerter: A new mechanical element with memory. *Advances in Mechanical Engineering*, 10(6):1687814018778428.

Zhang, X.-L., Geng, C., Nie, J.-M., and Gao, Q. (2020). The missing mem-inerter and extended mem-dashpot found. *Nonlinear Dynamics*, 101(2):835–856.

Zhang, Y.-W., Lu, Y.-N., Zhang, W., Teng, Y.-Y., Yang, H.-X., Yang, T.-Z., and Chen, L.-Q. (2019b). Nonlinear energy sink with inerter. *Mechanical Systems and Signal Processing*, 125:52–64.

Zhao, D., Xiao, M., Ling, C. W., Chan, C. T., and Fung, K. H. (2018). Topological interface modes in local resonant acoustic systems. *Physical Review B*, 98(1):014110.

Zhao, H., Liu, Y., Wang, G., Wen, J., Yu, D., Han, X., and Wen, X. (2005). Resonance modes and gap formation in a two-dimensional solid phononic crystal. *Physical Review B*, 72(1):012301.

Zhao, Z., Chen, Q., Zhang, R., Pan, C., and Jiang, Y. (2020). Energy dissipation mechanism of inerter systems. *International Journal of Mechanical Sciences*, 184:105845.

Zheng, W., Wang, H., Tan, P., Li, J., and Liu, Y. (2022). Numerical modeling and experimental validation of sliding-lrbs considering hysteretic strength degradation. *Engineering Structures*, 262:114374.

Zhou, C., Yang, J., Zhu, Y., and Zhu, C. (2023). Energy transfer and vibration suppression of laminated composite plates coupled with a line hinge. *Mechanics of Advanced Materials and Structures*, pages 1–19.

Zhou, C., Yang, J., Zhu, Y., and Zhu, C. (2024a). Vibration energy transfer in variable stiffness laminated composite panel with a cutout. *Mechanics of Advanced Materials and Structures*, 31(1):230–245.

Zhou, C., Zhu, C., Guo, W., Xu, H., and Yang, J. (2024b). Vibration energy transfer in forced laminated composite box structure. *Mechanics of Advanced Materials and Structures*, pages 1–20.

Zhou, J., Wang, K., Xu, D., and Ouyang, H. (2017a). Multi-low-frequency flexural wave attenuation in euler–bernoulli beams using local resonators containing negative-stiffness mechanisms. *Physics Letters A*, 381(37):3141–3148.

Zhou, W., Wu, B., Muhammad, M., Du, Q., Huang, G., Lü, C., and Chen, W. (2018). Actively tunable transverse waves in soft membrane-type acoustic metamaterials. *Journal of Applied Physics*, 123(16).

Zhou, Y., Wei, P., Li, Y., and Tang, Q. (2017b). Continuum model of acoustic metamaterials with diatomic crystal lattice. *Mechanics of Advanced Materials and Structures*, 24(13):1059–1073.

Zhou, Y., Ye, L., and Chen, Y. (2021). Investigation of novel 3d-printed diatomic and local resonant metamaterials with impact mitigation capacity. *International Journal of Mechanical Sciences*, 206:106632.

Zhu, C. and Yang, J. (2022). Vibration transmission and energy flow analysis of variable stiffness laminated composite plates. *Thin-Walled Structures*, 180:109927.

Zhu, C., Yang, J., and Rudd, C. (2021a). Vibration transmission and energy flow analysis of l-shaped laminated composite structure based on a substructure method. *Thin-Walled Structures*, 169:108375.

Zhu, C., Yang, J., and Rudd, C. (2021b). Vibration transmission and power flow of laminated composite plates with inerter-based suppression configurations. *International Journal of Mechanical Sciences*, 190:106012.

Zhu, H., Rui, X., Yang, F., Zhu, W., and Wei, M. (2019). An efficient parameters identification method of normalized bouc-wen model for mr damper. *Journal of Sound and Vibration*, 448:146–158.

Zhu, R., Liu, X., Hu, G., Sun, C., and Huang, G. (2014). A chiral elastic metamaterial beam for broadband vibration suppression. *Journal of Sound and Vibration*, 333(10):2759–2773.

Ziolkowski, R. W. (2014). Metamaterials: The early years in the usa. *EPJ Applied Metamaterials*.